Solar Probe Thermal Protection System Risk Mitigation Study

FY 2006 Final Report

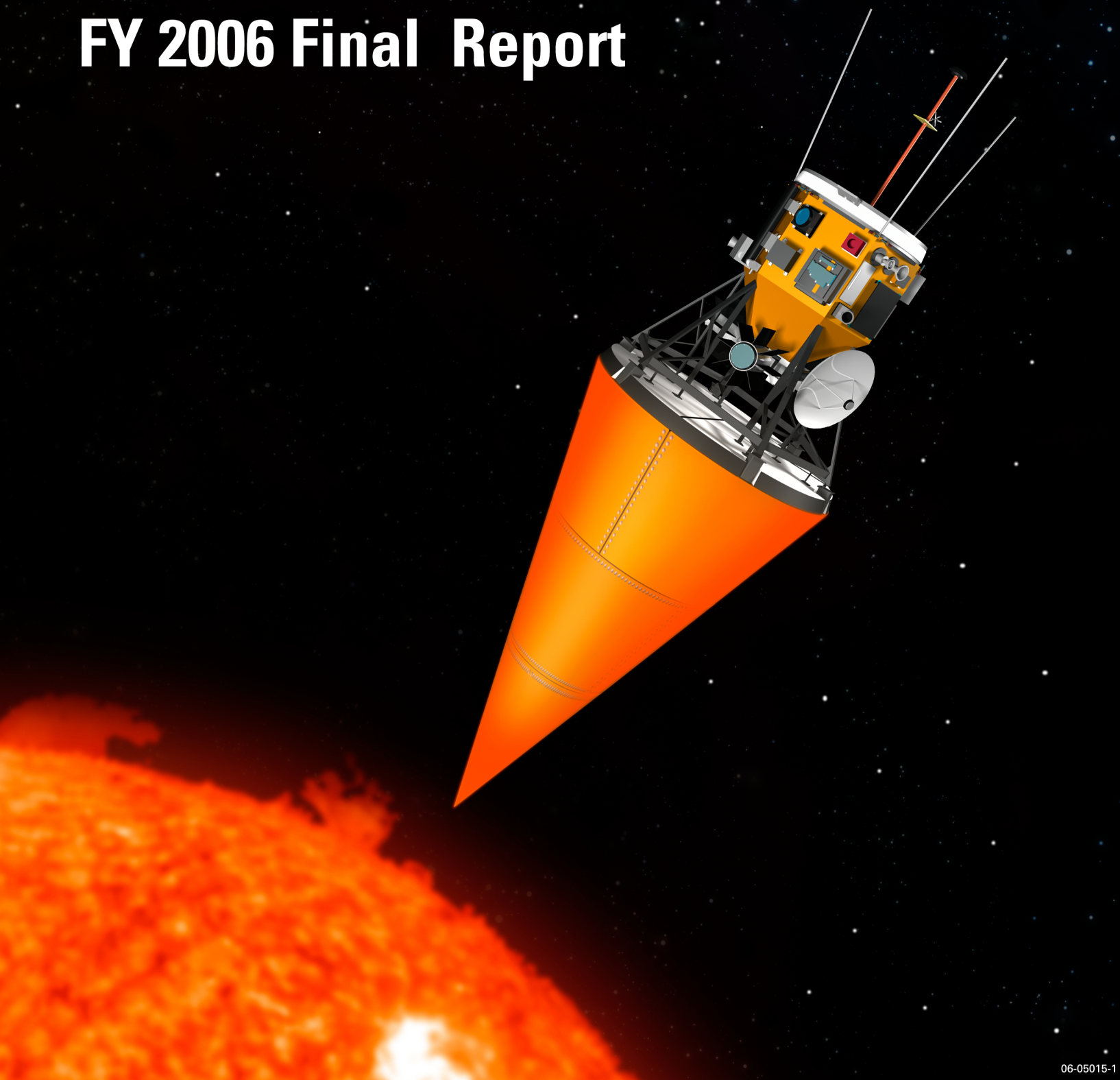

06-05015-1

Solar Probe

Thermal Protection System
Risk Mitigation Study

FY 2006 Final Report

Submitted to

APL NASA Management Office

and

NASA Goddard Space Flight Center
Living With a Star Program Office

November 30, 2006

Prepared by The Johns Hopkins University Applied Physics Laboratory,
Laurel, Maryland

Work performed under Contract NAS5-01072

Acknowledgments

NASA GSFC Management
- Ms. Haydée Maldonado, NASA GSFC, Solar Probe Study Manager
- Ms. Mary DiJoseph, NASA GSFC, LWS Program Manager
- Dr. Chris St.Cyr, NASA GSFC, LWS Senior Project Scientist

JHU/APL Management
- Dr. Ken Potocki, APL Solar Probe Project Manager
- Mr. Andy Dantzler, APL LWS Program Manager
- Mr. Doug Mehoke, technical lead
- Mr. David Drewry, materials and structures

Science Team
- Dr. Dave McComas, Southwest Research Institute, Solar Probe STDT Chair
- Dr. Ralph McNutt, STDT science measurements
- Dr. Ed Sittler, NASA GSFC, solar environment definition
- Dr. Wally Vaughn, NASA LRC, NASA carbon–carbon applications

Mechanical Systems Design
- Mr. Ted Hartka, spacecraft system design and integration
- Mr. Stan Gantz, integrated system and component detailed design
- Mr. Dave Persons, structural design
- Mr. Ray Dirling, SAIC, carbon–carbon component design, fabrication, and testing

Analytical Modeling
- Mr. Martin Annett, integrated spacecraft structural analysis
- Mr. Don King, TPS thermal analysis and document coordinator
- Dr. Michael Thomas, optical properties
- Ms. Jennifer Tanzman, structural analysis
- Dr. Lawrence Hunter, mass loss and chemical interaction modeling
- Dr. Cesar Carrasco, UTEP, high-speed particle impact
- Dr. Jerry Emhoff, science environment contamination
- Dr. Perry Malouf, RF analysis

Materials
- Mr. Keith Caruso, mass loss and radiation experiments
- Mr. Paul Wienhold, composite materials and process development
- Dr. Dennis Nagle, JHU/WSE, ceramics and carbon–carbon materials
- Dr. Craig Ohlhorst, NASA LRC, carbon–carbon material testing

Spacecraft Charging
- Dr. Jennifer Sample, charging response of materials in radiation environment
- Dr. Michelle Donegan, mission-based environment definition
- Mr. Tom Wolf, NASCAP-2K modeling
- Mr. Myron Mandell, SAIC, NASCAP-2K charging consultation

Testing
- Ms. Erin Dreyer, mechanical material testing
- Dr. Michael Rooney, mechanical material testing
- Mr. Michael Mattix, optical property measurements
- Mr. Neal Bachtell, test specimen preparation and instrumentation
- Mr. Andy Webb, high-temperature mass loss testing
- Mr. Hadi Navid, vibration testing
- Mr. Justin Jones, JHU/WSE, nondestructive evaluation
- Mr. John Newman, Laser Technology, Inc., laser shearography & thermography
- Mr. Tim Sledz, Micro Photonics, Inc., micro- and nano-CT inspection
- Dr. J.R. Dennison, USU, electronic material property characterization
- Mr. Steve Brown, NASA GSFC, low-energy proton/electron radiation testing
- Dr. Nate Jacobson, NASA GRC, high-temperature, vacuum mass loss testing
- Dr. Edbertho Leal, PUPR, low-energy plasma testing
- Dr. Barbara von Przewoski, IUCF, high-energy proton testing
- Mr. Jacques Cuneo, SoRI, high-temperature material testing

Material-Component Suppliers
- Mr. Francis Schwind, C-CAT, carbon–carbon component manufacturing
- Mr. Dominic Calamito, HITCO, carbon–carbon component manufacturing
- General Electric Advanced Ceramics, PBN
- Morgan Advanced Ceramics, PBN
- Ms. Elizabeth Schofield, Plasma Processes, Inc., Alumina
- Dr. Rama Nageswaran, SMAHT Ceramics Inc., BaZP
- Ocellus, Inc., carbon aerogel
- YLA, Inc., carbon/phenolic prepreg supplier
- Mr. Andrew Cain, SoRI, carbon aerogel impregnated carbon foam
- ERG, Inc., reticulated vitreous carbon (RVC) foam

Documentation
- Ms. Margaret Morris, document editing and production management
- Ms. Angela Hughes, document editing
- Ms. Eleanor Edgeworth, document layout and design
- Mr. Daryl George, graphics
- Mr. Jacob Elbaz, cover illustration

Contents

List of Acronyms

ACC	Advanced Carbon–Carbon
AICF	Aerogel Infiltrated Carbon Foam
Al_2O_3	Aluminum Oxide, Alumina
APL	The Johns Hopkins University Applied Physics Laboratory
AU	Astronomical Unit
BaZP	Barium Zirconium Phosphate ($BaZr_4P_6O_{24}$)
BN	Boron Nitride
BRDF	Bidirectional Reflectance Diffuse Function
BSE	Backscattered Secondary Electron
c	Speed of Light in Air
CAD	Computer-Aided Design
C-C	Carbon–Carbon
C-CAT	Carbon–Carbon Advanced Technologies, Inc.
CE	Chemical Erosion
CEA	Chemical Equilibrium with Applications
CI	Chemical Interactions
CLA	Coupled Loads Analysis
cm	Centimeter
CT	Computed Tomography
CTE	Coefficient of Thermal Expansion
CVD	Chemical Vapor Deposition
CVI	Chemical Vapor Infiltration
DSMC	Direct Simulation Monte Carlo
DUT	Device Under Test
EIRP	Equivalent Isotropic Radiated Power
E_{max}	Energy at Which Maximum Electron Yield Takes Place
EOL	End of [Mission] Life
EUV	Extreme Ultraviolet
f	Frequency
FEM	Finite Element Model
FY	Fiscal Year
g	Acceleration of gravity
GaAs	Gallium Arsenide
GHz	Gigahertz
GRC	Glenn Research Center
GSFC	Goddard Space Flight Center
HFSS	High-Frequency Structure Simulator
Hz	Hertz
ILT	Interlaminar Tensile Coupons
in.	Inch
Ir	Iridium
IR	Infrared
IUCF	Indiana University Cyclotron Facility
JHU	The Johns Hopkins University
JSC	Johnson Space Center
K	Kelvin
kg	Kilogram
ksi	Thousands of Pounds per Square Inch
lb	Pound
LHCP	Left-Hand Circularly Polarized
LRC	NASA Langley Research Center
LRSI	Shuttle Low-Temperature Reusable Surface Insulation
LV	Launch Vehicle
LWS	Living With a Star
m	Meter
MLI	Multilayer Insulation
mm	Millimeter
MMIC	Monolithic Microwave Integrated Circuit
MMRTG	Multi-Mission Radioisotope Thermoelectric Generator
Msi	Millions of Pounds per Square Inch
NDE	Nondestructive Evaluation
NZP	Sodium Zirconium Phosphate, $NaZr_2P_3O_{12}$
OG	Outgassing

PAE	Power Added Efficiency
PBN	Pyrolytic Boron Nitride
PCU	Power Conditioning Unit
PI	Particulate Impact
ppi	Pores Per Linear Inch
PS	Physical Sputtering
Pt	Platinum
PUPR	Polytechnic University of Puerto Rico
RCC	Reinforced Carbon–Carbon
RES	Radiation-Enhanced Sublimation
RF	Radio Frequency
RHCP	Right-Hand Circularly Polarized
R_J	Radius of Jupiter
RMS	Root Mean Squared
R_S	Solar Radius
RVC	Reticulated Vitreous Carbon
s	Second
SAIC	Science Applications International Corporation
SE	Secondary Electron
SEM	Scanning Electron Microscope/ Microscopy
SiC	Silicon Carbide
SoRI	Southern Research Insitute
SSPA	Solid-State Power Amplifier
STDT	Science and Technology Definition Team
STS	Space Transportation System
Ta	Tantalum
TaN	Tantalum Nitride
TDS	Time-Domain Spectroscopy
TGA	Thermogravimetric Analysis
THz	Terahertz
TIR	Total Integrated Reflection
TIS	Total Integrated Scatter
TML	Total Mass Loss
TPS	Thermal Protection System
TRL	Technology Readiness Level; *also* Thru-Reflect-Line
TV	Thermal Vaporization
USU	Utah State University
UTEP	University of Texas at El Paso
UV	Ultraviolet
W	Watt
WSE	The Johns Hopkins University Whiting School of Engineering
XRD	X-Ray Diffraction

α	Absorptivity
α-Al_2O_3	Alpha-Phase Alumina
α_λ	Spectral Absorptance
δ_{max}	Maximum Electron Yield
$\Delta\phi$	Phase Delay
Δx	Sample Thickness
ε	Emissivity
ε_λ	Spectral Emittance
γ-Al_2O_3	Gamma-Phase Alumina
λ	Wavelength
ρ	Reflectance
ρ_λ	Spectral Reflectance
τ_λ	Spectral Transmittance

Executive Summary

The Solar Probe mission will be historic, answering fundamental scientific questions about the heating of the Sun's corona and the acceleration of the solar wind. The report of the Solar Probe 2005 Science and Technology Definition Team (STDT) defined the key science objectives for a mission to the Sun.[1] The report also detailed the science payload and supporting spacecraft bus that would be needed to implement such a mission.

A key part of the spacecraft bus design is the Thermal Protection System (TPS), which must shield the bus and payload from the extreme solar heating around the spacecraft's closest approach to the Sun. While the TPS design builds on existing hardware and technology innovations of other flight programs, it is a large step forward in the evolution of lightweight carbon–carbon (C-C) structures for space. As such, it represents a high-risk item, and its Technology Readiness Level (TRL) needs to be increased to a level of 6 before the start of the flight program.

The Solar Probe risk mitigation effort began as an outgrowth of the STDT study. Its purpose is to demonstrate that the TPS design presented there is feasible by designing, fabricating, and testing a full-scale prototype. The TPS design stage, which has been completed, gave rise to the following conclusions:

- A full-size system can be built that meets the requirements and constraints defined in the STDT study. Critical TPS design, manufacturing, and inspection elements have been addressed that leverage prior and ongoing NASA and Department of Defense programs in high-temperature materials technology. Backup design options have been identified for all key features.
- The use of a ceramic coating significantly reduces mission risk by lowering the TPS operating temperatures. Baseline and backup coatings exist with the required stability over the range of mission environments (temperature and radiation).
- The proposed design meets the present mass loss and surface charging requirements. The mechanisms, materials, and predictive methods for both phenomena have been investigated as part of a science committee review of those requirements.
- Material coupon and element testing has been used to verify the analytical performance of the material properties used in the design

[1] *Solar Probe: Report of the Science and Technology Definition Team,* NASA/TM—2005–212786, National Aeronautics and Space Administration, Goddard Space Flight Center, Greenbelt, MD (2005).

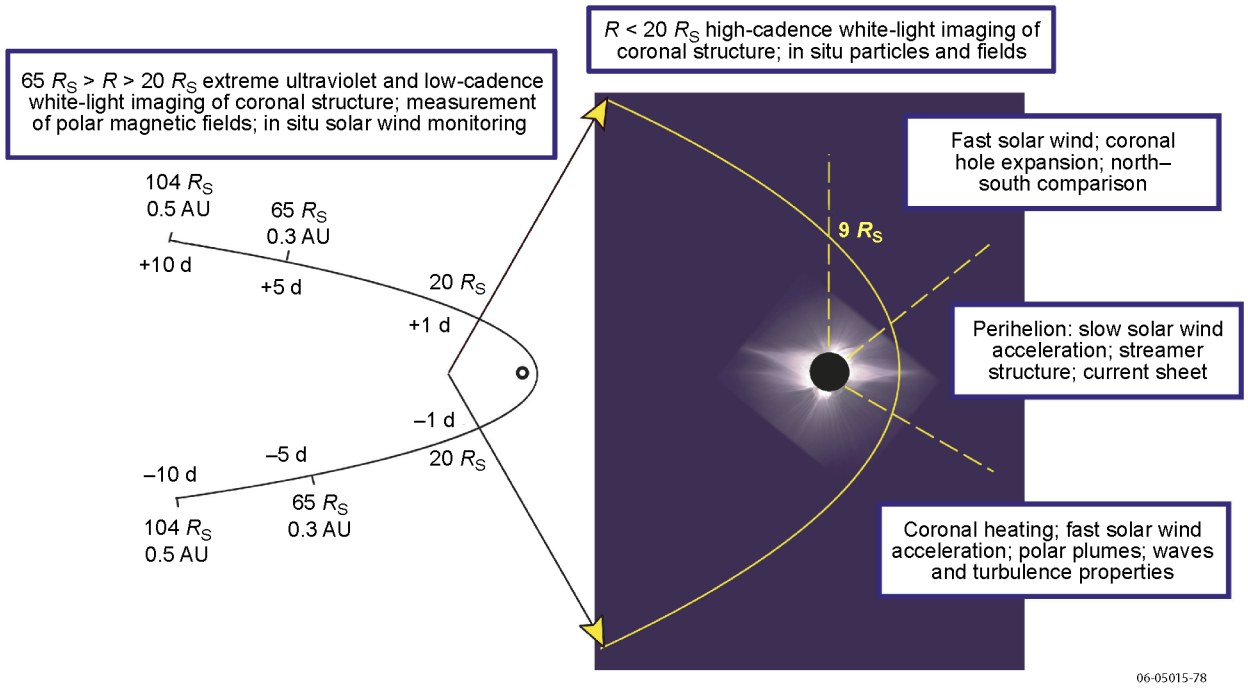

Solar Probe science measurements and objectives as function of orbital position.

and to ensure that the proposed TPS material property data are "in-family" with published values.

Goals of the TPS Risk Mitigation Study

The major goal of the Solar Probe Risk Mitigation Study is to prove that the TPS design shown in the 2005 STDT report can be built within the mass, volume, structural, and thermal insulating constraints listed in that report. To realize that goal, a multi-year study plan was developed. In the first phase, covering fiscal year 2006, the required material databases, design trade studies, and component testing necessary to design the TPS were completed. Plans for the second phase are to build a full-sized prototype and test it over the predicted mission environments. This report describes the results of the first phase of the study.

Baseline Solar Probe Mission

The baseline Solar Probe mission remains the same as that detailed in the 2005 STDT study. It includes two flybys of the Sun, separated by 4.6 years. The timing allows scientific measurements to be made of the solar wind and corona at different phases of the 11-year solar cycle, independent of the launch date.

Solar Probe will use a Jupiter gravity assist to achieve a polar orbit about the Sun with a perihelion of 4 solar radii (R_S) (that is, 3 R_S above the Sun's surface). The spacecraft will approach the Sun from the south about 4.1 years after launch. Its maximum velocity will be over 300 km/s, making Solar Probe the fastest ever human-made object. The encounter geometry allows real-time data to be received via a Ka-band telecommunications system. The Atlas 551 is baselined as the launch vehicle, although he mission design allows dual-launch compatibility with the Delta IV Heavy.

The Solar Probe spacecraft is designed to both support and protect the science payload over the extreme environmental variations that it will experience during the mission. The science payload is a single, integrated package consisting of both in situ and remote-sensing instruments. Moveable arms give specific instruments views near and beyond the edge of the TPS umbra during different parts of the mission. The spacecraft is a 3-axis stabilized bus that hides within the conical umbra of the TPS when close to the Sun. It is powered by three multi-mission radioisotope thermoelectric generators (MMRTGs). A monopropellant propulsion system is used for ΔV maneuvers and attitude control. The guidance and control system consists of redundant Star trackers, an inertial measurement unit, digital Sun sensors, 4 reaction wheels, and 12 thrusters. The spacecraft is equipped with one high-gain antenna, a medium-gain antenna, and two low-gain antennas.

TPS Design

The most prominent feature of the spacecraft bus is the large C-C structure protecting the payload and spacecraft bus around closest approach to the Sun. The TPS allows the payload and bus to get near enough to the Sun to make the needed scientific measurements.

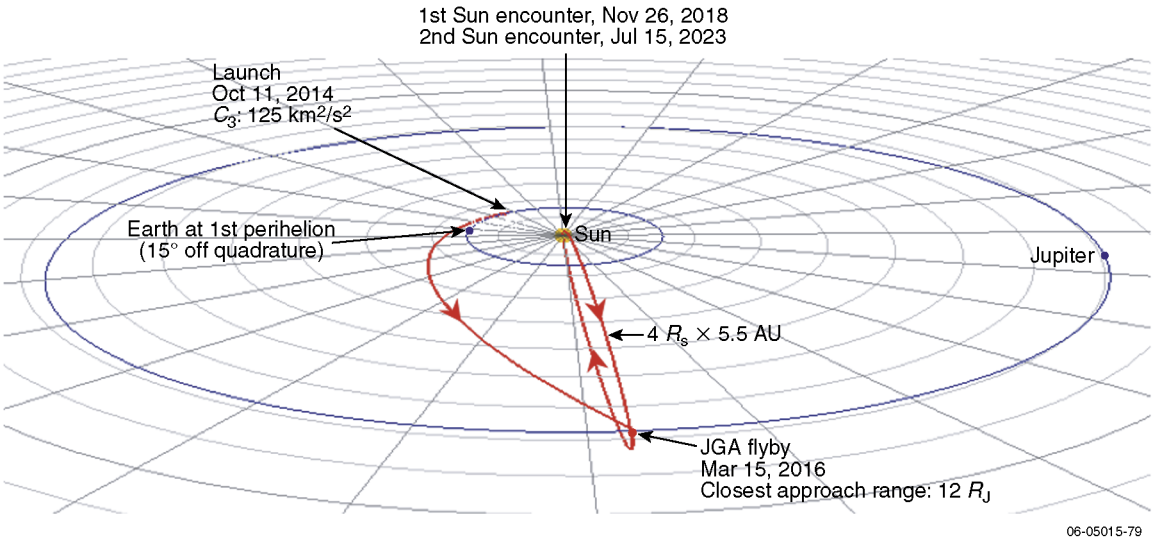

Solar Probe mission summary.

The 2005 STDT study defined system-level requirements for the TPS mass, umbra volume, thermal insulation, and mass loss. The nominal design presented there included a conical primary shield, a thermally insulating secondary shield, and supporting struts. During this study, detailed designs were developed for all three components that meet the requirements of the 2005 STDT report.

While the Risk Mitigation Study developed detailed designs for the nominal TPS presented in the 2005 study, it also "colored in" the trade space around those designs. While there is ongoing Department of Defense and NASA work in all of the materials used in the TPS, these materials do not have the level of design heritage found in conventional spacecraft structures. Furthermore, much of the design heritage that does exist is tied to the specific materials and the experience of a particular vendor with those materials. Therefore, the study was divided into design steps, where each step built on the experience obtained in the preceding efforts. This sequential flow, coupled with continuing input from the materials vendors, allowed us to develop a detailed view of the available design landscape and to alter our path across that landscape as conditions required.

The resulting TPS design presented here provides a technically feasible approach with an array of alternative options for every key component. Mechanical details are given for every part required to assemble a full-sized TPS. Design analyses are presented showing significant margin in all areas. Test data are given, based on available databases and on our own testing, that support the analytical properties used throughout. Finally, included in all of these discussions is an understanding of the strengths of the chosen materials and design features, on the basis of the supporting vendors' experience, that gives us confidence in our ability to proceed to the next phase.

C-C is used as the material for the high-temperature structures in both the primary and secondary shields. It is the only material with the required combination of stability at elevated temperatures and high specific stiffness. C-C material property data and design details have leveraged existing programs in the fields of high-temperature engines and atmospheric reentry vehicles. Input from experienced C-C vendors was used to support material choices, fabrication processes, and design features required by the TPS. With the use of existing materials databases, as well as the specific coupon and analog testing done as part of this study, the TPS design presented here is based on demonstrated material property data and proven design concepts.

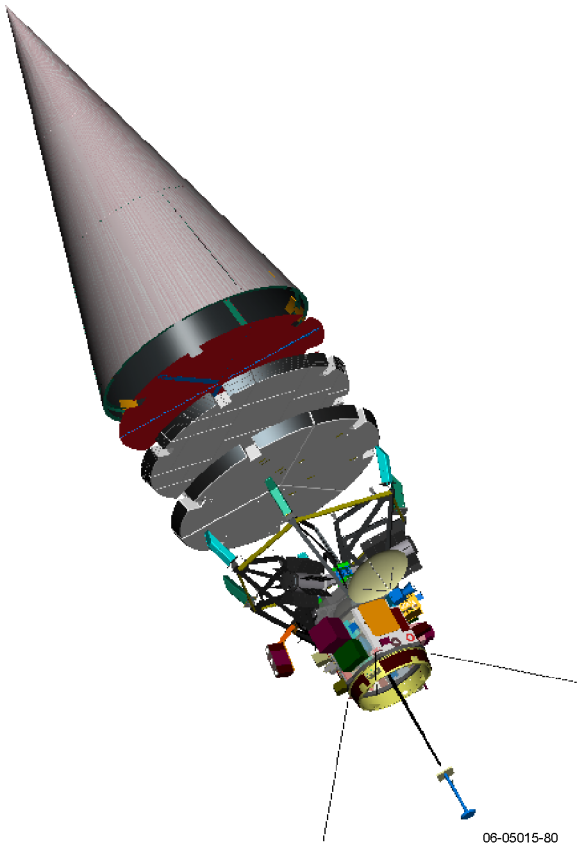

Exploded view of TPS and spacecraft bus.

Carbon foam is used as the primary insulating material in the secondary shield. It is a commercially available material with very low thermal conductivity and density. It is thermally stable over the required range of temperatures and provides the required temperature drop between the primary shield and the room-temperature spacecraft bus. Alternative materials exist in the form of carbon aerogels and aerogel infiltrated carbon foam (AICF), which promise mass reduction through improved thermal performance.

A major innovation in the TPS design, developed during this study, is the segregation of the support structure into higher- and lower-temperature regions. This design approach was enabled by a combination of factors: a reduction in primary shield temperature, improved thermal capabilities from the carbon foam, and transfer of the secondary shield support from the primary shield to the spacecraft bus. The addition of a lower-temperature

support region enabled the use of a traditional truss-flexure system for the primary structural loads. This truss-flexure system, operating below 350°C, is tailored to handle the large mismatches in coefficient of thermal expansion by using more efficient structural materials.

Coatings

A key finding of the 2005 STDT report was that the use of a ceramic coating on the primary shield was both beneficial and feasible for the Solar Probe mission. Whether coated or not, the temperature of the primary shield is a direct function of the optical properties of the exposed surface. Early work done as part of this effort showed that the variation in C-C optical properties was too large to leave the surface in an as-fabricated condition. Several ceramic coatings were identified that had the required optical properties and the needed adhesion capabilities on C-C. Of these, alumina is considered the baseline. Pyrolytic boron nitride (PBN) and barium zirconium phosphate (BaZP) also are being tested in parallel to ensure that alternatives exist in case of future problems.

The details of coating design have leveraged the extensive work performed to support high-speed missiles and reentry vehicles. That work focused on how coatings can be designed to better bond to the underlying substrate and to define the analyses and testing needed to ensure that the coatings stay intact. The design heritage from those programs was leveraged in the TPS coating effort.

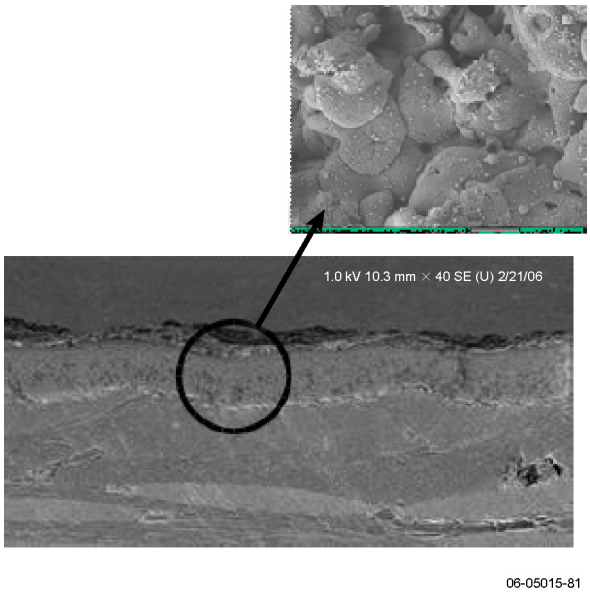

Plasma-sprayed Al_2O_3.

The stability of the coating optical properties was verified over the range of expected mission environments. Optical property testing for all materials included room-temperature and some high-temperature characterization, as well as characterization of susceptibility to radiation damage.

Mass Loss

Mass loss from the spacecraft comes from a variety of sources—thermal vaporization of coatings or C-C, high-temperature material interactions between C-C and the coating, coating spallation due to radiation and particle impacts, and high-temperature radiation damage. The present design meets the mass loss requirement of 2.5 mg/s. This mass loss requirement has been carried forward from previous studies[2] and is under review by the science committee. The mass loss mechanisms are described and quantified in this report.

Material mass loss data were obtained through a combination of literature reviews, analytical predictions, and testing performed for this study. All of the key materials used in the study have been tested. Chemical Equilibrium with Applications (CEA) modeling was used to predict vapor pressures and mass loss rates. FactSage was used to model the chemical interactions and interface stabilities between materials at high temperatures. The NASA Glenn Research Center (GRC) was involved

[2]Goldstein et al., *Spacecraft Mass Loss and Electric Potential Requirements for the Starprobe Mission*, A report of the Starprobe Mass Loss Requirements Group Meeting of September 29–30, 1980, NASA Jet Propulsion Laboratory, California Institute of Technology, Pasadena, CA (December 1980).

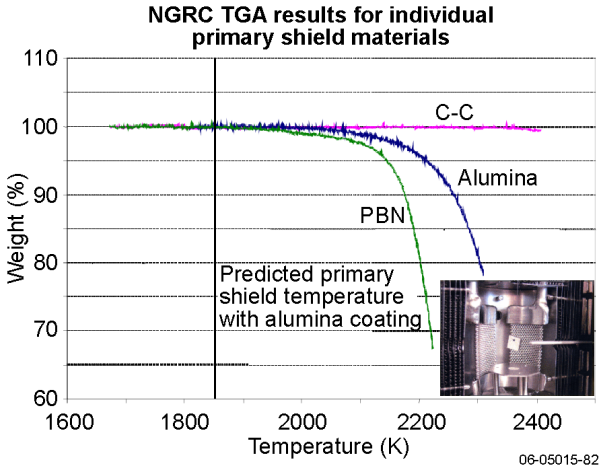

Primary shield candidate materials are stable at key temperatures when tested individually.

as part of a collaborative effort to characterize the temperature and vacuum stability of the primary shield materials. Additional materials testing was done at The Johns Hopkins University Applied Physics Laboratory to corroborate the GRC data.

The test data and analytical predictions correlated well. At the TPS operating temperatures, the mass loss is dominated by the primary shield coating and is an order of magnitude below the limit. C-C outgassing approaches the required limit at temperatures over 400°C higher than the operating temperature. Mass loss due to radiation damage is quantified through data obtained from the nuclear industry, but the resulting mass loss is not appreciable. Future work is planned to refine the accuracy of the measured mass loss data.

Charging

Charging and radiation effects are important to both the health of the spacecraft and the quality of the in situ measurements taken. Specific charging and surface conductivity requirements are under review by the science committee, but it is clear that the phenomenon of charging is important to the Solar Probe mission. As part of this Risk Mitigation Study, the radiation environment, charging mechanism, material properties, and analytical codes related to charging were investigated.

All of the coatings investigated for Solar Probe, the baseline and the alternates, are ceramics with beneficial optical properties. These coatings are typically electrical insulators, but they become conductive as their temperature rises around closest approach to the Sun. The combination of varying critical properties (i.e., electrical conductivity, photoemission, and secondary electron emission) in the changing radiation environments produces a dynamic charging mechanism that changes as the spacecraft moves toward the Sun. It is during this same period that the science measurement phase is beginning. Therefore, as an input to the requirement definition effort underway, a goal of the risk mitigation effort has been to investigate the radiation environment, charging mechanism, and predictive capabilities needed to assess the impacts of charging on the required Solar Probe local environment.

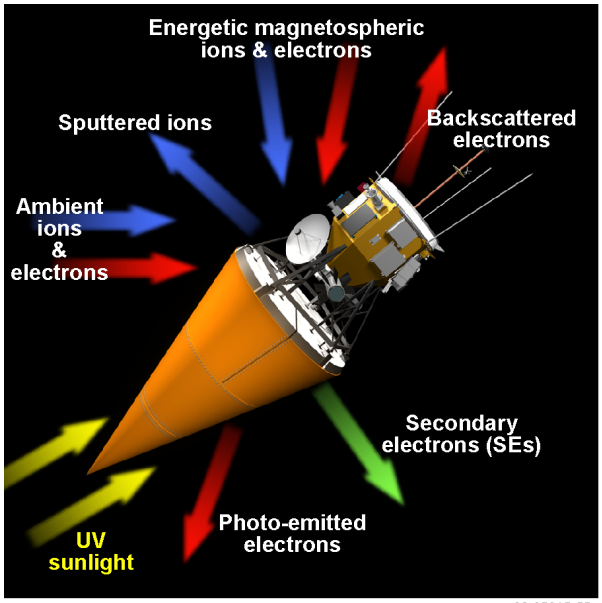

Major processes that impact spacecraft charging.

The effort was divided into three parts: definition of the radiation environment, generation of the appropriate material properties, and prediction of the spacecraft charging levels. Each part included the support of recognized experts in the particular fields. Dr. Edward Sittler of NASA Goddard Spaceflight Center (GSFC) consulted in the generation of the radiation environments. Dr. J. R. Dennison of Utah State University made the material property measurements necessary to quantify the behavior of the materials in the various environments, and Mr. Myron Mandel of SAIC consulted on modeling efforts and how the material properties were used in the NASCAP-2K analytical code.

The combination of these efforts led to a set of surface charging predictions covering all mission phases. Radiation estimates were reviewed from the earlier study for the near-Sun (4 R_S), start of science (0.3 AU), deep space, and Jovian environments. In addition, charging environments were generated for solar distances between 0 and 0.5 AU to show how the spacecraft will be affected as it moves toward or away from the Sun. The results show differential charging in the range of tens of volts at Jupiter dropping to a few volts uniform charging at closest approach.

Materials and Process Development

The TPS development plan stresses the use of existing materials and processes in all areas of the design. No new materials or developmental processes are required. As with any design, it is important to anchor the supporting thermal and structural analyses with established material property data. Because many of the materials in the TPS design are not widely used in space applications, the need for reliable material property data is even more important.

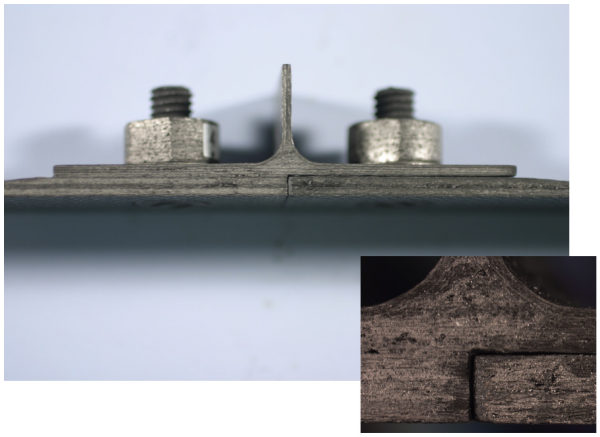

06-05015-83

Photograph of primary shield T-section test coupon prior to mechanical testing. Insert: blowup of joint region.

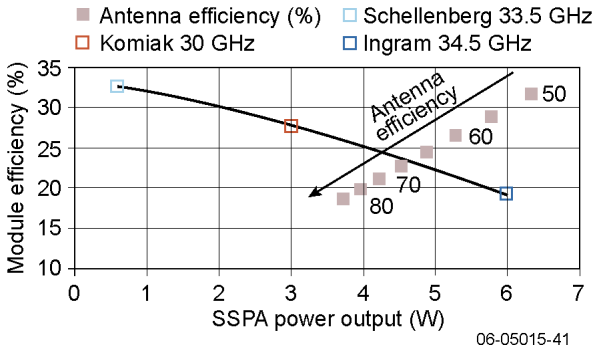

RF parameter trade-off used to define requirements for Ka-band design study.

A main part of the TPS Risk Mitigation Study has been to develop the required materials databases to support the proposed design. This effort included reviewing existing data from other programs and performing coupon testing of our own materials. Coupon testing ensured that the specific material property values used in the design were consistent with the data reported in the literature. All of the materials and processes planned for use in the TPS have been tested.

Risk Mitigation Results for the Ka-Band Portion of the Solar Probe RF Telecommunications Subsystem

A key finding of the 2005 STDT study was a requirement to have a real-time downlink during the first solar pass. As another part of the Solar probe risk mitigation effort, preliminary work on requirements and implementation of the Ka-band portion of the telecommunications subsystem was conducted. The results of that effort (summarized in the appendix) include an examination of the performance requirements in light of the state-of-the-art technology and a reasonable design for the Ka-band circuit.

A Solar Probe link analysis was completed to define the required radiated power. Next, a trade study was done to determine the antenna efficiency and power added efficiency of the solid-state power amplifier (SSPA) that could satisfy the link requirements. Optimistic antenna efficiency and SSPA performance goals make the hardware design task challenging and stress the need to minimize RF power losses.

A hardware design is proposed, and test data for three components of the design are presented and discussed. Computer modeling of a fourth component is described and compared with measurements made on test hardware of that component. Design options are discussed for all components, and recommendations are given for proceeding to the next level of effort.

Summary

Solar Probe is an exciting mission to one of the last unexplored regions of the Solar System. The 2006 risk mitigation effort completed the first of two steps necessary to demonstrate that the 2005 STDT TPS design is technically feasible and can be accomplished within realistic resources. The detailed design presented here shows that a large C-C structure can be built within the defined requirements. In addition to the baseline design, viable alternatives are presented for all key features. Maintaining these options is important in keeping the overall risk low while the study effort progresses to full-scale prototype development. The information gained in this study includes vendor, materials, and processing options that better define the trade space around the baseline design.

1 Design Status of the Solar Probe Observatory

1.1 Description of the Solar Probe Mission

> Solar Probe will be a historic mission, flying into one of the last unexplored regions of the solar system, the Sun's atmosphere or corona, for the first time. Approaching as close as 3 R_S above the Sun's surface, Solar Probe will employ a combination of in-situ measurements and imaging to achieve the mission's primary scientific goal: to understand how the Sun's corona is heated and how the solar wind is accelerated. Solar Probe will revolutionize our knowledge of the physics of the origin and evolution of the solar wind. Moreover, by making the only direct, in-situ measurements of the region where some of the deadliest solar energetic particles are energized, Solar Probe will make unique and fundamental contributions to our ability to characterize and forecast the radiation environment in which future space explorers will work and live.

Thus reads the opening paragraph of *Solar Probe: Report of the Science and Technology Definition Team*.[1] The report defined the science objectives, science implementation, and baseline mission for our first trip to the Sun. An important part of that effort was demonstrating that the mission objectives could be achieved with a specific science payload and spacecraft bus, and to allocate power, mass, and volume for that nominal design.

1.2 Focus of the Solar Probe Thermal Protection System Risk Mitigation Study

The spacecraft bus defined in the 2005 Science and Technology Definition Team (STDT) study reflects a nominal design approach with one large exception: the Thermal Protection System (TPS). The TPS is a shield that protects the spacecraft bus from the unimaginably intense solar heating. The 2005 study observatory design is shown in Figure 1-1 (2005 STDT report, p. ES-5).

One outcome of the 2005 STDT study was an assessment that the TPS, while appearing technically feasible, was a major risk that needed to be addressed before Solar Probe could proceed into a Phase A effort. Because of its size, materials, and operating temperatures, the TPS fell far enough outside normal design experience to require that its technology readiness level (TRL) be raised to 6 to retire the risk associated with the design. A risk mitigation effort was initiated to demonstrate the TPS design by building and testing a full-size prototype in the flight-like environments that it would have to endure during the Solar Probe mission.

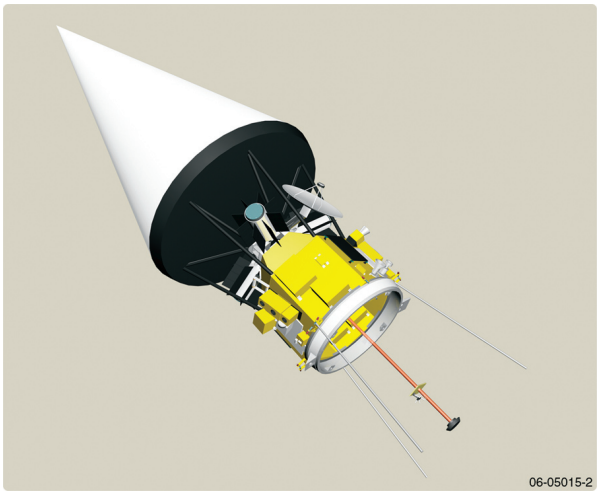

Figure 1-1. Solar Probe observatory design from the 2005 STDT report.

The risk mitigation study was separated into two phases. The first phase developed the specific design and supporting material databases for the TPS. The second phase plans to build and test a full-size system. This report covers the work done in the first phase of that effort during fiscal year (FY) 2006. The first phase had the following goals:

1. Develop detailed designs of the primary shield, secondary shield, and supporting structure.
2. Develop the engineering material and optical property databases required to support those designs.
3. Develop specific material and coupon testing methods needed to verify the construction.
4. Demonstrate critical design elements, manufacturing processes, and nondestructive evaluation (NDE) techniques by analog testing.

The second phase plans to fabricate and test a full-size TPS in simulated flight environments. Due to facility limitations, the structural testing and thermal testing will have to be done separately. Structural testing will be done using existing facilities at NASA's Goddard Space Flight Center (GSFC), and

[1] *Solar Probe: Report of the Science and Technology Definition Team*, NASA/TM—2005–212786, National Aeronautics and Space Administration, Goddard Space Flight Center, Greenbelt, MD (2005).

the thermal testing will require an upgrade of the facilities at NASA's Johnson Space Center (JSC).

1.3 Overview of the STDT Study

1.3.1 Spacecraft

The Solar Probe spacecraft will operate between 0.02 and 5.5 AU from the Sun, as well as in close proximity to Jupiter (within 12 Jupiter radii, R_J). It accommodates the science payload defined by the 2005 STDT study and the necessary spacecraft support subsystems. The major Solar Probe components are shown in Figure 1-2 (2005 STDT report, Figure 4-6). The spacecraft is powered by three multi-mission radioisotope thermoelectric generators (MMRTGs) supplying approximately 300 W at the end of mission life (EOL). Attitude control is 3-axis stabilized. The design includes power and mass allocations for the science payload, spacecraft subsystems, and the TPS. The most prominent design feature of the spacecraft is the TPS.

1.3.2 Thermal Protection System

The TPS will protect the spacecraft bus and instruments within its umbra during the solar approach and at solar distances closer than 0.8 AU. The TPS has three basic design requirements:

- Provide thermal protection for the spacecraft and instruments defined in the STDT study.
- Survive the various environments from launch through multiple solar passes.
- Support the in situ measurements during closest approach by limiting spacecraft interactions with the local environment.

The TPS design consists of three parts: the primary shield, whose purpose is to limit the temperature and reject most of the solar heat to space; the secondary shield, which reduces heat transfer to the bus to a manageable level; and the struts, which support the TPS shields a safe distance from the spacecraft bus. The importance of the TPS performance can best be explained by noting that the approximately 21 MW of solar flux incident on the TPS must be reduced to less than 50 W transmitted to the spacecraft bus.

The primary shield provides the first step in solar protection by reflecting and emitting most of the incident flux away from the observatory. It reduces the solar heat input by 75% by minimizing its view factor to the Sun and maximizing the view to space. A 40% reduction of the remaining input is achieved through the use of a suitable coating. The primary

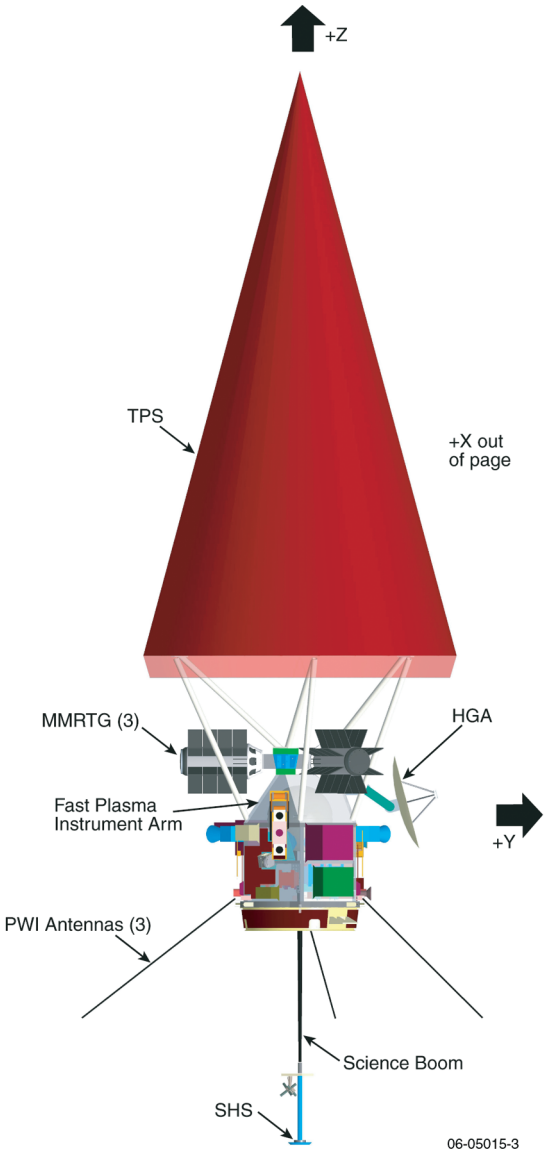

Figure 1-2. Spacecraft and instruments defined in the 2005 STDT report.

shield is 2.7 m in diameter and 5.1 m high. It is made of a carbon–carbon (C-C) shell 0.8 mm thick. The cone has a half angle of 15°. Through changing the primary shield cone angle and optical coating properties, the primary shield temperatures can be made to vary from less than 1600 K to in excess of 2100 K. Potential coating materials, designed to provide beneficial optical properties, included aluminum oxide (alumina or Al_2O_3), pyrolitic boron nitride (PBN), and barium zirconium phosphate (BaZP). Elevated temperature optical property measurements of these materials resulted in a ratio of solar absorptivity to infrared (IR) emissivity (α/ε) that varied from 0.1 to 0.4. A design threshold

(for any coating) was set at $\alpha/\varepsilon = 0.6$, resulting in a primary shield temperature of 1850 K. Part of the FY2006 risk mitigation effort was aimed at validating these values. The mass allocation for the primary shield, including 30% margin, was 68.5 kg.

Beneath the primary shield, the secondary shield limits the heat flow from the primary shield through to the spacecraft. The secondary shield is made up of layers of carbon foam supported by upper and lower C-C facesheets. The top of the secondary shield is exposed to the primary shield temperature. The bottom facesheet radiates to the MMRTGs, the spacecraft, and space. Reticulated vitreous carbon (RVC) foam was selected as the baseline material because of its low thermal conductivity and because it is commercially available. Part of the FY 2006 risk mitigation effort was to investigate the options for developing new insulation materials. A low-emissive coating of multilayer insulation (MLI) was included on the lower surface of the shield to reduce the heat flow further. Temperatures for the bottom surface of the secondary shield were predicted to be 500 K (or less). The mass allocation for the secondary shield, including 30% margin, was 92.2 kg.

In the 2005 STDT study, 12 struts supported the TPS off the spacecraft bus. The struts were 5-cm-diameter, 0.5-mm-thick C-C tubes. The struts penetrated the secondary shield and were attached to the bottom of the primary shield cone. The struts provided a 0.6-m separation between the secondary shield and the spacecraft bus that maximized the amount of heat that could be rejected from the secondary shield to space. The separation distance is limited by the launch vehicle fairing size, the spacecraft volume in the conical TPS umbra, and the ability of the struts to support the TPS structurally. Since the struts are attached directly to the primary shield, they are a major source of heat input into the bus. In the study, a design contingency allowed for six of the struts to be thermally disconnected if their heat input into the bus was too large. A total mass of 13.3 kg, including 30% margin, was allocated for the struts.

1.4 TPS Design Drivers

During the 2005 STDT study, the driving requirements for the TPS were developed. These requirements can be grouped into environmental, configurational, and scientific categories. They are based on the STDT design study in terms of the science payload, spacecraft configuration, and mission, and are summarized in Table 1-1.

The TPS must survive all environments between launch and multiple solar passes. For the launch environment, 15 Hz lateral and 35 Hz thrust limits were assumed. These structural requirements are consistent with launch environments for either the Atlas V or Delta IV launch vehicles. The radiation environment is dominated by the electrons and protons at Jupiter closest approach (12 R_J). It also includes the MMRTG gamma radiation and solar protons. The design limit of 44 krad Si, including margin, was calculated assuming 2.5 mm of aluminum shielding. The solar flux at closest approach is 400 W/cm^2 or 3000 Suns. At Jupiter the TPS will fall to –200°C.

Table 1-1. STDT performance goals derived from the 2005 STDT report.

Requirement	Value
Environmental	
Structural	15 Hz lateral 35 Hz thrust
Ionizing radiation	44 krad Si
Solar flux	Max 400 W/cm^2 Min 0.005 W/cm^2
Configuration	
TPS mass	174 kg (with 30% margin)
Primary shield diameter	≥2.72 m
Primary shield length	≤5.1 m
Science measurements	
Mass loss	2.5 mg/s
Primary shield surface α/ε	0.6
Surface conductivity	Conductive
Heat flow into spacecraft	<50 W

The configuration requirements were set to provide the spacecraft volume and mass constraints for the defined instrument payload. The mass limit of 174 kg, including margin, is important. The total observatory mass is fixed by the launch vehicle. Increases in the TPS will have to be supplied by reductions elsewhere. Maximizing the science payload mass is an important goal of the mission. The TPS diameter, 2.7 m, is fixed by the required volume inside the umbra cone for the spacecraft bus and science payload. The required umbra cone

includes a 2° safety factor beyond the enclosed observatory. The cone height, 5.1 m, is limited by the ability of the observatory stack to fit within the launch vehicle fairing envelope.

The final set of requirements was placed on the TPS to ensure that it did not interfere with the planned science measurements. The first of these is a mass loss limit for the observatory of less than 2.5 mg/s. At closest approach to the Sun, the high temperatures will increase outgassing rates and other types of mass loss. At some point, the mass ejected by the spacecraft would overwhelm the particle measurements being made. The mass loss limit has been carried forward from previous studies and is under review by the science team. A related requirement is the primary shield coating optical property limit of $\alpha/\varepsilon \leq 0.6$. The safety of the mission is increased significantly with lower temperatures, which are driven by the optical properties of the cone surface. Analysis and testing done during the STDT study indicated that 0.6 was a realistic design requirement. Electrical charging of the primary shield surface is an important factor in the science measurements that need to be made. The study participants realized that the electrical charging of the cone would have to be controlled, although a numerical limit was not included. Surface charging has been a focus area of the FY 2006 risk mitigation study. The last 2005 STDT requirement was on the heat flow to the spacecraft from the TPS. Spacecraft heat flow occurs through both conduction and radiation. It affects the ability of the science instruments and spacecraft bus to survive the encounter.

2 Outline of the Solar Probe TPS Risk Mitigation Study

The Solar Probe risk reduction effort is aimed at elevating the Thermal Protection System (TPS) to a technology readiness level (TRL) of 6 over a multi-year plan. Since the TPS design would be the largest carbon–carbon (C-C) structure flown in space, retiring the associated risk requires full-scale testing for both mechanical and thermal conditions. The effort is roughly divided into two phases: the first phase for design and analysis, and the second for fabrication and test.

The goal of the first phase was to establish a design that met the requirements developed in the 2005 STDT study[1] (Table 1-1) and that could be successfully carried forward into fabrication and test. The first phase is now complete. This report provides the detailed results and achievements of the first phase of the TPS Risk Mitigation Study.

The risks addressed in the TPS Risk Mitigation Study include both programmatic and technical issues. Programmatic issues in the areas of cost and schedule are identified on the program and vendor side through completing the design and fabrication of a full-scale prototype. During the first phase, the team defined requirements, completed trade-off studies, surfaced design issues, demonstrated fabrication processes, and developed assembly techniques. On the technical side, these same activities identified the driving components in the design and determined the important parameters of those components. During the second phase, fabrication and test of a prototype unit will provide experience and heritage, which will be important in reducing cost, schedule, and performance problems for the flight program.

2.1 Risk Mitigation Study Approach

The TPS study trade space involved investigation of design options, material choices, and potential vendors. As a risk reduction effort, this study has focused not only on developing a design but also on documenting the design evolution. Component-level design details address specific derived requirements that support overall system performance. However, as with any design, there are several ways to satisfy the requirements. A process was required that allowed the design to be refined as the experience level grew.

[1] *Solar Probe: Report of the Science and Technology Definiton Team*, NASA/TM—2005–212786, National Aeronautics and Space Administration, Goddard Space Flight Center, Greenbelt, MD (2005).

The overall approach taken during the design phase of the TPS was to emphasize mass minimization and leverage vendor experience. A lightweight TPS frees up mass to be used elsewhere, especially to maximize the science return. TPS mass can be reduced both by the choice of structural materials and by reducing the primary shield temperature through the use of optical coatings. Vendor experience, especially in the areas of C-C design and fabrication techniques, played a major role in shaping the design. The evolution of C-C into a structural material is ongoing in several other NASA and Department of Defense programs. Materials and processes being developed on those programs were leveraged for the TPS effort. Three U.S. vendors, Goodrich, HITCO Carbon Composites, Inc., and Carbon-Carbon Advanced Technologies, Inc. (C-CAT), work extensively in the field of C-C composites. Each company has specific experience and expertise that was leveraged to support our effort. Finally, understanding the behavior of the optical coatings in the flight environment was a key part of establishing their viability for this mission.

2.2 First-Phase Effort: The Design

The design phase of the study was divided into four steps. The first step focused on developing the relevant material property databases. The second used those databases, plus the 2005 STDT configuration, to define a "zero-order" design as a starting point for this study. The third step completed that design and compared it against the study requirements. Initially, the fourth step was expected to be a refinement of the step 3 design. As will be discussed in chapter 3, the transition from step 3 to step 4 resulted in the replacement of the ball-and-strut design (step 3) with a more practical truss approach (step 4).

Figure 2-1 shows the components in the 2005 STDT configuration in black. The items added to the ball and strut design during steps 2 and 3 are shown in red italic type. Not shown, but listed in blue, are the step 4 changes that make up the new truss design.

2.2.1 Step 1: Develop Material Property Database

The first step in the TPS Risk Mitigation Study was to develop material databases for the necessary materials and processes. Three important material types were identified: C-C, high-temperature insulation, and C-C coatings. C-C is

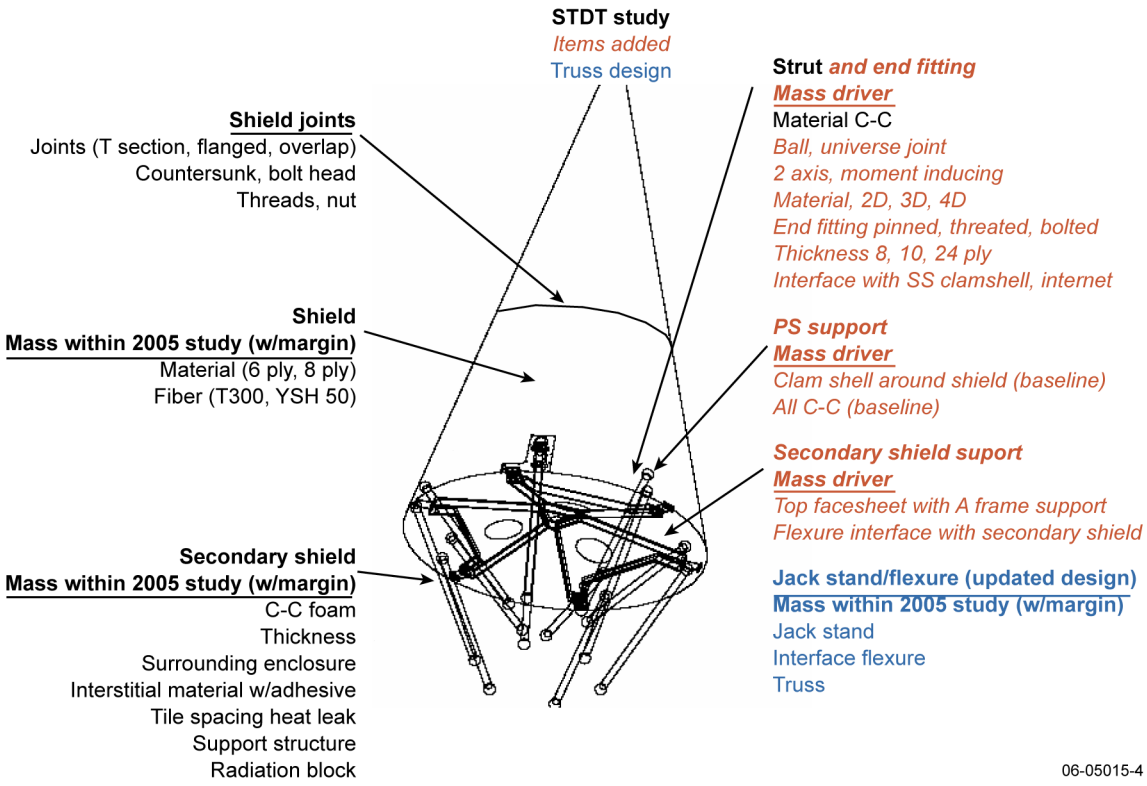

Figure 2-1. Evolution of the Solar Probe design from the 2005 STDT report to the 2006 TPS Risk Mitigation Study.

used in all the high-temperature structures. High-temperature insulation is required in the secondary shield to reduce the heat radiated to the spacecraft. Lastly, the optical properties, (ratio of absorptivity to emissivity, α/ε) of the coating are the key item in defining the operating temperatures of the system.

Carbon–Carbon. Over the past 10 years, C-C materials have evolved to the point where they are being used in a variety of large structural applications. Programs using C-C materials in this manner include Mars Sample Return, HyFly, X-37, and Falcon. All of these programs involve reentry or high-speed structures in atmospheric applications. Complex structures requiring special design features and assembly techniques have been developed and are being flown. Mechanical test property data for the C-C materials used on these programs have been published. The TPS study team contracted with two of the three potential vendors in the field to provide test coupons to ensure that the materials and design techniques investigated in the study are "in-family" within their existing experience base. The third vendor opted not to respond.

C-C materials are designed and fabricated much like conventional laminated graphite–epoxy composites. A carbon fiber and a matrix material are combined to produce a structural member. The principal difference in C-C materials is that the matrix material is also carbon. The non-carbon material in the original matrix is pyrolized (converted to carbon) in a series of high-temperature densification cycles. There are currently two such densification processes: resin impregnation and chemical vapor infiltration (CVI). Resin impregnation involves physically infusing a resin into the laminate (i.e., pulling resin into the material under vacuum) and then pyrolizing the entire laminate at high temperatures to produce carbon. Typically, six cycles are required to get the material to a structural level. The CVI process works much the same way, but the carbon is replaced in the matrix through a vapor infiltration process that uses a hydrocarbon gaseous precursor. Some machining is typically required during this process to expose the base material. Because of the differences in the two processes, a coupon test program was developed to test materials made using each of them.

The fiber, matrix, and ply stacking sequence are important parts of the structural characteristics of

C-C materials. The same fibers used in conventional composites are available for C-C designs. To date, much of the work in C-C design has been dominated by an emphasis on strength. That work involves intermediate modulus fibers (PAN-based T300), in larger tow yarns (3K), and thicker laminates (>2.5 mm). The TPS design is part of the transformation, started on other programs, toward stiffness-driven structures. These designs stress lower mass and thinner cross-sectional areas. Smaller tow yarns (1K) and thinner shell sections (~1 mm) are used, as well as higher-modulus fibers (pitch-based YSH 50). The TPS coupon test program includes the first data on these thinner, high-modulus materials.

High-Temperature Insulation. High-temperature insulation spans the area between the high-temperature primary shield and the nominal temperature zone around the spacecraft. Because of the temperatures in this area, insulation options are limited to carbon foams and aerogels. Current work in this field is aimed at developing insulation materials for reentry applications. Although the TPS temperature requirements are similar, the structural requirements on the insulation materials are lower in comparison. Currently available carbon foams meet the TPS requirements. Developmental work, presently underway, promises improved materials.

Formulation and testing of high-temperature insulation is a specialized field. At the required operating temperatures, carbon foams and aerogels are the only materials that meet the required combination of high temperature stability (i.e., outgassing), density, and thermal properties. Through an evaporative process, carbon can be processed into a foam material with very low densities (0.05 to 0.10 g/cm^3). One form of this material that is presently available is reticulated vitreous carbon (RVC) foam. Heat is transferred in these foams by both conduction in the material and radiation between the pore surfaces. At low densities and high temperatures, radiation is the dominant heat transfer mode. Typically, heat transfer in the insulation is defined in terms of a temperature-dependent thermal conductivity that rises significantly with temperature. Foam coupons with three pore densities—60, 80, and 100 pores per linear inch (ppi)—are being tested. As a method of reducing radiation heat transfer, carbon aerogels and foam–aerogel composites are being developed. Aerogels have very small pore size, lower strength, and slightly higher densities. Hybrids combine the foam strength and aerogel pore size to reduce high-temperature conductivity.

Optical Coatings. The optical properties of the external primary shield surface determine the maximum system temperatures and drive the thermal design of the entire observatory. Since C-C does not have a controlled optical property, some type of coating is required whose properties can be tested and verified. In the study, three ceramic coatings were investigated. Alumina is the baseline coating. It is extensively used as a monolithic material and as a coating. As backups, pyrolytic boron nitride (PBN) and barium zirconium phosphate (BaZP) also have beneficial properties. PBN is extensively used in the nuclear power industry as a high-temperature, plasma-facing, protective coating over carbon. BaZP is a derivative of NZP, which is used as a thermal protection system in furnaces and engines. The optical properties (i.e., reflectance, absorptance, and emittance) of alumina, PBN, and BaZP all result in temperatures that fall well within the requirements of the TPS.

Flight Environment Evaluation and Property Testing. The suitability of all materials considered for the TPS has been evaluated over the materials' predicted temperature range, plus margin. Room-temperature and elevated-temperature properties were obtained from the Mars Sample Return, X-37, and other programs. Room-temperature coupon testing of all candidate materials has been completed. Mechanical property testing ensured that the materials planned for the TPS are in-family with the data obtained from the other programs. The two vendors who participated in the study provided materials made with both of the C-C densification processes presently available. Both low- and high-modulus carbon fiber materials were also compared.

A significant amount of C-C coupon testing was performed to verify that the materials planned for the TPS had the same physical and structural properties as the data in the available literature. These coupon tests included density, ply thickness, tensile strength and modulus, compression strength and modulus, in-plane shear strength and modulus, flexural strength, interlaminar shear, and interlaminar tensile properties. C-C thermal conductivity is well documented. The mass of the primary shell is driven by the laminate thickness and material density.

The secondary shield insulation materials tested to date have focused on carbon foam, but preliminary work on carbon aerogels has also been completed. RVC foam thermal conductivities and coefficient of thermal expansion (CTE) were tested at

the coupon level for three different pore densities: 60, 80, and 100 ppi.

An additional set of material properties is needed to ensure that the TPS behaves as expected in the flight environment. These properties include α/ε, mass loss, charging, and radiation damage. Mass loss includes thermally induced and radiation-induced processes that cause the TPS to lose material in the solar environment. The 2.5 mg/s mass loss limit defined in previous Solar Probe studies was used for our effort, although that limit is under review and will be updated. In the 2005 STDT report, a surface charging requirement was not specified. The science team is presently developing a specific charging requirement. The material properties, charging environments, and computer codes used in the charging analysis have all been investigated. With the very large photo-emission of electrons at closest approach to the Sun, the surface charging requirement adds an electrical grounding requirement on the TPS support structure that affects the material choice. Finally, the impact of radiation on the optical properties of the coatings tested determines how the temperatures of the system will change over the mission. Because of the uncertainty in these topics, significant margin is held between the limit and the tested property of the material.

2.2.2 Step 2: Develop Zero-Order Design

The second step in the TPS risk mitigation effort developed a zero-order design from the approach presented in the 2005 STDT study. The zero-order design was a strawman used to focus the study into specific design areas. This design effort was performed without regard to mass but did develop all the structures needed to physically assemble and test the structure.

Two significant items were added during this step. Figure 2-2 shows the A-frame structure mounted off the primary shield, which was added to support the secondary shield. Also, a channel was added around the aft edge of the primary shield that included attachment provisions for the twelve struts. Because of the size of the shield, the mass penalty associated with these items was in the 10–20 kg range.

Several key design areas were identified as part of the zero-order design. These areas represent generic items that would be important for any TPS design. The first area was the shell-to-shell joint. Because of limitations in densification furnace facilities, the primary shield has to be built in sections and assembled. Therefore, a method is required to join

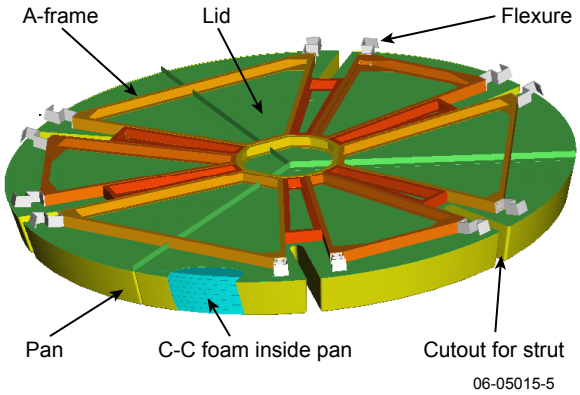

Figure 2-2. A-frame support for the secondary shield, mounted off the primary shield.

thin-walled shell segments. Second, at some point the thin-walled shell sections must be attached to the support system. Attaching a (basically) two-dimensional shell to a three-dimensional support structure requires the load to be spread out in the thin section. Last, the supporting strut end details, as well as the constraints in designing small closed section parts, needed to be defined. While such supports are not normally challenging designs, the limitations of C-C, and a desire to minimize the mass, combined to make these items overall design drivers. Figure 2-3 shows the design solution for the supporting struts.

As a way of investigating these joint designs without building a full-size TPS, it was decided to develop analog elements allowing each feature to be designed and mechanically tested separately. Three element designs were developed. First, the "T" section joint tested shell-to-shell joints. Second, the ball-and-strut interface was developed to test how the loads were carried from the supports into the thin-shell material. Last, struts were designed to test the end fitting and the load-carrying properties of long, thin-walled supports.

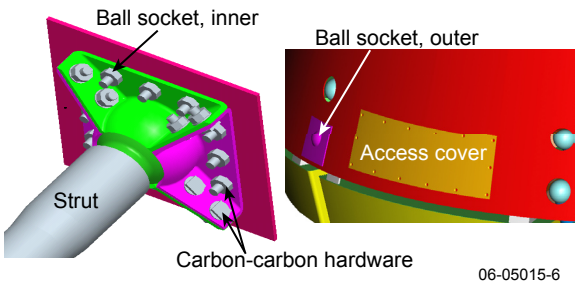

Figure 2-3. Ball-and-strut interface to primary shield.

2.2.3 Step 3: Develop Ball-and-Strut Design

The third step in the design phase was aimed at filling in the details associated with the zero-order design. A detailed CAD model was developed following the flight hardware design process. The typical thermal and structural analyses required to support the design were completed. Finally, the analog elements were converted into detailed designs based on inputs from the C-C vendors.

Unlike step 2, the ball-and-strut design included a focus on all the system-level requirements of the TPS. With the added features, the mass requirement became a particular issue. Assembly and transportation of the TPS were addressed. Coupon testing of all materials was undertaken to demonstrate survival in all of the expected mission environments.

Various shell-to-shell joints were investigated with respect to fabrication, assembly, and mass. A limiting wall thickness was defined based on vendor handling limitations, and a laminate ply stackup and minimum thickness were identified. The study decided that a T-section joint design was best for both the horizontal and vertical shell joints. A countersunk bolted attachment method was developed that minimized the local doubler required. Cone mass included all the local ply doubler thickness increases and bolt masses. A cone surface flatness requirement was identified based on the local thermal gradients around irregular areas. Finally, assembly and handling details were developed for the structure.

The support interface between the primary shield, secondary shield, and struts was a major mass driver. A 2 degree-of-freedom joint design was developed for the strut–shield interface to allow for CTE-based dimensional changes in the structure. C-channel wall thicknesses were updated based on the structural analyses, and a flexure support was designed for the A-frame to allow for differences in its CTE at temperature. The A-frame and primary shield C-channel mass were optimized. An attachment structure was developed on the primary shield to accept the strut end fittings. Finally, a secondary shield enclosure was designed, and the foam stacking configuration was defined.

The last focus area was the ball end struts. Ball size and layup were developed, the surface finish options on the ball were defined, and a pinned ball-to-strut attachment method was chosen. Strut wall thicknesses and local doublers were developed, and strut materials were identified.

2.2.4 Step 4: Truss Design

The last step in the TPS study sequence was to update the ball-and-strut design based on all the information gained throughout the earlier steps. At the end of step 3, we had identified three design drivers:

- The mass of the system was rapidly exceeding the limits defined in the system requirements.
- The secondary shield and strut interface with the primary shield had become very complex.
- The huge temperature variation in the struts limited their material choice and made the design difficult.

It was determined that all three issues would be improved by changing to a truss-based design. Chapter 3 of this report covers the design details of both the ball-and-strut and the truss designs.

The updated truss design, shown in Figure 2-4, has three new design features. First, a C-C jack stand support was included to separate the high-temperature shield areas from the lower-temperature truss area. Second, the 12 struts were replaced with 6 trusses, for which a wider set of material choices is available. Finally, the secondary shield support was moved from the primary shield to the trusses. The heavy C-C A-frame secondary shield support was replaced by many small titanium flexures between the bottom surface of the secondary shield and the top edge of the trusses. The net

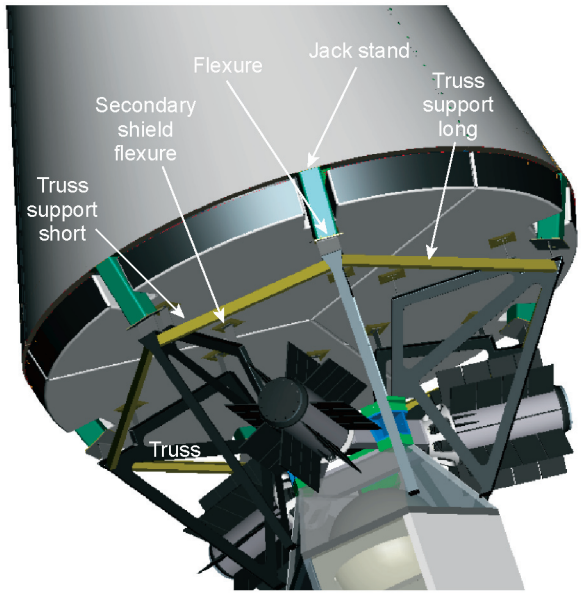

Figure 2-4- Truss design.

effect of these changes was to simplify the primary shield design, reduce TPS mass, eliminate C-C fasteners from highly loaded joints, and allow the use of more conventional materials for the trusses and flexures in the lower-temperature zone.

The main benefit of the jack stands is to separate the TPS support into high- and low-temperature zones. Located in radial cutouts of the secondary shield, the jack stands drop the high temperatures of the primary shield down to about 400°C at their base. The jack stands have a large surface area and an exposed view to space that are very effective at radiating heat. Radiative cooling drops the temperature enough at the base of the jack stand to allow the use of more conventional materials aft of that point. A key part of the jack stand design is the attachment method used between the jack stand and the primary shield. A co-processed joint was chosen to eliminate large C-C bolt flanges and support sections. Another positive result is the analysis optimization efforts can be focused on a single piece (the jack stand). In addition, the jack stand size makes it easy to test as an analog element. Below the jack stand, the lower temperatures allow the flexure design to be simplified by replacing low-strength C-C with high-strength titanium in both the flexure and in the bolted joint. Underneath the flexure, design temperatures around 300°C give much more flexibility in the choice of the materials that can be used for the truss.

The second new design feature was the change from struts to trusses. This approach has several positive features. The mass and complexity associated with the ball-and-socket strut interface with the primary shield are eliminated. The lower temperature allows more and simpler design options, which helps control mass. Also, the truss design allows the heat flow to the spacecraft to be tailored by using multilayer insulation (MLI) blanketing and the heat from the mount of the multi-mission radio isotope thermoelectric generator (MMRTG).

The last design change was moving the structural support of the secondary shield from the primary shield to the trusses. The truss configuration allows structural support points to be located across the base of the secondary shield. Changing the secondary shield support approach eliminates the A-frame and associated flexures. It also removes the complex primary shield structures needed to support those items. The support flexures between the truss and secondary shield are much simpler in design. Finally, the complex strength and stiffness requirements of the struts are separated into the simpler jack stand and truss components.

During step 4, the primary shield design was further refined based on coupon test data. Ply thicknesses and material densities were measured. Structural analyses determined that a higher-modulus material would be desirable in the lower sections of the primary shield design. To support this approach, additional test coupons, made with the higher-modulus YSH 50 fiber, were purchased.

2.2.5 TPS Design Configuration Matrix

Table 2-1 presents the configuration of the TPS as of the end of the design phase of the TPS Risk Mitigation Study. Baseline designs and alternates are presented for the key TPS components. The details of the design are discussed in Chapter 3.

2.3 Second Phase Effort

The second part of the TPS Risk Mitigation Study will involve the fabrication and testing of a full-scale prototype. That effort is currently unfunded. The TPS design is ready to proceed into the fabrication and test phase.

In the original plan submitted, mechanical testing of the complete TPS was proposed. Facilities exist at the Goddard Space Flight Center (GSFC) that are capable of providing both vibration and acoustics testing of the full-size TPS. Depending on cost and schedule constraints, a prototype or simulated secondary shield could be used. Additional strength and temperature testing are planned for the jack stand and truss. Handling and assembly of the TPS has been addressed, and preliminary approaches for the test ground system equipment have been completed.

During the study, we learned that the Johnson Space Center (JSC) has a Radiant Heat Test Facility that could be modified for use in TPS testing. The chamber size is adequate, but the hot zone area would have to be increased from about 30 in. on a side to 2.7 m in diameter. Preliminary discussions have been held with JSC on upgrading their facility, but no further action was taken. The thermal testing would include the TPS without the primary shield. Heat flows through the secondary shield and jack stand assemblies could be measured. Full-scale or symmetric section testing could be done. Thermal testing of the TPS would verify the thermal design approach and quantify temperatures at all key interfaces.

2.4 Lessons Learned

The design phase of the TPS Risk Mitigation Study generated a number of generic lessons

Table 2-1. TPS truss design details.

TPS Component	Description	Baseline Material	Alternative Material
Primary shield	Cone tip	C-C T300	NA
	Cone forward shell & joints	C-C T300	NA
	Cone middle shell & joints	C-C T300	NA
	(3) Cone aft shell w/ jack stand, ribs & joints	C-C YSH-50	C-C T300
	Jack stand aft flange & fasteners	Ti, 6Al-4V	Carpenter Low Expansion 42
	Shell fasteners	C-C T300	NA
Secondary shield	Foam	ERG RVC	Aerogel infiltrated carbon foam (AICF)
	Lid & clips	C-C T300	NA
	Pan & clips	C-C T300	NA
	Fasteners	C-C T300	NA
Truss	Frame	M55J/RS3	Ti 6Al-4V or T650/ AFR-PE4
	Secondary shield flexures	Ti 6Al-4V	NA
	Jack stand flexures	Ti 6Al-4V	NA
	Fasteners	Ti 6Al-4V	NA

learned about the design of the TPS. While there were many specific design conclusions in the different disciplines, the items discussed in the following paragraphs were found to be the large drivers in the overall system.

2.4.1 Structural C-C Materials Can Support the TPS Design

There has been an evolution in the use of C-C materials in structural applications over the past few years. Different materials and processes are available with substantial design heritage. No new material development processes are required as part of the TPS design. Experience with thin-shelled structures is limited, but the test data available for thicker sections is in-family with the thinner laminate test data produced as part of this study. There are different densification processes and different vendors, each with its own strengths and weaknesses. The fabrication and assembly processes that exist for C-C are very different from conventional metal structural designs. Adding coatings to C-C is a well developed field. The inspection techniques and repair methods for C-C, both in-process and end item, are mature.

2.4.2 It Is Important to Separate the High-Temperature Shield Zone From the Lower-Temperature Support Zone

There is a natural break in the functions between the high- and low-temperature support zones. Separating them allows different materials to be used in the areas where their strengths can be used to the best advantage of the system. Highly stressed areas, like flexures, are better suited to the lower temperature zone. High-temperature material property data are difficult to obtain accurately. Therefore, the design is simplified by limiting the complexity of the high-temperature support structure. Limiting the high-temperature zone reduces the risk in the overall design.

2.4.3 The Size of the TPS Makes Controlling Mass a Serious Issue

The TPS is large. It has a base perimeter of 8.5 m, is almost 5 m tall, and has a surface area of about 22 m^2. Small changes in shell thickness

or density result in large mass changes. For example, adding just two plys to the symmetric laminate stackup increases the primary shield mass by about 11 kg. Stiffening channels at the base of the cone also have a large impact on the TPS mass.

2.4.4 A Flexure Support for the TPS Is Required

The large temperature difference between the TPS zones requires a flexure design in the support system. Using a common material in the high-temperature zone limits the dimensional changes and stresses induced from bulk temperature swings. This simplification in the structural design makes the launch loads the dominant load case. Once in space, the system has only to maintain its structural integrity at the survival temperatures.

2.4.5 Supporting the Secondary Shield From the Spacecraft Bus Rather Than From the Primary Shield Results in Significant Mass Savings

Removing the requirement to support the heavy secondary shield from the primary shield saves mass and reduces design complexity. A thin-walled secondary shield enclosure is necessary to keep its mass low. The truss design allows for flexibility in supporting the secondary shield at more places across its base.

2.4.6 The Use of Co-Processed Rather Than Bolted Joints Results in Large Mass Savings

The strength of both C-C material and bolts is much lower than typical metals. Therefore, large flanges and bolt areas are required to transfer loads across bolted interfaces. Going from the flat primary shield to a complex support structure geometry can result in large, thick sections required at the interfaces. Co-processing is the C-C equivalent to a bonded joint. These joints eliminate the need for thick flange sections and efficiently use the large surface areas available in the design.

2.4.7 Coating Optical Property Data Supports the α/ε Requirements with Significant Margin

White ceramic coatings significantly reduce the temperature and the risk in the TPS design. These coatings have been used in space programs. A version on alumina is used on some of the Space Transportation System (STS) tiles. Ceramic coatings have been explored as laser hardening surfaces. Testing done in this phase of the TPS Risk Mitigation Study supports their adhesion, survivability, and degradation requirements. Chapter 4 presents detailed work on the three candidate coatings.

3 Solar Probe Thermal Protection System Design Study

As noted in previous chapters, this study is aimed at reducing the risk associated with the Solar Probe Thermal Protection System (TPS) by performing a design, fabrication, and test cycle. The following paragraphs describe the evolution of the TPS from that presented in the 2005 STDT report[1] through to the present design. The major drivers for the mechanical, structural, and thermal subsystems are presented. Then, detailed designs are given for the ball-and-socket and truss TPS configurations.

3.1 System Design Requirements

The present systems requirements for the TPS are shown in Chapter 1, Table 1-1. These requirements are the same as those developed in the 2005 STDT study. The TPS design developed as part of this effort demonstrates that a near-solar mission is feasible with the approach presented in that earlier effort. The requirements developed bound the expected environments that will be encountered over the mission, define the required configuration of the TPS, and support the scientific measurements being made.

One item not quantified in Table 1-1 is the requirement for surface conductivity. The nature and type of requirement needed by the observatory is being defined by the science team. This study effort has supported the development of those requirements by defining the local charging environments throughout the mission, measuring the effect those environments will have on the shield materials and coatings, and investigating the capabilities of the computer codes used to predict spacecraft performance.

3.2 Mechanical Design

3.2.1 Mechanical Design Drivers and Requirements

Primary Shield. The material selection for the primary shield is driven by the expected exterior temperature of 1850 K. Carbon–carbon (C-C) was the baseline material for the primary shield in the 2005 STDT report; it is one of the few structural materials that can survive this temperature and provide acceptable specific strength.

From a mechanical perspective, the ideal primary shield cone would be manufactured in one piece. This design would minimize mass by eliminating joints, allow the shape to be self-supporting, minimize tooling, and eliminate the risk of handling large, thin shell pieces. Unfortunately, there is no C-C facility with a furnace large enough for the densification process. The team will continue to monitor this situation as new facilities become available in the industry. In the meantime, the primary shield cone will need to be manufactured in pieces. The primary shield cone is divided into three sections vertically, with each of the smaller top and middle sections being made as one piece. The large-diameter bottom section will need to be made in three pieces. From a mechanical perspective, a three-piece assembly works better than a four-piece assembly due to the six interface locations of the jack stands. Each bottom primary shield piece interfaces with two jack stands. The three pieces of the bottom cone will be assembled into a frustum, and the middle and top cone sections will then be added onto the bottom frustum.

The only way for a cone of this size (5.1 m tall and 2.7 m diameter) to meet the tight mass estimates of the 2005 STDT study is for it to be made up of very thin-walled shell sections. Thicker wall sections have a ripple effect on the structure. The added thickness increases the load in the jack stands and flexures, the structure mass needed to meet the frequency requirements of the launch vehicle increases, and the bus structure mass needed to transfer the higher load and meet the stiffness requirements increases. Keeping the shell thin minimizes the overall mass of the system.

For thermal reasons, the outside of the primary shield cone should be as smooth as possible. Any geometric perturbations to the external conic shape will cause hot spots on the primary shield cone. This requirement has driven the threaded fastener section to the inside of the cone. In addition, for both thermal and coating reasons, flat-head bolts will be used on the primary shield assembly. This will keep the external conic shape clean and also provide a flat surface on the bolt head for coating.

Secondary Shield. The temperature on the upper surface of the secondary shield will be identical to the temperature of the primary shield. Thus, the same rationale for material selection is used on the secondary shield as was used on the primary shield. A thin C-C enclosure was the baseline chosen in the 2005 STDT study due to the high temperatures. The thermal environment also sets the thickness of

[1] *Solar Probe: Report of the Science and Technology Definiton Team*, NASA/TM—2005–212786, National Aeronautics and Space Administration, Goddard Space Flight Center, Greenbelt, MD (2005).

the secondary shield. Inside the secondary shield enclosure, the main ingredient is a C-C foam that insulates the spacecraft bus from the high temperatures of the primary shield. The target temperature for the bottom of the secondary shield is 350°C. The thickness of the foam is driven by both the surface temperature and heat flow through the secondary shield.

Just as manufacturing limitations have driven the design of the bottom of the primary shield into a three-piece assembly, the secondary shield enclosure must also be made from at least three pieces. The three-piece assembly works better than a four-piece because of the cutouts needed for the six jack stands that must pass through the secondary shield to reach the primary shield. Each secondary shield piece will have two jack stand cutouts. This allows for three identical parts and simplifies the design and detailing effort.

The 2.7-m-diameter enclosure pan and lid, supporting the insulating C-C foam, must be made from thin-walled shell pieces to meet the mass constraints in the 2005 STDT report. These secondary shield pieces will be made from the same layup as the primary shield cone.

To protect the instruments from possible contamination, the secondary shield enclosure surrounds the C-C foam. Should the launch environment generate any particulates, they will be captured by the pan and lid.

TPS Supports. The TPS supports that connect to the primary shield need to be thermal isolators to protect the spacecraft bus from the extreme thermal environment. Anything that interfaces with the primary shield will need to be made of C-C. This limitation set the material of the strut in the ball-and-strut design and the jack stand in the truss design. In both cases, there was a significant thermal sensitivity to the cross-sectional area of the pieces. To minimize conduction to the spacecraft bus, there was pressure to make the walls as thin as possible.

These thermal concerns conflicted with the structural concerns. Minimizing the stress in the C-C pieces and maximizing the natural frequency of the assembly required the wall thickness to be increased. Limiting the heat flow down the support led to decreased wall thickness. In the strut design, a 3.0-mm wall thickness was found to meet both requirements. In the truss design, the titanium flexure acted as another thermal isolator, allowing a larger cross-sectional area without increased conduction to the spacecraft bus. The 3.0-mm thickness of the jack stand resulted in a significantly larger cross-sectional area, which increased the overall stiffness of the design.

3.2.2 Description of the Ball-and-Strut TPS Design

Primary Shield. As described in the 2005 STDT report, the primary shield is a thin-walled C-C conic section 2.7 m in diameter and 5.1 m tall. This approach was the starting point for our 2006 Risk Mitigation Study effort. Because mass was a critical parameter tracked throughout the study, the minimum shell section practicable was required. Through initial discussions with the C-C vendors, that shell thickness was found to be 1.0 mm. The C-C vendors were also involved in the design of the shell joints. At the interface between each of the individual shell pieces, a T-section joint (Figure 3-1) will be used to attach the primary shield cone shell pieces together. The T-section will be manufactured integrally with one of the primary shield cone shell pieces to minimize mass. The other mating surface will slide over the T-section and be bolted to it using flathead C-C bolts. This same T-section will also be used to attach the three shell pieces that make up the bottom of the primary shield cone (see Figure 3-1). Once the three-piece cone bottom has been assembled, the middle cone section will bolt to the

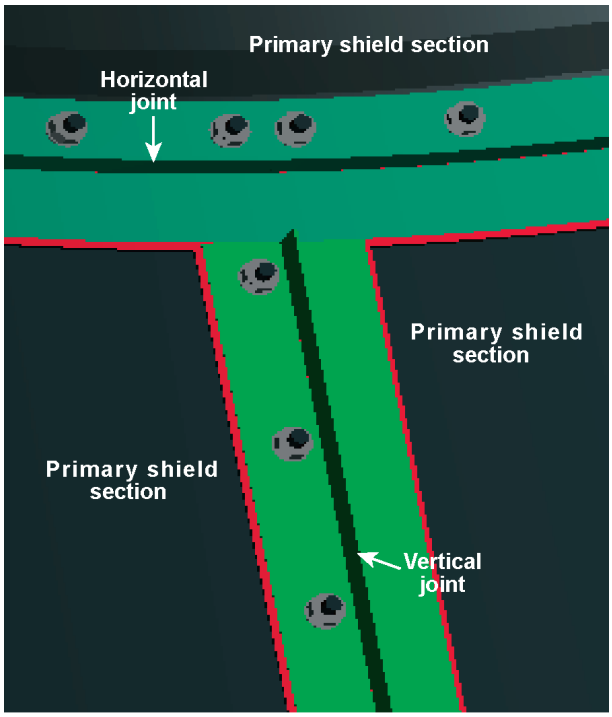

Figure 3-1. Primary shield section joint.

bottom cone section using the same T-section joint and C-C bolts.

The load path for the primary shield was through the 12 struts to the spacecraft bus. The load path for the secondary shield was through the A-frame, the primary shield, and the 12 struts to the spacecraft bus. Both the secondary shield A-frame and the 12 struts attached to base of the primary shield (see Figure 3-2). While the top and middle sections of the primary shield cone did not have additional stiffeners (other than what is inherent in the T-section joints), the bottom section of the cone had to be reinforced to support and spread the load from the struts and A-frame. A large, heavy C-channel section was needed to stiffen the bottom of the cone. Like the T-sections, the C-channel would be manufactured as part of the primary shield cone base to save hardware mass.

Due to the severe thermal environment, all hardware used on the primary shield will be C-C. To minimize hot spots, all hardware on the outside of the primary shield will be of flathead design. Because of C-C's mechanical properties, hardware made of C-C is much larger than what is normally used in metallic assemblies. Typically a 5/16-in. thread is the smallest that C-C vendors recommended for use in C-C assemblies. The design of the primary shield includes 5/16-in. C-C hardware throughout.

Secondary Shield. The main ingredient in the secondary shield is a 2.7 m diameter, 20-cm-thick reticulated vitreous carbon (RVC) C-C foam assembly. RVC insulation is an open-pore foam of pure carbon. It has very low density and can withstand very high temperatures. The foam is manufactured in 2.5-cm-thick sheets. The sheets will be cut into the various shapes needed to fill the required volume (see Figure 3-3). The foam sheets will be designed to eliminate thermal shorts; i.e., nowhere in the secondary shield will there be joints between foam pieces coincident through all of the layers. Testing is planned to determine if the foam sheets can be bonded together or if an interstitial carbon felt is required. The remainder of this section describes the structure required to support the foam.

The secondary shield foam sheets will be installed into a thin-walled, C-C three-piece pan. The pan pieces will be assembled with C-C bolts due to the thermal environment. A thin-walled, three-piece C-C lid will encapsulate the foam. Support was needed for the secondary shield to span the 2.7-m diameter of the primary shield. An A-frame was added, which bolted to the top of the lid and attached to the primary shield at the C-channel through flexures. The 13-piece C-C A-frame was designed out of C-channel sections and assembled by using C-C bolts (see Figure 3-4). A C-C flexure support is required between the A-frame and primary shield. While both are of C-C construction, the geometric differences between the parts will induce significant loads due to thermal distortion. The load path for the secondary shield foam is through the pan, lid, A-frame, flexure, primary shield, and struts to the spacecraft bus.

Struts. The C-C struts were designed to carry the load of the primary and secondary shields to the spacecraft bus. The six 146-cm-long struts interface with the bus near the centerline above the three multi-mission radioisotope thermoelectric generators (MMRTGs). The six 163-cm-long struts interface farther down the spacecraft bus (see Figure 3-2). The struts are 5.3 cm in diameter and have a wall thickness of 3.0 mm, which was found to be

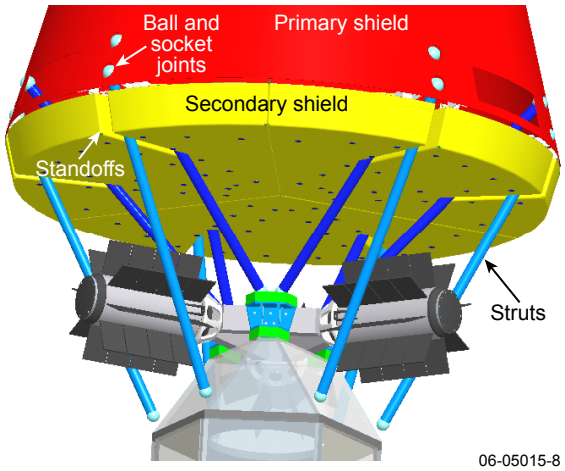

Figure 3-2. Ball-and-strut baseline design from the 2005 STDT report.

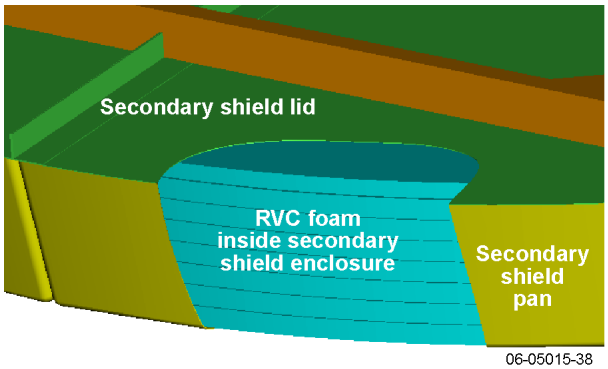

Figure 3-3. Carbon foam inside secondary shield enclosure.

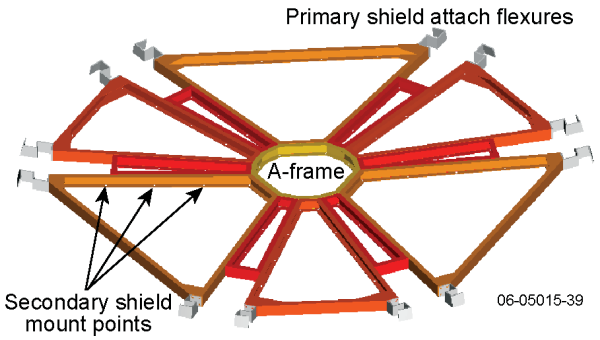

Figure 3-4. A-frame secondary shield support assembly.

a reasonable compromise between the thermal and mass desire for thin walls and the structural inclination for a large cross-sectional area.

The actual interface at both ends of the strut is a ball-and-socket joint. The ball-and-socket joint allows for 3 rotational degrees of freedom. Multiple fabrication techniques were investigated for attaching the 7.6-cm-diameter ball to the ends of the strut. Bolts, pins, and threads were considered. All had significant technical issues. After discussions with the C-C vendor, the team decided that the ball would be made separately but then integrated directly onto the strut. The first socket design was heavy, as it encapsulated the ball in a full clamp mounted to the inside of the primary shield. The second design eliminated 75% of the mass by centering the ball in the primary shield (see Figure 3-5) and clamping it with an inner and outer spherical fitting. This design left protrusions on the outside of the primary shield. It was as these difficulties were being addressed that the truss design evolved as more promising. As a result, the thermal analysis of these protrusions was not performed. The required coatings for the ball and socket were just beginning to be investigated when the effort shifted to the truss design, which eliminated the ball-and-socket element.

3.2.3 Description of the Truss TPS Design

Primary Shield. The primary shield of the 2005 STDT report is a thin-walled C-C conical section 2.7 m in diameter and 5.1 m tall. This design was the starting point for the TPS Risk Mitigation Study effort. As mass was one of the critical parameters tracked throughout the study, the minimum shell section practicable was required. Although initial discussions with the C-C vendors led to a shell thickness baseline of 1.0 mm, the processed coupons were found to be 0.81 mm thick. This thinner shell thickness and laminate density measurements cut over 5 kg from the mass of the primary shield presented at the Mid-Year Report.[2]

Most of the primary shield design is unchanged from the ball-and-strut design. The primary shield is divided into the same five sections, and the same T-section joints are used to hold the sections together. The differences can be seen in Figure 3-6. Smaller stiffening rings are required, and doublers are added at the interface to the support structure. These pieces will be reinforced with B-studs and co-processed together.

The load path for the primary shield is through the six jack stands, flexures, and trusses to the spacecraft bus (see Figure 3-7). The load path for the secondary shield has changed. It is no longer through the primary shield but rather through the

[2]JHU/APL, *Solar Probe Risk Mitigation Study*, 2006 Mid-Year Report.

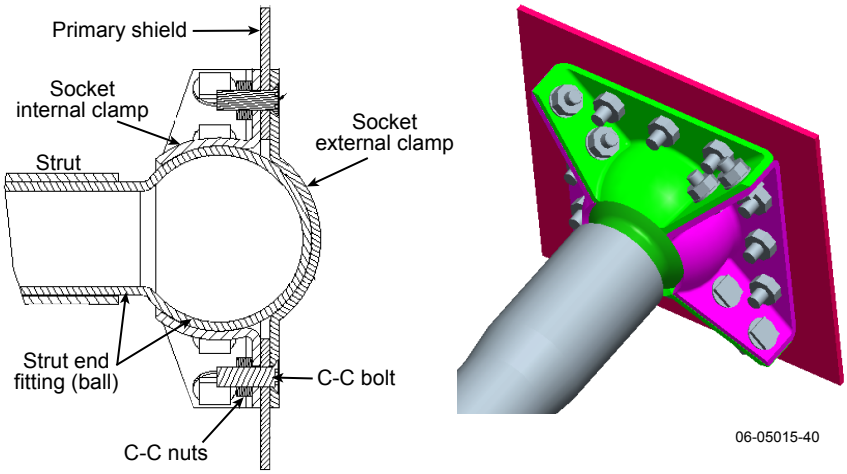

Figure 3-5. Ball and strut interface with primary shield.

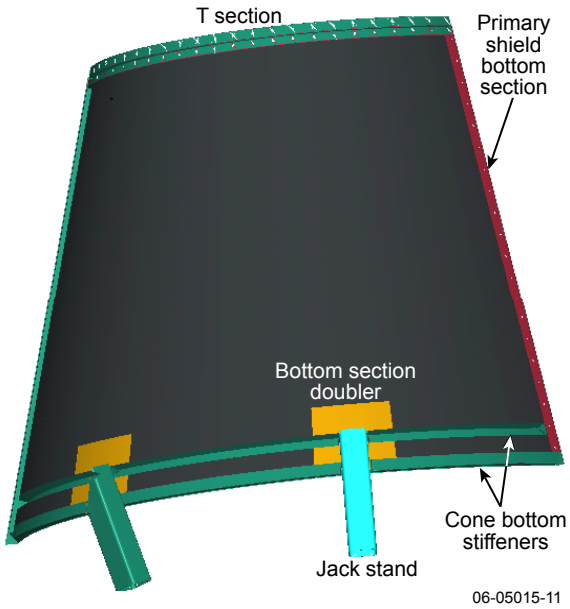

Figure 3-6. T-section, doubler, and jack stand primary shield interfaces.

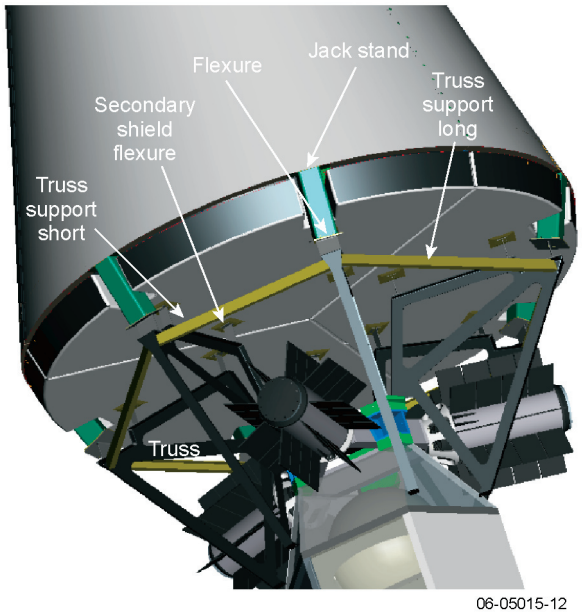

Figure 3-7. Truss design.

multiple secondary shield flexures and trusses to the spacecraft bus. This change cuts the load through the primary shield into the jack stand in half, allowing the primary shield base stiffener and doublers to become much lighter. It also decreases the load that must be taken by the jack stands. While the top and middle sections of the primary shield cone do not have additional stiffeners (other than what is inherent in the T-section joints), the bottom section of the cone must be reinforced to support and spread the load from the jack stands. A lightweight section made up of two thin angles and local doublers was needed to stiffen the bottom of the cone. Like the T-sections, the angles and doublers will be manufactured as part of the primary shield cone base to save hardware mass.

The jack stands are C-C thermal isolators as well as mechanical supports. They are 11-cm-square tubes with a thickness of 3 mm. Multiple types of mechanical attachments were investigated between the jack stands and the bottom primary shield cone sections. Through interaction with the C-C vendor, we determined that the jack stands will be processed integrally with the bottom primary shield cone sections; this will eliminate a problematic high-stress bolted or threaded joint. The jack stands will extend below the secondary shield (Figure 3-8). Between the jack stand and the truss is a titanium flexure that accommodates the mismatch in the coefficient of thermal expansion (CTE) between the C-C TPS and the truss. The length of the jack stand is such that the bottom of the flexure is about 350°C. This is important, because that lower temperature expands the material options for the truss material.

As a result of the severe thermal environment, all hardware used on the primary shield will be C-C. To minimize hot spots, all hardware on the outside of the primary shield will be of flathead design. The mechanical properties of C-C require that C-C hardware be much larger than what is normally used in metallic assemblies. Typically a 5/16-in. thread is the smallest recommended for use in C-C assemblies. The design of the primary shield includes 5/16-in. C-C hardware.

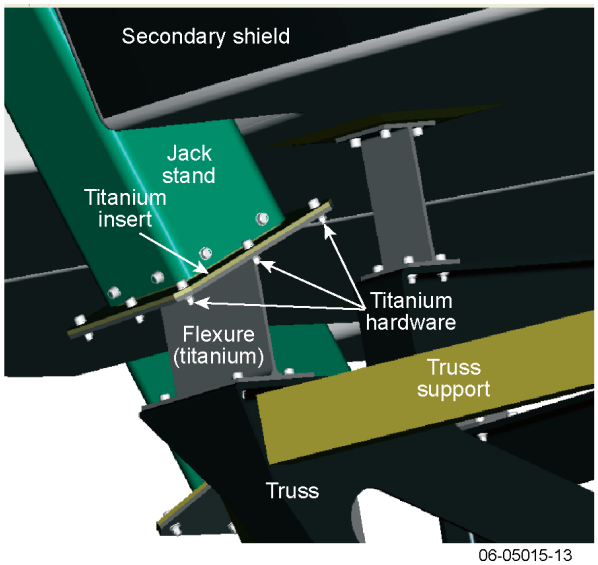

Figure 3-8. Jack stand, flexure, and truss interface.

Secondary Shield. The main ingredient of the secondary shield is a 2.7 m diameter of 15-cm-thick C-C foam assembly. Additional thermal analysis and testing has shown that the thickness reduction from 20 to 15 cm provides enough thermal resistance through the shield and does decrease secondary shield mass. The foam is RVC, an open-pore foam of pure carbon. It has very low density and can withstand very high temperatures. The foam is manufactured in 2.5-cm-thick sheets. The sheets will be cut into the various shapes needed to fill the required volume (see Figure 3-9). The foam sheets will be designed to eliminate thermal shorts; i.e., nowhere in the secondary shield will joints between foam pieces be coincident through all six layers needed for this secondary shield design. Testing is planned to determine if the foam sheets can be bonded together or if an interstitial carbon felt is required. The remainder of this section describes the structure required to support the foam.

The secondary shield foam sheets will be installed into a thin-wall, three-piece C-C pan. Due to the thermal environment, the pan pieces will be assembled with C-C bolts. A thin-wall, three-piece C-C lid will encapsulate the foam. The secondary shield is supported from below on flexures multiple-mounted to the trusses.

Truss. The truss supports both the primary and secondary shields. Each shield is supported by a different set of flexures. The titanium flexures are mechanically tailorable to provide the required compliance for the difference in CTE between the truss and the C-C primary and secondary shields. Due to the insulating effects of the jack stands and the flexures, it is possible to use a material with better mechanical properties than C-C for the truss. In addition, metallic hardware can be used at the truss interfaces, eliminating the need for C-C bolts. The truss attaches to the spacecraft bus at two places, the same end points where the struts interfaced in the ball-and-strut design. A material for the truss has been baselined, but the design will be the subject of a future trade study. Options under consideration include C-C, composite, and metallic materials.

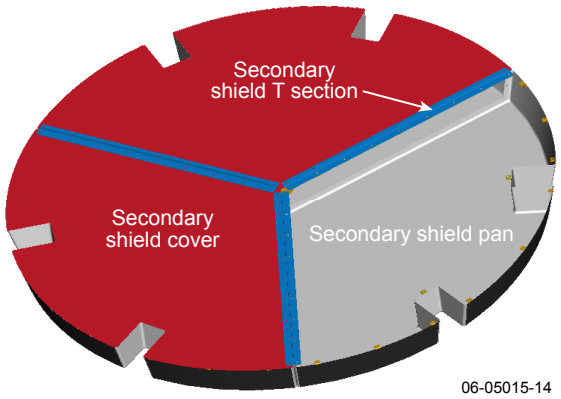

Figure 3-9. Secondary shield design details.

3.2.4 TPS Mass History

Table 3-2 lists the mass history of the Solar Probe TPS from the FY2002 Engineering Report[3] through the design phase of the FY2006 TPS Risk Mitigation Study.

The goal of the risk reduction effort is the maturation of the TPS design from concept to reality, from technology readiness level (TRL) 2 to 6. In the first phase, C-C coupons and representative pieces were manufactured and tested to confirm mechanical properties used in design and analysis. The mass margin applied to the TPS in the 2005 STDT was 30%, which is in line with both APL and NASA guidelines. After phase 1, with representative parts tested and thickness and density measurements made, the TPS is at or beyond the level of a preliminary design review (PDR). As such, a total of 25% margin will be applied to the TPS per APL System Engineering Standards for PDR[4] (see Table 3-1). It is anticipated that after the full-scale TPS is fabricated and tested in phase 2, the TPS mass will be at a critical design review (CDR) level and will be assigned a 15% margin, again in concurrence with the APL System Engineering Standards for CDR.[4]

3.3 Structural Design

3.3.1 Derivation of Environment and Design Requirements

The preliminary design loads for the TPS are derived according to the Atlas Launch System *Mission Planner's Guide*.[5] The expected flight levels provided in the launch guide are specified as quasi-static accelerations for the spacecraft center of gravity. These design loads assume a rigid spacecraft; therefore, the design loads for the TPS must

[3] *Solar Probe: An Engineering Study,* prepared by the Johns Hopkins University Applied Physics Laboratory, in partnership with the Jet Propulsion Laboratory, under contract NAS5-01072, Laurel, MD (November 12, 2002).

[4] Kusnierkiewicz, D., *Space Department Technical Review Requirements, Rev B*, QY2-6001, The Johns Hopkins University Applied Physics Laboratory (July 21, 2005).

[5] *Atlas Launch System Mission Planner's Guide*, Lockheed Martin Astronautics (January 1999).

Table 3-1. Mass history of the Solar Probe TPS, starting from the 2002 Solar Probe Engineering Study report and continuing through 2005 STDT report to the 2005 and 2006 risk mitigation efforts.

		2002 Engineering Study			2005 STDT Mass			Risk Reduction Study 11/11/2005 Zero-Order Design			Risk Reduction Study 2/23/2006 Mid-Year Report			Risk Reduction Study Ball-and-Strut Design			Risk Reduction Study Truss Design #1			Risk Reduction Study Truss Design #2		
Component	Quantity	Mass kg	Margin %	Total kg	Mass kg	Margin %	Total kg	Mass kg	Margin %	Total kg	Mass kg	Margin %	Total kg	Mass kg	Margin %	Total kg	Mass kg	Margin %	Total kg	Mass kg	Margin %	Total kg
Primary Shield		**39**	**20**	**46.8**	**52.7**	**30**	**68.5**	**79.2**	**30**	**103.0**	**65.3**	**30**	**84.9**	**76.7**		**95.9**	**76.7**		**95.9**	**59.5**		**74.4**
Top Section	1													5.2	25.0	6.6	5.24	25	6.55	4.49	25	5.61
Middle Section	1													13.2	25.0	16.4	13.15	25	16.44	10.56	25	13.20
T-Section	3 m																			*0.79*	*25*	*0.99*
Bottom Sections	3													44.2	25.0	55.3	44.22	25	55.28	19.70	25	24.63
T-Section	10.7 m																			*2.83*	*25*	*3.54*
Bottom Section Stiffener	3																			*7.18*	*25*	*8.98*
Bottom Section Doubler	6																			*0.97*	*25*	*1.21*
C-C Hardware	300													*2.1*	*25.0*	*2.6*	*2.10*	*25*	*2.63*	*1.05*	*25*	*1.31*
Coating														*12.0*	*25.0*	*15.0*	*11.97*	*25*	*14.96*	*11.97*	*25*	*14.96*
Secondary Shield		**79.1**		**107.3**	**70.9**		**92.2**	**73.7**		**95.8**	**73.8**	**30**	**95.9**	**77.6**		**96.9**	**82.7**		**103.4**	**62.9**		**78.7**
Facesheets		17.1	20	20.5	15	30	19.5	17.9	30	23.3												
Cover	3													9.5	25.0	11.9	9.52	25	11.90	7.31	25	9.14
Mounting Pads	84																			*0.26*	*25*	*0.33*
Pan	3													13.6	25.0	17.0	13.61	25	17.01	9.62	25	12.03
Mounting Clips	33																			*0.20*	*25*	*0.25*
Flex Mounting Pad	12																			*0.05*	*25*	*0.07*
Pan/cover C-C Hardware	114																*1.36*	*25*	*1.70*	*0.27*	*25*	*0.34*
Foam		62	40	86.8	55.9	30	72.7	55.8	30	72.5				54.4	25.0	68.0	54.42	25	68.03	41.50	25	51.88
T-Section	4.0 m																*2.45*	*25*	*3.06*	*0.97*	*25*	*1.21*
Flexure	12																*1.09*	*25*	*1.36*	*2.45*	*25*	*3.06*
Flexure Hardware (Ti)	96																*0.27*	*25*	*0.34*	*0.29*	*25*	*0.36*
TPS Support		**10.9**	**20**	**13.1**	**10.2**		**13.3**	**30.0**		**39.0**	**13.6**		**17.7**	**44.8**		**56.0**	**25.3**		**31.6**	**27.0**		**33.7**
Ball/Strut Design																						
Flexure/A-Frame/Hanger	1													*15.5*	*25.0*	*19.4*						
Ball/Strut Long	6				5.4	30	7.0	15.7	30	20.4	7.2	30	9.4	10.3	25.0	12.8						
Ball/Strut Short	6				4.8	30	6.2	14.3	30	18.6	6.4	30	8.3	9.7	25.0	12.1						
Ball Socket Inner	12													*4.4*	*25.0*	*5.5*						
Ball Socket Outer	12													*2.2*	*25.0*	*2.8*						
C-C Hardware														*1.8*	*25.0*	*2.3*						
Access Plate	3													*0.9*	*25.0*	*1.1*						
Truss Design																						
Truss	6																10.20	25	12.75	11.48	25	14.35
Flexure	6																4.76	25	5.95	3.86	25	4.83
Jackstand	6																9.52	25	11.90	7.84	25	9.80
Titanium Hardware	120																0.79	25	0.99	0.36	25	0.45
Truss Support Long	3																			2.04	25	2.55
Truss Support Short	3																			1.38	25	1.73
Total		**129**		**167.2**	**134**		**173.9**	**182.9**		**237.8**	**152.7**		**198.5**	**199.1**		**248.8**	**184.7**		**230.8**	**149.4**		**186.8**

be scaled up to account for the cantilevered natural frequency of the spacecraft and the axial center of gravity offset between the TPS and the spacecraft. The design loads for the TPS and the spacecraft are summarized in Table 3-2.

Spacecraft and subsystem design loads are more accurately computed by the launch vehicle (LV) manufacturer during coupled loads analysis (CLA), in which reduced dynamic models of the spacecraft are combined at the LV interface with the flight-verified vehicle dynamics model. The coupled model is then excited with flight forcing functions for various dynamic loading events. CLA loads succeed the preliminary design loads and have customarily proven to be lower than the *Planner's Guide* loads. There are typically two CLA cycles during a program, the first performed with a preliminary spacecraft dynamics model to aid spacecraft design, and the second with a test-verified spacecraft dynamics model to finalize flight margins. Loads analysis is performed by using the requirements levied in NASA-STD-5002, *Load Analysis of Spacecraft and Payloads*.[6]

The spacecraft is also exposed to an acoustic environment during takeoff and through transonic flight. This external acoustic environment is transmitted through the vehicle fairing to impinge onto the spacecraft and affects large-area, low-weight surfaces such as the TPS primary shield. The acoustic sound pressure levels are provided in the Atlas launch guide and vary according to spacecraft volume, payload fairing dimensions, and acoustic blanket placement. Results from preliminary acoustic analysis of the primary shield under effective root mean squared (RMS) pressures indicate that the quasi-static design loads listed in Table 3-2 remain the predominant load case. Other analytical methods involving finite element, boundary element, and statistical energy methods will be used to more accurately determine the response of the TPS structure over the entire acoustic frequency spectrum.

A minimum natural frequency for the spacecraft is specified in the *Planner's Guide* to ensure that design loads and displacements are not exceeded. The minimum natural frequency for the spacecraft is 8 Hz lateral and 15 Hz axial. The TPS natural frequency requirements are established with the anticipation that the discrete TPS frequencies will be reduced after coupling to the spacecraft. The TPS fundamental frequency design goals are therefore set at 15 Hz lateral and 25 Hz axial.

[6]*Load Analyses of Spacecraft and Payloads*, NASA-STD-5002, National Aeronautics and Space Administration (June 21, 1996).

Table 3-2. Solar Probe TPS design loads.

	Spacecraft	TPS
Lateral	±2 *g*	±20 *g*
Axial	+6 *g*, –2 *g*	±15 *g*

3.3.2 TPS Assembly and System-Level Verification Testing

System-level testing is conducted by using NASA-STD-7002, *Payload Test Requirements*,[7] and GSFC-STD-7000, *General Environmental Verification Standard (GEVS)*.[8]

Verification that the TPS and the spacecraft will withstand the design loads is achieved through low-frequency (5–100 Hz range) swept sinusoidal testing. The levels for the system-level sine vibration test are given in the *Planner's Guide*. These levels are typically notched to match TPS and spacecraft responses derived from the final CLA cycle.

Verification that the TPS and the spacecraft will withstand the acoustic environment is achieved through acoustic testing. The levels for the acoustic test are given in the *Planner's Guide*. Testing is conducted by using NASA-STD-7001, *Payload Vibroacoustic Test Criteria*.[9]

3.3.3 Materials Testing

Material properties for this analysis are summarized in Table 3-3. The material properties for titanium are based on MIL-HDBK-5H.[10] The C-C composite material properties are based on a survey of historical data from programs such as X-37 and Mars Sample Return (see Section 7.1.3) and supported by our own testing. Higher-modulus C-C properties for YSH-50 are estimated by using the ratio in fiber stiffness between T300 and YSH-50 and verified by testing. Carbon-polyimide composite material properties are based on data from the Joint Strike Fighter program (see Section 7.1.3).

[7]*Payload Test Requirements,* NASA-STD-7002, Rev A, National Aeronautics and Space Administration (Sept. 10, 2004).

[8]*General Environmental Verification Standards (GEVS) for GSFC Flight Programs and Projects*, GSFC-STD-7000, Goddard Space Flight Center (April 2005).

[9]*Payload Vibroacoustic Test Criteria*, NASA-STD-7001, National Aeronautics and Space Administration (June 21, 1996).

[10]*Metallic Materials and Elements for Aerospace Vehicle Structures*, Military Handbook MIL-HDBK-5H, U.S. Department of Defense (Dec. 1, 1998).

All composite materials properties are assumed to be quasi-isotropic. Interlaminar shear strengths are a function of laminate thickness, laminate stacking sequence, and matrix material. Therefore, minimum values from historical data are used for conservatism. It is evident that C-C exhibits relatively low interlaminar shear capability relative to conventional carbon fiber/resin systems. Material coupon testing has been performed to verify C-C interlaminar values.

Bolted and bonded joint analog test results are used to establish design "allowables." The first group of these analogs is in fabrication and will establish the allowable loads and stresses for the primary shield joint. The primary shield seams in both the longitudinal and the hoop directions are reinforced with "T" stiffeners. The T-stiffener has vendor heritage and is co-bonded and bolted to one panel, then bolted to the adjacent panel. The test coupons are shown in Figure 3-10 and will establish a load-per-length allowable for design.

Table 3-3. Summary of material properties for analysis.

Titanium (6Al-4V)	Density Young's modulus Poisson's ratio Tensile ultimate strength Shear strength	0.16 lb/in^3 16 Msi 0.31 145 ksi 93 ksi
Carbon-polyimide (T650/AFR-PE4)	Density Young's modulus Poisson's ratio Tensile strength Compressive strength Interlaminar shear strength	0.07 lb/in^3 10 Msi 0.2 120 ksi 75 ksi 4.6 ksi
Carbon-carbon (T300 fabric)	Density Young's modulus Poisson's ratio Tensile strength Compressive strength Interlaminar shear strength	See Chapter 7
Carbon-carbon (YSH-50 fabric)	Density Young's modulus Poisson's ratio Tensile strength Compressive strength Interlaminar shear strength	See Chapter 7

3.3.4 Analysis Methodology

The structural analysis of the TPS incorporates finite element models (FEMs) with detailed representations of all primary structural components, including the primary shield, secondary shield, and shield support structures (either struts or trusses.) The detailed FEMs are used to predict modes of vibration, regions of peak stress due to vibration, and quasi-static, thermal, and interface loads. Models are constructed with the pre-processor FEMAP and solutions are performed by using MSC/NASTRAN.

The mode shapes and modal strain energies are used to vary design parameters such as wall thickness, material stiffness, and stiffener placement to satisfy minimum frequency requirements. The peak stresses are also used to guide the design, with attention to maintaining predicted stresses below allowable stresses. Allowable stresses are derived by multiplying statistically derived material strength values by specific factors of safety found in NASA-STD-5001, *Structural Design and Test Factors of Safety for Spaceflight Hardware*.[11] For the composite materials, a factor of safety of 1.5 is used. For metallic materials, yield and ultimate factors of safety of 1.25 and 1.4 are used.

3.3.5 Analysis of Ball-and-Strut Design

The FEM of the ball-and-strut design is shown in Figure 3-11. The primary shield, A-frame, and secondary shield pan are modeled with plate elements and contain effective quasi-isotropic material properties for C-C. The secondary shield foam is represented with solid elements. The struts are modeled with bar elements and assumed to strictly

[11] *Structural Design and Test Factors of Safety for Spaceflight Hardware,* NASA-STD-5001, National Aeronautics and Space Administration (June 21, 1996).

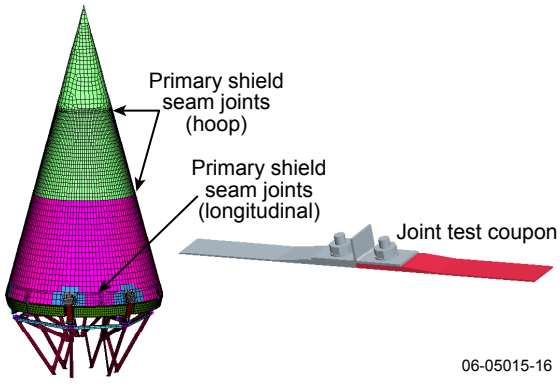

Figure 3-10. Primary shield seam joints.

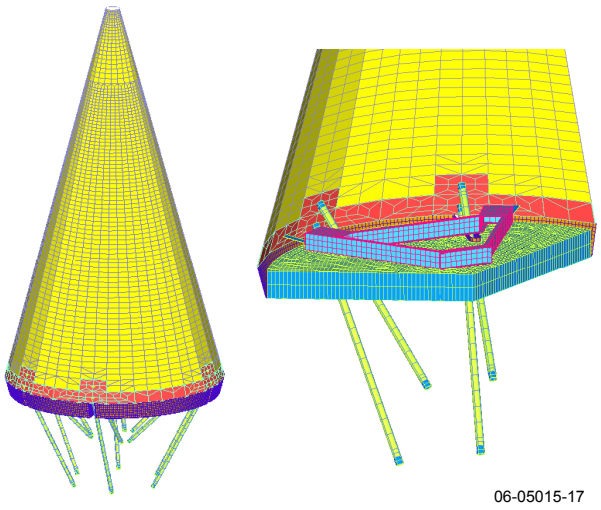

Figure 3-11. Finite element model of the ball-and-strut design.

carry axial loads along the strut length owing to the ball and sockets. At the time of this FEM, the secondary shield cover design had not matured to the point of inclusion. This omission has minimal impact on the loads from the secondary shield and A-frame to the primary shield.

The iterated design meets the frequency requirements. The primary shield interface with the ball and sockets and the A-frame is reinforced with doublers. The stiffness of the lower section of the primary shield and the struts is effectively doubled by exchanging the baseline T-300 C-C fabric with YSH-50. The lateral natural frequency is 16 Hz. The lateral mode shape (exaggerated for clarity) is shown in Figure 3-12. A torsional mode is also present below 10 Hz. This mode is not expected to produce high structural responses.

The predominant quasi-static load case is 20 *g* lateral. Principal stress plots for the primary shield are also shown in Figure 3-12. The stresses are considerably higher around the primary shield interface with the ball and struts and A-frame, exceeding 50 ksi in much of the region. The total weight with frequency compliance is approximately 160 kg. This exceeds the design allocation of 150 kg. Any efforts to meet the strength requirements would require an unfavorable thickness and mass increase, with potential effect of reducing the lateral natural frequency.

The peak strut loads, occurring during the 20 *g* lateral quasi-static case, are ±5,500 lb. The struts and ball-and-socket analogs will be tested to these loads to verify structural adequacy. It is not likely that this axial load will cause tensile or compressive failure of struts. It is anticipated that ball/strut lap shear bond failure, or bolt failure between the sockets and primary shield, will be identified as design drivers during the analog tests.

3.3.6 Analysis of Truss Design

The evolution of the TPS design from struts with ball and socket ends to trusses, jack stands, and flexures is a result of more extensive structural

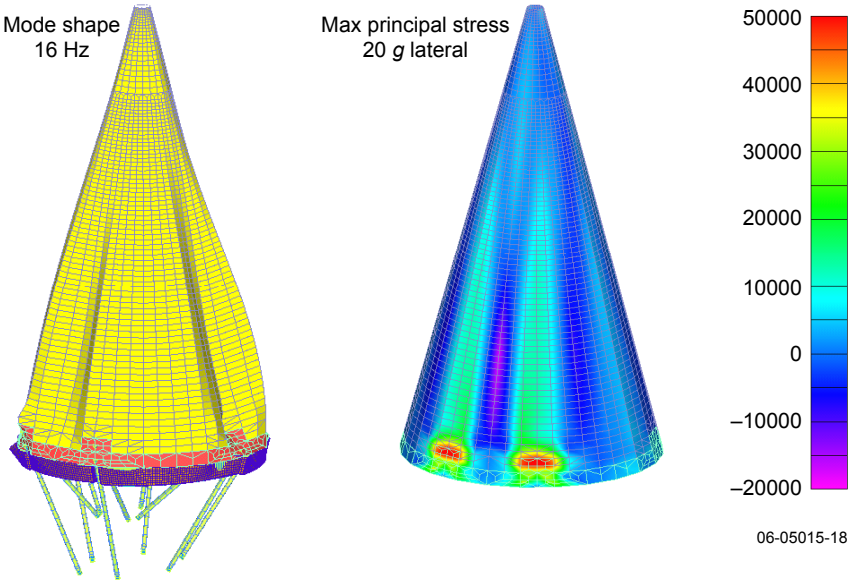

Figure 3-12. Ball-and-strut design mode shape and maximum principal stresses (psi).

analysis, which revealed the strengths and weaknesses of the configuration described in the 2005 STDT report. The ball-and-socket struts proved to be an obstacle after structural analysis revealed that the amount of mass required to achieve the stiffness goals and strength requirements was prohibitive. The truss design takes advantage of a key finding uncovered during the thermal analysis of the 2005 configuration, namely, in the areas of the ball-and-socket struts exposed to space, the temperature along the length of the strut drops quickly over a short distance. The truss design accommodates six C-C jack stands in exposed cavities along the outer edge of the secondary shield. Each jack stand needs to project only a few centimeters below the aft surface of the secondary shield to be cooled sufficiently. The reduced temperature permits the use of more conventional materials aft of the jack stand. Titanium and conventional carbon-fiber/resin composites are candidate materials.

The significant mass savings of the new design is realized because the mass of the C-C secondary shield is now carried by the titanium or carbon-fiber/resin composite trusses, not through the C-C A-frame and into the C-C primary shield, as in the older design. The jack stands, therefore, must support only the primary shield mass. Many discrete support points are available between the aft surface of the secondary shield and the top of the trusses. The size and number of these titanium support flexures is the subject of a future trade study.

The FEM of the truss design is shown in Figure 3-13. All components of the model except the secondary shield foam are represented with plate elements. More detailed design features are included in the truss design FEM model, including seam joints, flexure bolts, and secondary shield cover, than the in the ball-and-strut FEM. The weight of the truss design is 145 kg, which is consistent with the Pro/Engineer model and within the design allocation.

The lateral natural frequency of the truss design is 18 Hz. Figure 3-14 shows the exaggerated mode shape. The addition of cone stiffeners at the base with YSH-50 C-C yields a significant lateral stiffness increase with minimal weight increase. The ball-and-strut design did not exhibit such favorable sensitivity. The axial frequencies are decoupled, with the axial frequencies of the secondary shield and primary shield occurring at 22 and 78 Hz, respectively.

The stresses in the truss design are governed by the 20 *g* lateral load case. Plots of jack stand and primary shield principal stress and flexure von Mises stress (in psi) are shown in Figure 3-15. A summary of all critical stresses is provided in Table 3-4. The peak stresses at the base of the primary shield and the jack stand occur at their interface. The stresses for all components on the cone are acceptable, within their respective factors of safety. Structural evaluation of interfaces, such as the cone seams and jack stand/primary shield, will be performed after results are obtained from analog tests.

Table 3-5 lists the results from modal and static analyses for four truss candidate materials.

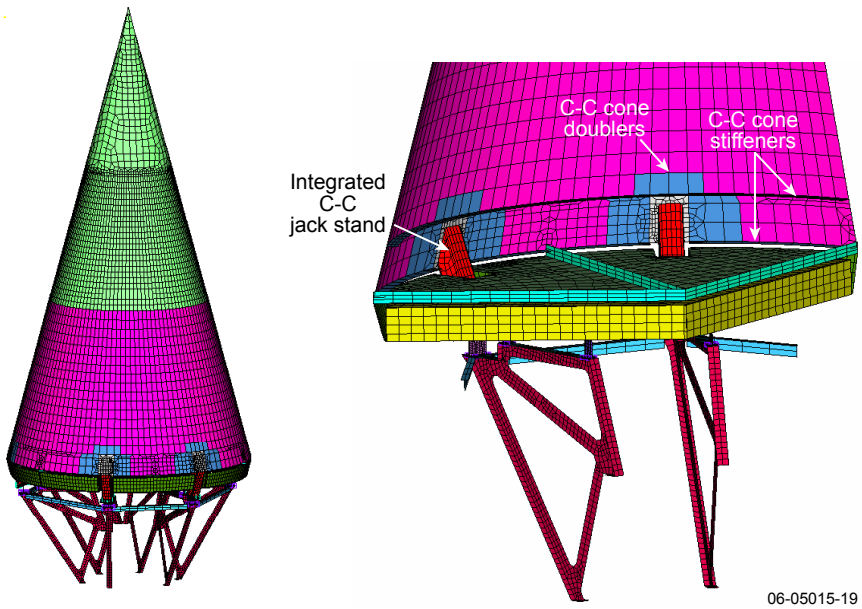

Figure 3-13. Finite element model of the truss design.

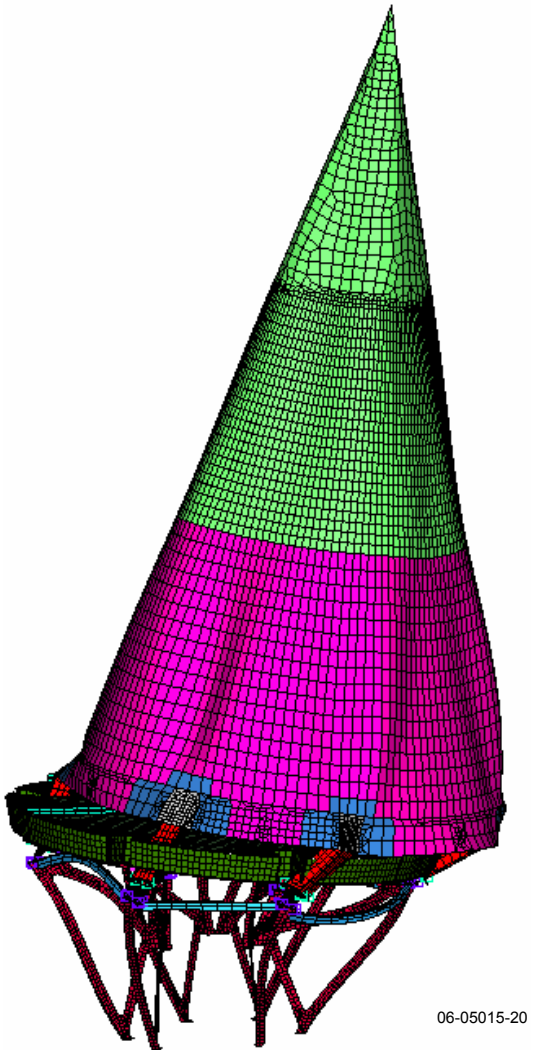

Figure 3-14. Truss design lateral mode shape.

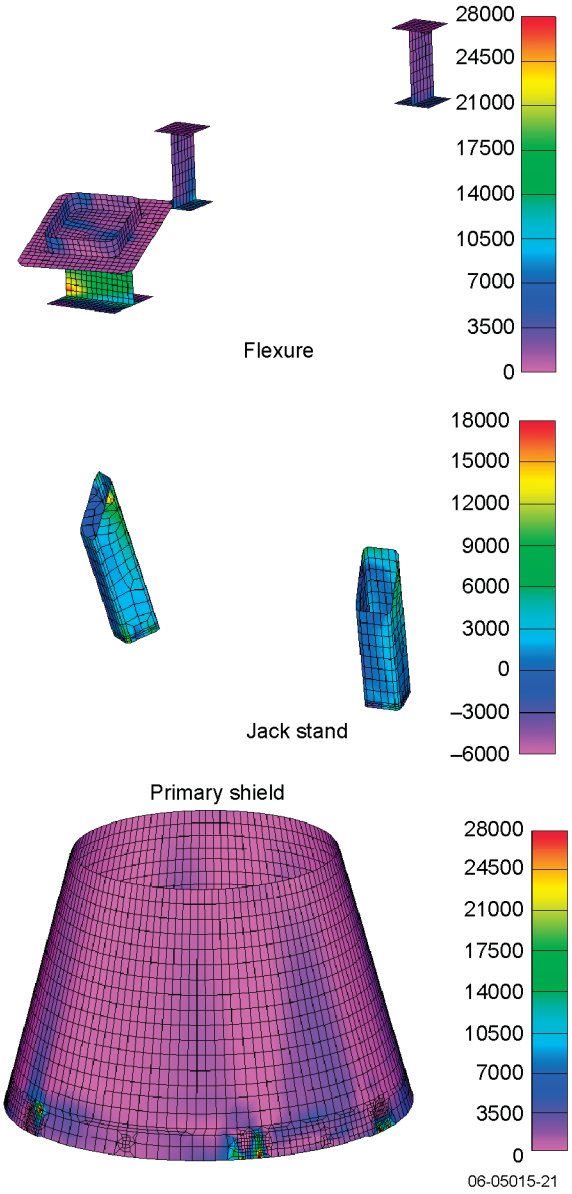

Figure 3-15. Jack stand design von Mises stress contours (psi).

Tradeoff parameters include weight, TPS natural frequency, stresses, and heat flow to the spacecraft. The values highlighted in red indicate design drivers. T650/AFR-PR-4 is a carbon/polyimide composite with stiffness and strength properties that also resemble carbon/cyanate ester composites. All tradeoff parameters for T650/AFR-PR-4 meet requirements, with considerable stress margin of safety, which provides a noteworthy advantage. YSH-50 is a higher stiffness C-C material that also meets all requirements but has low stress margin and would require increased thickness or adding doublers to reduced stress. Titanium provides good strength and low thermal conductivity. The titanium truss thicknesses were reduced until the minimum frequency was approached. The resultant weight of 45.4 lb exceeds the mass budget of 32.8 lb. It appears this weight can be further reduced without impacting natural frequency by changing the truss cross-sections from open sections to closed tubes. AlBeMet 162 has a high stiffness-to-weight ratio, and high strength, but very high conductivity. The heat flow into the spacecraft eliminates AlBeMet as a suitable candidate.

3.3.7 Conclusions

The truss TPS design meets all stiffness and strength requirements. The jack stands provide significant advantages over ball-and-socket struts, with increased stiffness and strength and manageable size for fabrication and test. Loads on the primary

Table 3-4. Summary of critical stresses in the truss design.

Component	Material	Stress Component	Stress (ksi)	Allowable (ksi)
Primary shield	YSH-50 and T300 C-C	Max principal	20	28
		Interlaminar shear	1	1.6
Jack stand	YSH-50 C-C	Max principal	22	28
		Interlaminar shear	0.9	1.6
Jack stand flexure	Ti 6Al/4V	von Mises	31	125
Secondary shield flexure	Ti 6Al/4V	von Mises	19	125

shield and jack stands are reduced with the addition of the trusses. The trusses support the secondary shield separately and eliminate the need for the A-frame support.

All highly stressed C-C joints are co-bonded, not bolted. The co-bonded joint can be strengthened efficiently by increasing bonded area, adding B-studs, or using doublers. C-C fasteners are used only in lightly loaded joint regions, such as the primary shield seams and secondary shield pan. All highly stressed joints with fasteners use conventional materials such as titanium and carbon fiber/polyimide.

3.3.8 Future Work

Analysis of the TPS FEM under comprehensive thermal profiles is required to assess the stresses induced in the flexures due to CTE mismatch. Vibroacoustic analyses will be performed with the TPS FEM to verify that current design loads are not exceeded. Broadband acoustic loads on the primary shield will potentially impact coating adherence and C-C matrix integrity.

Detailed stress analyses will be performed at the piece-part level by using the material allowables established by coupon and analog testing. The jack stand is the most highly stressed C-C

Table 3-5. Truss material tradeoffs (values in red italic type indicate design drivers).

	T650/AFR-PE-4	C-C, YSH-50	Ti 6Al/4V	AlBeMet 162
Tensile modulus	10 Msi	20 Msi	16 Msi	26 Msi
Poisson's ratio	0.3	0.2	0.31	0.3
Density	0.07 lb/in^3	0.06 lb/in^3	0.16 lb/in^3	0.076 lb/in^3
Thickness	0.1	0.1	0.05	0.1
Weight	33 lb	28 lb	*45.4 lb*	36.4 lb
Natural frequency	16.3 Hz	18.2 Hz	*15.6 Hz*	18.8 Hz
Tensile strength	75 ksi	*25 ksi*	145 ksi	38 ksi
Max stress (principal-composite, von Mises-metal)	25 ksi	*26 ksi*	50 ksi	26 ksi
Interlaminar shear strength	4.6 ksi	*2 ksi*		
Max interlaminar shear stress	1.7 ksi	*1.6 ksi*		
Shear strength			93 ksi	32 ksi
Max shear stress			26 ksi	13 ksi
Thermal conductivity	20 W/m C	41 W/m C	8 W/m C	*210 W/m C*
Heat flow to spacecraft	18 W	35 W	5 W	*170 W*

component and therefore will receive the most attention. A detailed jack stand FEM will be used to explicitly determine interlaminar peel and shear stresses, which are likely to influence the design. Bulk temperature change and thermal gradient load cases will also be applied to the detailed jack stand FEM to determine whether the jack stands will remain intact on orbit. Based on the results from these analyses, the best configuration of jack stand will be established, built, and tested. The proposed analog will include the entire jack stand and sufficient surrounding primary shield to produce accurate membrane and bending stresses within the jack stand and its interface with the primary shield.

A comparable level of detailed analysis will be performed on the truss after the material down-select. Detailed truss analyses will be performed to optimize cross-section stresses and weight. This truss FEM will be validated with static tests of a single truss under limit loads predicted from the TPS FEM.

3.4 Thermal Design

The system-level requirements that affect the thermal design are the huge swings in temperature between the Jupiter flyby and the approach to within 4 R_S of the Sun, the net change in the heat flow to the spacecraft between the hot and cold cases, and the overall mass requirement. As with any mission, the thermal design must maintain component temperatures within their operational limits over the entire mission. Because of the extremes in the Solar Probe mission, this standard requirement is much more complicated and includes the development of the TPS. The change in heat flow to the spacecraft over the mission impacts its temperature variation, as well as the system's ability to take and process data. Finally, the mass of the entire observatory is fixed by the lift capabilities of the launch vehicle. Adding more mass in one place means less mass is available elsewhere. Derived thermal requirements for the TPS are given in Table 3-6.

The derived requirements specify the limits on the thermal design space for the TPS. The limits support the development of specific component designs that support the system-level requirements. The key parameters that drive the primary shield temperature are the configurations, surface coating, solar offset angle, and surface irregularities. The secondary shield needs to reduce the heat flow from the primary shield through to the spacecraft. Key design features are the insulation material and its surrounding enclosure. Finally, from an analysis perspective, the support structure temperatures define what materials can be used in that area and what heat is transferred to the bus.

Table 3-6. Derived thermal requirements for the Solar Probe TPS.

Primary Shield Derived Requirements	
Cone α/ε	0.6
Cone half angle	15°
Solar offset angle	2°
Analysis type	Steady state
External primary shield surface	Smooth
Jack stand material & thickness	C-C 0.120 in.
Secondary Shield Derived Requirements	
Temperature gradient	~1000°C
Insulation thermal conductivity	<0.14 W/m-C
Insulation density	<0.05 g/cm^3
Surface emissivity	<0.8
Shield thickness	6 in.
Enclosed shell	Yes
Flexure/Truss Derived Requirements	
Jack stand/truss interface temperature	400°C
Truss interface temperature	350°C
Multilayer insulation (MLI)	Blanketed, partial flange open

3.4.1 Primary Shield

The primary shield thermal design drivers are the configuration and optical properties of the cone. Also, the primary shield temperatures can be locally affected by the solar offset angle and the presence of surface irregularities. Finally, while the mission is transient in nature, steady-state predictions can be used with reasonable accuracy.

The sensitivity of the primary shield to cone angle and optical properties is shown in Figure 3-16. Cone temperatures can range from 1200° to 2600°C. Using the solar absorbtivity/IR emissivty (α/ε) limit of 0.6 and the cone angle of 15° produces shield temperatures around 1580°C (1850 K). The limiting conditions are the increasing mass loss and heat flow as the α/ε limit is increased and the coating availability as the limit is decreased. The cone angle is limited by its height as the angle is

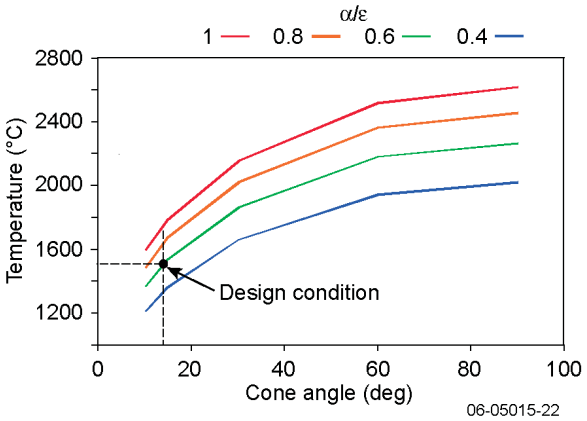

Figure 3-16. Primary shield temperature sensitivity to cone angle and optical properties.

decreased and by temperature as it is increased. The limits presented define an operating condition that is a balance between what can be achieved and what is needed.

An estimate of the optimal cone angle, with the specified α/ε, is given in Figure 3-17. The secondary shield, primary shield, and total masses are shown as a function of cone angle. As the cone angle increases, the cone mass decreases and its temperature increases. This temperature increase requires the secondary shield thickness, and mass, to increase to provide the same thermal insulating ability. The lowest system mass occurs somewhere between cone angles of 15° and 20°. A 15° angle gives the optimal thermal performance at the lowest mass.

Primary shield temperature variations occur due to non-uniform heating and irregular surfaces on the cone. Figure 3-18 shows effects on primary shield temperatures as the TPS is pointed off the center of the Sun. The TPS protective umbra includes a 2° envelope margin. With the Sun offset by 2°, primary shield peak temperatures increase by about 40°C. A nominal requirement on primary shield temperature variation was set at 100°C based on

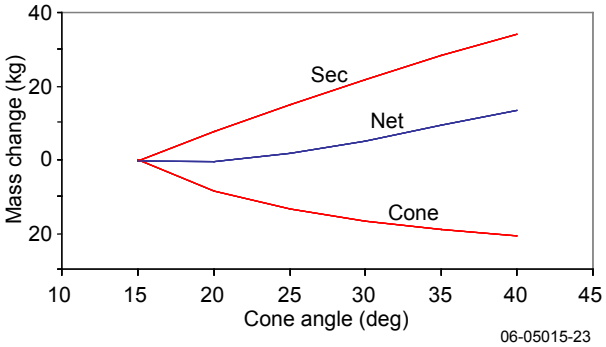

Figure 3-17. Optimal cone angle.

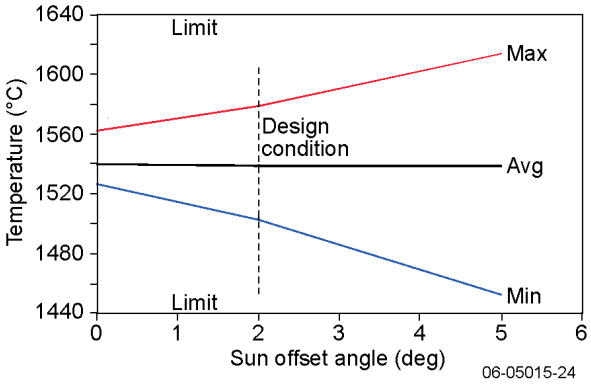

Figure 3-18. Primary shield temperature sensitivity to solar offset angle.

outgassing concerns. The 2° requirement falls well within this limit. Figure 3-19 shows the impact of a 1/4-in. bump on the primary shield surface, representing an exposed bolt. The plot shows the local variations in surface temperature due to the uneven surface heating. The temperature swings are well in excess of the 100° limit, so a requirement for a smooth surface was imposed on the primary shield.

Finally, while the pass by the Sun occurs quickly, the thermal analyses simulating the event are reasonably bounded by a steady-state analytical approach. Predicted primary shield temperatures for the time period when the spacecraft is within 1 AU are shown in Figure 3-20. On an exploded scale, Figure 3-21 shows the transient and steady-state temperatures for the bottom surface of the secondary shield. The plot shows the steady-state prediction is a relatively accurate representation of the transient value.

3.4.2 Secondary Shield

Secondary shield design drivers are the insulating material in the shield and the enclosure that

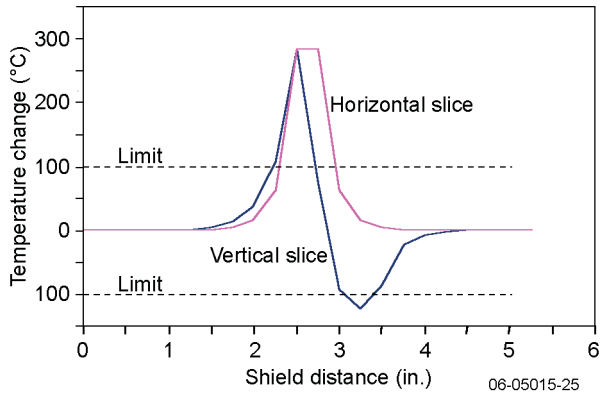

Figure 3-19. Primary shield temperature sensitivity to surface irregularities.

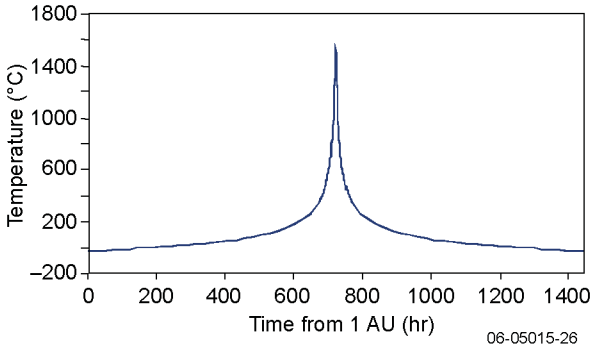

Figure 3-20. Primary shield temperatures within 1 AU.

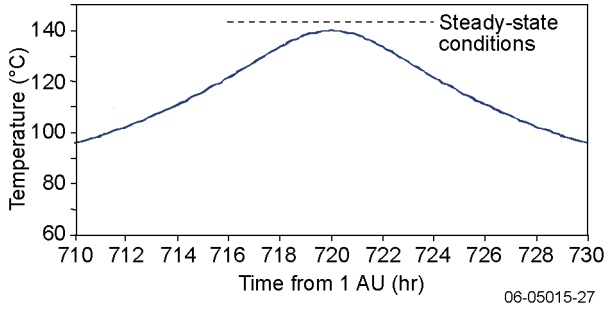

Figure 3-21. Steady-state and transient secondary shield shell temperature through closest approach.

surrounds it. The purpose of the secondary shield is to reduce the heat flow to the spacecraft. It does this by limiting the heat being conducted through the insulation. However, as heat is also conducted around the edges of the enclosure, the support pan configuration and the access holes through it are important.

Nominally, the carbon foam in the secondary shield provides the main thermal resistance between the hot primary shield temperatures and the spacecraft. Figure 3-22 shows the thermal conductivity of two of the candidate insulation materials as a function of temperature. The Ultramet and RVC foams both have low conductivities. However, the Ultramet conductivity increases more rapidly with temperature than the RVC foam does. For the 2005 STDT study, a constant thermal conductivity of 0.14 W/m-°C was used. The real material should have an effective conductivity below this value. RVC foam is the baseline secondary shield insulation material.

The temperature decline through the secondary shield is shown in Figure 3-23. The graph shows thermal contours for foam with constant and temperature-varying thermal conductivities, as well as for two different shield thicknesses. An 8-in. secondary shield thickness was used for the 2005 STDT study.

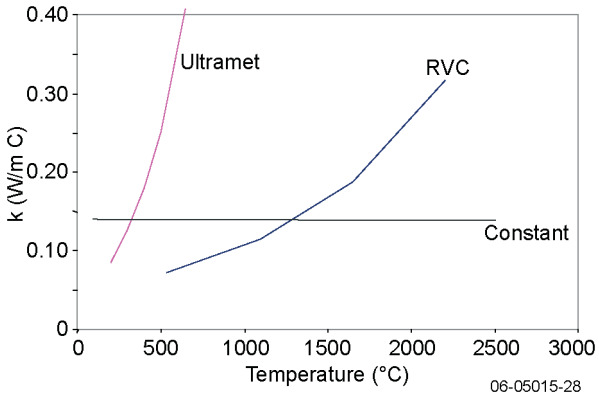

Figure 3-22. Secondary shield insulation thermal conductivities.

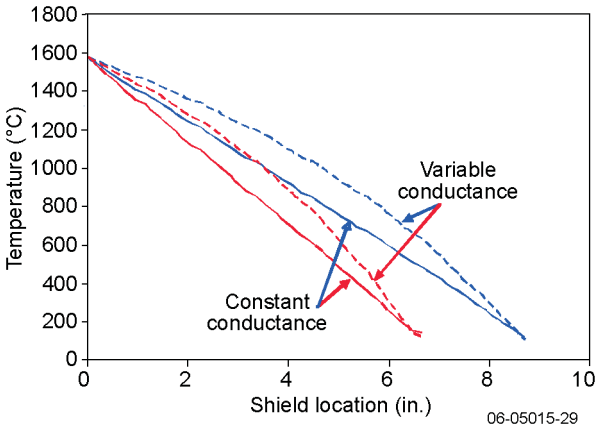

Figure 3-23. Secondary shield temperature contours.

A comparison of SS bottom surface temperatures against shield thickness and thermal conductivity is shown in Figure 3-24. The graph shows that the foam variable conductivity has a large effect for lower system temperatures. Using the variable conductivity for the foam, the shield thickness could be reduced by 25% and still maintain the same bottom surface temperature.

Heat flow between the secondary shield and the spacecraft occurs as the heat that is conducted through the insulating foam is radiated off the bottom surface of the secondary shield. The sensitivity of heat flow through the secondary shield to its surface emissivity is shown in Figure 3-25. The plot shows the impact of surface emissivity on shell temperatures and heat flows. The bottom surface temperature varies between 350° and 125°C as the emissivity is varied between 0.1 and 1.0. However, over the same emissivity variation, the heat flow through the secondary shield varies by about 10%. The large thermal

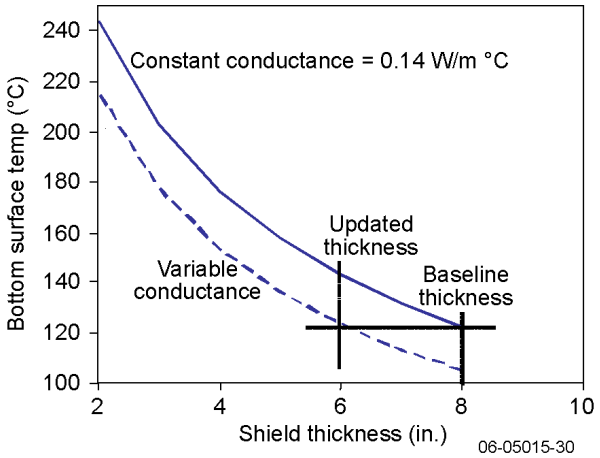

Figure 3-24. Secondary shield surface temperature comparison.

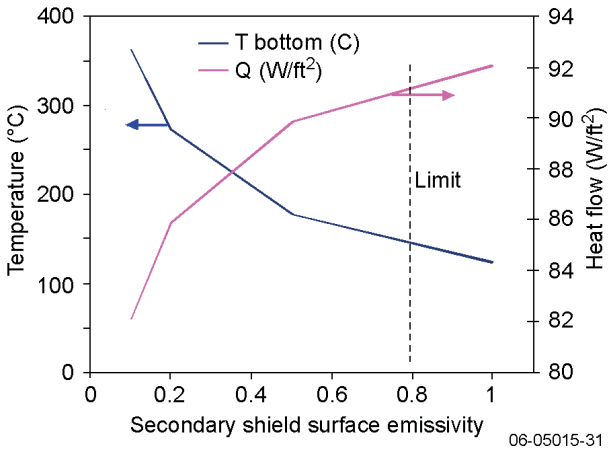

Figure 3-25. Secondary shield shell temperature and heat-flow sensitivity to surface emissivity.

resistance in the secondary shield foam dominates the heat flow through the system, so it is relatively insensitive to the secondary shield bottom surface emissivity.

The key parts of the secondary shield thermal design are the features that increase the heat flow through the structure and increase the peak temperatures of the shield. In a comparison between the ball-and-strut and the truss designs, the truss configuration shows clear advantages. Figure 3-26 shows the cutouts in the secondary shield required by the support structures for the two designs. The edges on these cutouts are areas where the temperature is shorted from the top of the shield. The ball-and-strut design has more edge area because of the deep notches in the shield. There are two types of cutout edges: internal and external. External edges have a good view to space, while internal edges have a limited view out. Thermal radiation

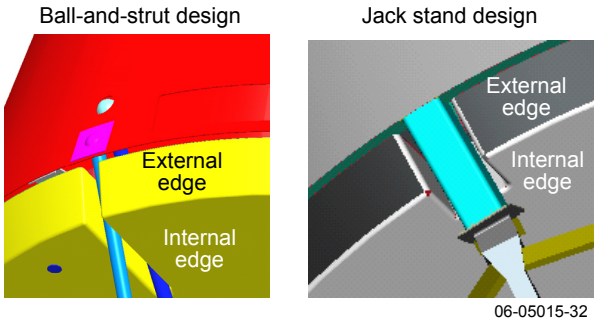

Figure 3-26. Secondary shield shell cutouts for the ball-and-strut and the truss designs.

to space is much more efficient in dropping the shell temperatures along external edges than it is along the internal edges, as shown in Figure 3-27. Therefore, the thermal design, and the certainty in that design, is better for the design with fewer internal edges. The truss design is clearly better than the ball-and-strut design in this respect.

A comparison of the external views of the ball-and-strut with the truss designs is given in Figure 3-28. The ball-and-strut design requires a variety of features on the outside of the primary shield to accommodate the strut attachment structure and access panels. These features raise the local shell temperatures as a result of the surface irregularity effect discussed above. The higher temperatures

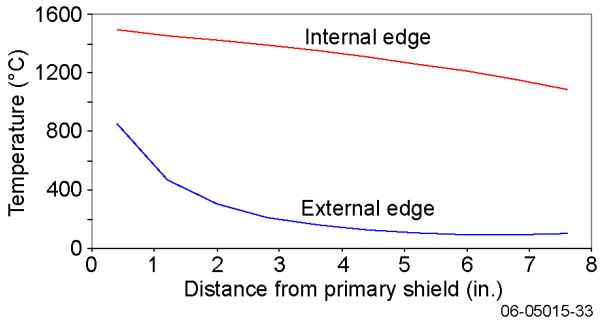

Figure 3-27. Edge temperature drops for internal and external edges.

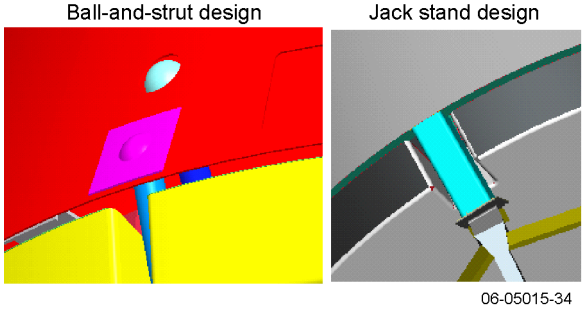

Figure 3-28. External surface configuration.

near the top of the secondary shield result in higher heat flows through the secondary shield enclosure. Again, the truss design has fewer complicating factors than the ball-and-strut design, making it a lower-risk approach.

3.4.3 Support Structure

The support structures for the ball-and-strut and the truss designs are significantly different. The thermal drivers in both cases are the conductive and radiative heat leaks between the primary shield and the spacecraft. Important design parameters are the temperatures of the support structure, the structure material, and its configuration.

A key finding from the thermal analyses is the rapid drop in temperature along external exposed surfaces connected to the primary shield. As shown in Figure 3-29, there is a temperature drop of over 1000°C along the outside face of the secondary shield. The truss design uses that approach, with the jack stand dropping the temperatures from 1580° to about 400°C. The break in the structure at the bottom of the jack stand allows the use of different material in the lower-temperature regime. The ball-and-strut design has the same temperature drop, but there is no opportunity to change the material along the length of the strut.

In the truss design, a titanium flexure located below the jack stand further reduces the temperatures before the interface with the truss. Temperatures at the top of the flexure average less than 400°C. At the bottom of the flexure, the temperatures have dropped to below 200°C. Keeping a significant margin for design uncertainty, the temperature limit at the flexure/truss interface is set at 350°C.

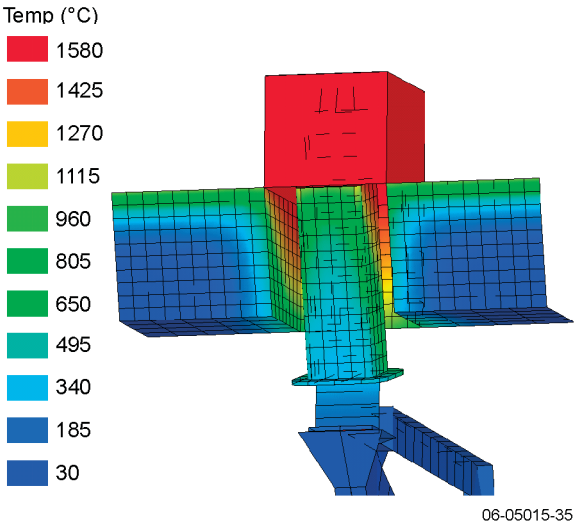

Figure 3-29. Temperature contours along the secondary shield and the jack stand.

The truss itself provides one of the main advantages of the truss design over the ball-and-strut design. The structural support provides a thermally conductive link between the primary shield and the spacecraft bus. The net difference in the heat flows between the hot and cold cases must be absorbed by the spacecraft thermal design. In the system requirements, 50 W was set as that limit. The truss design, with its connection to the MMRTG mount structure, can be tailored to virtually eliminate the heat flow into the spacecraft.

Figure 3-30 shows the temperature distribution in the support truss. The truss had three conductive attachment points: the primary shield flexure (about 200°C), the MMRTG mount (200°C), and the spacecraft mount (30°C). Radiative heat transfer from the MMRTGs and the rest of the TPS is

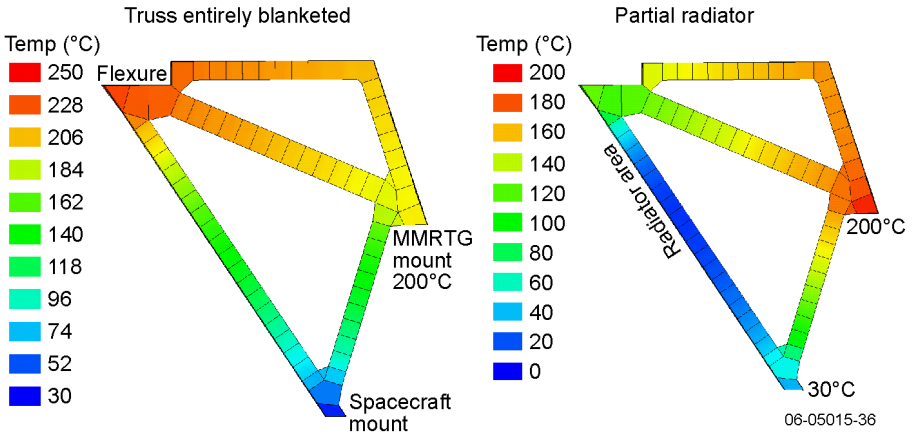

Figure 3-30. Truss temperatures with and without tailored multilayer insulation.

minimized through the use of multilayer insulation (MLI) blankets. Heat transfer to the spacecraft occurs through both the legs connected to the MMRTG and flexure. The spacecraft heat flow can be reduced by partially exposing the truss and letting it radiate to space. As Figure 3-30 shows, truss temperatures along the external leg can be reduced to a point that produces a net loss to the spacecraft. With this design addition, the truss heat flow becomes dominated by the MMRTG mount, which is relatively constant over the mission.

A comparison of the spacecraft heat flows for various truss materials is shown in Table 3-7. Thermally, the low conductivity in the truss material is desired to keep the spacecraft heat flow low. Preferred truss materials are in the 20- to 40-W/m-°C range. Also, by tailoring the MLI on the truss and letting the MMRTG heat leak dominate, the spacecraft heat flow can be virtually eliminated.

Table 3-7. Comparison of spacecraft heat flows for various truss materials

Case	Truss Conductivity (W/m-°C)	Spacecraft Heat Flow (W)
Full MLI	20	17.4
Full MLI	40	35.4
Full MLI	181	147.1
Tailored MLI		
Hot case	20	10.7
Cold case	20	10.5

3.4.4 Conclusions

The 2006 Risk Mitigation Study design and analysis shows the TPS can meet all of its thermal design requirements. Temperatures and spacecraft heat flows are well within their limits. All key thermal design drivers have been addressed satisfactorily. Enough options continue to be available to adjust the design in the future if unforeseen contingencies make that necessary.

The TPS truss design has several advantages over the ball-and-strut design. It allows a separation between the hot and normal temperature zones, permitting different materials to be used in the different zones. This separation means a high-strength material can be used as the PS flexure. Finally, the spacecraft heat flow can be reduced through the connection to the MMRTG mount structure.

4 Coatings

Historically, coatings are designed to either enhance the performance of a component or protect it from a harsh environment. Coatings commonly are employed as thermal management systems, accomplished by tailoring optical properties such as emittance (ε), absorptance (α), and reflectance (ρ) to control temperature. Coatings also are used as barriers to prevent interaction with harsh environments. In the case of the primary shield on the Solar Probe spacecraft, the chief interest is in thermal management.

4.1 Requirements

The specific requirements for the optical coating applied to the external surface of the primary shield include

- Optical properties—ratio of solar absorptivity to infrared (IR) emissivity; $\alpha/\varepsilon < 0.6$
- Resistance to radiation damage—inert to radiation damage including proton and electron bombardment and extreme ultraviolet (EUV) exposure
- Chemical stability—thermodynamically stable in the Jovian and solar environments
- Charging—no impact to spacecraft or instrument operation or disturbance of local plasma environment
- Structural properties—able to maintain structural integrity after surviving launch vibroacoustic loads, temperature extremes (77 to 1850 K), and temperature cycling
- Particulate impact—able to survive solar wind particulate impact with minimal degradation to optical–thermal performance

4.2 Identification of Candidate Materials

During the 2005 study conducted by the Solar Probe Science and Technology Definition Team (STDT),[1] the optical properties of carbon–carbon (C-C) materials were studied to determine variability in α/ε as a result of surface finish. This investigation yielded α/ε values as high as 1.16 for the as-manufactured conditon. Alternative C-C surface finishes were investigated, including glassy carbon (as shown in Figure 4-1), which yielded an α/ε value of 2.4. Pyrolytic graphite (a candidate material from previous studies) also was evaluated, and its α/ε values range from 0.7 to 1.4. Additional margin has to be carried on top of measured optical properties to account for surface variability and aging and environmentally based degradation of the material.

The implications of a hot spacecraft with no additional thermal management to control temperature would be severe from both technical and programmatic perspectives. Earlier study findings indicated that, at these temperatures, the struts (connecting the primary shield to the bus) must be severed after launch (thus introducing additional mass and design complexity). Additionally, the secondary shield would either (1) have to be made extremely thick (inducing a significant mass penalty) if made from existing high-temperature insulation materials or (2) incorporate immature material technologies (with lower thermal conductivities and/or densities) to remain within the secondary shield's mass budget. The latter approach would run the risk of incurring the cost and schedule penalties associated with a costly material development program. Also, at these temperatures, mass loss from the hot C-C structures could increase to levels that potentially compromise scientific measurements.

As the mission concept has matured, the metrics of mass, cost, and risk have received higher scrutiny. To satisfy these metrics, it became obvious that a controlled optical surface on the primary shield was a necessity. Investigations were begun into optical surfaces in the form of engineered coatings that would have a significant impact on reducing equilibrium temperature but would remain stable in the space environment.

This study has shown that an α/ε limit of 0.6 allows significant margin above measured α/ε values for the coatings of interest. The resultant lower primary shield temperatures enable the design evolution described in this report. Total spacecraft mass estimates are consistent with the 2005 STDT study. The strut design no longer requires a severance system and has been replaced by a lower-mass truss system with improved structural margin. The secondary shield has been significantly reduced in volume and mass while still incorporating mature insulation materials, and heat-shield materials are below temperature-driven mass loss thresholds.

Ceramic materials that are visibly white generally provide the optical characteristics compatible with the proposed primary shield passive thermal management strategy. These characteristics

[1] *Solar Probe: Report of the Science and Technology Definition Team,* NASA/TM—2005–212786, National Aeronautics and Space Administration, Goddard Space Flight Center, Greenbelt, MD (2005).

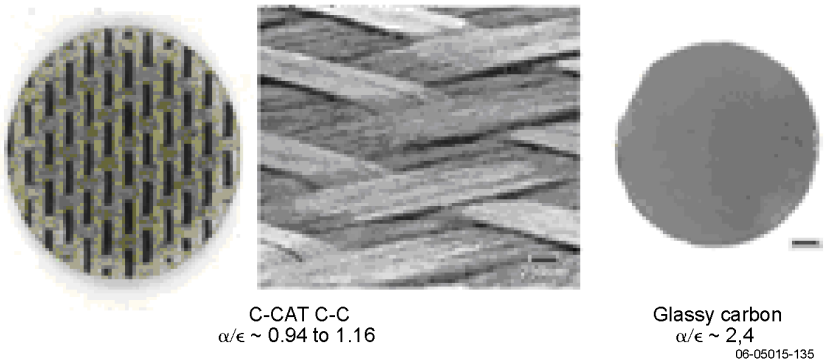

Figure 4-1. Optical characteristics of C-C and graphite.

are low solar absorptivity and high IR emissivity. Thermodynamic stability and chemical compatibility with C-C are additional differentiators that further narrow the list of candidate ceramics. Aluminum oxide (Al_2O_3, commonly called alumina), barium zirconium phosphate ($BaZr_4P_6O_{24}$, commonly designated BaZP), and pyrolytic boron nitride (PBN) notionally satisfy these basic characteristics, as shown in Figure 4-2.

4.3 Material Heritage

Alumina (Al_2O_3) is the baseline coating material for the thermal protection system (TPS). Al_2O_3 has been the industry workhorse for ceramic components over the past 50+ years. Some key characteristics of Al_2O_3 include low solar absorptivity, high IR emissivity, hardness, thermal stability at elevated temperatures, high strength and stiffness, and high electrical conductivity at elevated temperatures. Industrial and military uses of alumina include ballistic armor, electronic substrates, wear surfaces, grinding media, and laboratory instrument sample holders.

The use of alumina for thermal management control on the Space Shuttle low-temperature reusable surface insulation (LRSI) tiles (white tiles on the upper surfaces) is similar to the proposed application for the Solar Probe primary shield. In the LRSI tiles (as shown in Figure 4-3), alumina is incorporated into a silicate glass matrix to control the tiles' α/ε to 0.4. This value has been established to account for aging and contamination in space and has been substantiated through extensive ground testing and flight usage.

PBN has been used extensively in the nuclear industry to protect components exposed to radiation plasma. Some of the key characteristics of PBN that make it ideal for this application include low solar absorptivity, high IR emissivity, low thermal expansion, good thermal-shock resistance, chemical inertness, and thermodynamic stability in contact with carbon to high temperatures in ultra-high vacuum. Other industrial uses include electronic parts, crucibles for single crystal growth of compound semiconductors, plasma arc insulators, high-temperature furnace fixtures and supports, masks for EUV lithography, and graphite/PBN heaters for silicon wafer processing equipment. The heater application is designed to operate in high-temperature, ultra-high-vacuum conditions similar to Solar Probe environments, as shown in Figure 4-4.

BaZP is from the family of sodium zirconium phosphate, $NaZr_2P_3O_{12}$, (NZP) ceramics, with barium replacing sodium for higher temperature stability. Some of the key characteristics for these materials include low solar absorptivity, high IR emissivity, low thermal expansion, high thermal-shock resistance, high strength at elevated temperatures, and thermal dimensional

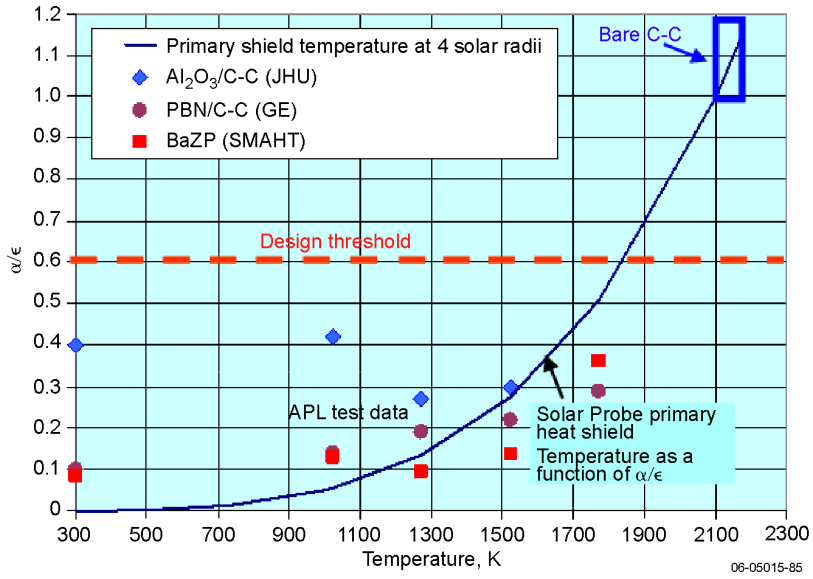

Figure 4-2. Performance of white ceramic coatings versus bare C-C primary shield.

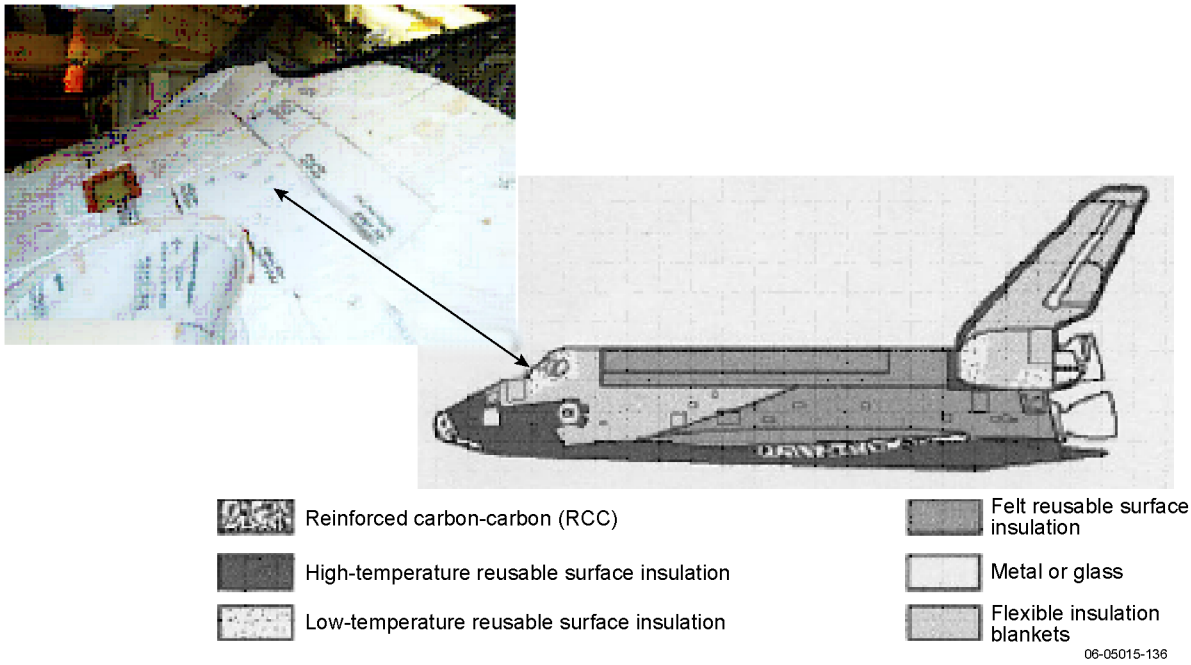

Figure 4-3. Shuttle LRSI tiles incorporating Al_2O_3 for thermal management.

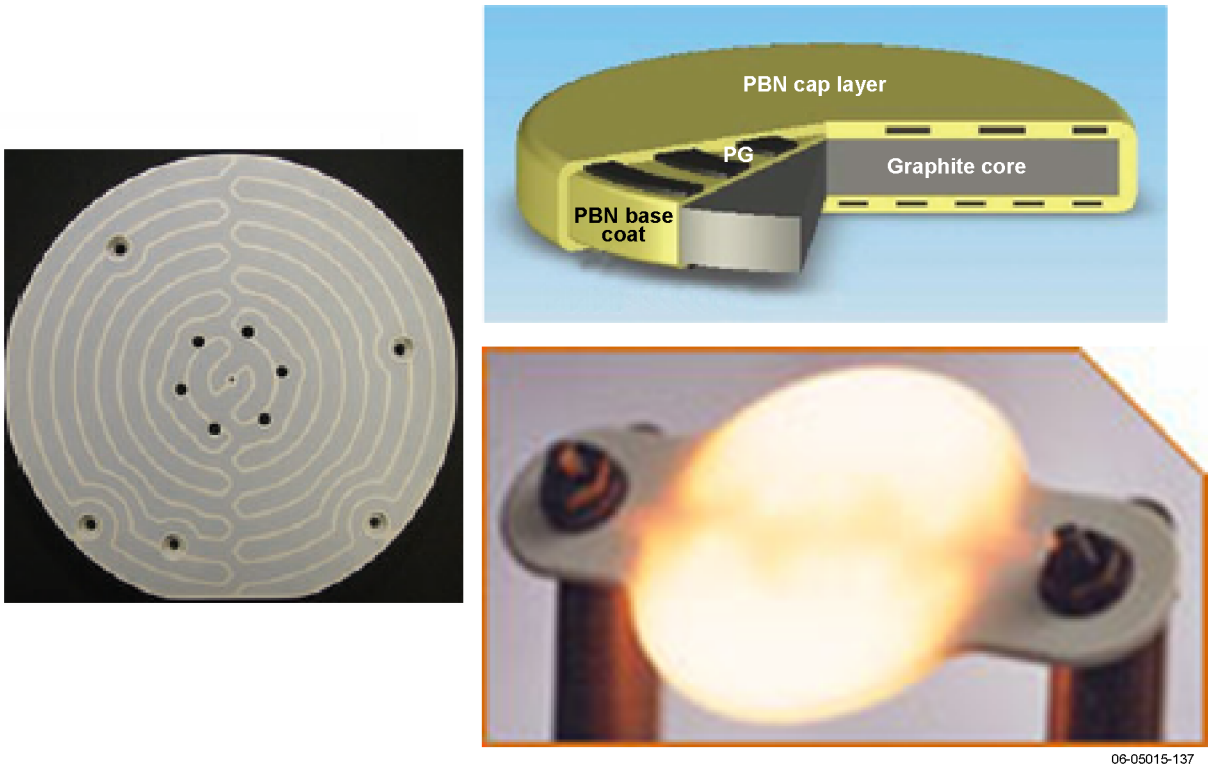

Figure 4-4. PBN/pyrolytic graphite (PG) heater manufactured by GE Advanced Ceramics.

stability at elevated temperatures. Industrial uses for NZP include optical benches, semiconductor wafer benches, furnace support structures, and thermal insulation for diesel engine exhaust ports, as shown in Figure 4-5.

4.4 Primary Shield Coating Design

Generally, the coating-to-substrate interface takes one of three forms, as illustrated in Figure 4-6: (1) direct application of coating to substrate, (2) a functionally graded coating, or (3) a multilayered coating. In any of these cases, a compliant transition from the substrate to coating is desired to minimize coefficient of thermal expansion (CTE) effects and reduce thermal and mechanical stress/strain gradients. The interface also is designed on the basis of strength requirements, service life, cyclic loading, environmental conditions, and coating application methods.

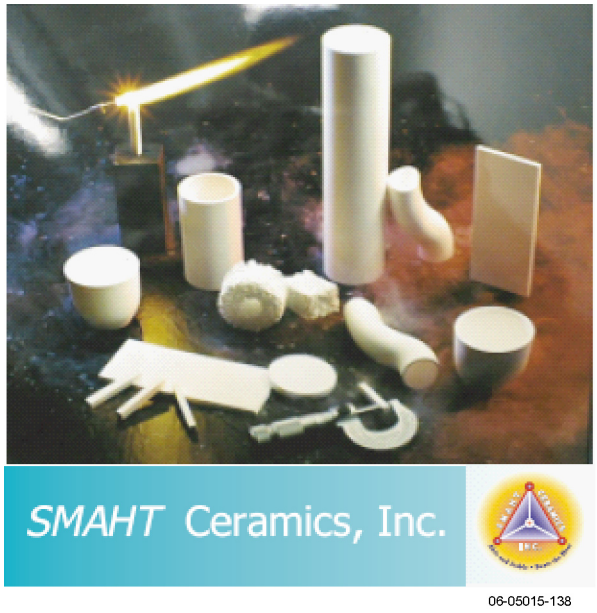

Figure 4-5. High-temperature NZP products.

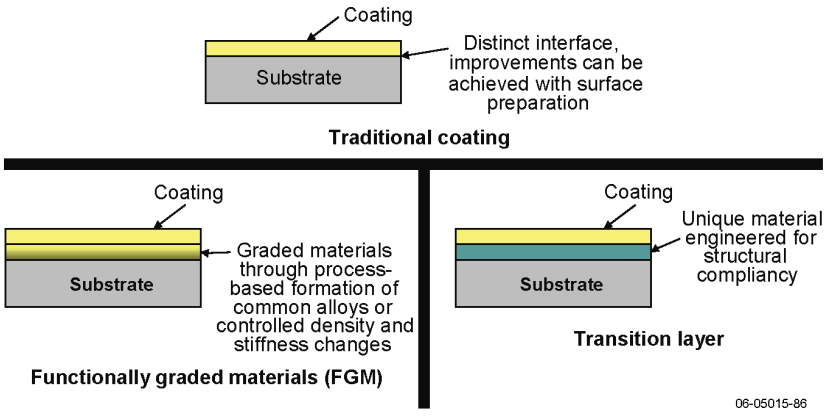

Figure 4-6. Coating design options.

Classic coating designs for thermal and oxidation protection, e.g., high-speed reentry and missile applications, generally include multiple layers for enhanced structural integrity, performance optimization, and redundancy, as Figure 4-7 shows for the Space Shuttle's reinforced C-C (RCC). In most cases, multiple material layers are integrated into a functional ceramic coating: a bond layer, a transition layer, and an outer overcoat layer. Notionally, for a C-C substrate, a bond layer would be integrated into the outer region of the substrate. This material commonly takes the form of a carbide, which is developed through a chemical conversion process. This process creates a strong interface with functional grading effects as shown in the silicon carbide (SiC)-converted C-C matrix in Figure 4-7. This layer is followed by a transition layer that enables a gradual change to the bulk properties of the outer material. This layer is typically a hybrid material that contains some constituents of both the bond layer and the overcoat layer.

The surface characteristics of the C-C substrate are extremely important to promote proper coating adhesion. The local surface density, fabric weave pattern, and fiber tow size influence the mechanical interlocking of coatings with the substrate. Scanning electron microscope (SEM) images were collected for C-C panels processed to increasing levels of densification, designated as advanced C-C (ACC). ACC is manufactured by using multiple densification steps like those used for RCC. Figure 4-8 shows that surface texturing changes only through the first three carbonization cycles. Using C-C with a surface layer that has porosity and roughness similar to the initial densification stages may improve the mechanical bonding ability of the applied coatings.

C-C is widely known as a low-CTE material over a large range of temperatures from cryogenic to very hot. Published data on alumina, PBN, and BaZP indicate good CTE match with carbon over the mission temperature range of 77 K in the Jovian environment to 1850 K at closest approach to the Sun. The CTE of C-C and ceramic coating materials must be characterized further

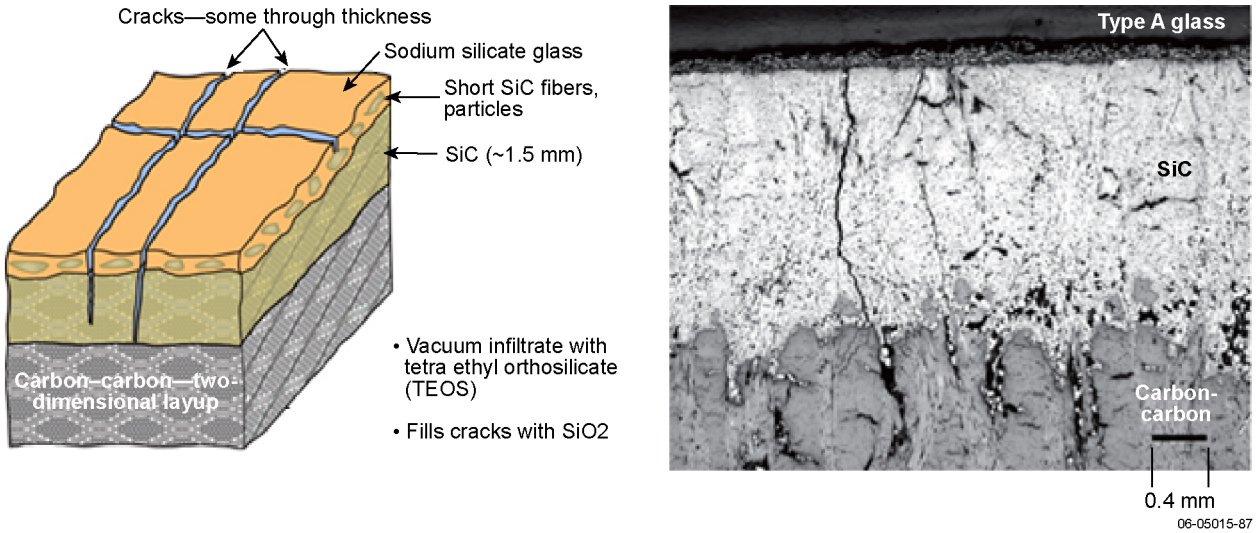

Figure 4-7. Space Shuttle RCC with multiple layers for thermal and oxidation protection.

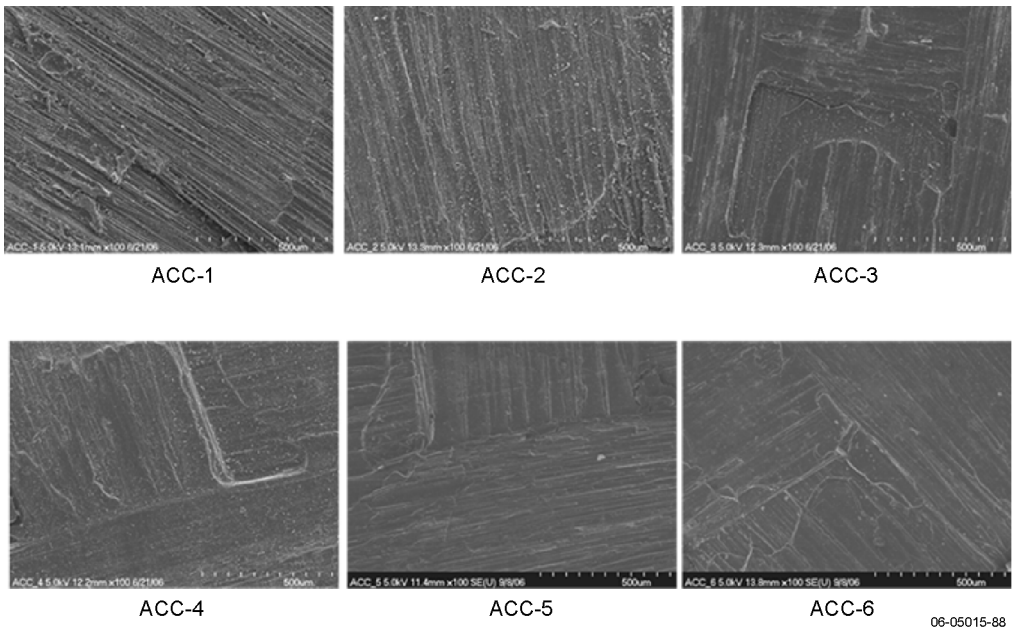

Figure 4-8. SEM images of C-C surface characteristics as the number of carbonization cycles increases. The surface texturing changes only through the first three cycles.

to provide an understanding of thermally induced stresses in different coating stacks. CTE in plasma-sprayed materials can be affected by porosity and quantity of grain boundaries and defects.

4.4.1 Al_2O_3 Coating Design

Initial coating experiments performed in 2005 and early 2006 indicated that Al_2O_3 applied directly to C-C satisfied material performance requirements. Experiments designed to evaluate performance included measurement of optical properties at ambient and elevated temperatures, high-temperature thermodynamic stability in inert and low-vacuum (10^{-2} torr) environments, and structural integrity (vibration and thermal cycling). Alumina was applied directly to the outer surface of an as-manufactured ACC-6 C-C surface with a conventional plasma-spray process, as shown in Figure 4-9.

Plasma spraying involves spraying powders (metals, metal/carbide blends, and oxides) under controlled conditions onto substrate materials (see

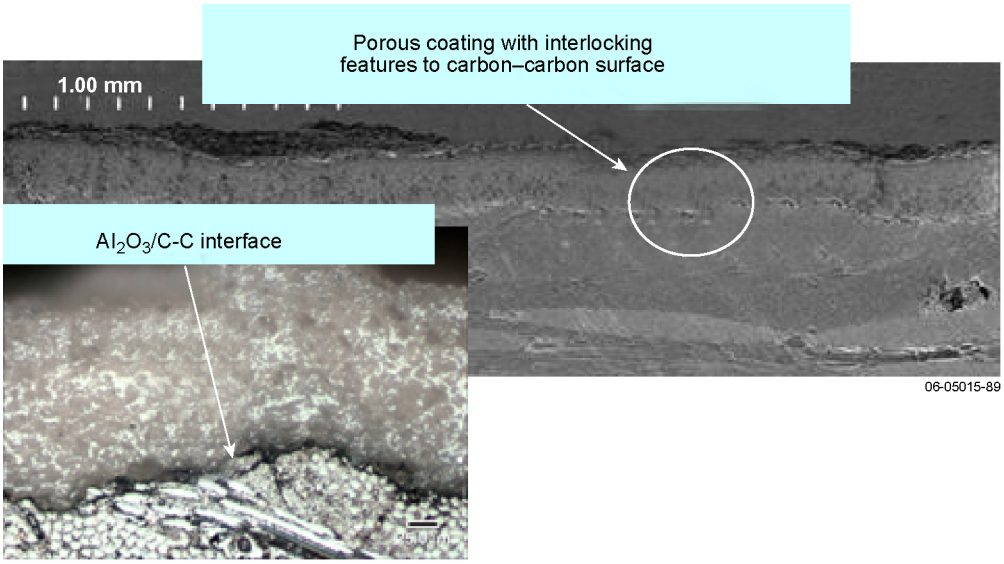

Figure 4-9. ACC-6 C-C substrate coated with Al_2O_3.

Figures 4-10 through 4-12) to build up a coating through the accumulation of "splats" (Figure 4-10). In the process of plasma-spraying alumina in air, the plasma is generated by a free-burning arc between two water-cooled electrodes. This causes ionization of the arc-gas atoms as they pass the burning arc. During the ion/electron recombination process, the ions recombine, releasing the ionization energy principally as heat. Because the energy source is separated from the substrate, plasma spraying maintains a relatively cold substrate. The C-C material temperature can be kept at a low level to avoid oxidation by the air environment. Any material that can be manufactured as a powder, that is chemically stable to high temperatures, and that melts can be plasma-sprayed. The coating is built up particle by particle; each molten particle impacts the surface and fills in the local irregularities. This results in mechanical anchoring to the surface and good coating adhesion. Alumina plasma-sprayed coatings have a low CTE similar to carbon and have an elastic modulus similar to C-C (~10 Msi), which enhances their ability to stay bonded during mechanical and thermal stresses.

Plasma spraying inherently creates a coating-to-substrate interface with mechanical interlocking features as the splats conform to the C-C fibers and stack to form lamellae until the desired thickness is achieved. The ability of the coating to conform to the substrate surface and grip around the carbon fibers can be seen in the SEM images in Figure 4-13 (800× and 1600× magnifications). These images show the underside of a plasma-sprayed alumina

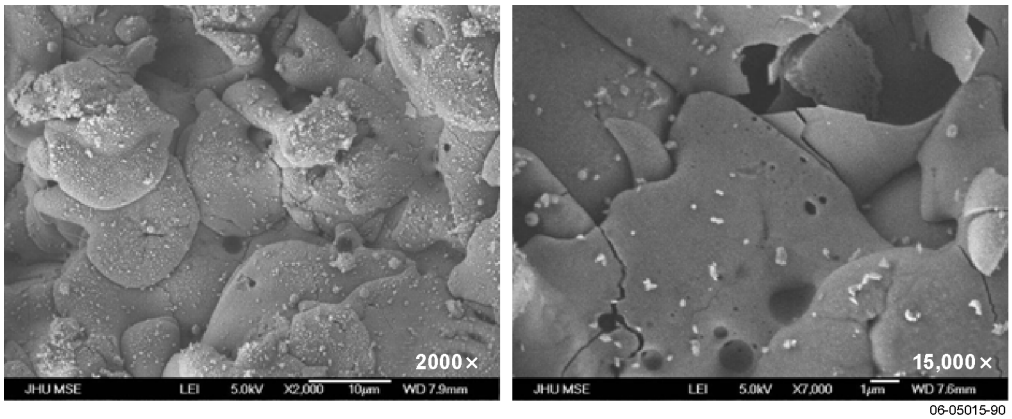

Figure 4-10. Plasma-sprayed alumina splats.

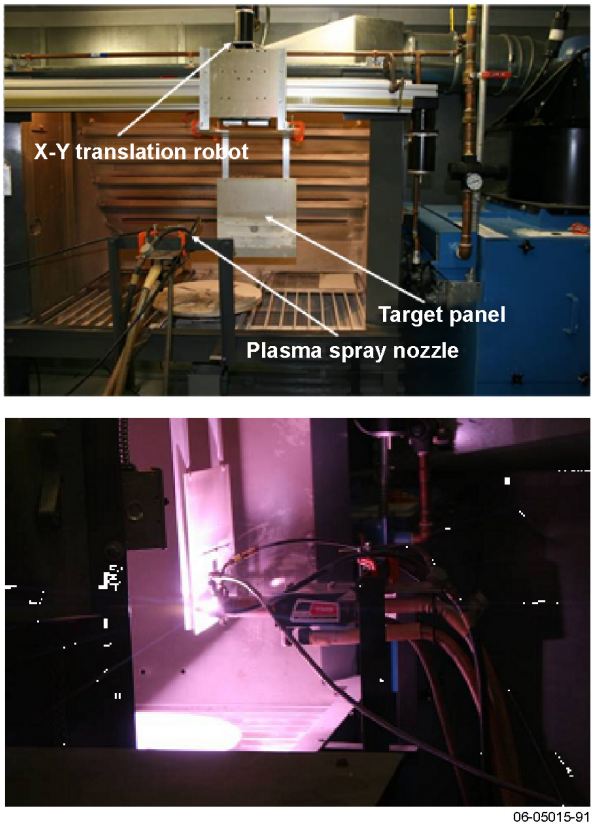

Figure 4-11. Setup and operation of the plasma-spray facility at the Johns Hopkins University Advanced Technology Laboratory.

coating on a C-C panel after removal of the C-C by oxidation.

For plasma-sprayed ceramics, parameters affecting the coating characteristics include particle size of the base powder material, substrate and deposition temperature, cooling rate, spray standoff and velocity, and additives to the alumina powder. Tailoring the processing characteristics in combination with substrate surface morphology can serve to further enhance the degree of mechanical interlocking and thus add structural robustness to the interface. Plasma-spray coatings can be applied to large surfaces and complex shapes with excellent control of thickness and microstructure uniformity.

Plasma-sprayed ceramics such as alumina are not in thermodynamic equilibrium upon deposition because of the rapid solidification inherent to the process. Rapidly quenched alumina tends to nucleate into a metastable disordered cubic structure known as gamma-phase alumina (γ-Al_2O_3), which is stable until heated to temperatures above 900°C. Exposure to high temperatures will result in phase transformations to the stable alpha phase (α-Al_2O_3), crystal restructuring, and grain growth. Therefore, control of microstructural changes is critical. Heat treatment is the mechanism used to stabilize the material, as shown in Figure 4-14. Heat-treating can significantly affect adhesion of the alumina coating to the C-C substrate. Mechanical attachment

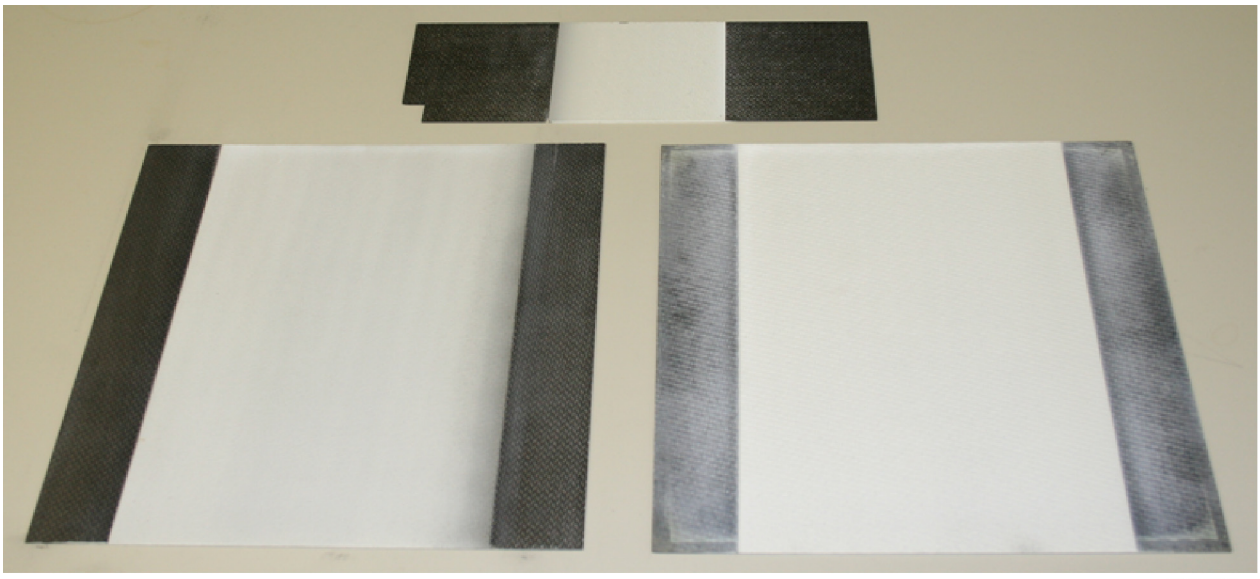

Figure 4-12. Representative (alumina) plasma-sprayed panels.

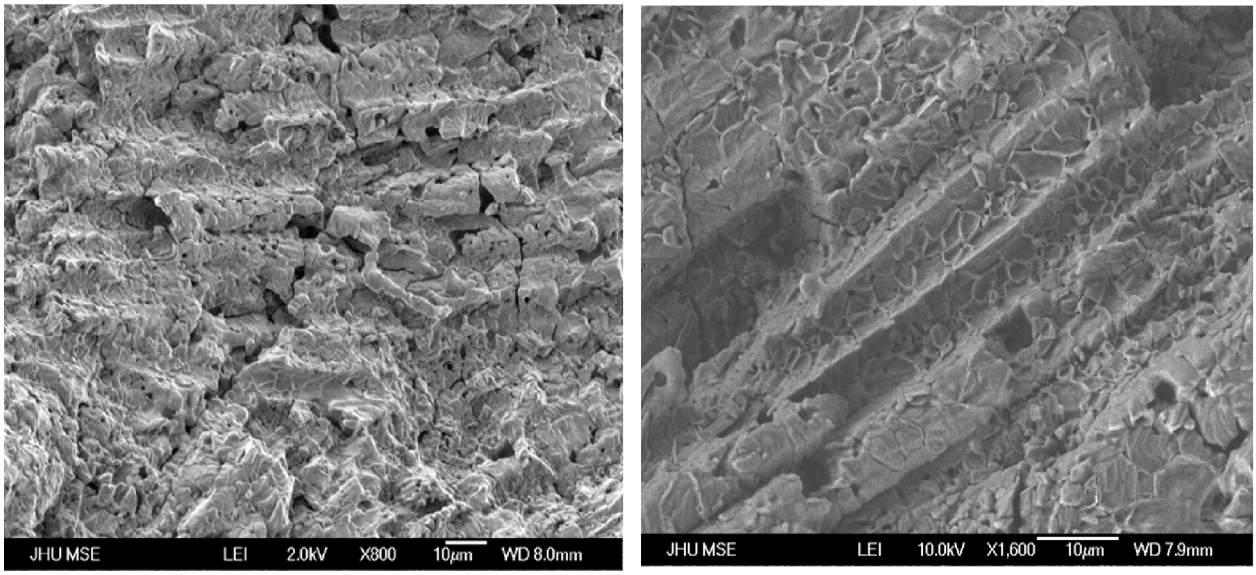

Figure 4-13. Underside of plasma-sprayed alumina coating after removal from C-C.

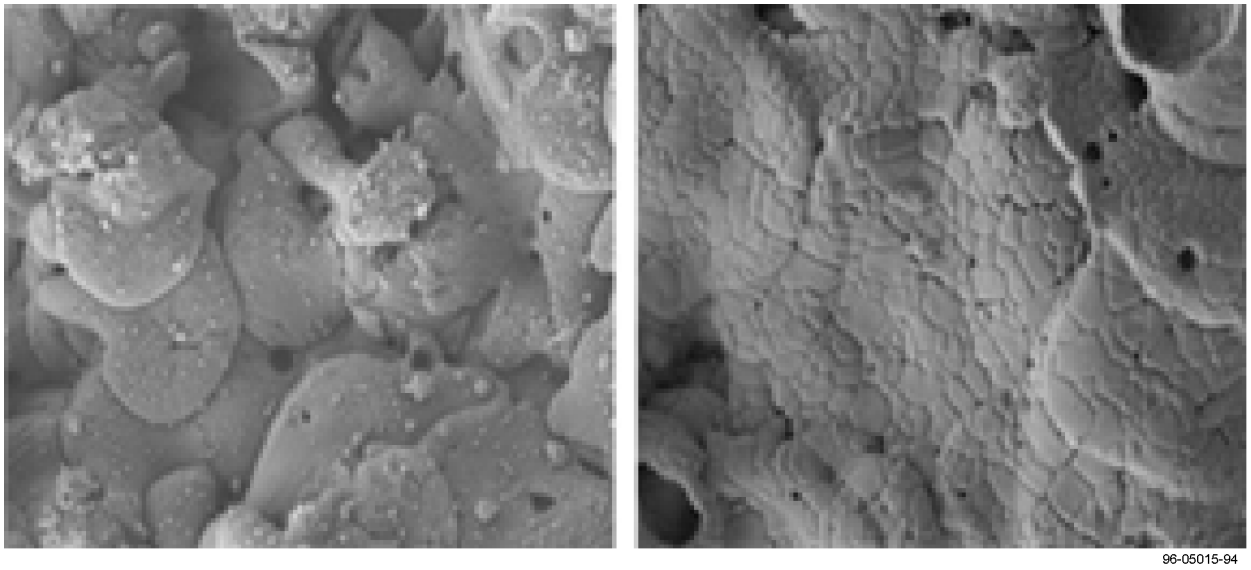

Figure 4-14. Plasma-sprayed alumina splats before and after 1850 K heat treatment.

to the underlying C-C structure may be affected by changes in density and porosity, surface reordering and terracing, and grain growth. Note that the predicted primary shield temperature at closest solar approach (1850 K) is very close to a common sintering temperature for alumina materials. Grain growth inhibitors (i.e., MgO) can be added to the alumina powder before spraying to tailor crystal restructuring.

During 2006, higher-fidelity, high thermodynamic stability experiments were performed at NASA's Glenn Research Center (GRC). These experiments were structured to expose coupons of individual materials and representative ceramic-coated C-C coupons to high vacuum (10^{-9} torr) and elevated temperatures (2100 K) for notional closest solar approach durations. Both C-C and alumina were shown to be stable under these conditions as individual materials. However, when combined, a carbothermal reduction of alumina [via $Al_2O_3(s) + 5/2C(s) = Al(g) + (1/2)Al_2O(g) + (5/2)CO(g)$] occurs under high-temperature and high-vacuum conditions. The vapor pressures of CO(g), Al(g), and $Al_2O(g)$ are all $>10^{-6}$ atm at T = 1650 K.

Although the vaporization behavior of the outer surface of Al_2O_3 is acceptable at temperatures <2000 K, the Al_2O_3/C interface can degrade at lower temperatures. This reduction process resulted in debonding of the coating from the substrate at approximately 1650 K (as is discussed in greater detail in Chapter 5). The temperature at the point of debonding is equivalent to an α/ε of 0.4. This is below our design goal of 1850 K (or an α/ε of 0.6), and therefore requires the incorporation of additional material layers to separate oxygen from carbon. Notably, this process does not occur as readily under inert and low-vacuum conditions.

By using the RCC material as a design model, similar features can be incorporated into the primary shield configuration with negligible performance penalties or mass/volume impact. Separation of the alumina from the C-C can be achieved by inserting thin layer(s) of refractory metals, nitrides, carbides, or oxides. A compliant graded transition from the C-C is desired to minimize CTE mismatches and reduce stress/strain gradients. Critical to achieving this graded effect is the formation of the bond or base layer. Bond layers typically are applied in a manner that promotes conversion of the outer surface and near-surface region of the substrate. Processes that are desirable for C-C are those that produce ionic interactions between the base metal and free carbon in the substrate so that reactions can take place within the local porosity of the substrate surface. Processes that have been investigated for Solar Probe are conversion and sputtering, both of which are scalable to large-scale, complex-geometry components.

Conversion processes involve packing of a part in a reactive powder or liquid/gaseous bed. The entire packed assembly is enclosed in a container where the environment and temperature can be closely controlled. The entire assembly then is heated to a temperature where a reaction can occur between the reactive components of the powder bed and the substrate. In this reaction process, diffusion also occurs, yielding an adherent, graded substrate-to-coating interface. This process, which relies on intimate contact, therefore is applicable to large, complex shapes. The resulting converted layer requires minimal to no dimensional change. The coating is mechanically robust because the converted matrix of the C-C is anchored by the intermixed carbon fibers (see Figure 4-15).

As stated above, separation of alumina and C-C can be accomplished by depositing thin interlayers of stable materials including refractory metals, nitrides, carbides, oxides, or a combination thereof.

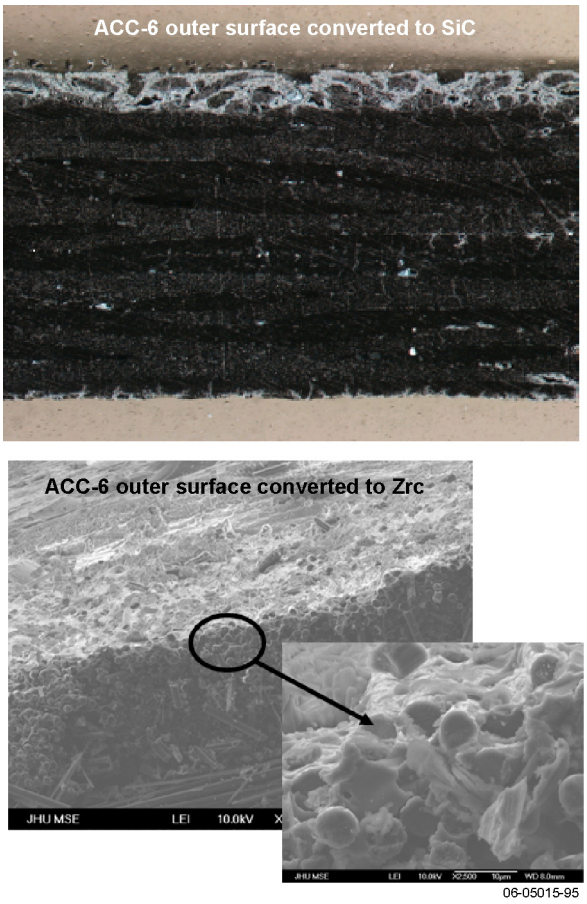

Figure 4-15. Outer region of C-C converted to high-temperature carbide.

Four examples of tested coupons with barrier layers between C-C and alumina are pictured in Figure 4-16. The first sample was covered with 4-μm-thick platinum (Pt), deposited by electron beam evaporation, then plasma-sprayed with alumina. Noble metals such as Pt and iridium (Ir) have high-temperature capability and do not form carbides and, thus, should provide a stable interlayer between C-C and a top coating of alumina. For the second and third samples, 3-μm-thick layers of tantalum (Ta) were deposited on the C-C surface by sputtering. The second sample immediately was coated with plasma-sprayed alumina. The third sample was converted to tantalum nitride (TaN) by heat-treating in a nitrogen purge at 1850 K for 4 hours. The TaN coating then was coated with plasma-sprayed alumina. The last sample pictured is a zirconia interlayer between C-C and alumina. The zirconia powder contains small weight percent additives of ceria and yttria to further stabilize the zirconia at elevated temperatures. High-temperature vacuum testing to maximum operating temperatures indicated that reduction of alumina by C-C was

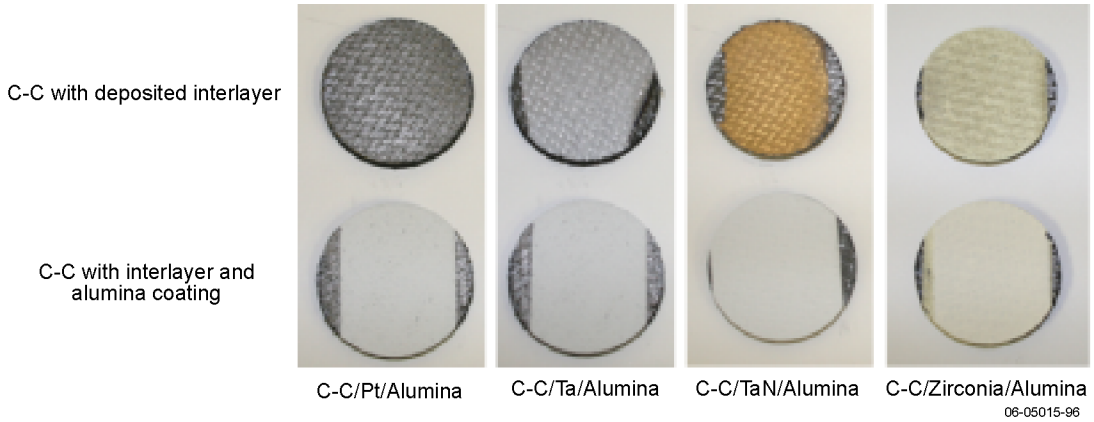

Figure 4-16. High-temperature interlayers incorporated between C-C and alumina.

suppressed by using the interlayer approach. For the refractory interlayers, mass loss was reduced from >2% for C-C/alumina to <0.25% for the Pt and TaN interlayers, thus indicating that interactions were substantially reduced. Additional details regarding mass loss experiments may be found in Chapter 5.

4.4.2 PBN Coating Design

From literature (corroborated by APL thermal cycling as well as APL and GRC mass loss testing), a strong, thermodynamically stable interface exists between the C-C substrate and the PBN overcoat layer to temperatures in excess of 1850 K. PBN commonly is referred to as "white graphite," because it has the same hexagonal structure as carbon graphite (Figure 4-17). PBN is applied to the C-C substrate through a chemical vapor deposition (CVD) process during which boron chloride reacts with ammonia to form boron nitride (BN) and hydrochloric acid in a chamber. A thin layer, analogous to pyrolytic graphite in crystalline form, composed of laminar hexagonal BN is formed on the C-C surface. This crystal structure promotes chemical bonding to carbon.

BN in this pyrolytic form has greatly increased thermal stability compared with cubic BN because there are fewer sites for nitrogen dissociation. Unlike plasma-sprayed alumina, PBN has a perfectly ordered structure upon deposition that does not change with heat treatment. PBN is very ductile (with an approximate modulus of 3×10^6 psi), which allows the coating to handle strain levels in the stiffer C-C substrate.

The CVD process relies on adsorption and surface diffusion to create a uniform coating with mechanical ties to the substrate as well as chemical bonding at the atomistic level. The CVD process is performed at low pressure and temperature, allowing refractory materials such as metals, carbides, nitrides, and oxides to be deposited at a small fraction of their melting temperature. This process provides a highly uniform, dense coating that can be applied to large, complex shapes with high deposition rates, as shown in Figure 4-18. High deposition rates, similar to plasma spraying, can be achieved with control over the morphology, crystal structure, and orientation of the applied coating. One advantage of the CVD process over line-of-sight methods such as plasma spraying is that uniform coatings can be achieved on a curved surface with substantial contours without rotation of the part.

Several basic steps describe the deposition of a CVD coating onto a substrate:

1. Gas-phase reactions leading to formation of coating material precursors
2. Transport of the coating precursors to the deposition surface
3. Adsorption of the coating precursors onto the growth surface

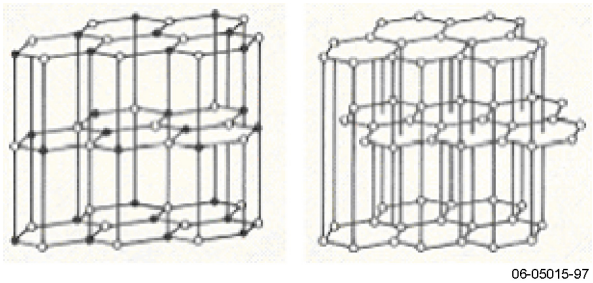

Figure 4-17. Crystal structure of PBN compared with pyrolytic graphite.

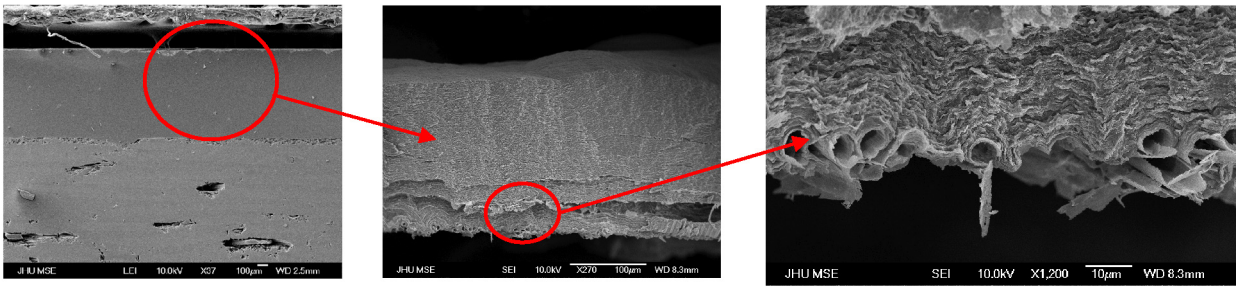

Figure 4-18. The ability of PBN to conform and bond to the C-C surface.

4. Surface diffusion of the coating precursors to the growth sites
5. Surface reactions to incorporate the coating constituents into the growing coating
6. Desorption of surface reaction by-products and transport away from the surface

Although testing of thermodynamic stability, optical properties, and structural integrity has indicated that the C-C-to-PBN interface is acceptable, modifications to the substrate to increase surface area and reduce sheen may be advantageous to improve interface structural margin and repeatability. The addition of surface texturing can provide these desired surface characteristics. Texturing can be achieved via grit-blasting, plasma-etching, or growth of nanoscale surface features such as nanotubes or nanostructures.

The effects of high-energy and low-energy plasma-etching on the C-C surface were investigated. High-energy etching occurs normal to the C-C surface, creating bumpy surface texturing (Figure 4-19). Low-energy plasmas etch the surface from all directions, creating "tree-like" patterns (Figure 4-20). These surface textures increase the adhesion surface area, thus creating a more mechanically robust coating/C-C interface. The etching pattern can be tailored to produce the desired effects by changing the plasma energy, masking direct etching to pre-determined regions, and adjusting the exposure duration.

4.4.3 BaZP Coating Design

BaZP coatings have been applied to C-C by using either plasma-spray or CVD processes for the plasma-spray process as shown in Figure 4-21. Coupons manufactured by using both processes demonstrated coating adherence. Initial thermal stability testing has indicated depletion of phosphate at temperatures above 1500 K. These data appear to be somewhat in contradiction to published data for NZP, which indicates thermal stability to temperatures >1850 K. Investigations are underway to further characterize the thermal stability of BaZP and the BaZP-to-C-C interface. Consequently, extensive structural testing has not been performed for this coating at this time.

4.5 Relationship of Optical Properties to Heat-Shield Equilibrium Temperature

The incorporation of optical coatings onto the primary shield provides a passive thermal management approach designed to reduce the primary shield equilibrium temperature. The substrate material, C-C, inherently absorbs visible energy because of its black color, but it also is a good energy emitter at IR wavelengths. As shown in Figure 4-22, the peak levels of solar irradiance are located in the visible region. Ideally, a coating would reflect a majority of energy in the visible wavelengths and then either emit or be transparent in the IR region so that the IR emittance of the C-C can be used. The notional function of an ideal coating on the C-C is depicted in Figure 4-23.

Literature surveys (corroborated by test-generated data during the engineering study conducted at APL in support of the 2005 Solar Probe STDT) revealed the mission-enabling potential of white ceramic coatings for thermal control of the Solar Probe primary shield near the Sun. To characterize these coatings, optical data (as a function of temperature and wavelength) were collected over the anticipated exo-atmospheric solar spectrum by using both discrete wavelength lasers and a continuous wavelength spectrophotometer (as shown

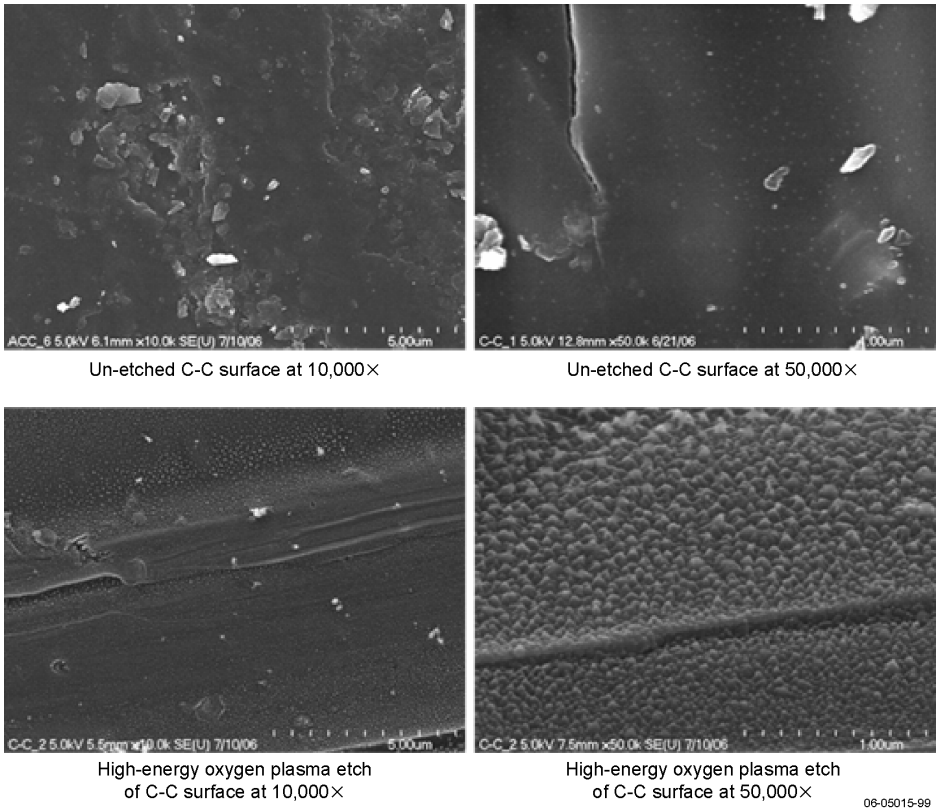

Figure 4-19. High-energy plasma-etching of C-C surface.

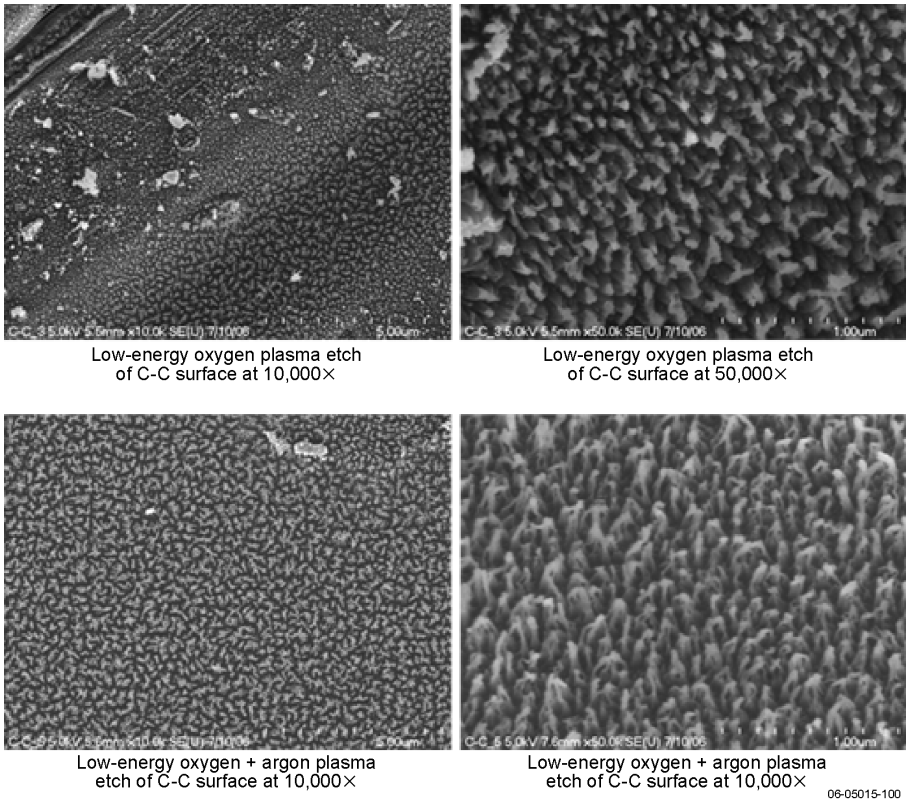

Figure 4-20. Low-energy plasma-etching of C-C surface.

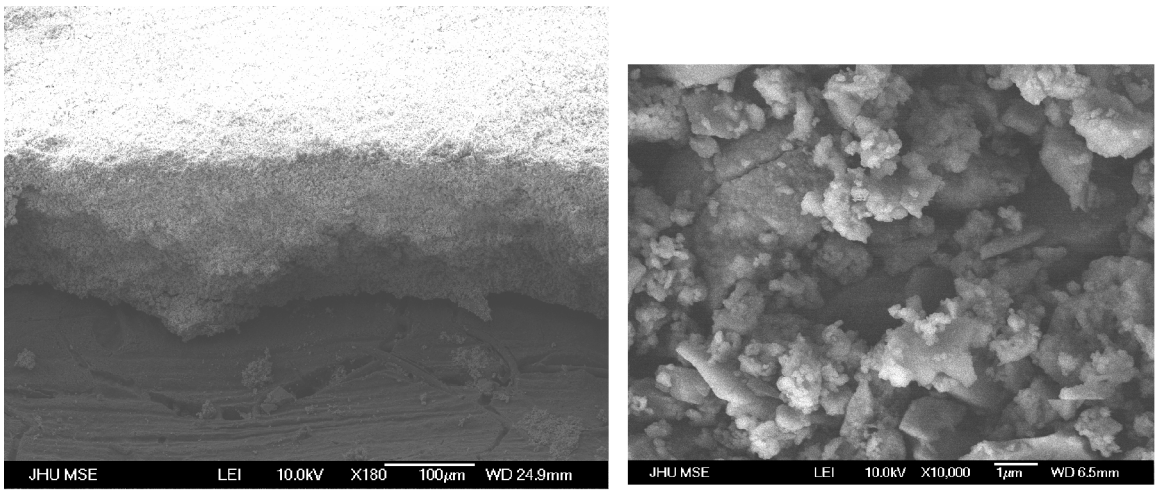

Figure 4-21. BaZP applied to C-C via CVD (left) and plasma-spray (right) processes.

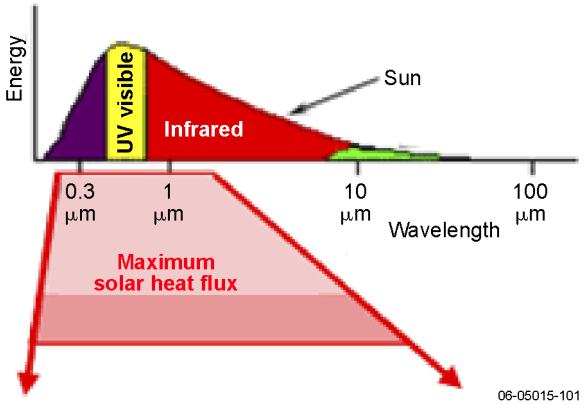

Figure 4-22. Distribution of solar heat flux.

in Figure 4-24). The discrete lasers were selected to replicate significant portions of the solar spectrum and to capture data in the near- to mid-IR band. These lasers were used to measure test coupons both at room temperature and at elevated temperatures. The spectrophotometer (which operated only at room temperature) enabled validation of the discrete laser results and characterization of the materials in the ultraviolet (UV) range, and it filled the gap between the visible/near-IR and mid-IR lasers. The resulting data then were incorporated into a spectral-based radiant thermal model to predict the spacecraft's primary shield temperature as a function of distance from the Sun.

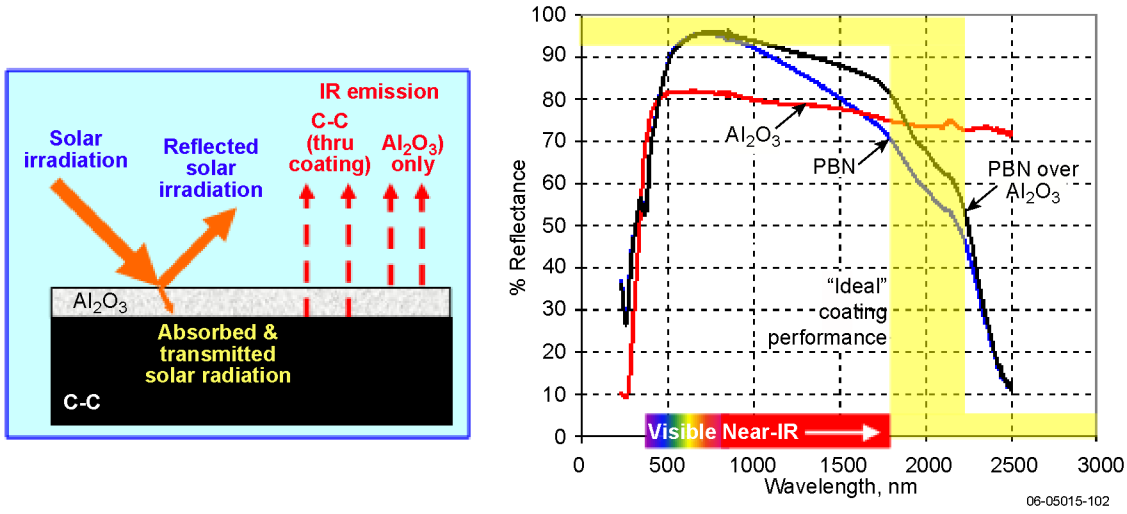

Figure 4-23. Functionality of coating on primary shield.

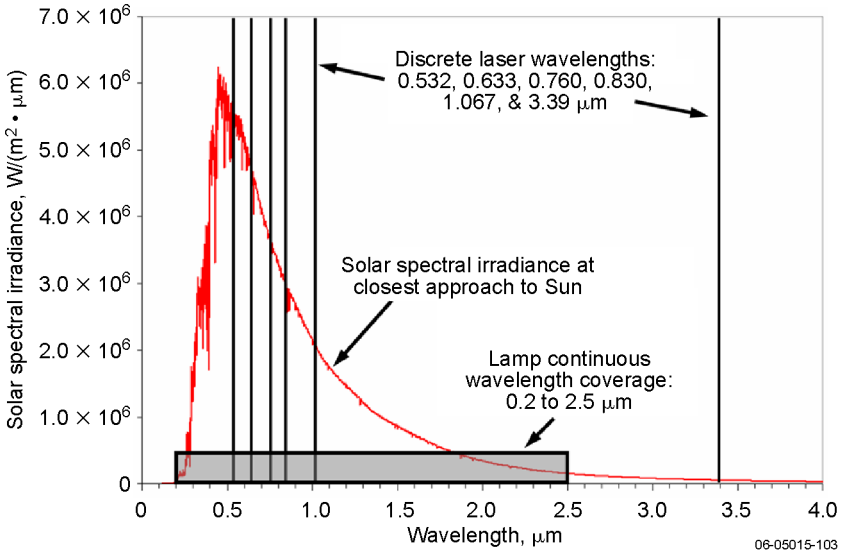

Figure 4-24. Solar irradiance profile and test wavelengths.

The accuracy of the primary shield equilibrium temperature prediction is influenced by the local solar environment (heat flux), the geometry of the heat shield (reflectance area, emittance area, and thickness), and the optical properties of the heat shield (absorptance, emittance, reflectance, and transmittance). A level of uncertainty is associated with each of these variables. This study has focused on investigating the uncertainties related to the primary shield's geometry and optical properties through a combination of modeling and controlled laboratory testing. By empirically and analytically characterizing the effects of uncertainty on primary shield performance, we will further our understanding of the influence of each variable on the primary shield equilibrium temperature. Such knowledge will focus development of the coating's future design and manufacturing requirements on those variables that have the most influence on primary shield performance.

4.5.1 Test Methodology

Reflectance was measured at specific wavelengths over a range of temperatures (from room temperature to the predicted equilibrium temperature). Room-temperature hemispherical and elevated-temperature "near-normal" reflectance were measured on intact coating–substrate and coating material-only specimens. Hemispherical transmittance through the coating was measured (at room temperature) after removal of the substrate (via oxidation at an elevated temperature). The solar absorbance or IR emittance then was calculated by using the total power law:

$$\alpha_\lambda = 1 - \rho_\lambda - \tau_\lambda , \quad (1)$$

which for a diffuse surface by Kirchhoff's law ($\alpha = \varepsilon$) can be written as

$$\varepsilon_\lambda = 1 - \rho_\lambda - \tau_\lambda , \quad (2)$$

where

λ = wavelength,
α_λ = spectral absorptance,
ε_λ = spectral emittance (= α_λ),
ρ_λ = spectral reflectance, and
τ_λ = spectral transmittance (for coating-only tests).

As shown in Figure 4-22, the bulk of the solar irradiance on the primary shield occurs between 0.3 and 1.5 μm. The basis for calculating the solar absorptivity was reflectance measurements ranging across those wavelengths. Optical measurements were conducted by using a variety of methods, including bidirectional reflectance diffuse function (BRDF), total diffuse reflectance (by using two different total integrating sphere test facilities), total transmittance (of the coating only), and measurements of near-normal reflectance as a function of elevated temperature. Figure 4-25 illustrates these various methods and summarizes the test approach.

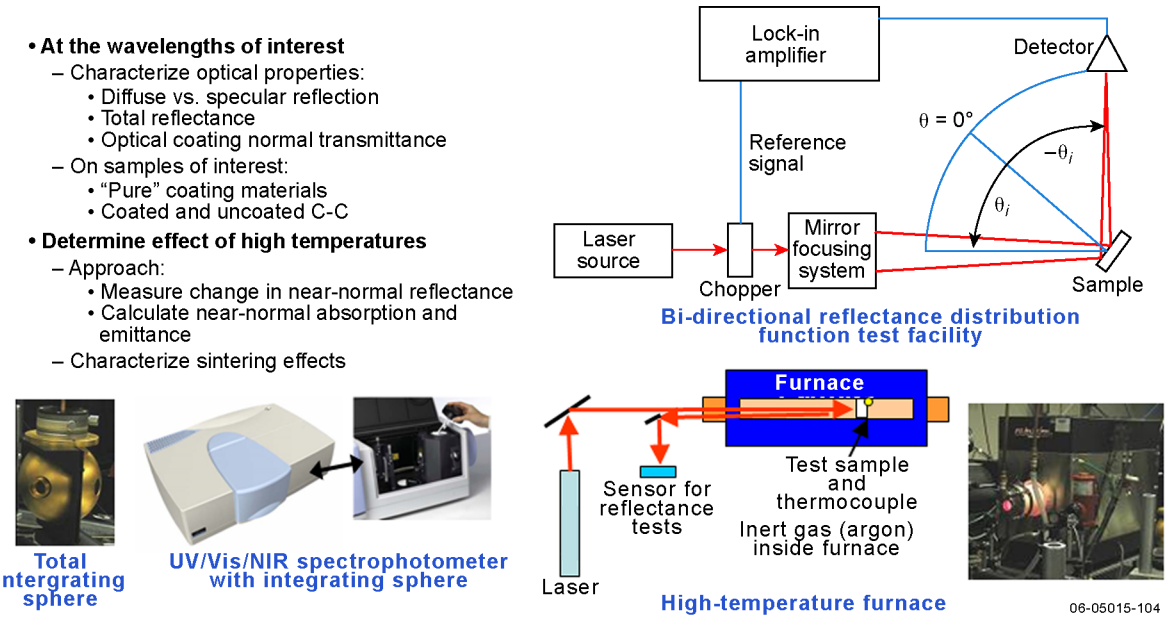

Figure 4-25. Optical testing approach.

Room-temperature BRDF measurements were conducted to verify the diffuse nature of the ceramic-coated C-C specimens. The apparatus used to measure the BRDF is shown schematically in Figure 4-25. The source laser beam was chopped, expanded, and focused onto a detector mounted on a rail, which was in turn mounted on a rotational stage. The detector was rotated around the sample, and a lock-in amplifier, whose reference signal was derived from the chopper, recorded the detector output. The sample was mounted at the center of rotation of the detector-rail system at various angles with respect to the incident beam. The 0° angle in the data corresponded to the surface normal of the sample. Based on initial measurements, symmetric reflectance (with respect to the surface normal, i.e., the reflected intensity has no dependence on the azimuth angle) was assumed for the remaining measurements. The data were post-processed via an algorithm that used the cosine factor for calculation of the Lambertian-phase function. This method enabled matching a model to the measured results. The resulting model then was integrated (over a hemisphere) to calculate the total integrated reflectance. These tests were conducted during the APL engineering study that supported the 2005 STDT.

Because the setup, execution, and data analysis of BRDF tests were labor- and time-intensive and because the materials being evaluated proved to be diffuse, a quicker approach was implemented: total integrated scatter (TIS). The TIS measurements were conducted at room temperature by the following method. First, a baseline measurement was recorded by using a Lambertian (i.e., diffuse) sample of known reflectivity. A second measurement then was made by using the ceramic-coated C-C sample under testing. The TIS was simply the ratio of the sample measurement to the normalized baseline measurement. Two different test facilities were used to collect these data. The first facility included the discrete wavelength lasers shown in Figure 4-25 and two integrating spheres (one for the visible band and another for IR wavelengths). The second TIS method used a Perkin-Elmer Lambda 950 UV/Vis/IR spectrophotometer providing continuous wavelength coverage from 0.2 to 2.5 μm, thus covering near-UV, visible, and near-IR bands.

As shown in Figure 4-25, a high-temperature ceramic tube furnace filled with argon gas was used to determine the change in "near-normal" reflectance of the ceramic-coated C-C samples as a function of temperature. The normalized change in reflectance was multiplied by the room-temperature TIS results to calculate the change in total integrated reflectance due to elevated temperatures. Kirchhoff's law then was used to determine the total diffuse emittance as a function of temperature.

4.5.2 Optical Test Results

A systematic optical testing program was conducted to elucidate the fundamental response of the C-C substrate, the ceramic coatings, and the integrated substrate/ceramic-coating material system.

Additional testing was performed to characterize the effect of grazing angle on optical performance.

Emittance Characteristics of C-C Substrate. The room-temperature IR emittance of various C-C samples was measured by using the spectrophotometer. Results are shown in Figure 4-26. The emittances of various bare C-C coupons have a slightly negative slope across the near-IR spectrum, whereas C-C with a thick or a thin SiC surface conversion layer shows a moderate positive slope. For comparison, a sample of pyrolytic graphite also was measured. Its average near-IR emittance (~0.63) fell below that of the C-C samples.

Diffuse Reflectance Measurements of Ceramics. No specular reflection was observed during visual inspection of the ceramic-coated C-C samples, indicating that they were diffuse. This belief was confirmed by the BRDF measurements. Figure 4-27 illustrates typical BRDF measurements, verifying that Al_2O_3-coated C-C was diffuse in both the visible and mid-IR bands (similar results were obtained for PBN and BaZP). Lasers of differing wavelengths (0.532, 0.633, and 3.39 μm) were directed onto the test specimens at varying incidence angles (20°, 45°, and 60°; shown in Figure 4-27 by the "cut-outs" in the BRDF results when the sensor swept between the laser and the test specimen). The results reveal good diffuse properties in the visible band ($\lambda = 0.633$ μm). The results show slightly less diffuse reflection in the mid-IR band ($\lambda = 3.39$ μm; note the slight skewing of the BRDF curve for a 60° incidence angle as opposed to a narrow, tall peak that would indicate significant near-specular reflection). Interest in the mid-IR band is primarily on heat-shield emission (which will occur diffusely) and not on IR reflectance. At the high incidence angles expected during operation, any specular reflection would serve to decrease the temperature of the primary shield (by reflecting more solar energy than a diffuse surface), so the use of diffuse surfaces in the thermal modeling process is a conservative approach. Thus, the BRDF test results supported modeling the primary shield as a diffuse

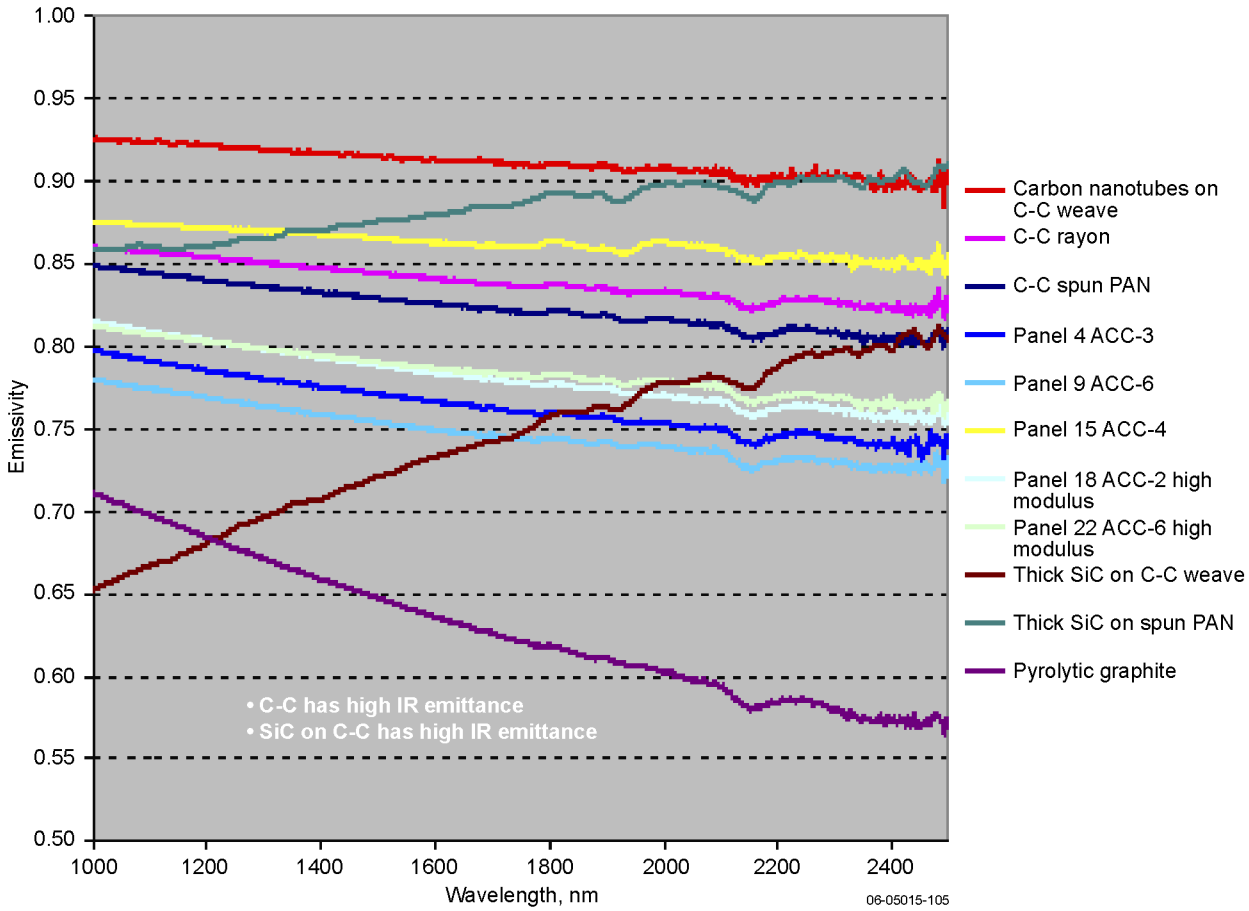

Figure 4-26. C-C emittance measurements.

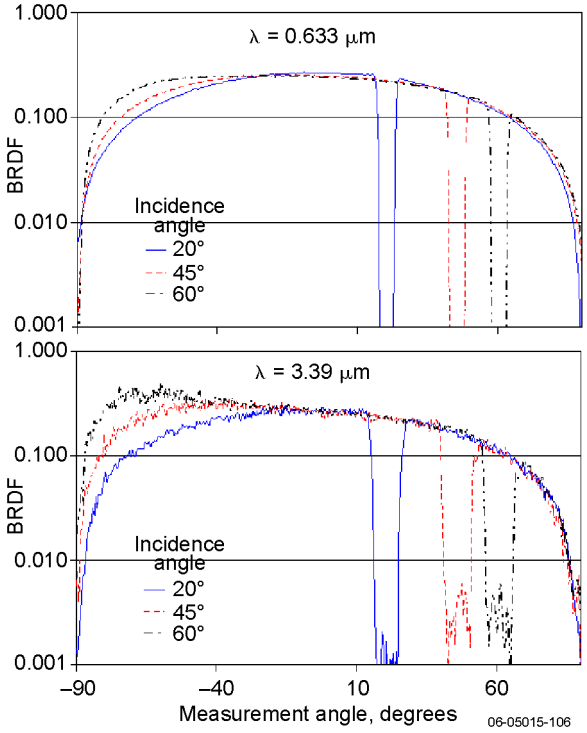

Figure 4-27. BRDF results confirm Lambertian properties.

surface for both solar reflection and IR emission studies.

Optical Properties of Ceramic Coatings. The BRDF tests enabled calculation of the spectral total integrated reflection (TIR) of the coated specimens. For the results shown in Figure 4-27, the TIR at $\lambda = 0.633$ μm was approximately 0.85 for all angles, and the TIR at $\lambda = 3.39$ μm was 0.4 for incidence angles of 20° and 45° and 0.48 for an incidence angle of 60°. Because there is no transmission through a coated C-C sample, knowing the spectral TIR of such a sample allows calculation of the spectral absorptance or emittance via Kirchhoff's law. For the sample tested in Figure 4-27, this corresponds to a room-temperature α/ε range of 0.25 to 0.29 (results that fall within the range of the TIS measurements).

The TIS test results (taken at room temperature) for both bare C-C and Al_2O_3-coated C-C samples are shown in Figure 4-28. The dashed curves are from tests performed at the discrete laser test facility, while the solid line shows a test from the spectrophotometer. Comparing the two curves for the Al_2O_3-coated samples reveals good agreement between the spectrophotometer and discrete laser test setups.

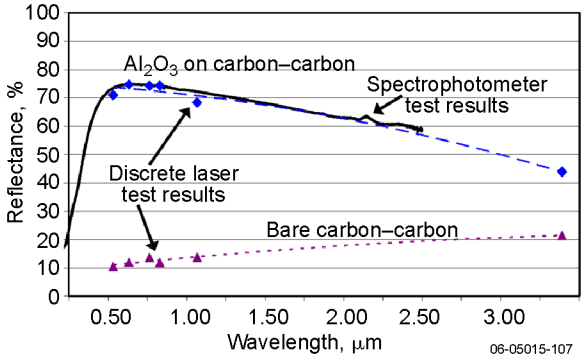

Figure 4-28. TIS reflectance test results.

Transmittance through the Al_2O_3 and PBN ceramic coatings was measured after removal of the C-C substrate (via oxidation at elevated temperatures). Transmission measurements (at normal incidence) through the resulting thin (typically <0.005-in.-thick) layers were performed with the Lambda 950 spectrophotometer. These measurements revealed that the transmittance through the coating increases with increasing wavelength (see Figure 4-29) until the coatings become IR energy emitters. The PBN curve in Figure 4-29 illustrates this transition (from a reflector/transmitter to an emitter) at >2 μm. These bands of IR transmittance allow some radiant heat energy to be radiated from the C-C substrate through the coatings and out to space.

Microstructural Effects on Optical Properties of Plasma-Sprayed Alumina. Plasma-sprayed ceramics such as alumina are not in thermodynamic equilibrium upon deposition because of the rapid solidification inherent in the process. Rapidly quenched alumina tends to nucleate into a metastable disordered cubic structure known as gamma-phase alumina (γ-Al_2O_3), which is stable until heated to temperatures above 900°C. Alumina deposited by plasma spray also can contain a high density of lattice and other defects at many microstructural levels. Exposure of this material to high temperatures will result in a phase transformation to the stable alpha phase (α-Al_2O_3), with its intrinsic crystal restructuring and grain growth.

Microstructural changes during heat treatment can have a considerable effect on critical properties of the primary shield's Al_2O_3 coating. Changes in reflectivity will affect the optical properties of the coating (α/ε) and, thus, affect the overall primary shield steady-state temperature. Also, mechanical attachment to the underlying C-C structure may be

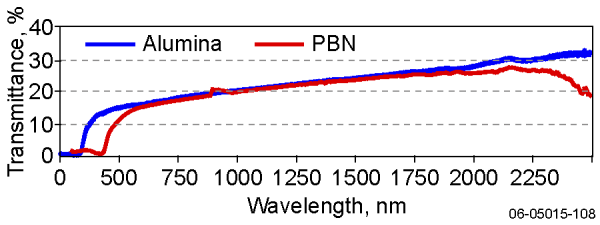

Figure 4-29. Transmittance through ceramic coatings.

affected by changes in density and porosity, surface reordering and terracing, and grain growth. It should be noted that the predicted primary shield temperature at closest solar approach (1850 K) is very close to a common sintering temperature for Al_2O_3. Treatments in this temperature range are used in industry to consolidate sprayed products and make them thermally stable.

The effects discussed above were studied by heat-treating plasma-sprayed alumina on C-C substrates for 2 hours at critical phase transformation temperatures of 900°C, 1050°C, 1180°C, 1380°C, and 1550°C. Changes in optical properties as a function of heat-treatment temperature then were measured by using the spectrophotometer. Phase transformations and physical changes to the microstructure were studied with X-ray diffraction (XRD) and scanning electron microscopy (SEM). High-resolution XRD scans of the as-sprayed and heat-treated alumina coatings are shown in Figure 4-30. As-sprayed material consists primarily of γ-Al_2O_3, with some α-Al_2O_3 particles present that were never melted during the spray process. Phase changes are occurring during the heat-treatment cycles (the most likely sequence is $\gamma \rightarrow \delta \rightarrow \theta \rightarrow \alpha$-$Al_2O_3$). Only thermally stable α-Al_2O_3 is present after heat treatment above 1180°C.

SEM images at 2000× magnification of heat-treated alumina (Figure 4-31) show minimal effect to the microstructure at 900°C and 1050°C but major surface reordering and terracing at 1180°C and 1380°C and significant grain growth at 1550°C. Higher-magnification SEM images (Figure 4-32) show that grain growth begins at 1180°C and grain size becomes increasingly large during 1380°C and 1550°C treatments.

The effect of microstructural changes (density, porosity, morphology, etc.) on Al_2O_3 coating optical properties is apparent from the reflectivity measurements of the heat-treated alumina samples

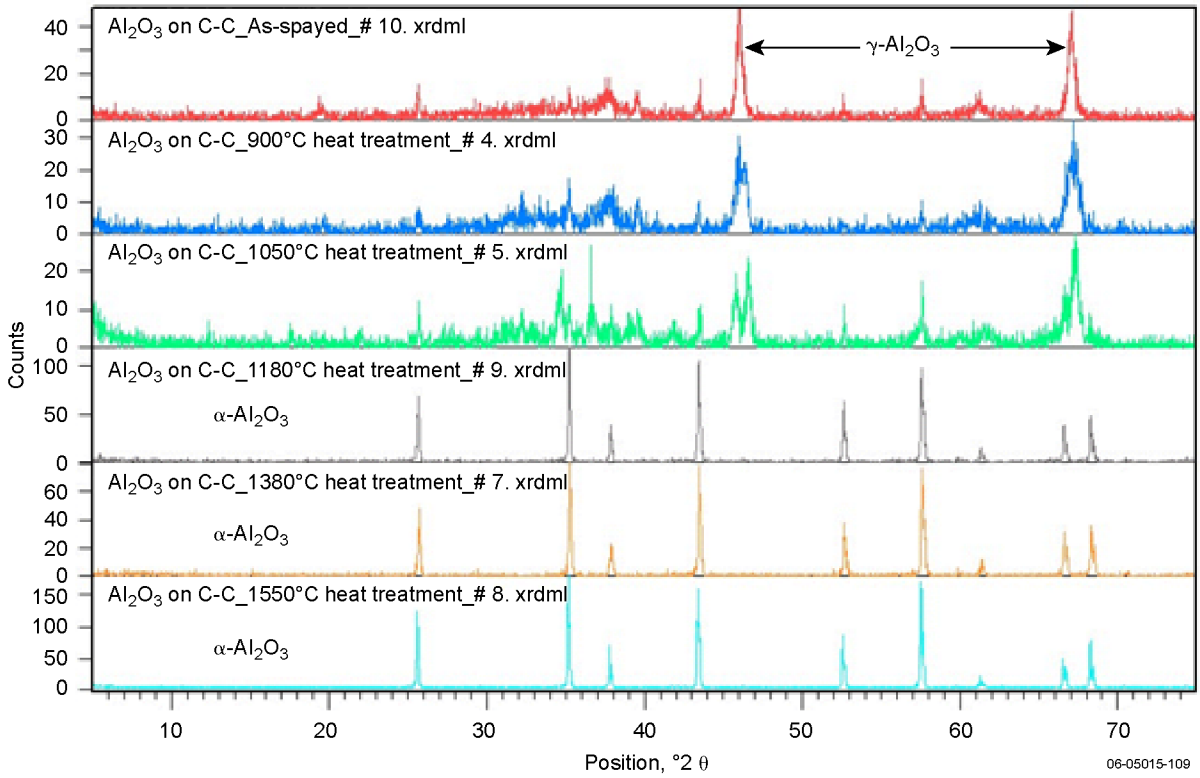

Figure 4-30. XRD scans of plasma-sprayed alumina on C-C after 2-hour heat treatment at increasing temperatures.

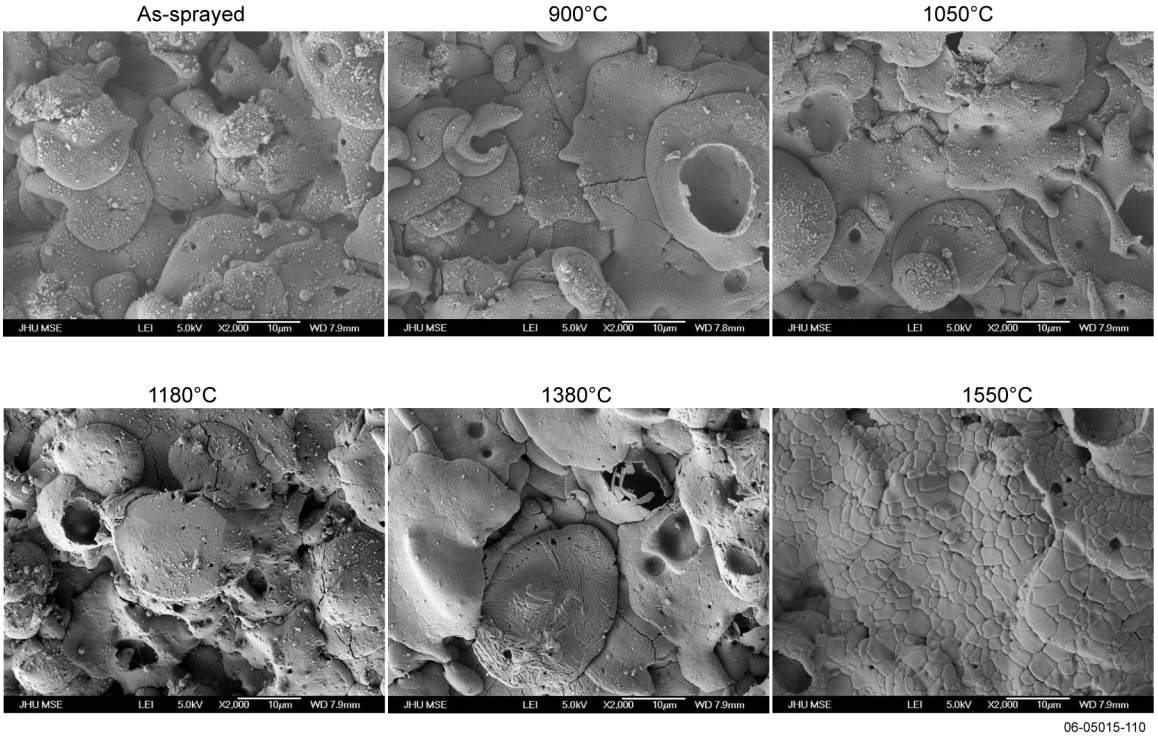

Figure 4-31. SEM images at 2000× magnification of plasma-sprayed alumina on C-C after 2-hour heat treatment at each temperature.

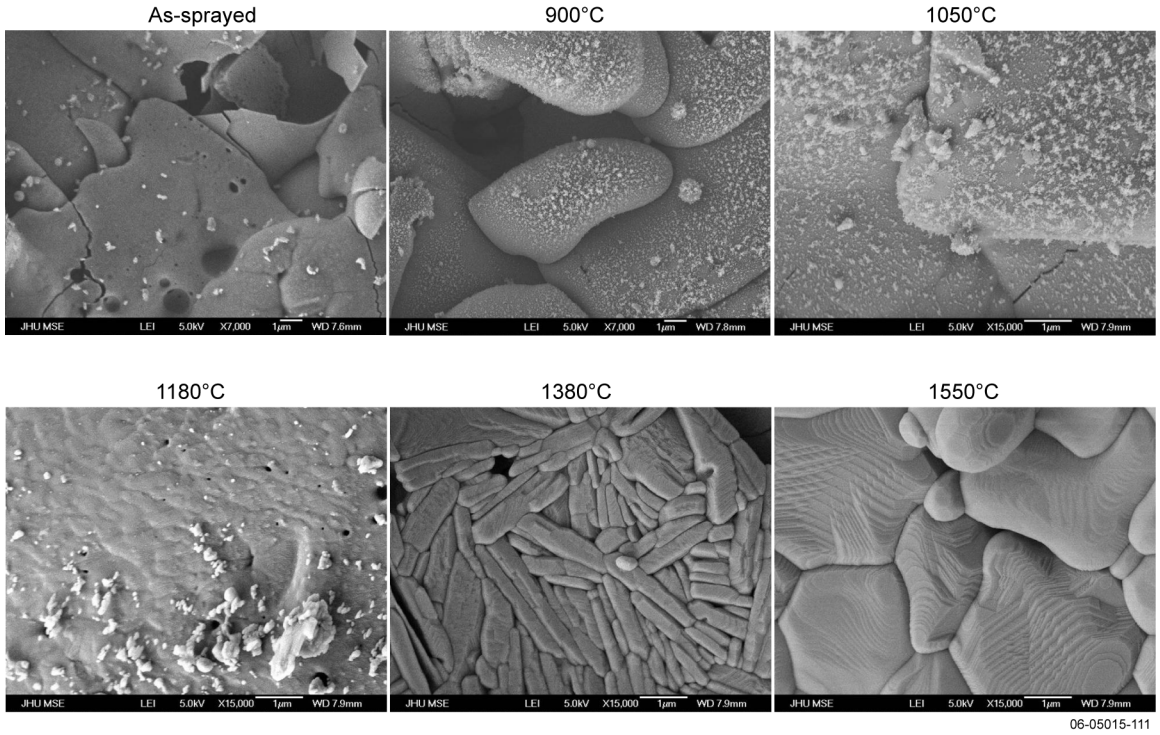

Figure 4-32. SEM images at 15,000× magnification of plasma-sprayed alumina on C-C after 2-hour heat treatment at each temperature.

shown in Figure 4-33. Reflectivity increases dramatically during heat treatments at temperatures up to 1180°C, with a resulting decrease in solar absorptance from 0.29 for as-sprayed material to 0.13 after 1180°C heat treatment. Heating above 1180°C causes a decrease in reflectivity as grain growth progresses, resulting in an increase in absorptance from 0.13 at 1180°C to 0.23 at 1550°C. Note that even with this increase, the absorptance of stabilized α-Al_2O_3 with large grains is lower than that of the as-sprayed coating.

Ceramic Coating Thickness Effects. Room-temperature spectrophotometer results illustrating the effect of coating thickness on optical properties are plotted in Figure 4-34. As would be expected, thicker coatings lead to slightly higher reflectance. Applying the total power law to these higher values of reflectance shows the corresponding lower values of solar absorption and IR emittance. Of primary interest is the change in α/ε as the coating thickness increases. For non-sintered Al_2O_3-coated C-C, the room-temperature α/ε remained ~0.5 for both thicknesses, thus indicating that making the coating thicker (which entails more mass) is not necessary. The thinner coating of PBN had an α/ε of ~0.4, while the thicker coating's α/ε was ~0.2. These results (combined with data from high-temperature testing) indicate that although a thin PBN coating can provide adequate optical performance, further trade studies should be performed to optimize the PBN coating thickness.

Grazing Angle Effects. The effect of grazing angle (measured from the surface normal) on reflectance is illustrated by Figure 4-35. Al_2O_3, PBN, and BaZP coatings on C-C were measured at an increasing series of grazing angles. As expected from the Fresnel relations, the amount of sunlight reflected increases as the grazing angle increases. The primary shield half-cone angle of 15° is equal to a grazing angle of 75° and results in an increase in reflectance of >5%.

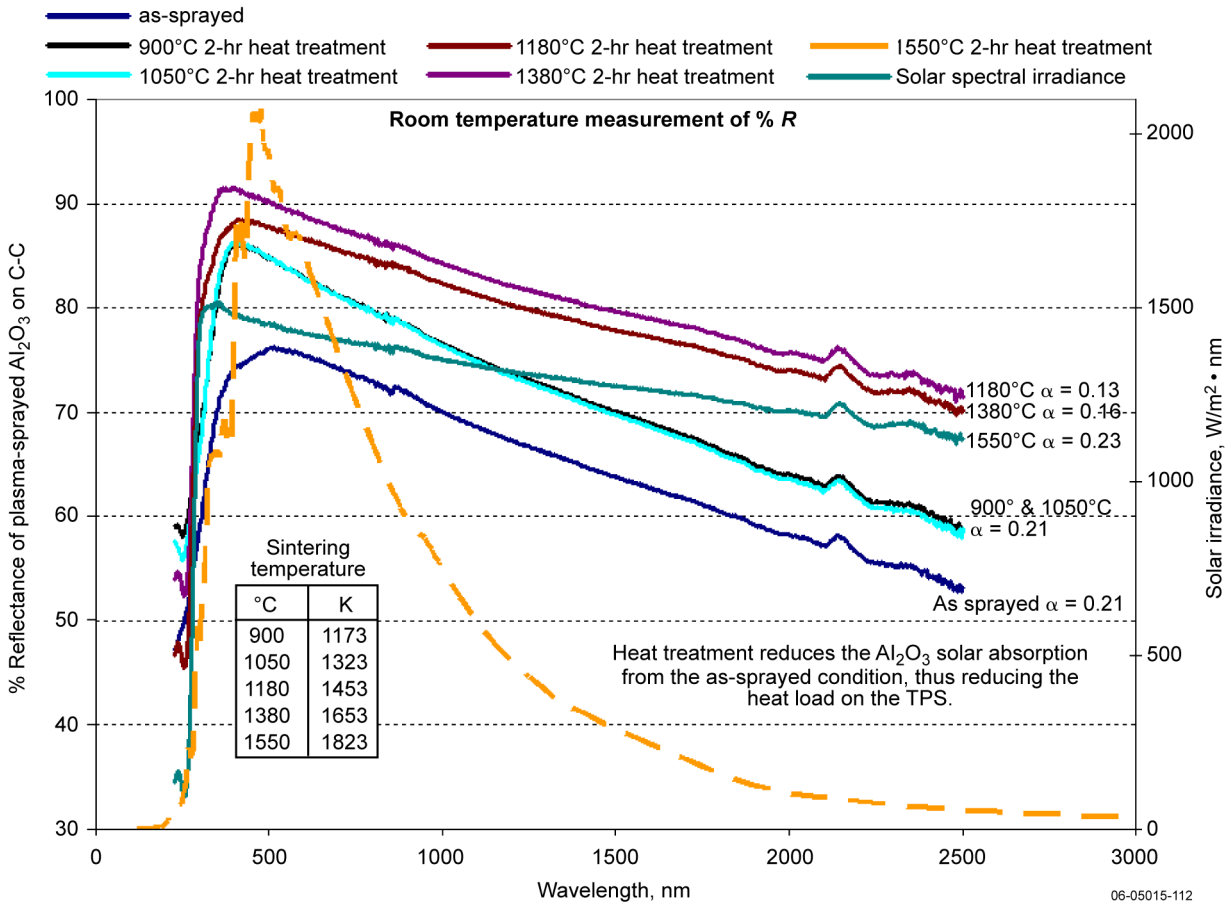

Figure 4-33. Alumina optical properties after sintering.

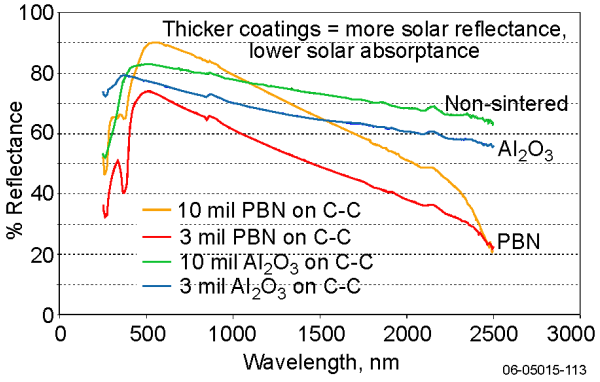

Figure 4-34. Coating thickness effect on optical properties.

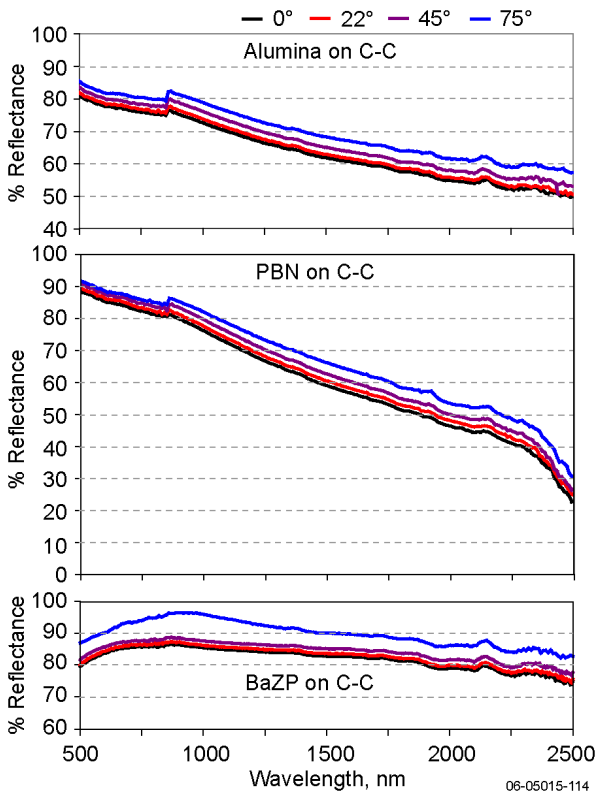

Figure 4-35. Grazing angle effect on reflectance of ceramic coatings applied to C-C.

4.5.3 Summary of Results

The TIS tests provided a baseline against which to measure changes in spectral reflectance as a function of temperature. Application of Kirchhoff's law enabled calculation of α/ε in the solar spectral irradiance bands of interest (the solar absorptance was calculated by using reflectance data collected from the 0.532- to 1.067-μm lasers, whereas the IR emittance was calculated by using reflectance data from the 3.39-μm laser). The temperature-dependent α/ε results from coupons (of different materials and/or suppliers) tested from room temperature to 1773 K are shown in Figure 4-36. In addition, Figure 4-36 shows the resulting primary shield temperature at a distance of 4 solar radii from the Sun as a function of α/ε. To find the predicted primary shield temperature for any of the coatings tested, look for the intersection of the α/ε test data with the primary shield temperature curve. The test data shown in Figure 4-36 indicate that application of a ceramic optical coating to a C-C substrate will result in $\alpha/\varepsilon < 0.6$ (the current system design goal) with a reduction in the primary shield temperature to <1850 K.

4.5.4 Optical Modeling and Comparison to Literature

Alumina. Operation of the baseline system (composed of an alumina optical surface on top of the C-C heat shield) is shown in Figure 4-37. The bulk of the incoming solar radiation is reflected by the Al_2O_3 coating layer on the primary shield. The non-reflected thermal radiation then is either absorbed by the Al_2O_3 or transmitted through

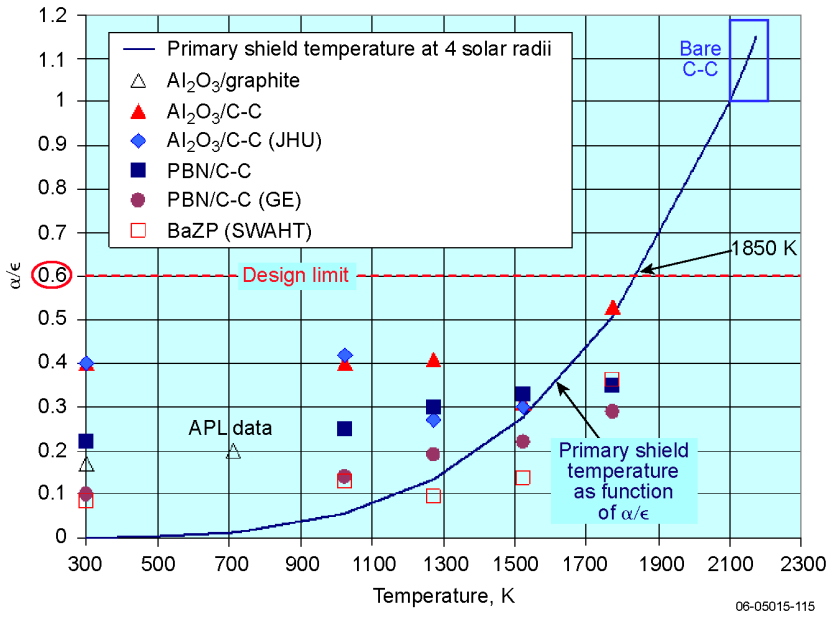

Figure 4-36. Optical coating performance at primary shield temperatures.

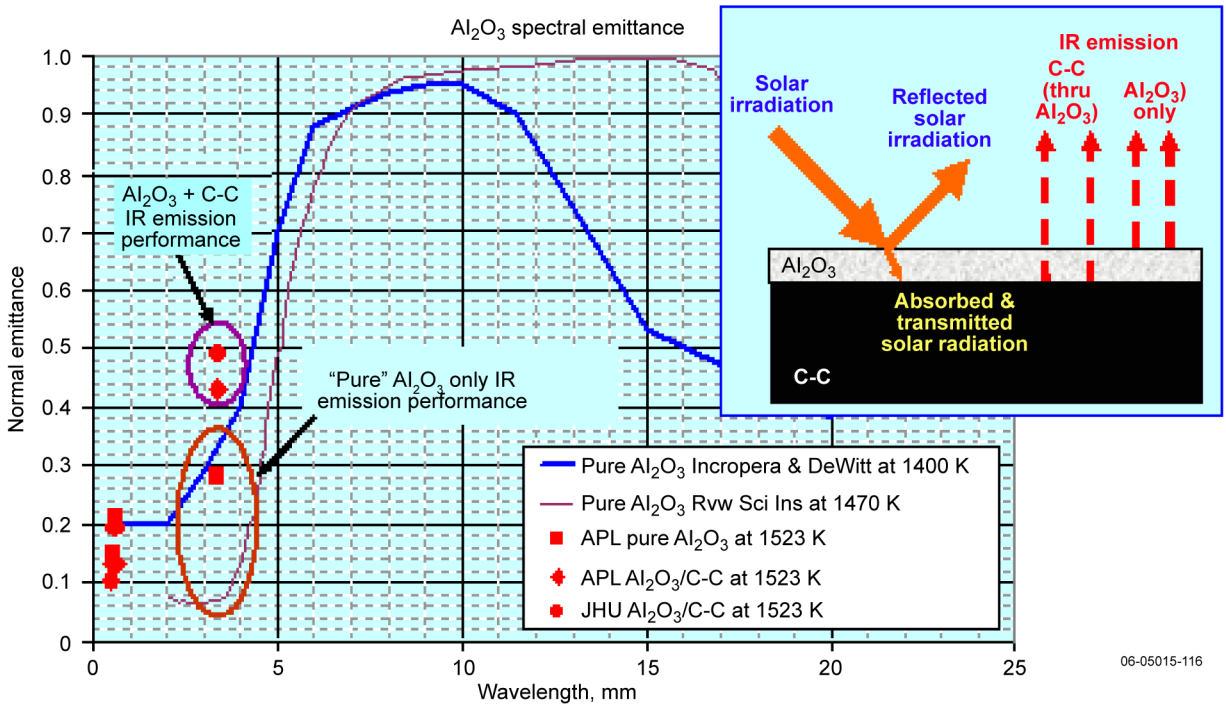

Figure 4-37. Optical model for alumina (Pure Al_2O_3 data from Incropera, Frank, and David DeWitt, *Fundamentals of Heat and Mass Transfer*, 4th ed., John Wiley & Sons, New York, 1996, p. 657).

the coating (through the previously discussed small window of transparency between the upper limit of the visible band and the near-IR band) and absorbed in the C-C substrate. The solar energy absorbed by the coating and substrate then is reradiated back to space via either direct emission from the Al_2O_3 coating or indirect emission through the thin Al_2O_3 coating from the C-C substrate (because the alumina coating's spectral-dependent transparency allows energy to be radiated directly from the C-C substrate). As the wavelength of the emitted energy increases, the transparency of the alumina decreases, and the coating becomes a very effective IR radiation emitter (as shown in Figure 4-37 by the rise in normal emittance from $\varepsilon = 0.2$ at $\lambda < 1$ μm to $\varepsilon > 0.8$ at $\lambda > 6$ μm).

PBN. The PBN-coated primary shield will operate similarly to the Al_2O_3-coated primary shield in that the majority of the incident solar radiation is reflected away by the PBN outer coating. The non-reflected solar energy then is absorbed by either the coating or the C-C substrate and reradiated to space. As with the Al_2O_3-coated primary shield, the thermal radiation occurs either by emission from the PBN coating or by emission from the C-C substrate through the coating's window of transparency. As shown in Figure 4-38, the window of transparency for PBN is not as wide as that of Al_2O_3. Comparing Figure 4-38 with Figure 4-37 shows that the IR emittance of PBN begins to rapidly ramp up at ~2 μm, whereas the IR emittance of alumina does not begin to dominate until ~4 μm.

4.5.5 Trajectory-Based Primary Shield Equilibrium Temperature Predictions

Figure 4-39 illustrates the primary shield temperature reduction due to use of optical coatings as a function of distance from the Sun's

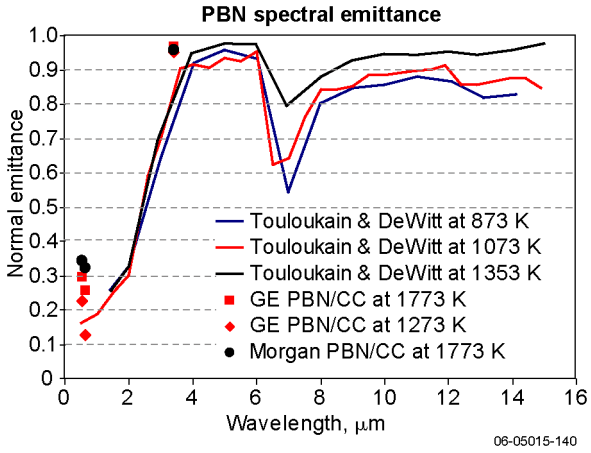

Figure 4-38. PBN performance (Touloukian, Y. S., and D. P. DeWitt, *Thermophysical Properties of Mattter, Vol. 8: Thermal Radiative Properties: Nonmetallic Solids*, IFI/Plenum, New York, 1972, pp. 1043–1046).

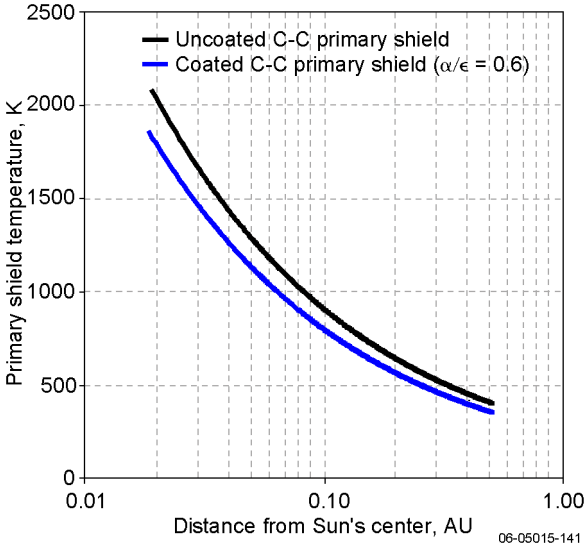

Figure 4-39. Predicted primary shield equilibrium temperature along trajectory.

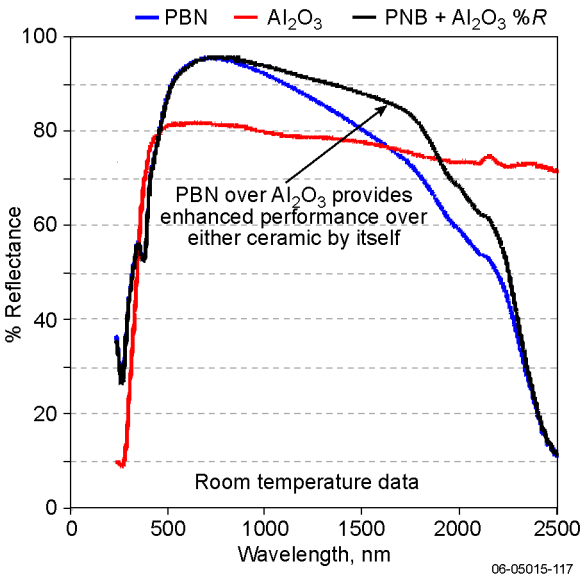

Figure 4-40. Effect of layering PBN over alumina.

center. The equilibrium temperature of the baseline primary shield (using an optical coating with $\alpha/\varepsilon = 0.6$) is compared with that of a non-coated primary shield (i.e., a C-C gray-body emitter controlled to a nominal $\alpha/\varepsilon = 1$). The optical coating will cause a significant reduction (i.e., >200 K) of the primary shield temperature during near-solar scientific measurements. Note that this predicted temperature reduction is conservative in that it does not take into account additional reflectance of solar energy due to grazing angle effects.

4.5.6 Coating Optimization

Composite Coatings. Composite coatings incorporating two or more materials offer the ability to optimize the spectral response of the primary shield surface. Figure 4-40 shows the results from a preliminary study of placing a layer of PBN on top of alumina. Non-linear, synergistic behavior is revealed in which the PBN–Al_2O_3 composite performs better than either PBN or Al_2O_3 by itself. Additional studies in this area hold promise of yielding higher-performing composites. Evaluating the applicability of such materials to the primary shield would require further trade studies in the areas of fabrication, mass, charging, and outgassing.

Interlayers. The effects of interlayers between C-C and alumina, as shown in Figure 4-16, were studied to evaluate the impact on optical performance. Samples containing refractory material interlayers were fabricated and then tested (via room-temperature spectrometer measurements) to compare reflectance of the C-C/interlayer/alumina samples to C-C/alumina-only samples. The reflectance curves of the C-C/interlayer/alumina samples had similar slopes to those of C-C/alumina-only samples (Figure 4-41), indicating that all the samples had similar α/ε values. (The observed differences in reflectance are likely attributable to slightly different alumina coating thicknesses for each sample rather than to an effect generated by addition of the interlayer). The difference in reflectance between the test specimens does not adversely affect α/ε.

4.6 Radiation Resistance of Coating Materials

Space materials such as organic-based coatings (for thermal control) experience solar UV degradation in near-Earth orbit. This degradation commonly

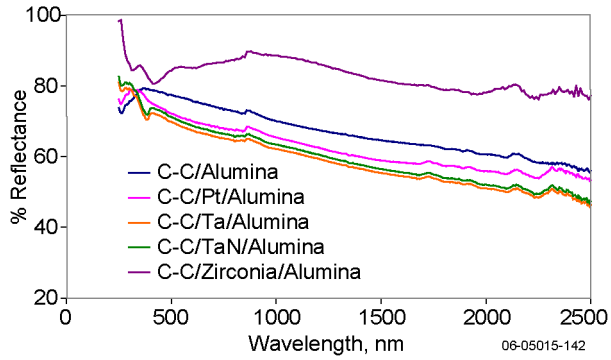

Figure 4-41. Reflectance of C-C/alumina coupons with high-temperature interlayers.

is referred to as "color center" formation because these materials often darken with UV exposure. In the case of polymer materials, color centers are caused by energetic UV radiation breaking organic bonds, resulting in a loss of oxygen atoms. Materials may be permanently degraded by UV, but coloration also can be reversed when oxygen is reintroduced upon reentry into the terrestrial atmosphere.

Color centers also can be formed in ceramics in the presence of ionizing radiation. The mechanism for color center formation in ceramics is different than for UV degradation of polymers in near-Earth orbit. Anions or cations are removed from the crystal lattice, and electrons or holes are trapped at the resulting vacancies. Enough trapped electrons or holes can change the fundamental UV/Vis absorption characteristics of the crystal lattice, resulting in yellow or brown coloration. Many types of color centers can be formed (e.g., F centers, F+ centers, and V centers), each with unique absorption and emission spectra. The rate and extent of color center formation are highly temperature-dependent; released anions or cations "floating" in the band gap recombine with vacancies more readily at increased temperatures. Therefore, coloration of ceramic coatings is expected to be minimal in the near-solar environment because irradiation will occur at elevated temperatures.

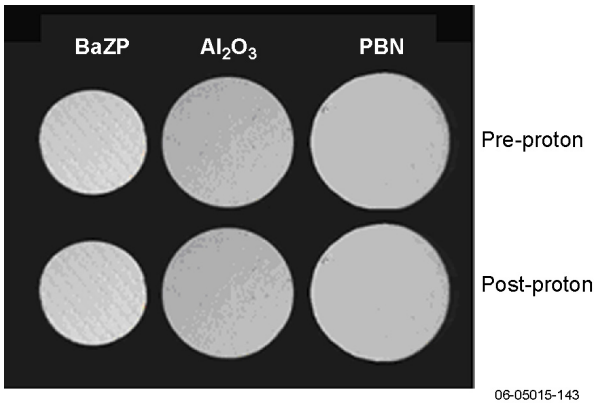

Figure 4-42. Ceramic-coated C-C samples before and after proton exposure.

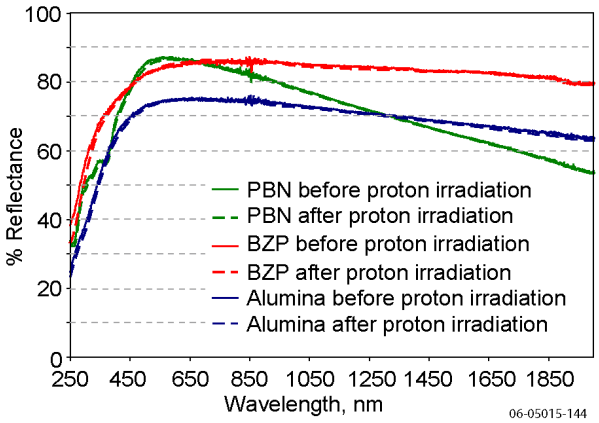

Figure 4-43. Optical properties of ceramic coatings before and after proton irradiation.

4.6.1 NASA GRC Radiation Testing

Proton and electron radiation exposures were performed at the NASA Goddard Space Flight Center (GSFC) Radiation Test Facility to evaluate performance of ceramic-coated C-C coupons against "worst-case" radiation conditions of deep space, Jupiter, and solar environments. Of primary interest from the radiation testing are changes in optical properties of the coating or microstructural damage that would affect structural integrity or lead to significant mass loss. These initial screening tests were structured to distinguish between radiation damage to the fundamental ceramic materials and other potentially complex effects such as material impurities or test chamber contamination.

In this set of testing, the alumina, PBN, and BaZP were exposed to large electron and proton fluences (2.8 × 1014 p/cm^2) to simulate worst-case near-solar and Jovian environments. Radiation energy of 150 keV was chosen as having potential for damage to ceramic coatings. Proton irradiation (the predominant near-solar component) did not color the ceramic coatings (Figure 4-42) or affect optical properties (Figure 4-43). Electron irradiation (the predominant Jovian component) resulted in coloration of all three ceramics, most noticeably in alumina (Figure 4-44). Optical properties of PBN and BaZP were affected only marginally, whereas alumina showed a significant increase in UV/Vis absorption (decreased reflectivity) from 250–560 nm due to the formed color centers.

Some color centers are relatively unstable and will readily recombine at ambient conditions as soon as irradiation is stopped. Other point defects are more stable and require thermal bleaching to move the displaced atoms back into their lattice positions, returning ceramics to their original white color. Heat treatment at 200°C for 1 hour removed the electron coloration of all samples, bleaching the coatings back to their original white color and restoring the original optical properties. Figures 4-45 through 4-47 show the measured reflectivity of ceramics coatings pre-exposure, post-exposure, and after heat treatment. Our hypothesis is that as

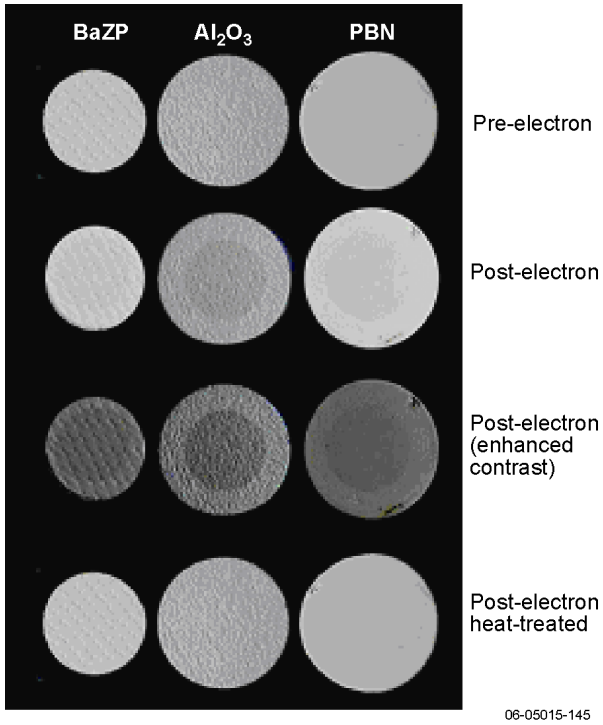

Figure 4-44. Ceramic-coated C-C samples before and after electron exposure.

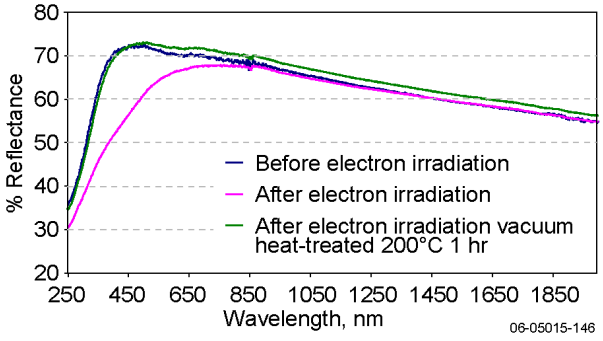

Figure 4-45. Optical properties of alumina coating before and after electron irradiation.

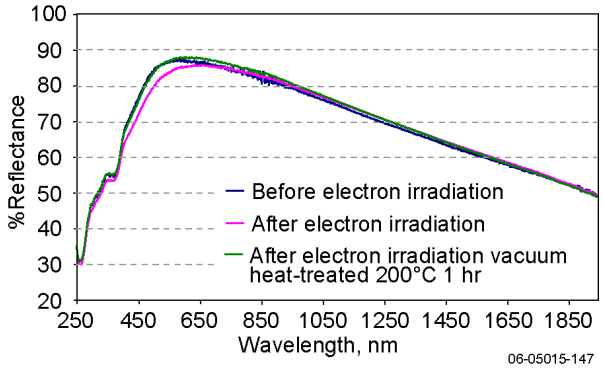

Figure 4-46. Optical properties of PBN coating before and after electron irradiation.

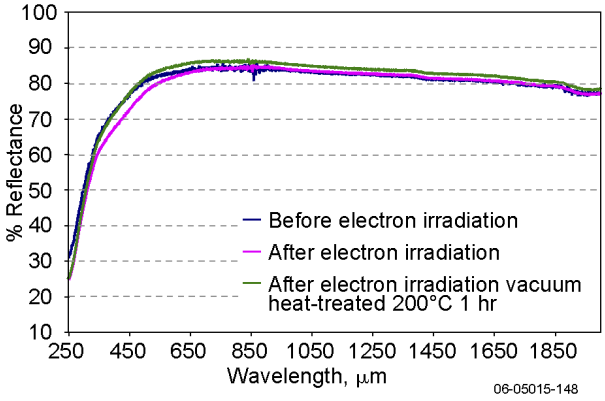

Figure 4-47. Optical properties of BaZP coating before and after electron irradiation.

the heat-shield equilibrium temperature increases upon solar approach, α/ε (in particular, the reflective component) will not be measurably affected by radiation sources.

There was no visual evidence of microstructural damage or coating spallation due to the radiation exposures. Samples were weighed pre- and post-test with no measurable mass loss. XRD scans were taken pre- and post-test to inspect for damage to the ceramic bulk crystal structure. XRD peak shifts or peak broadening would be evidence of permanent damage caused by the radiation. No such effects were apparent for any of the ceramic coating materials.

4.6.2 PUPR Plasma Testing

Experiments to understand the effects of plasma radiation on the optical properties of the ceramics were performed at the Polytechnic University of Puerto Rico (PUPR). Table 4-1 shows the plasma densities and energies used to simulate those found in the solar and Jovian environments. The plasma used was generated from hydrogen and is shown in Figure 4-48.

The material coupons, when removed from the plasma environment, exhibited no yellowing or discoloration, as shown in Figure 4-49. As shown in Figures 4-50 to 4-52, the optical properties of the PBN, BaZP, and C-C composite (% reflectance as a function of wavelength) were completely unaffected by PUPR plasma irradiation. In addition, the materials exposed were precisely weighed before and after irradiation, and zero mass loss was detected in any materials under any of the conditions tested. The alumina coupons were the only materials that exhibited minimal optical property degradation after plasma exposure and only under certain

Table 4-1. Plasma densities and energies used to simulate those found in the solar and Jovian environments.

	Environment	Density, el/cm^3	Energy, eV	Duration
Sample set 1 (cumulative exposure)	1st solar pass	2.00×10^5	68	12 hours
	Jupiter	4.30×10^4	40.3	7 minutes
	2nd solar pass	4.30×10^5	31	12 hours
Sample set 2 (solar-only exposure)	1st solar pass	2.00×10^5	68	12 hours
Sample set 3 (Jupiter-only exposure	Jupiter	1.60×10^6	29.6	7 minutes
C-C coupon #2 (Jupiter-only exposure)	Jupiter	2.33×10^5	4.8	7 minutes
C-C coupon #3 (solar-only exposure)	Solar	3.24×10^7	14.5	7 minutes

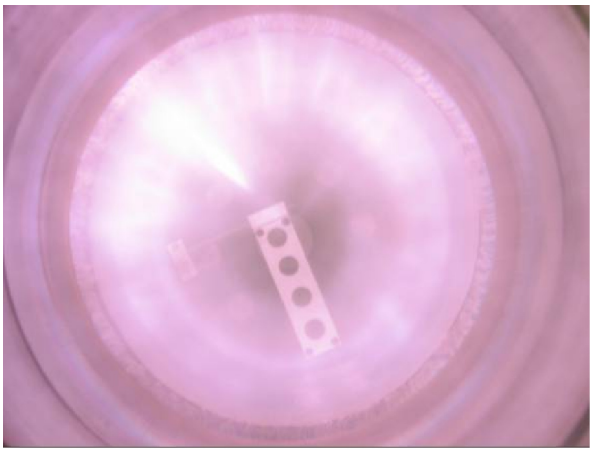

Figure 4-48. Plasma environment in Polytechnic University of Puerto Rico (PUPR) facility.

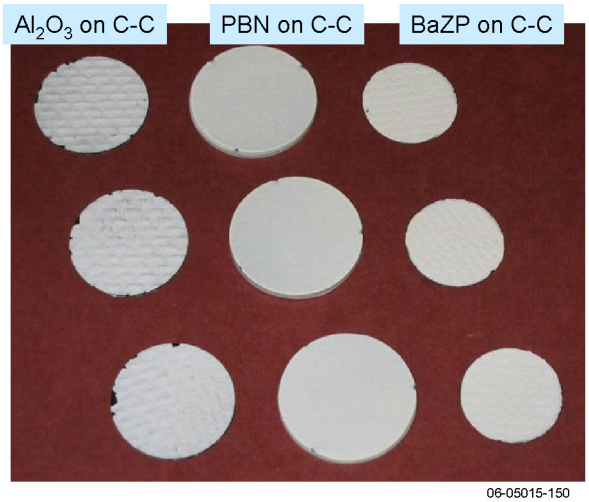

Figure 4-49. Post-test visual inspection of PUPR coupons.

conditions. This minimal degradation reversed after exposure to a moderate temperature (~473 K). The primary shield will reach this equilibrium temperature at a distance of ~0.3 AU from the Sun, so any optical property degradation due to the radiation environments will be negated well before the solar heat flux approaches the TPS design requirement (400 W/cm^2 at 4 R_S).

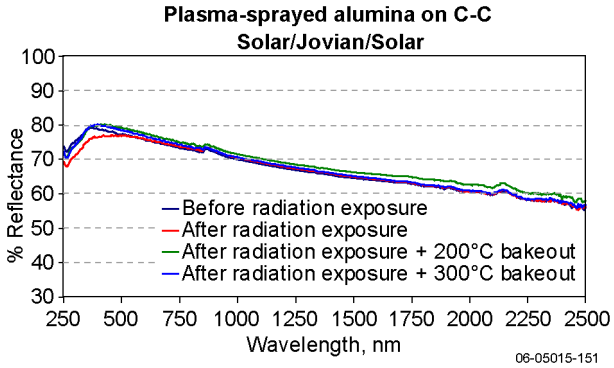

Figure 4-50. Alumina optical results after simulated solar/Jovian/solar exposure at PUPR.

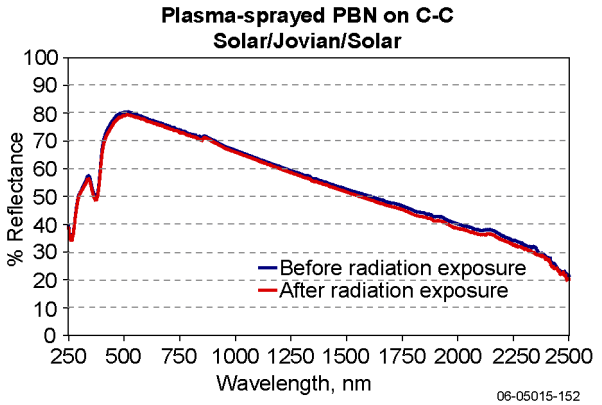

Figure 4-51. PBN optical results after simulated solar/Jovian/solar exposure at PUPR.

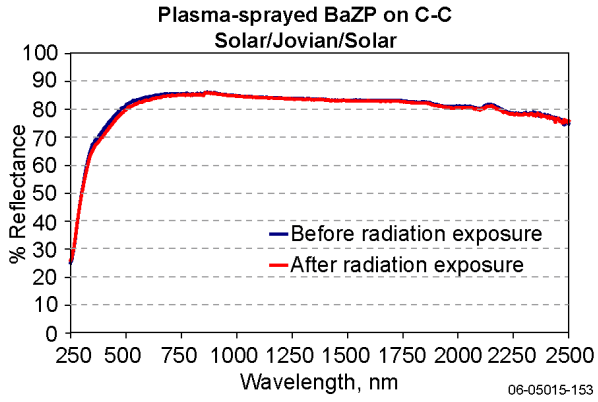

Figure 4-52. BaZP optical results after simulated solar/Jovian/solar exposure at PUPR.

4.6.3 IUCF Radiation Testing

At the Indiana University Cyclotron Facility (IUCF), beam radiation testing was conducted to evaluate the response of the candidate primary shield materials to high-energy protons (>50 MeV) as summarized in Table 4-2. These tests were conducted in an ambient environment at room temperature. No visual surface damage was noted for C-C, pyrolytic graphite, Al_2O_3, PBN, or BaZP as shown in Figure 4-53. Optical properties were measured at room temperature and indicated no measurable change. These results were reported in the 2005 STDT Report.

4.7 Coating Structural Integrity

The structural integrity of the primary shield coating is critical to its function as an optical-based thermal management system. Structural integrity includes the coating as well as the coating-to-substrate interface. During operation, the coating will be subjected sequentially to vibro-acoustical loads during launch, extreme thermal excursions and thermal cycling during flight, and environmental effects such as radiation and high-speed particle impact. Because of these extreme conditions, applied coatings must remain robust and adherent under cumulative stresses.

Table 4-3 shows a high-level test matrix for studying both coating integrity and coating adhesion; checks indicate areas that have been considered thus

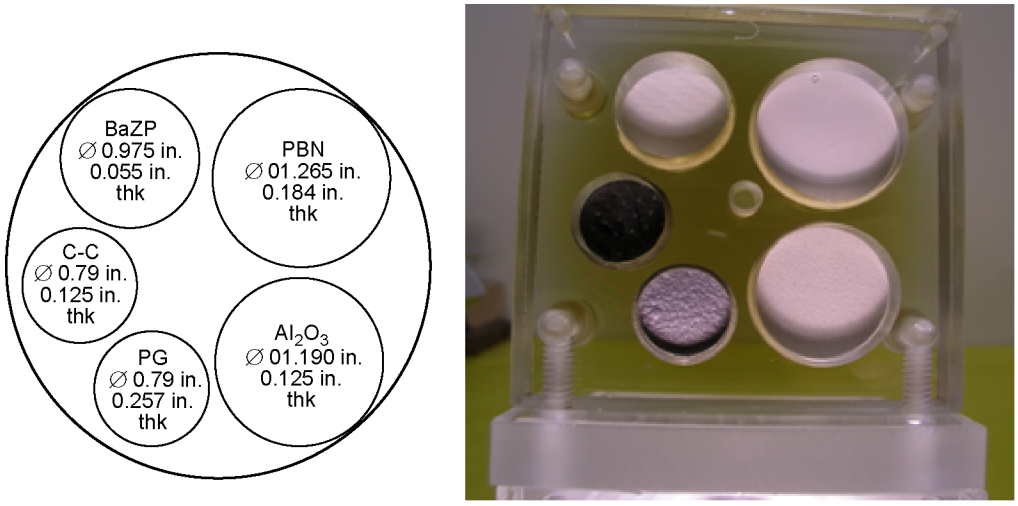

Figure 4-53. Coupons after irradiation testing at Indiana University Cyclotron Facility (IUCF).

Table 4-2. IUCF irradiation test environments.

Run	Proton Energy, MeV	Trays	Vacuum, mtorr	Fluence, no./cm^2	Simulation
1	54.7	1,4	60	8.50×10^{10}	12 events
2	73.7	2,4	80	3.80×10^{10}	
3	104.2	3,4	80	2.00×10^{10}	
4	104.2	5	80	1.84×10^{13}	Single event near Sun ($1/r^2$)
	73.7	5	60	7.98×10^{12}	
	54.7	5	60	4.20×10^{12}	

Table 4-3. Test matrix for study of coating structural integrity.

Coating on C-C	Vibro-Acoustical Testing	Thermal Cycling (77–1850 K)	Radiation Exposure	Residual Strength Characterization
Alumina	√	√	√	√
PBN		√	√	
BaZP		√	√	

far. The actual exposure tests for each category provide a qualitative assessment as to the integrity of the coating based on a pass–fail criterion. Coupons used in these tests then can be dissected and manufactured into interlaminar tensile coupons (ILT) to establish a first-order quantitative assessment of interface strength and potential cumulative damage.

4.7.1 Vibro-Acoustic Tests

Vibration tests were conducted during the 2005 STDT study at ambient temperature to produce strains representative of launch. As shown in Figure 4-54, test specimens (Al_2O_3-coated C-C, 1 in. wide × 9 in. long × 0.05 in. thick) were affixed with simply supported ends to a vibration table. Laser velocimetry and strain gages were used to measure displacements and strain. In addition to multiple sweeps at varying frequencies and acceleration levels, the coupon was excited by 6 *g* acceleration at the measured natural frequency of 164.3 Hz to achieve a worst-case strain level of 330 μin./in. at the center of the specimen (equivalent to a ±0.080-in. displacement). This level was maintained for 15 min with no coating or coating-to-substrate interface damage observed.

4.7.2 Thermal Exposure Tests

Thermal exposure experiments to simulate temperature extremes and thermal cycling were performed by using ceramic-coated C-C coupons measuring 1 in. in diameter with substrate thicknesses of 0.1125 in. and coating thicknesses nominally 0.005 in. Spacecraft temperatures are predicted to range from 77 K in deep space to 1850 K at 4 R_S.

Alumina Results

- Exposed to temperatures between 1600 and 1650 K in high vacuum (10^{-8} torr); no detectable cracking or debonding
- Exposed to temperature of 1850 K in inert environment; no detectable coating cracking or debonding
- Prior thermal cycling (during 2005 STDT study) in inert environments from 77 to 1600 K; no detectable coating cracking or debonding
- Thermal cycling from 100 K (16-hour hold) to 1273 K (4-hour hold); no detectable coating cracking or debonding
- Thermal-cycled coupons mechanically tested (in ILT configuration); no reduction in strength (see Section 4.7.4)

PBN Results

- Exposed to temperatures between 2100 and 2200 K in inert and high vacuum

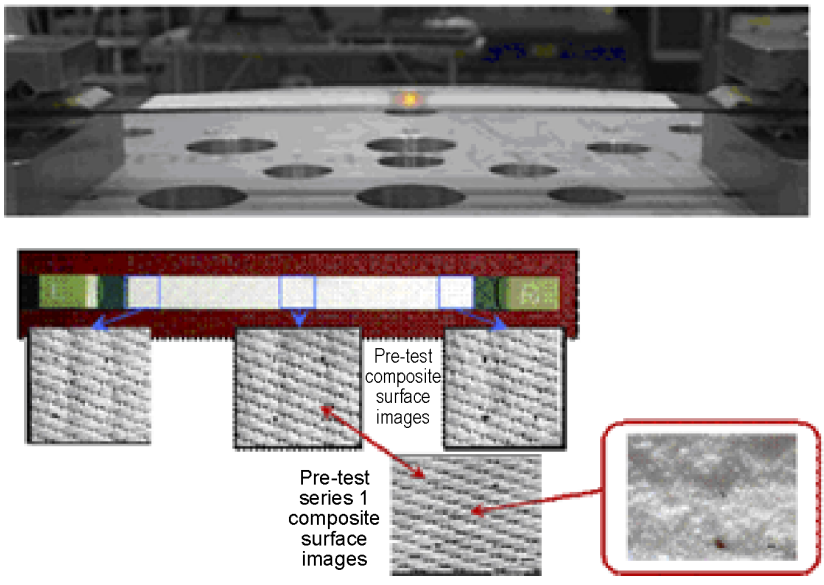

Figure 4-54. Vibration testing of alumina-coated C-C coupon to simulate the launch environment.

(10^{-8} torr); no detectable coating cracking or debonding

- Thermal cycling from 100 K (16-hour hold) to 2100 K (4-hour hold); no detectable coating cracking or debonding

BaZP Results

- Thermal cycling from 100 K (16-hour hold) to 1273 K (4-hour hold); no detectable coating cracking or debonding

Additional testing is planned in FY 2007 to further characterize the coating and coating–interface structural integrity of alumina-coated C-C, PBN-coated C-C, and BaZP-coated C-C. These tests will include vibro-acoustical testing of coated C-C panels (9 × 9 in.), structural testing of coated C-C primary shield joint coupons, thermal cycling from 77 to 1850 K in high vacuum (10^{-8} torr), radiation exposure, and cumulative effects of loads and environments. ILT and shear coupons will be removed from the larger test specimens to provide a quantitative measure of coating adhesion characteristics (tension, shear, and mixed mode).

4.7.3 Radiation Exposure Tests

Ceramic-coated C-C coupons were exposed to various levels and types of radiation to simulate the space environment as described in Section 4.6. These tests consisted of high-level protons, high- and low-level protons and electrons, and hydrogen-based plasmas. Testing was performed at ambient temperatures in combinations of inert and vacuum environments. None of the coupons experienced any detectable structural damage (including either cracking or debonding), as noted in Figures 4-45, 4-46, and 4-47 for the alumina, PBN and BaZP, respectively.

4.7.4 Residual Strength Characterization

ILT coupons were manufactured from Al_2O_3-coated C-C (1 in. wide × 9 in. long × 0.05 in. thick), as shown in Figure 4-55. These coupons were tested as "virgin" (or unexposed) after vibration cycling, as described in Section 4.7.1, and after vibration and thermal cycling (100 to 1273 K), as described in Sections 4.7.1 and 4.7.2. Test results, as summarized in Table 4-4, indicate no reduction in coating adhesion strength due to vibration or thermal cycling. Figure 4-56 contains post-test images of the ILT coupons indicating a tensile adhesive failure (with minimal peel effects) of the C-C to alumina interface in all cases. Variations in strength are most likely due to test coupon preparation and the mechanical test setup. ILT tests historically produce high standard deviations in strength values but provide a first-order quantitative assessment of strength characteristics.

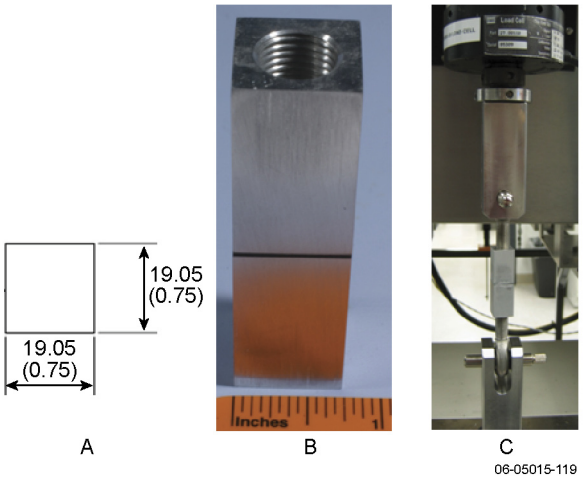

Figure 4-55. ILT testing of alumina-coated C-C coupon.

4.8 Established Vendors

Following the trends of material heritage, larger corporations have invested in the development of Al_2O_3 and PBN databases and processing technologies. For the 2005 STDT study and continued here, APL has studied the response of the candidate ceramics in pure bulk form (manufactured by using hot-press sintering methods) as compared with the ceramics applied to C-C substrates with their respective coating techniques.

The premier alumina research and manufacturing center is at Coorstek, and their materials are the standard. However, Coorstek does not do plasma

Table 4-4. ILT test results for alumina-coated C-C coupon after vibration cycling (vib) and after vibration and thermal cycling (v&t).

Specimen ID	Failure Location	Peak Stress, psi
Unexposed 1	C-C/Al_2O_3 interface	7
Unexposed 2	C-C/Al_2O_3 interface	109
Unexposed 3	C-C/Al_2O_3 interface	116
Sample 1 v&t	C-C/Al_2O_3 interface	127
Sample 2 v&t	C-C/Al_2O_3 interface	141
Sample 5 vib	C-C/Al_2O_3 interface	234
Sample 6 vib	C-C/Al_2O_3 interface	156

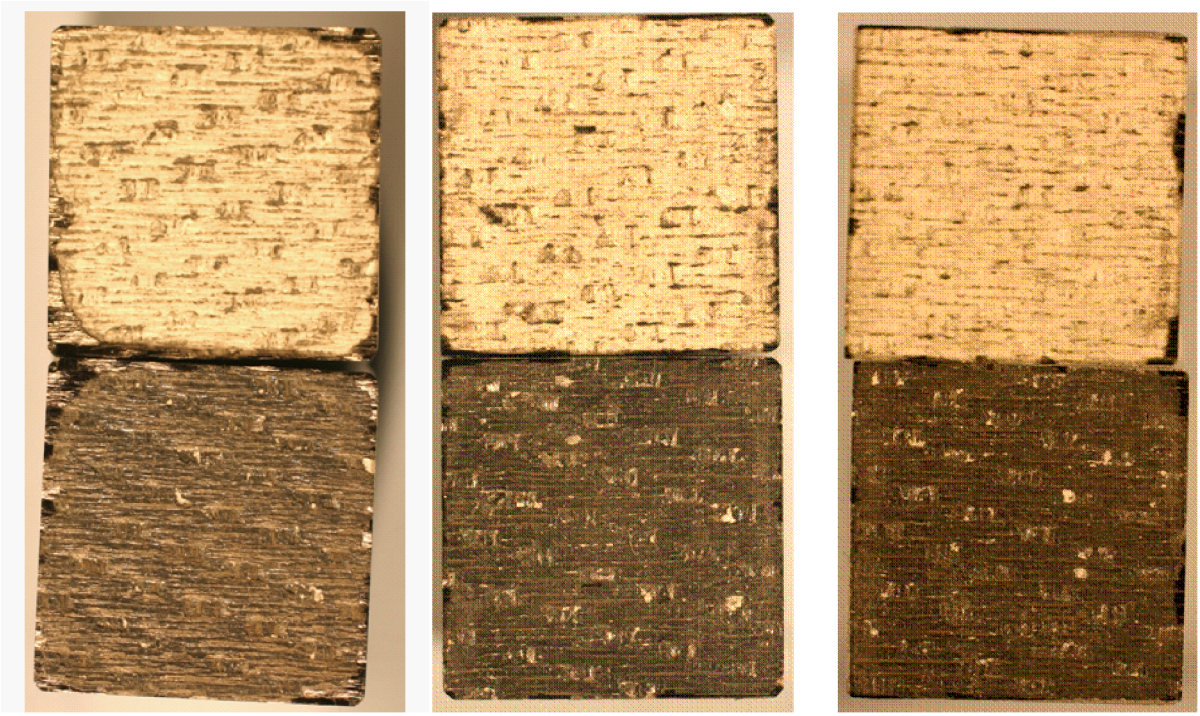

Figure 4-56. Post-test images of alumina-coated C-C ILT coupons.

spraying. Therefore, the coating services of companies that specialize in plasma-spray technology, but not necessarily in alumina technology, are required. In this study, we investigated plasma-sprayed alumina coupons coated by Plasma Processes, Inc., located in Huntsville, AL (our baseline vendor; see Figure 4-57), as well as coupons coated by the Johns Hopkins University (JHU) Advanced Technology Laboratory in Baltimore, MD.

The premier PBN research and manufacturing center is GE Ceramics, making their materials the standard and our baseline vendor. Other candidate vendors explored during this study include Morgan Advanced Ceramics and Ultramet. Although all materials achieved similar results, GE's quality control and manufacturing capabilities (including high-rate production and one-off articles) make them the clear leader for high-quality coatings.

One of the leading research centers for BaZP (and NZP) is a small business named SMAHT Ceramics, Inc., located in Salt Lake City, UT. This small business specializes in technology development but lacks the infrastructure for high-rate production or large, one-of-a-kind structures. BaZP powder from SMAHT was supplied to Plasma Processes for plasma-spray application onto C-C coupons for this study.

Figure 4-57. Large-scale plasma spraying at Plasma Processing, Inc.

4.9 Nondestructive Evaluation

Nondestructive evaluation (NDE) is the branch of materials science and materials evaluation concerned with the identification of flaws, anomalies, and property variations in materials by using nondestructive and sometimes noninvasive means. The purpose of these experiments is to provide an assessment of how the different NDE methods perform in detection of the different types of flaws that are possible on Solar Probe. The work outlined herein is by no means intended to provide an exhaustive study

of any of these flaw types or techniques but, rather, is intended to identify the strongest NDE candidate techniques and their basic capabilities.

For a composite system, as in the Solar Probe TPS, several critical flaw types and failure modes may exist. These include, but are not limited to, cracks, delaminations, density/porosity variations, and out-of-specification thicknesses. The NASA standard NASA-STD-5013, *Nondestructive Evaluation Requirements for Fracture Critical Composite Components* (currently under draft by the NASA NDE Technical Warrant Team), will address NDE requirements for the various modes of failure for composite systems and, thus, also will be upheld as a compliance standard for this research.

An exhaustive NDE assessment of the quality of the ceramic coating and its adhesion to the C-C substrate is necessary to preclude spallation, crack growth, and degradation of the coating during the mission. NDE will be used as a final inspection process to qualify the Solar Probe TPS for flight. The inspection methodology therefore must be capable of flaw detection at the size scale of the final product.

NDE of the ceramic coating involves numerous steps, starting with raw material procurement, baseline materials characterization, sample preparation, flaw creation, method validation, and verification for employment on the final product. For this study, an emphasis has been placed on understanding the strengths and weaknesses of NDE methods for inspection of coatings. Various sample types and scenarios were evaluated during these experiments, including

- Ceramic coatings of different pore sizes
- NDE test panels with programmed flaws (delaminations) of different sizes
- Ceramic coatings subjected to different heat treatments
- Coatings in which the substrate is oxidized away (to visualize interfacial structure)

Several techniques have been investigated to assess the chemical composition, microstructure integrity, coating thickness, and nature of coating adhesion. Some of these techniques have the potential to be used as large-scale NDE inspection methods, whereas others, due to various limitations, are useful only for materials characterization on small-scale samples and witness coupons. Table 4-5 outlines these techniques and their potential.

4.9.1 Candidate NDE Inspection Techniques

The following sections describe the top candidate techniques that have been evaluated to date for the purpose of selecting an NDE method for final inspection.

Terahertz Spectroscopy. Terahertz (THz; ~1012 Hz) is an electromagnetic wave regime that resides between IR and microwaves. This technique uses a THz wave-generating emitter and detecting receiver to measure impedance and scattering effects from a sample. Experiments can be set up in either transmission mode (pitch-catch) or reflection mode.

Table 4-5. Candidate NDE inspection techniques and characterization methods for ceramic coating investigation.

	Full-Field Image	Cracks	Delaminations (Adhesion)	Thickness	Density/ Micro-structure	Tested Yet?
Potential NDE Inspection Methods and Measurement Capabilities						
THz spectroscopy	No	Some	Possibly	Yes	Yes	Yes
THz imaging	Yes, raster	Yes	Yes	Yes	Potentially	No–Dec. '06
Shearography	Yes	Some	Yes	No	No	Yes
Ultrasonics	Yes, raster	Yes	Yes	Yes	Possibly	No
IR imaging	Yes	Yes	Yes	Possibly	Possibly	Yes
Eddy current	No	Yes	Yes	Yes	No	Yes
Characterization Methods (Not Suitable Final Inspection Methods)						
CT/micro-CT	Yes, 3D	Yes	Yes	Yes	Yes	Yes
SEM	Yes	Yes	Yes, some	Yes	Yes	Yes
XRD	No	No	No	No	Yes	Yes

Wave responses can be analyzed in the time or frequency domain. Methods such as THz time-domain spectroscopy (THz TDS) are sensitive to variations in material composition and microstructure and are useful in assessing the potential performance of these materials nondestructively. A THz imaging NDE technique might ultimately be used for the detection of various flaws such as cracks, corrosion, and material phase variations in the ceramic coating for Solar Probe. Images can be built up either by rastering or by using multiple-point detector arrays. For imaging applications, THz frequencies provide higher resolution than standard microwave systems do, because of the shorter wavelengths in this region of the spectrum. THz also can penetrate to significant depths in many materials and scatter off subsurface features, providing image contrast for features that may be missed by using IR imaging methods. This technique is in early stages of development for imaging purposes, but possesses promising capabilities for detecting flaws, thicknesses, and density (porosity) variations. It is currently a leading NDE technique for inspection of the Space Shuttle external tank's TPS, which consists of an aluminum substrate and ceramic foam coating. It also is being investigated as a technique for the inspection of the Space Shuttle's thermal tiles. The experiments discussed here are being performed on a single-point, small-scale level at APL and can be done on a full-field, large-scale level at NASA Langley Research Center in Hampton, VA.

Scattering elements such as grain boundaries, impurities, and interfaces in a ceramic coating impede the transmission of THz and result in overall signal loss. THz TDS was performed on various alumina test samples to gauge the capability of THz technology for detecting pore size or grain size. In one set of samples, each test piece had a specific pore size with sizes ranging from 0.25 μm to 15 μm. These experiments were performed with a transmission mode system and show that the technique is sensitive to changes in pore size and, more generally, to changes in the size and number of scatterers. Figure 4-58 shows the magnitude of the THz transmission obtained by using standard Fourier transform methods for samples with different pore sizes. Signal reduction above 1.5 THz in the fully dense material indicates that grain scattering plays an important role at these high frequencies. Additional scattering by the pore structure reduces THz transmission further, with the greatest scattering occurring for the material with the largest pore size. Peaks and troughs in the spectral magnitudes below approximately 0.1 THz

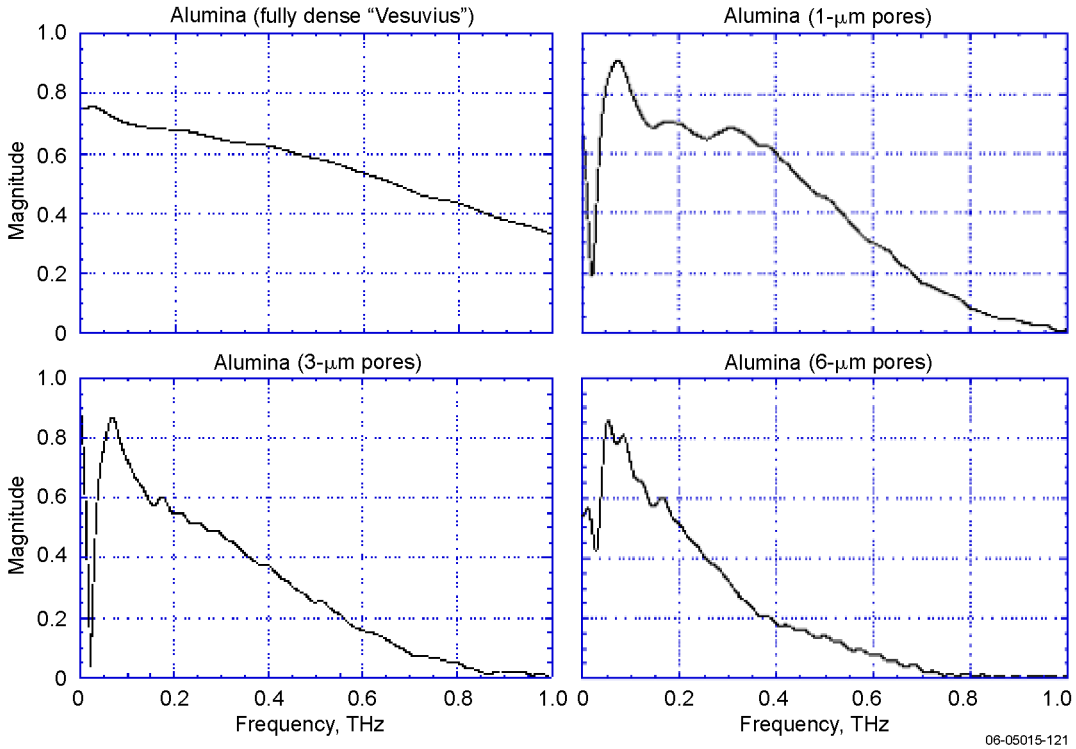

Figure 4-58. Transmission magnitudes for bulk Al_2O_3 ceramics obtained by using THz TDS.

are data processing artifacts and are not related to material variations.

Beyond amplitude variations, THz phase delays also can be used to determine the refractive indices for these materials. Because phase-sensitive detection methods are used in THz TDS, index of refraction measurements for alumina can be accomplished quite easily. Figure 4-59 shows the phase delay of the deconvolved THz signal and the associated refractive index as functions of frequency. Because the index of refraction, n, is directly related to signal delays in the material, the unwrapped phase can be used to calculate the index. Because the phase delay is measured relative to a reference signal in air, the relationship between the two is given as follows:

$$n = \frac{c\Delta\phi}{2\pi f \Delta x} + 1,$$

where c is the speed of light in air, $\Delta\phi$ is the phase delay, f is the frequency, and Δx is the sample thickness.

In addition to porosity and refractive index experiments on bulk alumina, THz scans are being performed on alumina that has been plasma-sprayed onto C-C substrates. For this material system, the THz is set up in reflection mode because C-C composite materials do not transmit well at THz frequencies. These test scans are intended to provide a capability assessment for Solar Probe applications.

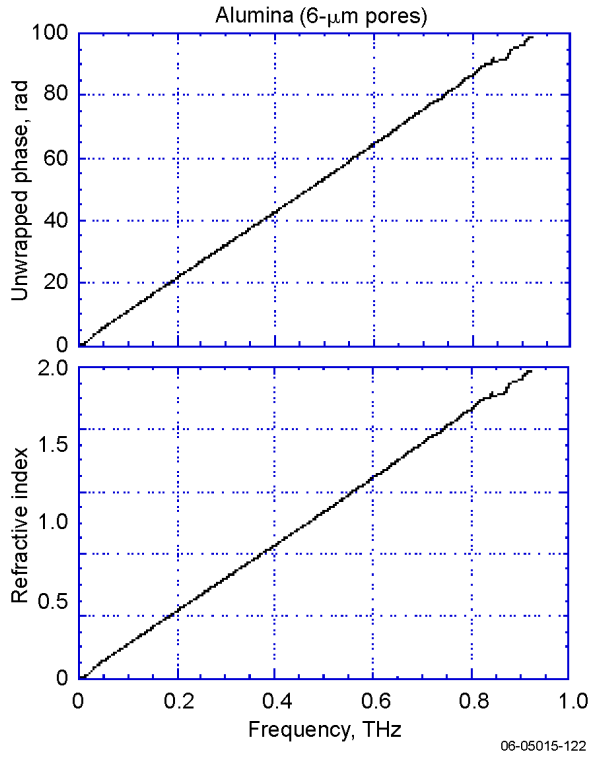

Figure 4-59. Phase delay and refractive index for bulk Al_2O_3 ceramic obtained by using THz TDS.

The porosity results indicate that the THz transmission is reduced at higher frequencies as porosity increases. The attenuation is a result of scattering because of grains and pores in the material. Theoretical models are under development to assist in the interpretation of these signal losses. These models assume that the transmission spectra are a result of time delays of the various rays as they scatter off microstructural elements. This work confirms that current THz technology is capable of detecting and quantifying these material characteristics. In addition, the ease with which the refractive index can be obtained makes this technique very useful for assessing the quality of alumina for coating applications. Beyond mechanical and thermal transport behavior, these coatings must have well-controlled optical properties to maximize optical reflectivity if they are to be used for thermal protection. Based on results obtained to date, THz TDS has the potential for providing useful and necessary information about ceramics and coatings used in the TPS.

Shearography. Shearography is a full-field imaging technique that provides information with regard to delaminations and surfaces stresses (see Figure 4-60). The technique is remote and uses reflected light and shearing interferometry to measure small changes in surface slopes. A material can be excited thermally, acoustically, or by a vacuum source to induce a stress field in the coating. Images before and after stress are compared to identify regions of the coating that are not adhered properly. Also, high-stress regions such as those that concentrate at crack tips can be identified in the sheared image. The images in Figure 4-60 were taken at Laser Technologies, Inc., in Allentown, PA. For these demonstrations, we used programmed flaw samples composed of an alumina coating (~10 mils) on C-C substrates with circular delaminations. Shearography has the potential to yield quantifiable indications of delaminations and partially bonded regions.

IR Imaging. Infrared (IR) imaging is a commonly used NDE technique for inspection of thin materials or thermally conductive materials in which high-sensitivity (~25 mK) images of surface thermal events are produced. A common approach called "active thermography" uses an external heat source (a flash lamp) to deposit heat onto the front surface of the material. The temperature decay of the

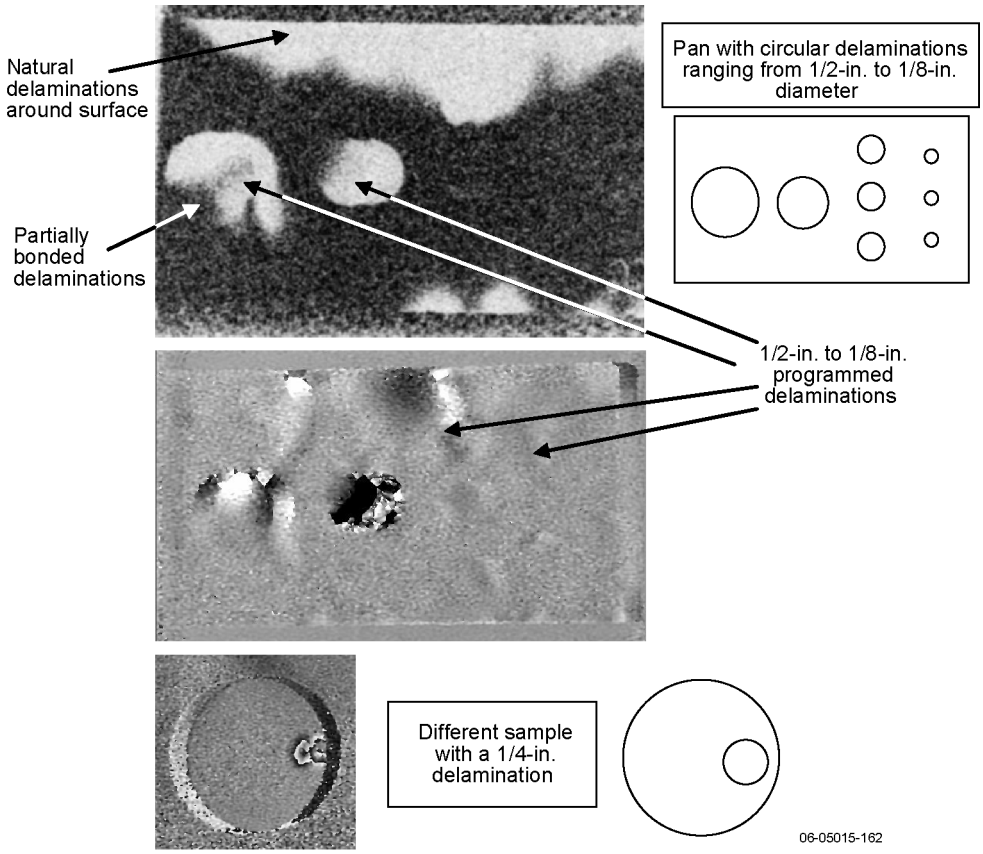

Figure 4-60. Shearography of programmed circular delamination defects in alumina coatings on C-C (top image is via acoustic excitation, and middle and bottom images are via thermal excitation).

front surface (or rise of the back surface) can be viewed with an IR camera. Surface and subsurface anomalies affect the flow of heat from the surface and can be visualized. The images in Figure 4-61 also were taken at Laser Technologies, Inc., in Allentown, PA. For these demonstrations, we used programmed flaw samples made of alumina coating (~10 mils) on C-C substrates with circular delaminations. Thermography has been shown to be a viable technique for detection of subsurface flaws and material property deviations.

Eddy Current. Eddy current is a commonly used technique for measuring coating thicknesses and detecting flaws in electrically conductive materials. An eddy current probe is energized with current and, when placed in proximity to a conductive material, the electrical impedance is modified by the bulk material properties as well as by anomalies and discontinuities in the material. This technique is not ideal for imaging large-acreage areas and identifying multiple types of defects, but it is a useful and simple technique for point-by-point thickness measurements of the coating. These experiments have been performed at APL and can, if necessary, be contracted out to Quality Material Inspection, Inc. (QMI), in Huntington Beach, CA. Alumina coating thickness measurements collected by using the eddy current technique are summarized in Figure 4-62.

4.9.2 Characterization Techniques

Some standard techniques for materials characterization are necessary beyond the NDE techniques listed above. These techniques provide pertinent information about the system and general understanding of the coating and processes. These techniques are distinguished from the candidate NDE techniques because they either are destructive or are constrained by sample size limitations.

CT/Micro-CT Imaging. Computed tomography (CT) uses X-ray attenuation profiles at various angles to reconstruct 3D images that could allow

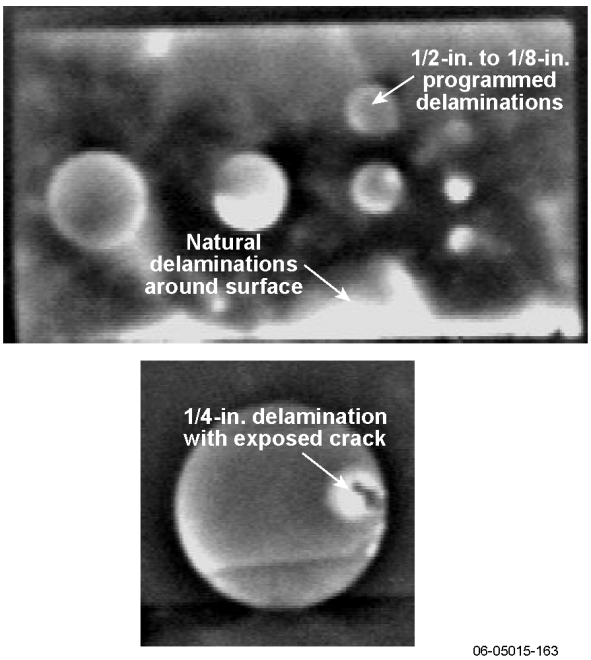

Figure 4-61. Active thermography of programmed circular delamination defects in alumina coatings on C-C.

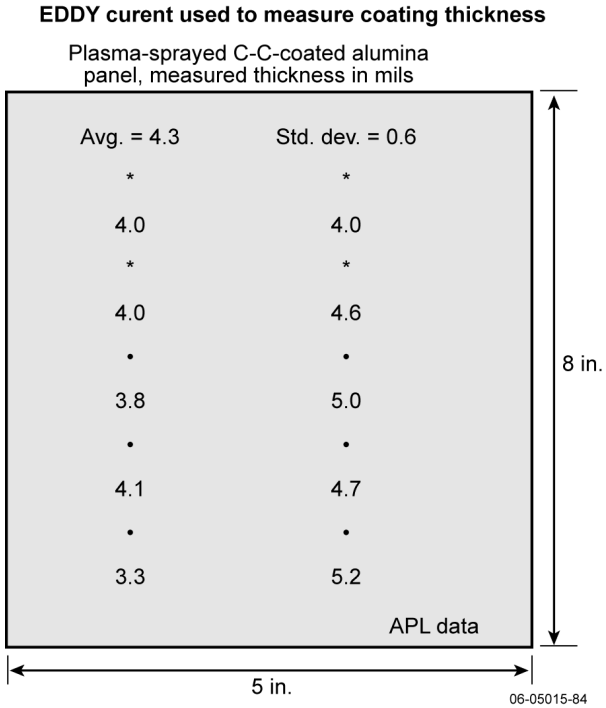

Figure 4-62. Eddy current measurements of alumina coating thickness.

anatomical understanding of the coating/substrate system. Micro-CT is similar to conventional large-scale CT imaging but at micrometer resolution, which dramatically improves interface information. The current state-of-the-art technique enables resolutions approaching nanometer dimensions. This technique can be used to build a 3D anatomic computer model of the structure of a C-C substrate and surface (with enough resolution to visualize individual fibers). There are some drawbacks to these approaches. CT and micro-CT systems produce very large data files. Because higher-resolution and higher-magnification date cubes are inherently very large files, the computer reconstruction algorithms are time-consuming. As a result, to scan a highly magnified volume with micro-CT, samples sizes must necessarily be small, so this technique is able to provide useful information for characterization purposes but is impractical as an inspection method. Small coupons of alumina on C-C with artificial delaminations are being tested to determine whether the interfacial structure and morphology of this bonded region is discernable. These experiments are being carried out at Micro Photonics, Inc., in Allentown, PA.

Electron Microscopy. High-resolution electron micrographs (via SEM) of samples allow for the characterization of coatings from different processes and heating treatments. Because this technique uses a detector to measure deflected electrons off a surface, the materials must either be naturally conductive or coated with platinum so as to avoid charging. For this reason, and also because the samples must be small, this technique is not practical as an inspection method. But as a characterization method, it provides invaluable very high-magnification images that show interfacial features and crystal microstructure. Also, elemental analysis can be performed on coating surfaces. The experiments shown in Figure 4-63 were performed at the JHU Homewood campus in the Materials Science Department.

X-Ray Diffractometry. X-ray diffraction (XRD) is another commonly used materials evaluation technique that measures the diffraction peaks from a sample as an X-ray beam rotates about the surface. From this, crystal structure and particle size can be determined to characterize coating samples from different processes and heating treatments. Crystal structure and phase information can be determined from the peak locations. Particle sizes (for small particles) can be estimated by measuring the peak width and implementing Scherer analysis. Figure 4-30 provided an example of the sensitivity of this technique in identifying phases in alumina samples that have been heat-treated to various temperatures. As the alumina is heated, it transforms from the

as-sprayed gamma-phase alumina to the stable alpha-phase alumina. The experiments shown in Figure 4-30 were carried out at the JHU Homewood campus.

4.10 Study Design Recommendations

During this risk mitigation effort, the emphasis has been on highlighting performance and manufacturing limitations of the candidate coating materials and identifying coating design improvements to enhance performance and durability and to provide redundancy. Although our coating designs to this point have been applied directly to the C-C substrate, the mindset always has been that multilayer coatings may serve to reduce risks. The study established that three ceramic coating options currently are available for the primary shield (alumina, PBN, and BaZP); however, the leading candidates remain Al_2O_3 and PBN. Based on the data in hand (with additional tests still remaining as part of the FY 2006 study), the findings for the candidate coatings are as follows.

4.10.1 Al_2O_3

- Optically, material provides $\alpha/\varepsilon < 0.3$.
- Radiation damage is not permanent; optical properties are returned with temperature.
- Structural integrity is sufficient for launch and thermal cycling loads.

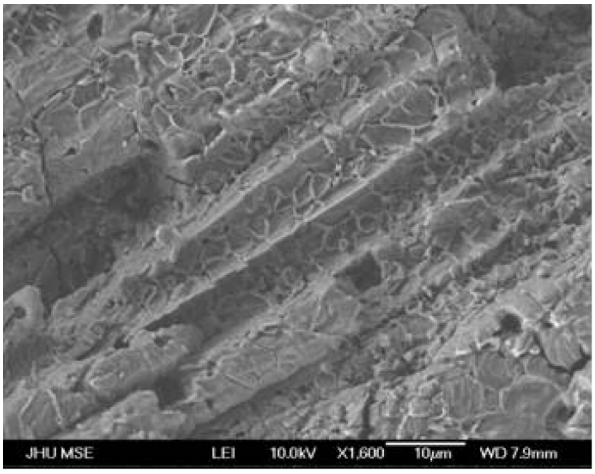

Underside view of plasma-sprayed alumina coating in which the C-C substrate has been burned away

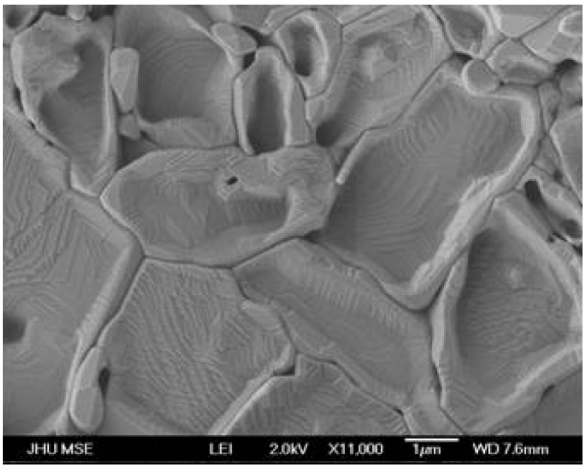

High-magnification view of plasma-sprayed alumina surface showing thermal faceting due to heat treatment

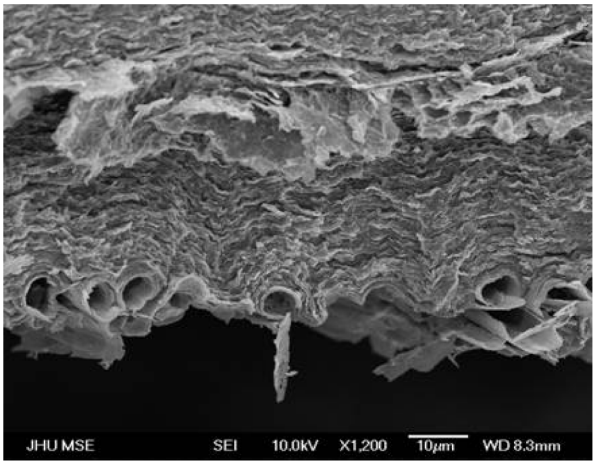

Cross-section view of PBN CVD coating in which the C-C substrate has been burned away (from the bottom)

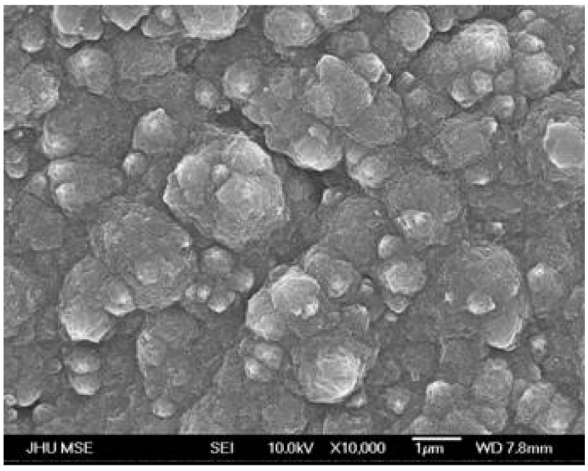

High-magnification view of PBN CVD surface growth structures

06-05015-164

Figure 4-63. SEM images of alumina and PBN coatings.

- Mass loss is marginal at elevated temperatures >1600 K due to carbon and oxygen interactions.
- Recommend incorporating bond and transition layers to separate C-C and Al_2O_3 to eliminate chemical interactions leading to mass loss.

4.10.2 PBN

- Optically, material provides $\alpha/\varepsilon < 0.3$.
- Radiation damage is not measurable.
- Structural integrity is sufficient for thermal cycling loads.
- Mass loss is acceptable to >1950 K.
- Recommend interfacing directly onto C-C substrate and enhancing interface properties by using controlled surface texturing.

4.10.3 BaZP

- Optically, material provides $\alpha/\varepsilon < 0.2$.
- Radiation damage is not measurable.
- Mass loss is not acceptable to >1600 K due to phosphate depletion.
- Recommend exploring stabilization of phosphate component at elevated temperature before investing in coating optimization.

4.11 Remaining Work

The work remaining under this study will investigate methods to optimize optical performance, enhance structural integrity, add margin to mass loss thresholds, and further characterize NDE techniques for assessing coating and coating-interface quality. Specifically, the following studies will be conducted.

- Barrier coatings will be explored for the alumina in an attempt to limit the interaction between alumina and carbon at elevated temperature in an ultra-high-temperature environment.
- Surface texturing techniques that are compatible with large surface areas will be explored to enhance the interface strength of the CVD-applied PBN material.
- Optimization of optical properties will continue through tailoring of the microstructure and exploration of composite material systems (such as alumina and PBN).
- Continued characterization of the NDE capabilities to detect flaws, including THz and micro-CT scanning for evaluation of microstructures and laser shearography for interrogation of interfaces.

5 Mass Loss

5.1 Background and Description of Total Mass Loss Considerations

Characterizing the total mass loss (TML) from the Solar Probe spacecraft is necessary to determine the impact that the spacecraft will have on the local plasma environments being measured. Mass loss levels will not be large enough to affect the function of the Thermal Protection System (TPS) as a thermal management system, only large enough to serve as a source of contamination to the scientific data. Total mass loss for the spacecraft in such an environment can be defined in terms of thermal vacuum, radiation, and particle impact effects:

$$\mathrm{TML} = (\mathrm{OG} + \mathrm{TV} + \mathrm{CI}) + (\mathrm{PS} + \mathrm{RES} + \mathrm{CE}) + (\mathrm{PI}) , \quad (1)$$

where

- Thermal vacuum effects:
  - Outgassing (OG) = loss of water and organic volatiles
  - Thermal vaporization (TV) = vaporization of materials at high temperatures
  - Chemical interactions (CI) = interactions between materials at high temperatures
- Radiation effects:
  - Physical sputtering (PS) = spallation due to energetic atom impacts
  - Radiation-enhanced sublimation (RES) = diffusion and thermal desorption of carbon atoms
  - Chemical erosion (CE) = reaction of implanted H^+ with carbon to form CH_4
- Impact effects:
  - Particulate impact (PI) = debris discharges due to hypervelocity impacts

The total allowable mass loss rate from the Solar Probe spacecraft components due to these effects is 2.5 mg/s at any time during the mission.[1] The basis for the TML budget was established during previous Solar Probe studies and is currently under review by the Science Committee. Mass loss is both temperature- and radiation-dose-dependent, and thus trajectory-dependent, as summarized in Figure 5-1. Prior to the start of science measurements at 0.3 AU (and to 0.083 AU), mass loss is produced primarily from outgassing, particle impact, and physical sputtering effects, as spacecraft temperatures are predicted to be below 600°C. From 0.083 to 0.029 AU (between 600°C and 1200°C), mass loss is dominated by particle impact, physical sputtering, and chemical erosion sources. Inside of 0.029 AU and around 4 R_S (where critical science takes place and TPS temperatures are greater than 1200°C), thermal vaporization, chemical interactions, particle impact, physical sputtering, and radiation-enhanced sublimations are the dominant mass loss mechanisms.

Materials commonly associated with mass loss from spacecraft are those that contain large amounts of water, hydrocarbons, or other organic materials that can degrade in the space environment. In the case of Solar Probe, organics have been eliminated from high-temperature regions of the TPS. Materials under investigation include the candidate ceramic coatings, the carbon–carbon (C-C) structural materials, the carbon foam thermal insulation, ceramic adhesives, and multilayer insulation. Since the materials that cover the largest surface areas are the ceramic coatings and C-C, this Risk Mitigation Study initially focused on fundamental characterization of these materials. Literature investigations have indicated that the major effects contributing

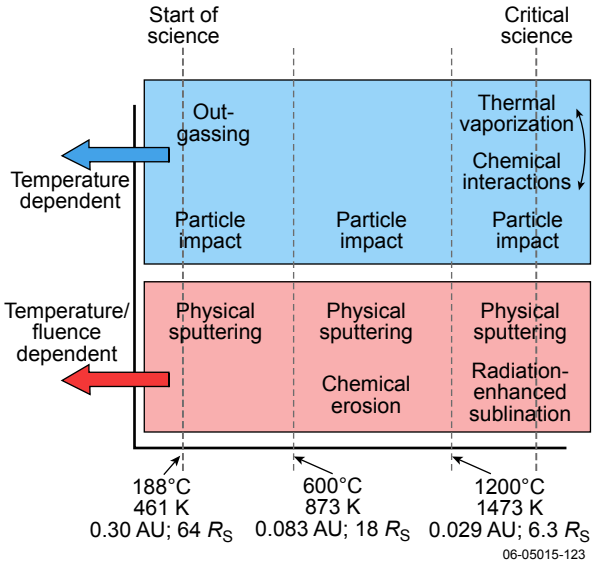

Figure 5-1. Relationship between mass loss effects and temperature.

[1]Goldstein et al., *Spacecraft Mass Loss and Electric Potential Requirements for the Starprobe Mission*, A report of the Starprobe Mass Loss Requirements Group Meeting of September 29–30, 1980, NASA Jet Propulsion Laboratory, California Institute of Technology, Pasadena, CA (December 1980).

to mass loss for these materials will come from the thermal vacuum effects.

An important finding of this study was that chemical interactions significantly lower the allowable-use temperature of alumina-coated C-C below 1650 K in ultra-high vacuum. This interaction, based on coupon test data, can be reduced adequately through the use of a refractory interlayer as discussed in Section 4.4.1. Pyrolytic boron nitride (PBN) does not show a similar interaction. More testing is planned to duplicate these results with larger sample sizes and with the mass loss products identified.

5.2 Thermal Vacuum Effects

The components of mass loss considered part of the thermal vacuum effects include outgassing, thermal vaporization, and chemical interactions. For the purposes of this discussion, outgassing is defined as the loss of water and other volatiles from the base material due to the effects of vacuum and temperature. Thermal vaporization is the loss of the base material through the increasing vapor pressure at higher temperatures. Chemical interactions refer to interactions between the base material and coating that cause chemical changes within the substrate/coating interface at high temperature. Of the three thermal vacuum-related effects, thermal vaporization is the dominant mass loss mechanism for the TPS.

Thermal and vacuum environmental effects on the TPS mass loss have been quantified by both analysis and testing. Thermal vaporization and chemical interactions can be approached analytically. Effects due to outgassing, thermal vaporization, and chemical interactions also can be measured experimentally. Two goals of the TPS Risk Mitigation Study were to (1) define the mass loss characteristics of the TPS and (2) investigate the accuracy and constraints of both modeling and test methodologies used to quantify those characteristics over the range of expected environments.

Mass loss for typical spacecraft applications focuses on outgassing due to the much lower system temperatures. Outgassing occurs as volatile materials change state with increasing temperature and in vacuum conditions. Mass loss rates are low while the volatiles are in the liquid or solid state, and they increase quickly as they move into the vapor state and are released from the base material. Thermogravimetric analysis (TGA) is a type of testing that determines the quantity of the outgassed materials by continuously measuring sample weight as a function of temperature during sample heating. For Solar Probe, system outgassing would occur early in the mission.

For this study, TGA testing also was used to experimentally determine the temperature-related mass loss due to thermal vaporization of the TPS candidate materials at elevated temperatures. While thermal vaporization is a different mechanism than outgassing, both phenomena involve a change in mass as the test specimen temperature is raised. It was found that the onset of mass loss for all candidate materials did not occur until above the expected operating temperature.

5.2.1 Testing

Thermal stability testing of candidate materials was conducted in a high-temperature carbon furnace at APL (Figure 5-2) under inert and low-vacuum (10×10^{-2} torr) conditions. The test samples were approximately 5×5 cm. A variety of materials were ramped up to a constant temperature, held for 4 hours, and then returned to room temperature. Sample temperatures between 1650 K and 2250 K were tested. Pre- and post-test weight measurements were compared to determine the mass loss rate at the test temperature. Sample weighing was done outside the furnace, so the

06-05015-64

Figure 5-2. APL high-temperature carbon furnace.

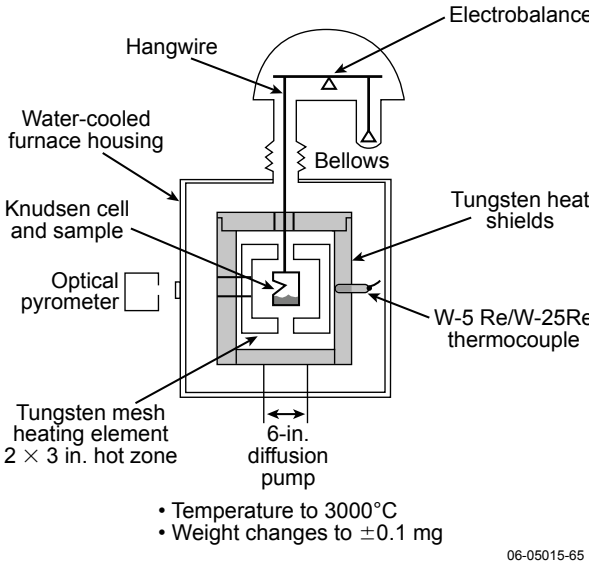

Figure 5-3. NASA GRC vacuum thermogravimetric apparatus.

effects of moisture loss and recovery were characterized and accounted for. This test method had the advantages of allowing a relatively large sample and having good chamber accessibility. It had the disadvantage of limited accuracy for the shorter heat-soak durations tested. In future testing, increased accuracy can be achieved through the use of longer soak times in the temperature range where the onset of mass loss was identified for the test material.

High-temperature stability of primary shield materials under high vacuum (10×10^{-7} torr) is being studied in partnership with NASA Glenn Research Center (GRC) in a vacuum TGA apparatus. In the GRC test chamber, shown schematically in Figure 5-3, material samples are ramped from room temperature to a minimum of 2000 K at a rate of 2 K/min under high vacuum, and sample weight is continuously recorded by using an electrobalance outside the chamber. The sample is hung inside the chamber on a tungsten wire connected to the electrobalance (Figure 5-4). Table 5-1 lists the test conditions achieved for each sample. These TGA tests allow materials to be screened for thermal stability, and temperatures can be identified at which onset of mass loss occurs for each material. Further testing, such as long-term holds at critical temperatures, will need to be performed for increased resolution and accuracy on mass loss rates.

5.2.2 Outgassing

Outgassing measurements were made for all candidate materials as part of the TGA testing done at GRC. During the lower-temperature portion of the testing, moisture and organic volatiles were released as the sample moved through their respective vaporization points. All the candidate materials are stable at these temperatures, so any

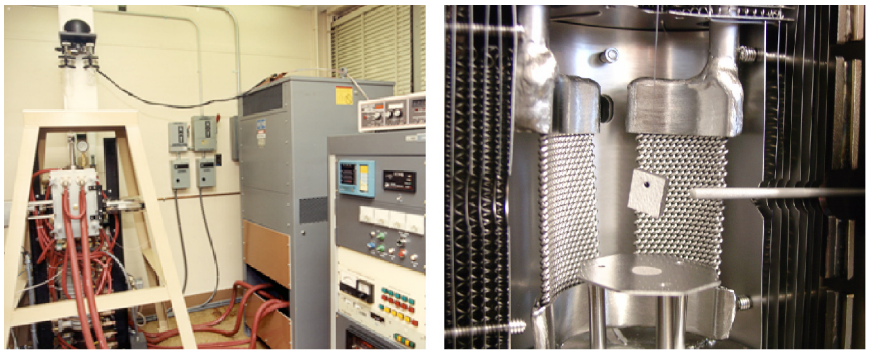

Figure 5-4. NASA GRC vacuum thermobalance (left) and alumina-coated C-C sample in the test chamber (right).

Table 5-1. NASA GRC TGA test conditions achieved.

Sample	Test	Hold
C-C	7.1°C/min to 1334°C, 1.7°C/min to 2134°C	1334°C ~20 h
PBN	7.1°C/min to 1334°C, 1.7°C/min to 1952°C	1334°C ~20 h
PBN coating on C-C	2°C/min to 1754°C	None
PBN coating on C-C	7.1°C/min to 1334°C, 1.7°C/min to 2078°C	1334°C ~20 h
Alumina	6.2°C/min to 1534°C, 1.7°C/min to 2035°C	None
Alumina coating on C-C	7.1°C/min to 1334°C, 1.7°C/min to 1618°C	1334°C ~20 h
Alumina coating on C-C with SiC interlayer	7.1°C/min to 1334°C, 1.7°C/min to 2068°C	1334°C ~20 h

mass loss seen in the sample can be traced to volatile materials. The identification and quantification of these materials is unnecessary because they are lost by the system prior to launch or early in the mission.

Bare C-C [advanced C-C coupon ACC-6 from Carbon-Carbon Advanced Technologies (C-CAT)] and the ceramic coating materials were tested both individually and in combinations in the GRC TGA apparatus. C-C exhibits an approximately 1% weight reduction at low temperatures due to loss of trapped moisture, as shown in Figure 5-5; no evidence of entrapped volatiles was noted. Once the trapped moisture is lost at temperatures below 500 K, C-C is stable with no evidence of mass loss until 2000 K, as shown in Figure 5-6. Figures 5-5 and 5-6 also show that no measurable mass loss was evident for alumina (Al_2O_3), PBN, and barium zironium posphate (BaZP) below the 500 K temperature level, indicating that moisture absorption by the candidate ceramics is negligible and there are no entrapped organic constituents. For the Solar Probe mission, outgassing will occur over the approximately 4 years prior to the first solar pass. As the spacecraft approaches the Sun, TPS temperatures will exceed 500 K between 0.3 and 0.2 AU. After this point, all moisture and volatiles will have been eliminated, and no appreciable outgassing will occur near closest approach to the Sun.

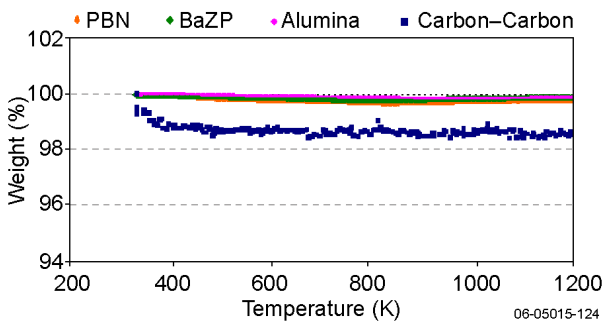

Figure 5-5. Outgassing of C-C and ceramics below 500 K.

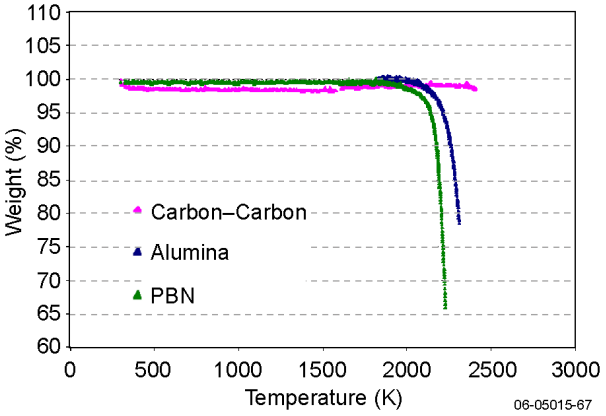

Figure 5-6. Mass loss of individual primary shield materials.

5.2.3 Thermal Vaporization

Mass loss due to thermal vaporization occurs in the base material as the vapor pressure above the base material increases at higher temperatures. For the materials in question, at low to moderate temperatures there is virtually no mass loss. At high enough temperatures, measurable material loss begins and continues to increase until it becomes the dominant mass loss mechanism for the system.

Significant published data exist on thermal stability of carbon, alumina, and PBN. Sublimation of carbon and graphite under high-temperature/high-vacuum conditions has been studied extensively for decades by using Knudsen cell techniques. Carbon and graphite are stable with extremely low vapor pressure (mass loss) to temperatures exceeding 2200 K. Al_2O_3 is widely used in high-temperature testing applications and is known to be stable above 1850 K under high vacuum. PBN is used extensively in the nuclear industry as a coating on carbon plasma chambers, which operate in high-temperature, vacuum, and radiation environments for extended periods of time. PBN-coated graphite cores also are used as heaters in high-vacuum chambers for temperatures of 2100 K. No relevant thermal test data were found for BaZP.

NASA's Chemical Equilibrium with Applications (CEA) modeling software[2] was used to predict vapor pressures of the individual materials by finding the equilibrium state of as many as 600 gas-phase species, with any number of condensed species. The restriction is that the condensed species must be pure and non-interacting. When these solutions are non-ideal, activity coefficient input is needed. CEA outputs the partial pressure of each evolving chemical species from a given material. The partial pressures of all species can be used to calculate total vapor pressure. In turn, this total vapor pressure can be converted to material mass loss rate by use of the Hertz-Knudsen-Langmuir equation, which accounts for vaporization from the surface area of the components. The CEA program was developed by NASA. The calculations use the

[2]NASA Glenn Research Center, *Chemical Equilibrium with Applications,* http://www.grc.nasa.gov/WWW/CEAWeb/.

full JANAF database of thermochemical properties along with properties from other key databases, as illustrated in Table 5-2.

Figures 5-7 through 5-9 show the predicted vapor pressure into a vacuum of each evolving species from alumina, carbon, and boron nitride (BN) as a function of temperature, as predicted by CEA. The major species evolving from alumina are Al and O; from carbon, C and C_3; and from BN, N_2. Knowing the exact outgassed components of each material will allow better prediction of key interactions with the spacecraft. Figure 5-10 shows the total vapor pressure (all evolving species) for C-C as well as for Al_2O_3 and conventional boron nitride (since PBN was not available in the CEA database). Vapor pressures of C-C and Al_2O_3 are very low at the critical mission temperature of 1850 K. The vapor pressure of BN is two orders of magnitude higher than that of Al_2O_3. Note that this is the cubic structure variety of BN (the only BN variety modeled by CEA), which is much less stable than PBN.

Table 5-2. Thermochemical database supporting CEA [Chemical Equilibrium with Applications] analysis software (from Jacobson, N., Use of tabulated thermochemical data for pure compounds, *J. Chem. Ed.*, **78**(6), 2001, Table 1).

Source and Reference*	Format	Quantities**
Chase et al. *JANAF Thermochemical Tables*, 1998 (1)*	Tabular, electronic	$C_p°(T)$, $S°(T)$, FEF(298), $H°(T) - H°(T_r)$, $\Delta_f H°(T)$, $\Delta_f G°(T)$, log K_f, $\Delta_{tr} H$
Gurvich et al. *Thermochemical Properties of Individual Substances*, 1989 (2)	Tabular, electronic	$C_p°(T)$, FEF(0), $H°(T) - H°(0)$, $S°(T)$, log K_f, $\Delta_f H°(0)$, $\Delta_f H°(298)$, $\Delta_{tr} H°$
Barin. *Thermochemical Data of the Indivual Substances*, 1995 (3)	Tabular	$C_p°(T)$, $S°(T)$, FEF(298), $H°(T)$, $H°(T) - H°(298)$, $G°(T)$, $\Delta_f H°(T)$, $\Delta_f G°(T)$, log K_f, $\Delta_{tr} H$
Pankratz. *Thermodynamic Properties of Elements and Oxides; Thermodynamic Properties of Halides; Thermodynamic Properties of Carbides, Nitrides, and Other Selected Substances* (4)	Tabular, analytic functions	$C_p°(T)$, $S°(T)$, FEF(298), $H°(T) - H°(298)$, $\Delta_f H°$, $\Delta_f G°(T)$, log K_f, $\Delta_{tr} H$
Pankratz et al. *Thermodynamic Properties of Sulfides; Thermodynamic Data for Mineral Technology* (4)	Tabular	$C_p°(T)$, $S°(T)$, $H°(T) - H°(298)$, $\Delta_f H°(T)$, $\Delta_f G°(T)$
Dinsdale, *SGTE Data for Pure Elements* (5)	Analytic functions	$G - H_{SER}$
SGTE Database (6)	Electronic	$G - H_{SER}$; or $C_p°$, $\Delta_f H°(298)$, S°(298) for some compounds
Database for HSC (7)	Electronic, analytic functions	$\Delta_f H°(298)$ S°(298), $C_p°(T)$
Cox et al. *CODATA Key Values for Thermodynamics* (8)	Tabular	$C_p°(T)$, FEF(0), $H°(T) - H°(0)$
Hultgren et al. *Selected Values of the Thermodynamic Properties of the Elements* (9)	Tabular	$C_p°$, $H°(T) - H°(298)$, $S°(T) - S°(298)$, FEF(298), $\Delta_{vap} G°$, $\Delta_{vap} H°$, $\Delta_{tr} H$, log P (vapor)
Robie and Hemingway. *Thermodynamic Properties of Minerals and Related Substances at 298.15 K and 1 Bar Pressure and Higher Temperatures* (10)	Tabular	$S°(298)$, $\Delta_f H°(298)$, $\Delta_f G°(298)$ for many minerals; $C_p°(T)$, $S_T°(T)$, $H°(T) - H°(298)$, FEF(298), $\Delta_f H°(T)$, $\Delta_f G°(T)$, log K_f, $\Delta_{tr} H(T)$ for selected minerals
Kubachewski. *The Thermodynamic Properties of Double Oxides* (11)	Analytic functions	$\Delta_f G°$
Kubachewski et al. *Materials Thermochemistry* (12)	Tabular, analytic functions	$C_p°(T)$, $S°(298)$, $\Delta_f H°(298)$, $\Delta_{tr} H$
Mills. *Thermodynamic Data for Inorganic Sulfides, Selenides, and Tellurides* (13)	Tabular	$C_p°(T)$, $S°(T)$, FEF(298), $H°(T) - H°(298)$, $\Delta_f H°(T)$, $\Delta_f G°(T)$, log K_p

*Numbers in parentheses refer to references cited in Jacobson, N., Use of tabulated thermochemical data for pure compounds, *J. Chem. Ed.*, **78**(6), 814–819 (2001).

**The symbol "°" designates the standard state, generally the most stable form of aggregation of a pure element or compound at 1 bar (10^5 Pa). C_p = heat capacity; f (as subscript) = formation; FEF = free energy function; G = Gibbs free energy; H = enthalpy; K = equilibrium constant; P (as variable or subscript) = pressure; S = entropy; T = temperature.

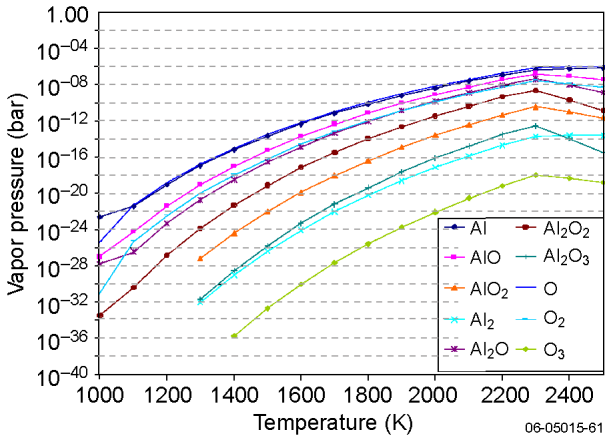

Figure 5-7. CEA analysis results for vaporization of alumina into a vacuum.

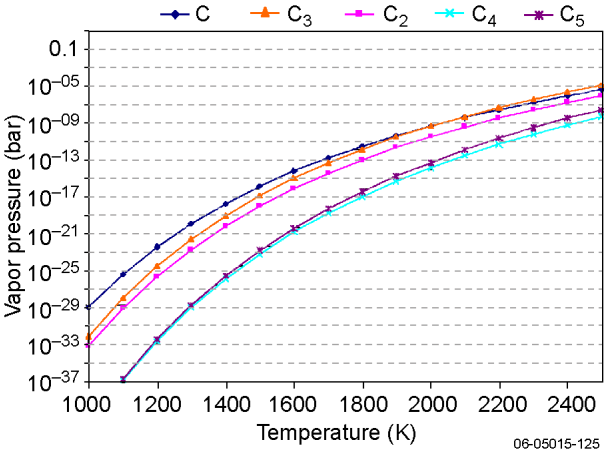

Figure 5-8. CEA analysis results for vaporization of carbon into a vacuum.

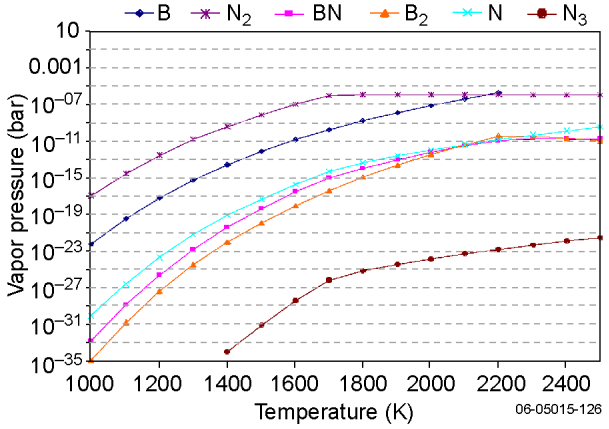

Figure 5-9. CEA analysis results for vaporization of BN into a vacuum.

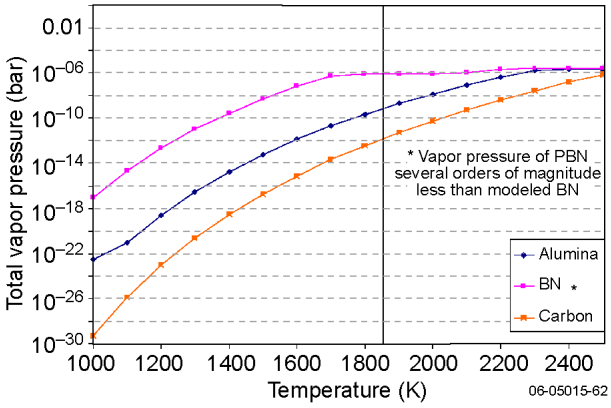

Figure 5-10. CEA analysis results for alumina, BN, and carbon.

CEA databases do not include BaZP, but the suspected mass loss mechanism is the phosphate component being driven off above 1500 K, resulting in a high mass loss rate. Discussions with SMAHT ceramics have indicated potential improvements in thermal stability of BaZP through the use of additives. This option remains open but has not been explored yet because of the positive results from the other coatings.

The Hertz-Knudsen-Langmuir equation (see eq. 2) was used to calculate primary shield mass loss rate from vapor pressure. According to this relation, the mass loss rate is a function of vapor pressure, temperature, primary shield surface area, and the molecular weight of evolving species. Figure 5-11 shows the results of this analysis, where critical points are the intersection of the mass loss rate budget (2.5 mg/s) with the primary shield design temperature of 1850 K. The predicted mass loss rate of alumina is below 2.5 mg/s for temperatures up to

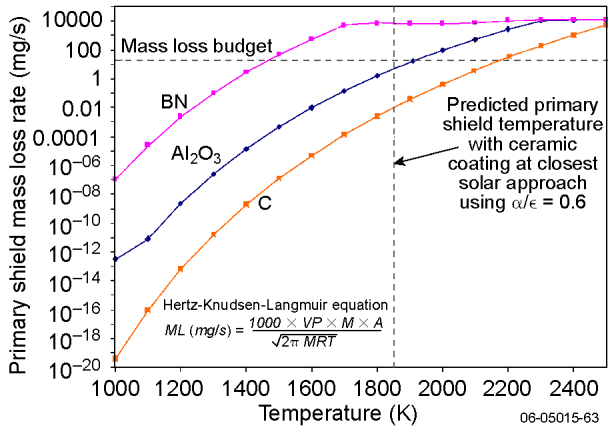

Figure 5-11. CEA analysis results converted from vapor pressure to primary shield total mass loss rate.

1950 K, 100 K above the predicted primary shield temperature. The predicted mass loss rate of C-C is below 2.5 mg/s for temperatures up to 2200 K. The predicted mass loss rate of BN is above 2.5 mg/s at the key temperature, but this result was not unexpected. PBN is known to be similar to Al_2O_3 in high-temperature stability and much more stable than the cubic BN used in the CEA. The mass loss of PBN at elevated temperatures is expected to be lower than that predicted by CEA's BN model.

$$ML_{\text{rate}} = \frac{1000 \times VP \times M \times A}{\sqrt{2\pi\ MRT}}, \qquad (2)$$

where

VP = vapor pressure above the material (atm)
M = molecular weight of evolving species (g/mol)
A = primary shield surface area (cm^2)
T = temperature (K)

A correlation to the analytical mass loss predictions was obtained through the TGA testing done at GRC. Changes in the sample mass over the test period show the temperature at which mass loss begins. While more qualitative than quantitative, these temperatures can be compared against the analytically determined mass loss figures. Mass loss measurements are reported as a percentage change in the test sample. The test conditions for the samples are given in Table 5-1; the sample details are given in Table 5-3. The test data indicate the region over which the samples are thermally stable and where the significant mass loss begins. The noise in the data does not allow meaningful calculations of the mass loss rate at a specific temperature.

Figure 5-12 shows the TGA data for the C-C sample. The data show that the C-C is stable until about 2300 K. Figure 5-13 shows the test data for alumina, showing that bare alumina is stable to about 2000 K. Figure 5-14 shows the TGA data for PBN, which is stable to above 1900 K. Figure 5-15 shows data for BaZP for tests conducted in an APL TGA chamber under nitrogen purge; BaZP is unstable above 1500 K.

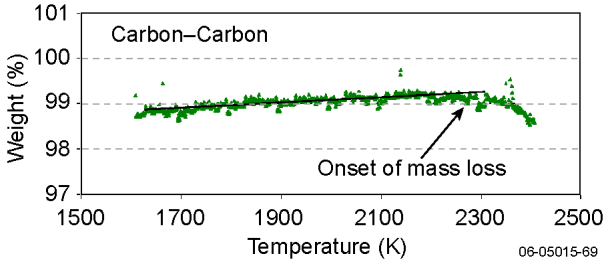

Figure 5-12. High-temperature/vacuum TGA plot for C-C.

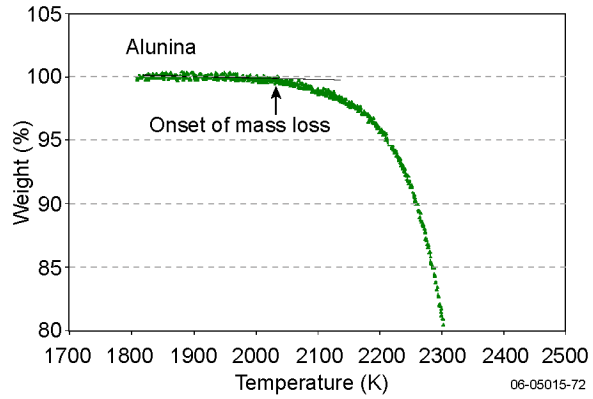

Figure 5-13. High-temperature/vacuum TGA plot for alumina.

Figure 5-16 shows the analytical results obtained by using CEA with the TGA-based temperature data on mass loss onset. The BN results are omitted because of the lack of similarity of BN to PBN. The C-C and alumina data show the onset temperatures for both materials are aligned and near the mass loss requirement. This alignment of the

Table 5-3. NASA GRC TGA test sample dimensions and weight measurement.

Sample	Specimen Shape	Dimensions (cm)	Wt Before (mg)	Wt After (mg)
C-C	Quarter disc	Dia. = 1.225, Thickn. = 0.3	49.528	49.35
PBN	Rectangle	1.265 × 1.127 × 0.331	90.955	89.175
PBN coating on C-C	Rectangle	1.043 × 0.996 × 0.271	42.493	42.375
PBN coating on C-C	Rectangle	1.015 × 0.967 × 0.276	41.02	40.823
Alumina	Rectangle	1.081 × 0.993 × 0.274	108.066	105.759
Alumina coating on C-C	Rectangle	1.093 × 0.989 × 0.311	55.256	48.545
Alumina coating on C-C with SiC interlayer	Rectangle	1.013 × 0.975 × 0.150	27.401	15.022

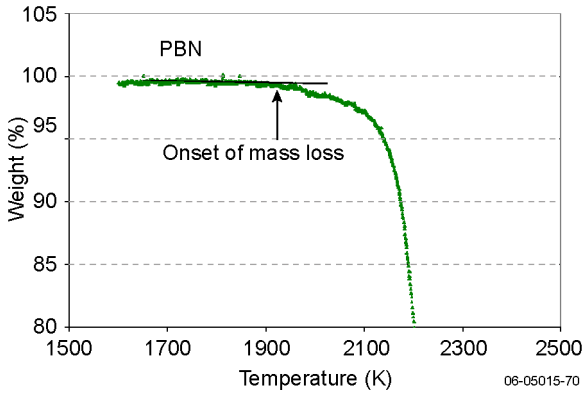

Figure 5-14. High-temperature/vacuum TGA plot for PBN.

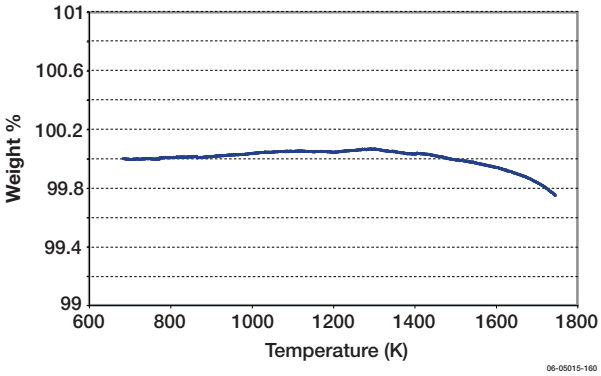

Figure 5-15. BaZP TGA test under nitrogen purge. Mass loss begins around 1500 K, which corresponds to the primary shield temperature at 4 R_S with $\alpha/\epsilon = 0.25$.

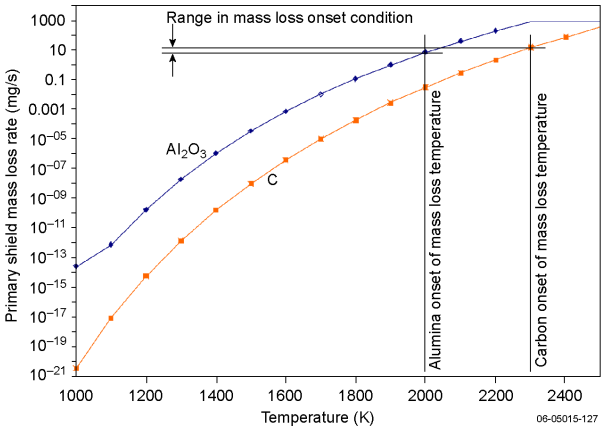

Figure 5-16. Comparison of analytical predictions and TGA data.

analytical and test data supports the basic results. However, the data also suggest that the critical mass loss requirement is exceeded just above the onset temperature. To accurately quantify the mass loss characteristics of the TPS, more accurate material mass loss values need to be obtained between 1600 and 2000 K.

The data for the APL and GRC testing are summarized in Table 5-4, and both the mass loss estimate and the test environment are given. The inert and 10^{-2} torr vacuum environments refer to APL test data. The high-vacuum data refer to GRC testing. The data show that the mass loss values for alumina are consistent for the different tests and are

Table 5-4. NASA GRC TGA test sample dimensions and weight measurement.

Material	Temperature (K)							
	1650		1850		2050		2250	
C-C	Inert	NT	Inert	NT	Inert	NT	Inert	NT
	10^{-2} torr	2.0 mg/s	10^{-2} torr	5.2 mg/s	10^{-2} torr	12 mg/s	10^{-2} torr	30 mg/s
	10^{-7} torr	0.0 mg/s*	10^{-7} torr	0.0 mg/s*	10^{-7} torr	0.0 mg/s	10^{-7} torr	1.0 mg/s*
Alumina	Inert	0.0 mg/s	Inert	0.27 mg/s	Inert	NT	Inert	NT
	10^{-2} torr	0.0 mg/s	10^{-2} torr	0.30 mg/s	10^{-2} torr	1.4 mg/s	10^{-2} torr	13 mg/s
	10^{-7} torr	0.0 mg/s*	10^{-7} torr	0.42 mg/s*	10^{-7} torr	25 mg/s*	10^{-7} torr	420mg/s*
PBN	Inert	0.0 mg/s	Inert	0.14 mg/s	Inert	NT	Inert	NT
	10^{-2} torr	0.0 mg/s	10^{-2} torr	0.15 mg/s	10^{-2} torr	0.25 mg/s	10^{-2} torr	24 mg/s
	10^{-7} torr	0.0 mg/s*	10^{-7} torr	0.30 mg/s*	10^{-7} torr	10 mg/s	10^{-7} torr	>312 mg/s*
BaZP	Inert	36 mg/s	Inert	195 mg/s	Inert	NT	Inert	NT
	10^{-2} torr	26 mg/s	10^{-2} torr	110 mg/s	10^{-2} torr	NT	10^{-2} torr	NT
	10^{-7} torr	NT	10^{-7} torr	NT	10^{-7} torr	NT	10^{-7} torr	NT

*NT = not tested; best estimate of mass loss rate using curve fits of TGA data. Long-term holds at temperature needed to obtain mass loss rates of higher accuracy.

well below the required value at the design primary shield temperature (1850 K). The C-C and PBN data show some different results between the APL and GRC testing. For C-C, the higher APL values at the lower temperatures indicate that the data may be flawed, as the coupons were slightly oxidized. The similarities in the test data between the different test methods suggest that the approach is reasonable. The variations in the data suggest that more testing at higher resolution is required to obtain accurate values in the 1600 to 2000 K range.

5.2.4 Chemical Interactions

Equally important with the thermal stability of the individual coating materials is their stability as coatings in contact with the C-C substrate. Carbon is known to react with many materials at high temperatures. Notably, most metals react to form metallic carbides, and most oxides can be thermally reduced by carbon to produce CO. High-vacuum conditions can change the kinetics of these reactions, making them occur faster or at lower temperatures. Conversely, nitrides and noble metals (such as Pt and Ir) are stable in the presence of carbon at high temperature. Therefore, a major consideration in the design of the primary shield ceramic coatings is characterizing and controlling high-temperature/vacuum interactions between the carbon substrate and the coating material.

At NASA GRC, two vacuum thermogravimetric tests were conducted with PBN coating on C-C and two tests with alumina coating on C-C. Data from both tests of PBN on C-C showed no evidence of mass loss until 1950 K (sample 1 showed no evidence of significant mass loss up to 2020 K), as shown in Figure 5-17. The data suggest lack of significant chemical interactions between C-C and PBN, also predicted by FactSage modeling of the BN in contact with carbon (PBN was not available in the software database). The FactSage analysis program models chemical interactions between materials at high temperatures. This activity is part of a collaborative effort with NASA GRC to characterize the thermal stability of primary shield candidate materials. FactSage results predicted nitrogen dissociation as the primary means of mass loss, with minimal formation of boron carbides, which is the same mass loss mechanism as for PBN alone.

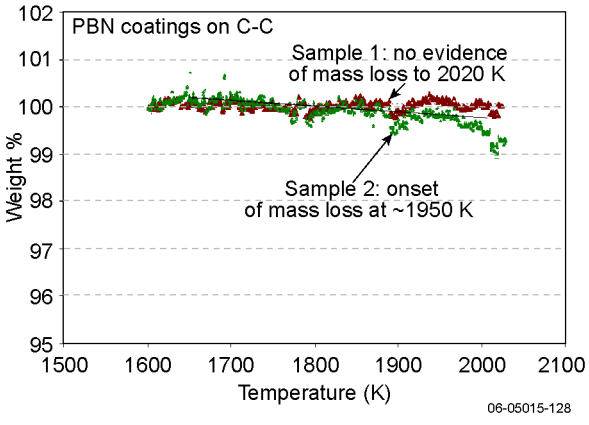

Figure 5-17. TGA results for PBN-coated C-C.

PBN surface layers and the PBN/C-C interface also need to be investigated further. PBN is known to decomposes via the reaction BN(s) = B(s) + $1/2N_2$(g). Loss of N_2 will result in a high rate of mass loss from the outer surface of the BN layer and the formation of a B-rich layer (the effect on optical properties must be considered). This mechanism of mass loss does not appear to be significant at the predicted equilibrium temperature of the primary shield at 4 R_S. Also, a continuous B-rich layer on the surface of the BN coating could be beneficial in reducing the rate of further N_2(g) loss by acting as a diffusion barrier for N transport to the vacuum. Any short-circuit paths through the BN coating will allow N_2 to be lost from the PBN/C-C interface and cause the activity of B, a(B), to increase. While the B-N-C system does not contain any ternary compounds, any increase in a(B) will result in the formation of B_4C at the PBN/C-C interface. This scenario is unlikely, because PBN is a pore-free coating and thus would allow no path from the C-C/PBN interface to deep space. The thermal stability concerns of PBN/C-C are not great, but the stability and vaporization behavior of these interfaces need to be better understood.

Alumina on C-C showed no evidence of mass loss until ~1650 K; at that point, immediate reaction with carbon caused measurable mass loss, as shown in Figure 5-18. Carbon reduces alumina at elevated temperatures by carbothermal reduction (via Al_2O_3(s) + 5/2C(s) = Al(g) + $1/2Al_2O$(g) + 5/2CO(g)). The Al_2O_3/C interface most likely does not form binary or ternary compounds (Al_4C_3, Al_2OC, and Al_4O_4C have been identified as existing in the Al-C-O system) at the interface for temperatures below 2000 K. However, the low $p(O_2)$ ($<10^{-20}$ atm at 1650 K) of the {Al_2O_3 + C} interface equilibrium under vacuum represents a significant problem. Under these reducing or low $p(O_2)$ conditions, the vapor pressures of CO(g), Al(g), and Al_2O(g) are all greater than 10^{-6} atm at 1650 K. Therefore, while the vaporization behavior of Al_2O_3, under oxidizing or high $p(O_2)$

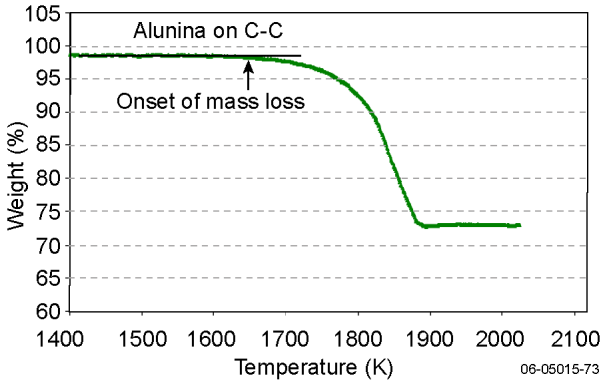

Figure 5-18. Alumina-coated C-C high-vacuum TGA results from NASA GRC.

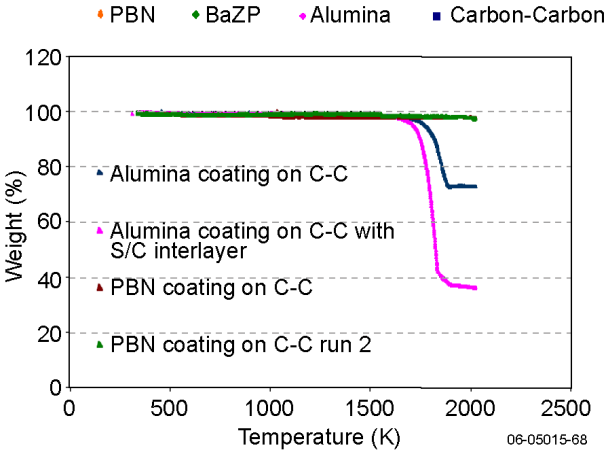

Figure 5-20. TGA mass loss of primary shield coatings on C-C from NASA GRC.

conditions (i.e., the outer surface of an Al_2O_3 layer in a vacuum), is acceptable for $T < 2000$ K, the Al_2O_3/C interface will degrade rapidly if there are any short-circuit paths (cracks, pores, or grain boundaries through the Al_2O_3 layer) that allow the "high-pressure" {CO(g) + Al(g) + Al_2O(g)} vapor to reach the vacuum.

This degradation of the interface results in oxidized ("charred") C-C with a delaminated Al_2O_3 coating. Figure 5-19 shows a C-C/alumina coupon that became debonded as a result of a ramp to 2000 K. The formation of a ternary compound at the Al_2O_3/C interface could improve this situation by reducing $a(Al_2O_3)$ and a(C), which will in turn reduce p(CO), p(Al), and $p(Al_2O)$. Unfortunately, testing indicates that significant degradation occurs before binary or ternary compounds are formed. FactSage modeling of carbon in contact with alumina was performed at NASA GRC and confirms high vapor pressures of CO starting at 1650 K due to carbothermal reduction of alumina.

In Figure 5-20, the stability of the PBN-coated C-C is evident beyond 1850 K. Conversely, the alumina-coated C-C shows instability starting at approximately 1650 K when a stable interlayer is not present. Experimental investigations are ongoing to identify interlayer options that will stabilize the interface and not degrade optical properties.

As described in Chapter 4, alumina and C-C can be separated by depositing thin interlayers of stable materials such as refractory metals, nitrides, carbides, oxides, or a combination thereof. A C-C/alumina sample with a SiC interlayer was tested to investigate the difference between alumina in contact with carbon and alumina in contact with a high-temperature carbide. SiC was chosen because it is traditionally used as a protective interlayer in high-temperature, oxidizing applications. This coupon also experienced mass loss starting at approximately 1650 K, as shown in Figure 5-21. FactSage modeling also was performed to study the C-C/SiC/alumina system with similar results; the vapor pressures of CO (3.5×10^{-5} atm), SiC (3.5×10^{-5} atm), Al (2.5×10^{-5} atm), and Al_2O (1.6×10^{-5} atm) were again high, starting at 1650 K. The activity of carbon for a SiC coating on C-C is similar to that for C-C alone, so the same interactions with alumina occur.

Four additional examples of tested coupons with barrier layers between C-C and alumina are pictured in Figure 5-22. The first sample was covered with 4-μm-thick platinum (Pt) followed by a top coat of alumina. The second

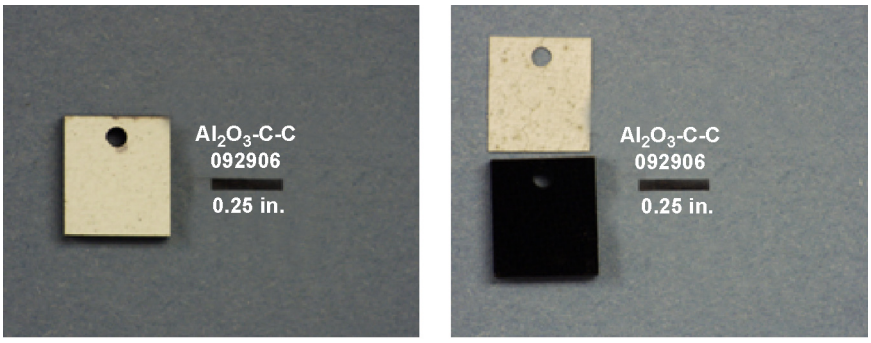

Figure 5-19. Alumina-coated C-C tested under high vacuum to 2000 K.

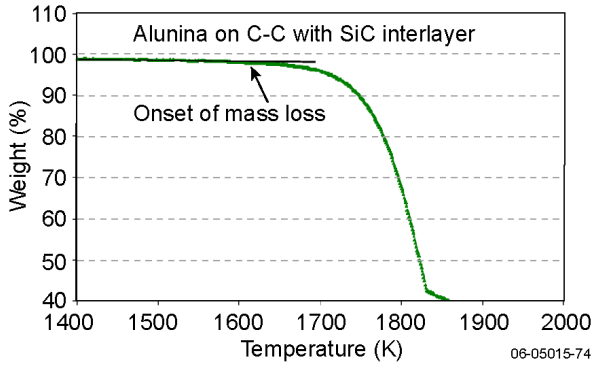

Figure 5-21. Alumina-coated C-C with SiC interlayer high-vacuum TGA results from NASA GRC.

Table 5-5. Mass loss testing of C-C/alumina with and without interlayers.

Material Combination	% Weight Loss at 1750 K	% Weight Loss at 1850 K
C-C/alumina	1.97	2.04
C-C/Pt/alumina	0.12	0.23
C-C/Ta/alumina	—	2.30
C-C/TaN/alumina	0.13	0.24
C-C/Zirconia/ alumina	—	3.30

and third samples, 3-μm-thick layers of tantalum (Ta) and tantalum nitride (TaN) were applied followed by a topcoat of alumina. The last sample pictured is a zirconia interlayer between C-C and the alumina topcoat, where the zirconia powder contains small weigh % additives of ceria and yttria to further stabilize the zirconia at elevated temperatures.

These coupons were tested thermally in an APL high-temperature furnace under nitrogen purge at 1750 and 1850 K. Mass loss was greatly reduced by the addition of Pt or TaN interlayers, while samples with pure Ta or zirconia had mass losses similar to C-C/alumina with no interlayer (see Table 5-5). The suspected mechanism for mass loss with Ta was the formation of a carbide at the C-C/interlayer interface. Platinum does not form a carbide and Ta converted to TaN appears to be more stable than Ta alone, resisting strong carbide formation through the interlayer thickness. Examination of the tested zirconia coupons indicated carbothermal reduction of the zirconia interlayer in contact with C-C. It is believed that a zirconium carbide conversion layer on the outer surface of the C-C would prevent this from occurring. No interaction between the zirconia and the alumina was detected.

The test data from the APL and GRC testing are summarized in Table 5-6, and both the mass loss estimate and the test environment are given. The inert and 10^{-2} torr vacuum environments refer to APL test data. The high-vacuum data refer to GRC testing. The data show that the mass loss values for PBN-coated C-C are consistent for the different tests and are well below the required value at the design primary shield temperature (1850 K). The similarities in the test data between the different test methods suggest that the approach is reasonable. The variations in the data suggest that more testing is required to obtain accurate values in the 1600 to 2000 K range.

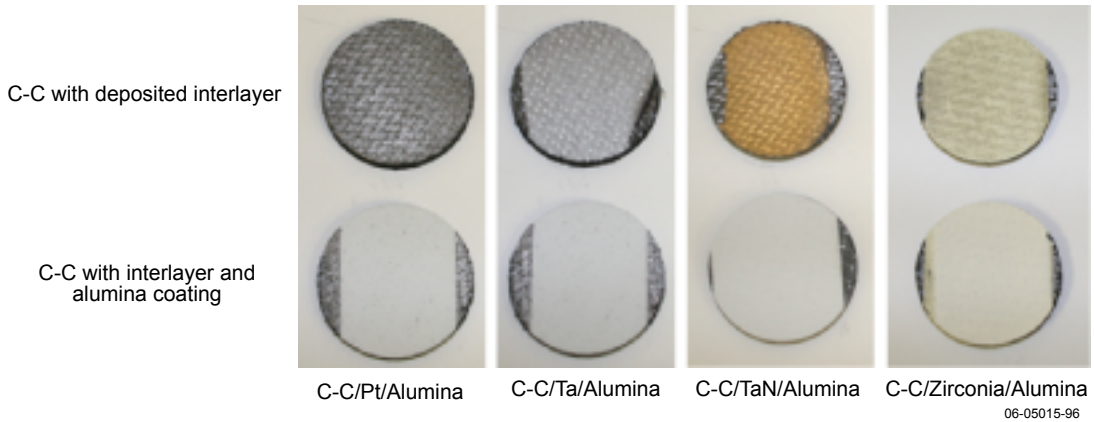

Figure 5-22. High-temperature interlayers incorporated between C-C and alumina.

Table 5-6. Summary of results from mass loss testing.

Material	Temperature (K)							
	1650		1850		2050		2250	
Alumina/C-C	Minimal mass loss to 1650 K, alumina/C-C unstable above 1650 K*							
Alumina/SiC/C-C	Minimal mass loss to 1630 K, alumina/SiC/C-C unstable above 1650 K*							
PBN/C-C	Inert	NT*	Inert	NT	Inert	NT	Inert	NT
	10^{-2} torr	0.0 mg/s	10^{-2} torr	0.1 mg/s	10^{-2} torr	1.3 mg/s	10^{-2} torr	NT
	10^{-7} torr	0.0 mg/s*	10^{-7} torr	0.0 mg/s*	10^{-7} torr	8.3 mg/s*	10^{-7} torr	NT

*NT = not tested; best estimate of mass loss rate using curve fits of TGA data. Long-term holds at temperature needed to obtain mass loss rates of higher accuracy.

5.3 Mass Loss Due to Radiation Effects

The Solar and Jovian radiation environments are a combination of low- and high-energy plasmas. These plasmas consist of electrons, protons, neutrons, and ions such as H^+ and He^+. For the notional mission trajectory, the radiation environments are summarized in Table 5-7. The Jovian environment is dominated by high- and low-energy electrons; conversely, the near solar environment is dominated by high- and low-energy protons. Testing has utilized a combination of radiation test facilities to envelop the actual mission environments.

Radiation effects are a function of temperature and radiation dose. They include physical sputtering, chemical erosion, and radiation-enhanced sublimation. Physical sputtering is spallation of material due to energetic impacts; thus it is applicable to both ceramics and carbon. In this event, the kinetic energy of target atoms is greater than the surface binding energy of the target material. Excessive spallation can dramatically affect mass loss rate. Radiation-enhanced sublimation occurs when interstitial carbon atoms created during the physical sputtering event diffuse along damage sites, reach the surface, and then are thermally desorbed. Chemical erosion occurs when implanted H^+ reacts with carbon atoms, forming methane, which then is thermally desorbed or released by incident ions. Both the sublimation and erosion events are inherent to only carbon-based materials—in this case C-C.

Prior investigations performed by JPL[3] considered all of the radiation effects on a C-C primary shield with no protective coating. In this study, JPL considered worst-case solar wind radiation consisting of H^+ and He^+ ions and a broad range

[3]Sokolowski, et al., Erosion of carbon/carbon by solar wind charged particle radiation during a Solar Probe Mission, In *AIAA/ASME/ASCE/AHS/ASC Structures, Structural Dynamics, and Materials Conference,* 32nd, Baltimore, MD, Technical Papers. Pt. 1 (A91-31826 12-39). Washington, DC, American Institute of Aeronautics and Astronautics, AIAA-1991-979, p. 73-79 (1991).

Table 5-7. Radiation environments for notional mission trajectory.

	Near Sun		Deep Space		Jupiter 12 R_J		Jupiter 12 R_J		
	4 R_S	0.3 AU	2.5 AU	5.0 AU	12 R_J Outside (Double Maxwellian)		12 R_J Outside (Double Maxwellian)		12 R_J Below
p+ (m^{-3})	10^{11}	3.50×10^7	7.00×10^6		6.00×10^5	1.30×10^6	4.00×10^6	2.00×10^6	4.00×10^6
e− (m^{-3})	10^{11}	3.50×10^7			2.00×10^5	1.20×10^6	3.00×10^7	2.00×10^6	3.00×10^7
Te− (eV)	100	29	15		200	2.80×10^4	130	2.00×10^4	130
Tp+ (ev)	100	75	965.3		400	2.75×10^4	32	2.00×10^4	32
Photons	7.34×10^{21}	EUV does not apply past 4 R_S for our design purposes							
λ ($\nu\mu$)	2.5–200								
T_{PS} (K)	2100	460	<100		<100		<100		<100
(C)	1827	187	−173		−173		−173		−173
Debye length (m)	1.66×10^{-1}	5.748977	10.8		1.11×10^2	7.68×10^2	6.88	5.26×10^2	6.88

of temperatures, from <600 K, to 600–1200 K, to >1200 K. By using empirical relations developed by the nuclear industry for plasma-facing carbon materials, analysis results indicated that predicted mass loss for these combined conditions was 0.03 mg/s. APL confirmed these findings by performing a series of calculations where estimated mass loss levels due to thermal radiation effects were negligible. Additionally, JPL also concluded that thermal vaporization is the dominant mass loss mechanism for carbon-based materials in the near solar environment. These radiation effects are even less likely to affect mass loss with the current TPS design, as carbon no longer faces plasma because a ceramic coating has been added.

5.3.1 High-Energy Proton Irradiation (IUCF)

At the Indiana University Cyclotron Facility (IUCF), beam radiation testing was conducted to evaluate the response of the candidate primary shield materials to high-energy protons (>50 MeV), as summarized in Table 5-8. These tests were conducted in an ambient environment at room temperature as shown in Figure 5-23. No mass measurements were taken before or after the test; however, no visual surface damage was noted for C-C, pyrolytic graphite, Al_2O_3, PBN, or BaZP as shown in Figure 5-24, thus qualitatively indicating minimal mass loss. Additional testing is planned to get more quantitative results and to investigate temperature and vacuum effects.

5.3.2 Mid-Energy Proton and Electron Irradiation (NASA GSFC)

At NASA Goddard Space Flight Center (GSFC), beam radiation testing was conducted to evaluate the response of the candidate primary shield materials to mid-energy (~150 keV) protons and

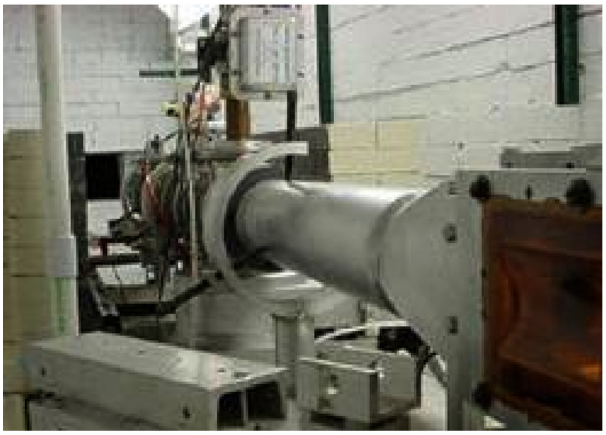

IUCF: View along beamline

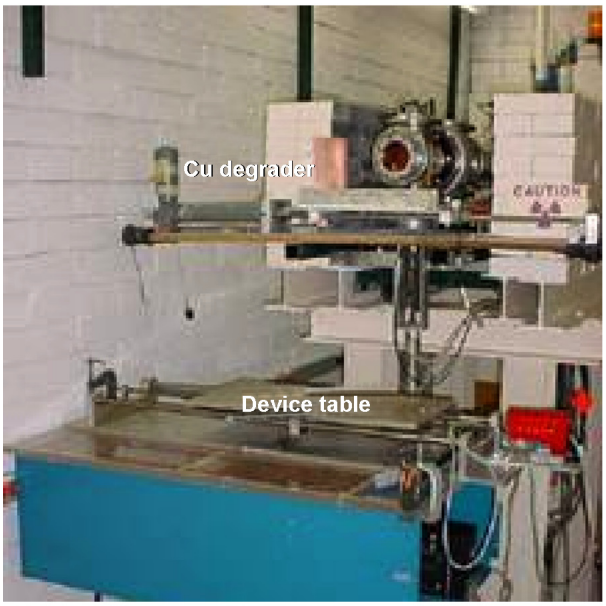

IUCF: End of beamline

06-05015-130

Figure 5-23. Proton testing at the Indiana University Cyclotron Facility.

Table 5-8. Summary of high-energy proton irradiation tests conducted at IUCF.

Run	Proton Energy (MeV)	Trays	Vacuum (mtorr)	Fluence #/cm^2	Simulation
1	54.7	1, 4	60	8.50×10^{10}	
2	73.7	2, 4	80	3.80×10^{10}	12 Events
3	104.2	3, 4	80	2.00×10^{10}	
4	104.2	5	80	1.84×10^{13}	Single event near Sun ($1/r^2$)
	73.7	5	60	7.98×10^{12}	
	54.7	5	60	4.20×10^{12}	

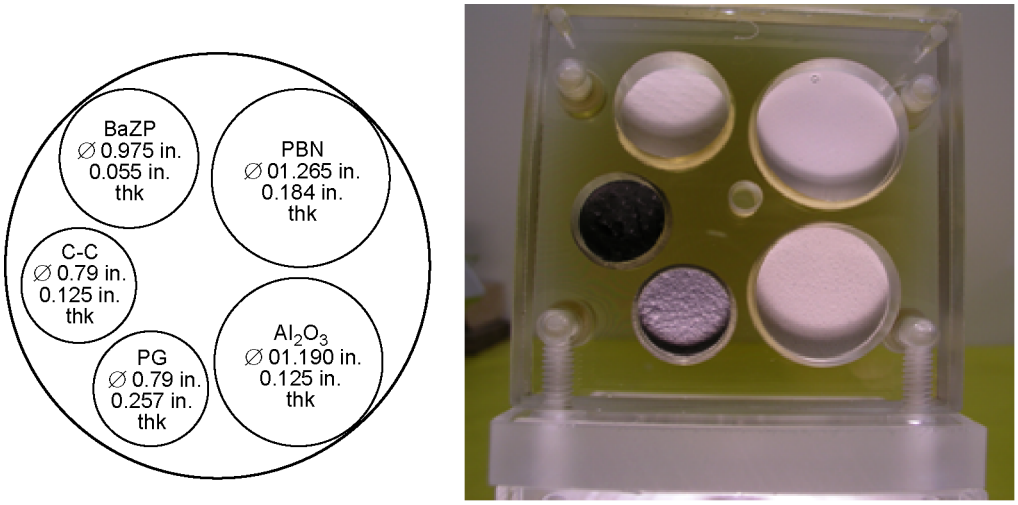

Figure 5-24. Visual test results from IUCF proton testing.

electrons. These tests were conducted in a vacuum environment (10^{-5} torr) at room temperature, as shown in Figure 5-25. Mass measurements were taken pre- and post-irradiation, and visual inspections were conducted (Figure 5-26). Measured mass loss was negligible for C-C and for the composite coupons featuring the ceramic coatings on C-C, as shown in Table 5-9, for both the protons and electrons.

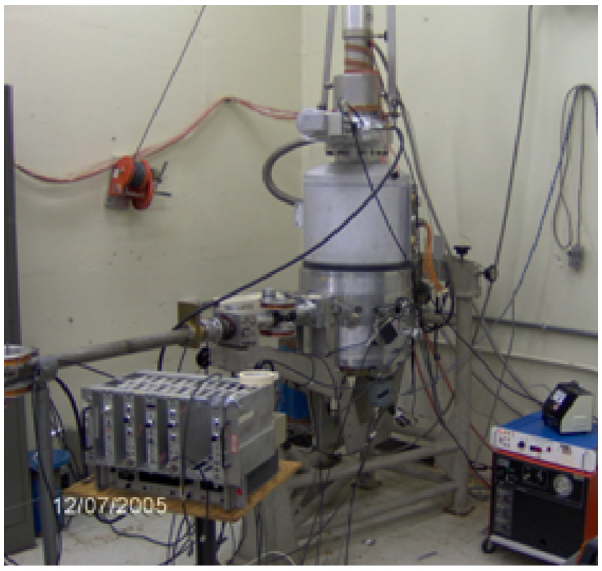

Figure 5-25. Radiation test equipment at NASA's Goddard Space Flight Center.

5.3.3 Low-Energy Plasma Irradiation (PUPR)

At the Polytechnic University of Puerto Rico (PUPR), plasma radiation testing was conducted to evaluate the response of the candidate primary shield materials to low-energy hydrogen plasma (~100 eV) consisting of protons and electrons. These tests were conducted in a vacuum environment (10^{-4} torr) at room temperature, as shown in Figure 5-27. The plasma levels were configured to represent various combinations of solar and Jovian environments, including a 2-solar-pass mission. Mass measurements were taken pre- and post-irradiation, and visual inspections conducted (Figure 5-28). Measured mass loss was negligible for C-C and for the composite coupons featuring the ceramic coatings on C-C, as shown in Table 5-10, for both the protons and electrons.

The lack of measurable mass loss or visual damage resulting from the combinations of radiation confirms that the ceramics and C-C are inherently robust in the Solar and Jovian environ-

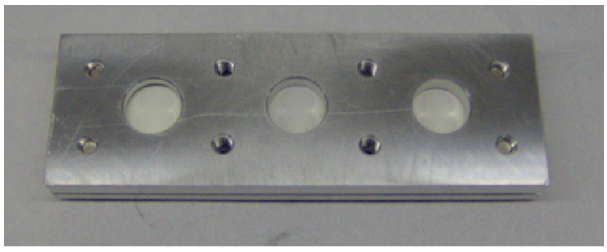

Figure 5-26. Test coupons after irradiation at NASA GSFC.

Table 5-9. Mass loss during NASA GSFC beam radiation testing.

Sample	Radiation Exposure	Pre-Radiation Exposure Weight (g)	Post-Radiation Exposure Weight (g)	% Weight Loss
C-C #1	150 keV electrons, 10^{15} p/cm^2	1.5642	1.5638	0.026
C-C #2	150 keV protons, 10^{15} p/cm^2	1.6431	1.6436	–0.030
C-C/A^{2}O^3 #1	150 keV electrons, 10^{15} p/cm^2	1.3082	1.308	0.015
C-C/A^{2}O^3 #2	150 keV protons, 10^{15} p/cm^2	1.3987	1.3982	0.036
C-C/PBN #1	150 keV electrons, 10^{15} p/cm^2	6.2627	6.263	–0.0048
C-C/PBN #2	150 keV protons, 10^{15} p/cm^2	6.485	6.4846	0.0062
C-C/BaZP #1	150 keV electrons, 10^{15} p/cm^2	1.118	1.1184	–0.036
C-C/BaZp #2	150 keV protons, 10^{15} p/cm^2	1.285	1.2843	0.054

ments. Additional elevated-temperature radiation testing is necessary to accurately predict mass loss rates. In addition to mass loss measurements, scanning electron microscope (SEM) images can be taken to investigate potential changes to the surface morphology.

PUPR plasma MC machine

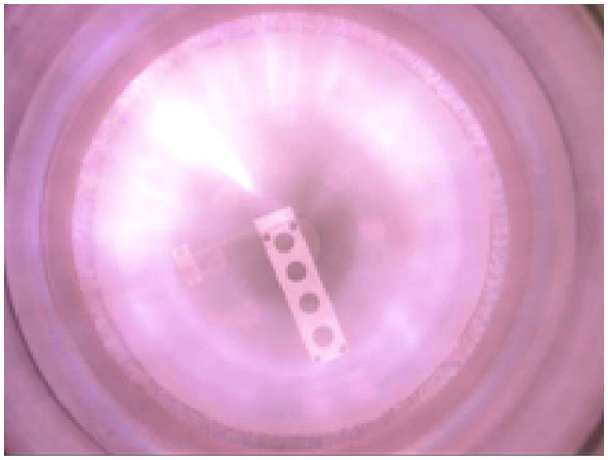

Hydrogen plasma with electrons and protons

06-05015-75

Figure 5-27. Radiation test facility at the Polytechnic University of Puerto Rico.

5.4 Mass Loss Due to Particle Impact

High-speed particulates are predicted to impact the Solar Probe spacecraft throughout the mission. These silica-based particles will range in size from submicrometer scale to tens of micrometers and will have consistencies ranging from solid to molten, depending on the location in the trajectory. It is estimated that the number of collisions is a function of the size of the particle, as shown in Table 5-11. The net impact velocity is predicted to be in excess of 450 km/s.

Currently, no test facility exists that can test the response of the primary shield to representative impact conditions. Shown in Figure 5-29 is a

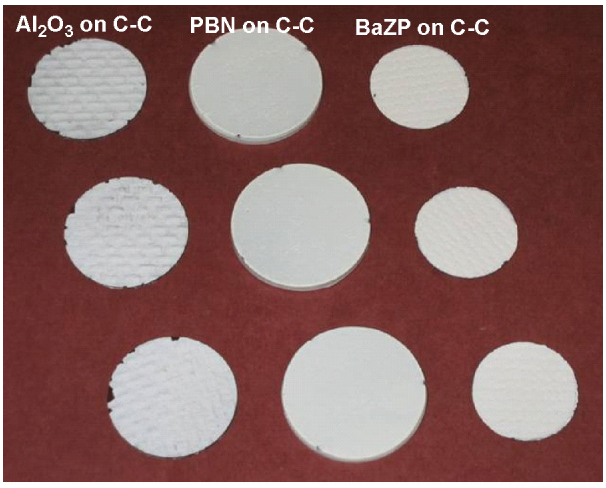

06-05015-133

Figure 5-28. Post-test irradiated coupons from tests at PUPR.

Table 5-10. Mass loss during PUPR radiation plasma exposures.

Sample	Radiation Exposure	Pre-Plasma Exposure Weight (g)	Post-Plasma Exposure Weight (g)	% Weight Loss
C-C #1	2 × solar + Jupiter	2.8467	2.8466	0.0035
C-C #2	Solar only	2.8422	2.8414	0.028
C-C #3	Jupiter only	2.8449	2.8445	0.014
C-C/A_2O_3 #1	2 × solar + Jupiter	1.2952	1.2948	0.031
C-C/A_2O_3 #2	Solar only	1.3851	1.3845	0.043
C-C/A_2O_3 #3	Jupiter only	1.2635	1.2632	0.024
C-C/PBN panel 5	2 × solar + Jupiter	3.9822	3.9835	–0.033
C-C/PBN panel 6	Solar only	4.2175	4.2185	–0.024
C-CPBN panel 9		4.4574	4.4582	–0.018
C-C/BaZP tray 2	Solar only	1.1272	1.1268	0.035
C-C/BaZP tray 3	Jupiter only	1.1082	1.1089	–0.063
C-C/BaZP Goddard electron	2 × solar + Jupiter	1.0867	1.0873	–0.055

summary of test facilities that are typically used throughout the Department of Defense and NASA. None of these facilities can provide the required combination of particle size and velocity. The shortfall for each of these test facilities is the appropriate match of kinetic energy and momentum.

Consequently, initial evaluations have focused on assessing the impact of particles on the functionality of the primary shield as a thermal protection system. System-level trade studies were performed to evaluate the effects of localized spallations on the primary shield equilibrium temperature. A finite element thermal model of a single impact location was developed and parametric studies were conducted to rank the effects of hole diameter, radius of spall zone, thermal conductivity of the substrate, and α/ε ratio of the primary shield. The results revealed that any significant temperature increase would be limited to the immediate region of the damage (where the optical surface has been removed and α/ε is that of the underlying C-C substrate, that is,

Table 5-11. Size distribution of solar wind particles.

Particle Diameter, μm	Expected Hits
1	33
5	29
10	25
50	7
100	2
150	<1
200	<1

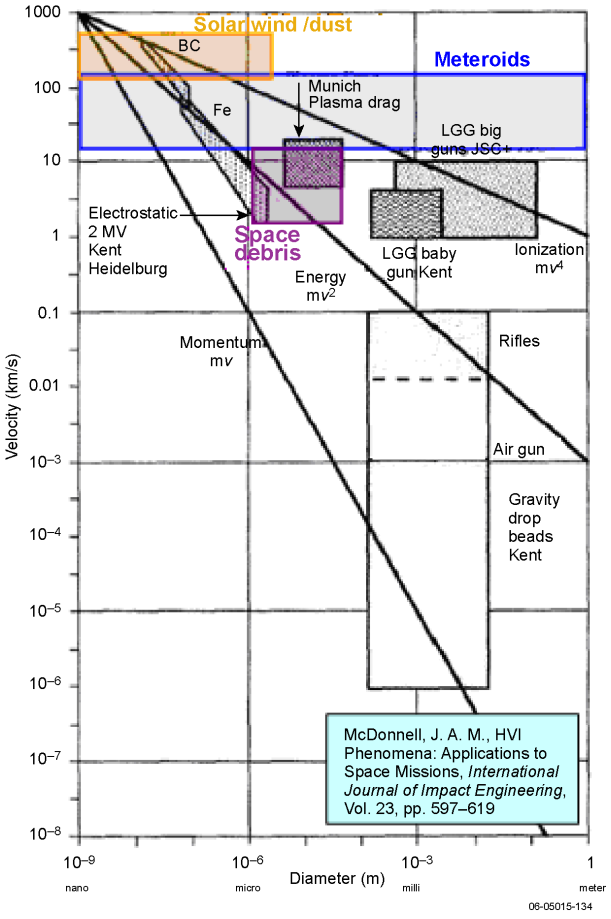

Figure 5-29. Limitation of high-speed impact test facilities.

$\alpha/\varepsilon \sim 1$). Because the (uncoated) C-C interior surfaces have high IR emissivity and the thermal radiation "view factor" between the interior surfaces is unity, radiation heat transfer between the damaged and undamaged sides of the heat shield serves to restrict any temperature increase to a small region around the damaged area.

After characterizing the local temperature change due to damage, the effect of damage on system thermal performance was parametrically evaluated by varying the total damage to the optical surface and calculating the resulting average equilibrium temperature of the primary shield, as shown in Figure 5-30. Damaged areas were treated as local hot spots (with elevated temperature), while undamaged areas remained cooler. An area-weighted average temperature then was calculated for the shield as a function of damaged area. The results reveal the robustness of the design. Over 20% of the primary shield would need to be damaged to increase the shield temperature by 100 K. Separate studies performed by Dr. Cesar Carrasco (of the University of Texas, El Paso) predicted primary shield damage level (due to estimated solar dust fluence, comprising a distribution of molten and solid silicon particles of micrometer to submicrometer size) is much less than 0.1%, thus indicating that no significant temperature increase is expected.

Mass loss due to particle impact is not expected to be a significant component of the total mass loss rate. Future work will investigate the impact footprint characteristics based on particle size, the internal and external spreading of the spallation plume, and the interaction of the external plume with the spacecraft.

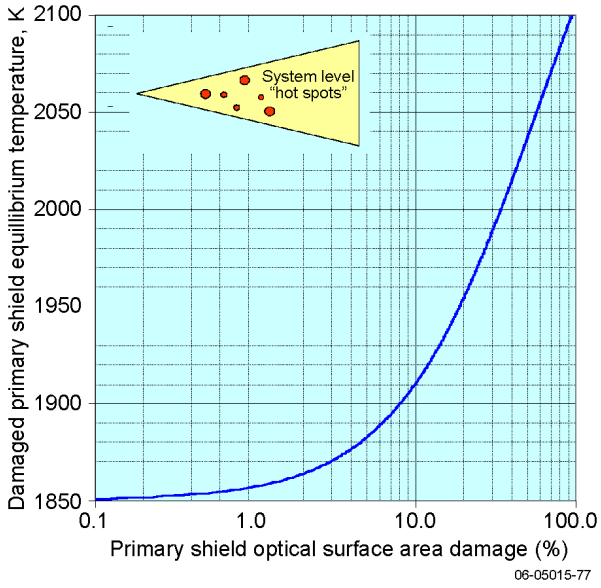

Figure 5-30. Relationship between damage area and equilibrium temperature.

5.5 Conclusions and Continuing Work

Estimates were made showing that the Solar Probe TPS is below the present mass loss requirement over all mission phases. Temperature, vacuum, and radiation effects have been characterized both analytically and by testing where possible. Thermal vaporization of the TPS materials is the dominant mass loss mechanism during the period around closest approach to the Sun. Predicted mass loss is a maximum of about 1 mg/s at closest approach and drops by an order of magnitude within 2 days on either side.

5.5.1 Specific Findings

- Outgassing:
  - Outgassing is a low-temperature phenomenon. The associated mass loss will occur early in the mission.
- Thermal vaporization:
  - Onset of mass loss for C-C, PBN, alumina, and PBN/C-C occurs at temperatures above the predicted steady-state temperature of the primary shield at closest solar approach.
    - Thermal vaporization of C-C is negligible at 1850 K.
    - Thermal vaporization of alumina and PBN is below the 2.5 mg/s budget at 1850 K.
    - BaZP is the least thermally stable ceramic coating being considered, showing signs of mass loss starting at ~1500 K. Optical properties must be investigated further before BaZP is eliminated as a coating option.
- Analytical predictions support the results of materials testing.
- Chemical interactions:
  - PBN is thermally stable both individually and as a coating on C-C.
  - C-C and alumina interact (carbothermal reduction of alumina) at temperatures above 1650 K. C-C/alumina interactions have been suppressed by using refractory interlayers to 1850 K.

- Radiation effects:
  - A prior JPL study showed that radiation effects are negligible; the predicted high-temperature radiation-induced mass loss rate is very low, 0.03 mg/s.
  - Radiation testing of sample coupons in a variety of high- and low-energy environments has supported that result; ambient-temperature radiation mass loss is negligible.
  - Materials have not degraded during aggressive beam and plasma radiation testing.

5.5.2 Continued Coatings Work and High-Temperature Testing and Analysis

Mass loss test data have been taken for all the candidate materials over all the expected mission environments. Test data accuracy is a function of the sample size and test duration. Test data indicate that the present accuracy for the best measurements taken is between 0.1 and 1.0 mg/s of total mass loss rate. The test program has identified the test methods and durations required to obtain more accurate results.

Further thermal vaporization testing is planned at APL and GRC, focusing on the critical temperature ranges for each of the materials. The testing includes extending the hot-soak condition from 4 to 40 hours and including more samples to allow statistical information to be gathered. High-temperature radiation effects also will be investigated.

Analytical efforts will focus on the interactions among the spacecraft, the local environment, and the mass loss plumes. The applicability of modeling techniques such as Direct Simulation Monte Carlo (DSMC) in the specific solar environment will be investigated. Methods to account for the tracking and ionization of particles will be assessed.

6 Charging

6.1 Background

Charging and radiation effects on ceramic coatings for the Solar Probe Thermal Protection System (TPS) have been and continue to be studied. These investigations have been structured to develop a fundamental understanding of the charging characteristics of candidate materials as well as the spacecraft's response in the near-Sun, Jovian, and deep-space environments. Charging is typically expressed in terms of surface voltage potential and is evaluated for both potential gradients and magnitudes. The spacecraft design process generally includes an assessment of the impact of such potentials on the functionality of electronics, sensors, and instruments. While these are indeed critical design parameters for Solar Probe, the interaction of the spacecraft with charged particles in the near-solar environment also must be considered from the perspective of science collection.

Spacecraft charging is an equilibrium process (Figure 6-1) in which the current into the spacecraft (in the form of incident ions and electrons) balances the current out of the spacecraft (due to photoemission, secondary electron emission, and backscattered electrons), such that a potential develops relative to the surrounding plasma "ground." Absolute charging develops when the entire spacecraft charges to the same uniform potential, and differential charging develops when different parts of the spacecraft charge to different potentials. This effect can be envisioned using the following scenario: one portion of the spacecraft is exposed to the Sun and experiences photoemission (photons in, electrons out), leading to a net positive charge, while another portion of the spacecraft is shaded. If these two spacecraft regions are not well grounded, differential charging will develop. The focus during the Risk Mitigation Study was to understand whether differential or absolute charging would develop, and to estimate the voltage potentials to which the spacecraft could charge, given its material properties and the radiation environments it will experience.

Surface charging potentials—both magnitudes and gradients—need to be controlled in order to minimize disruption to the spacecraft's functionality. This includes both the impact on spacecraft electronics due to arcing and the problem of contamination of sensitive science data collection. Charging may cause measurement contamination by disrupting instrument function and by disturbing the local environment. The specific levels of acceptable voltage potential for each of these cases is still under review; however, historical trends indicate that this number should be as low as possible, i.e., in the low hundreds of volts for electronics and the low tens of volts for science instruments.

Conventional materials used for thermal protection of spacecraft are also conductive, thereby preventing the buildup of charge. The extremely high temperatures that Solar Probe will encounter during solar approach require the use of refractory ceramic materials as a component of the passive thermal management system. Since ceramics are typically electrically insulating and therefore tend to collect surface charge, special attention has been devoted to understanding how their electronic properties vary at selected points along the Solar Probe trajectory and how their interaction with the radiation environment could potentially affect the overall spacecraft charging.

A sophisticated charging analysis program called NASCAP-2K was developed by Science Applications International Corporation (SAIC) and NASA for the purpose of modeling such potentials. This program is commonly used for charging analysis, since no other program rivals its usefulness and comprehensiveness in this field. The team used NASCAP-2K to assess the expected charging of the spacecraft in the spacecraft's anticipated radiation environments. A number of factors complicate the analysis (Figure 6-2). The NASCAP solver

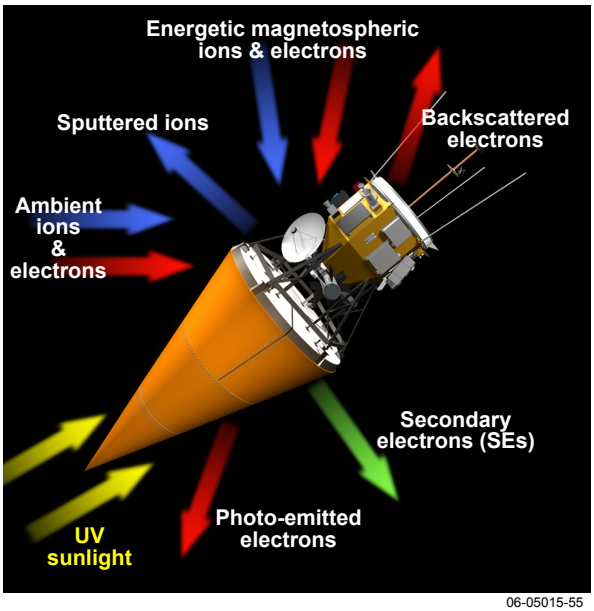

Figure 6-1. The major processes impacting spacecraft charging.

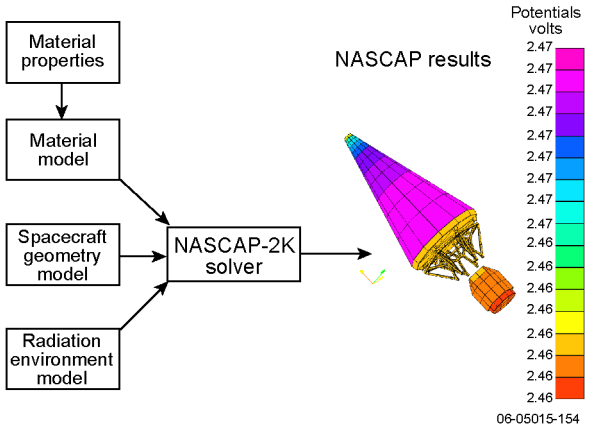

Figure 6-2. The factors influencing the fidelity of spacecraft charging predictions.

requires three types of inputs: material properties of the spacecraft components, the geometry of the spacecraft, and the radiation environment to which the spacecraft is subject.[1] Solar Probe charging investigations have been directed toward improving the accuracy of the inputs to the NASCAP solver in order to increase the fidelity of the predictions.

[1]Davies, V. A., B. M. Gardner, M. J. Mandell, and I. G. Mikellides, *NASCAP-2K Version 3.1 User's Manual,* Report no. SAIC 02/2047-R1 (July 2005).

6.2 Radiation Environments

The team assessed the performance of thin ceramic surfaces in multiple environments (Figure 6-3). The spacecraft will spend about 28 days in close proximity to the Sun, during which the resulting higher temperatures of the TPS will decrease the coating's volume resistivity such that it will become essentially conductive. The remaining 7 to 8 years will be spent in the Jovian and deep-space environments. In the Jovian environment, both electrons and ions will be present, but charging will be dominated by electron processes, including electron bombardment (which causes negative charging), secondary electron emission (which causes positive charging), and photoelectron emission (also positive).

The radiation environment parameters used for our NASCAP simulations are given in Table 6-1, and Figure 6-4 shows the radiation environment window within NASCAP-2K. The radiation environments that Solar Probe will experience are not very well understood; these estimates were made with the assistance of Dr. Ed Sittler at NASA Goddard Space Flight Center (GSFC).

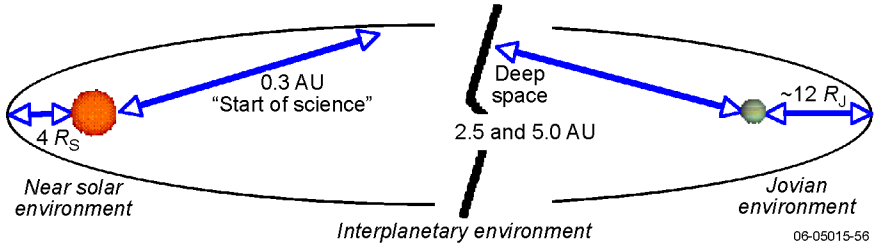

Figure 6-3. Radiation environments considered in evaluating spacecraft charging.

Table 6-1. Radiation environment parameters used in NASCAP-2K.

Parameter	Near Sun		Deep Space		Jupiter 12 R_J	
	4 R_S	0.3 AU	2.5 AU	5.0 AU	12 R_J (Double Maxwellian)	
Ion number density (m^{-3})	10^{11}	3.5×10^7	7.0×10^6	7.0×10^6	6.0×10^5	1.3×10^6
Electron number density (m^{-3})	10^{11}	3.5×10^7	7.0×10^6	7.0×10^6	2.0×10^5	1.2×10^6
Electron temperature (eV)	100	29	15	15	200	2.8×10^4
Ion temperature (eV)	100	75	965.3	965.3	400	2.75×10^4
EUV photons	7.34×10^{21}	Extreme ultraviolet does not apply past 4 R_S for our design purposes				
Wavelength range (nm)	2.5–200					
Primary shield temperature (K)	2100	460	<100	<100	<100	
Solar intensity (number of Suns)	2887	11.1	0.16	0.04	0.033	

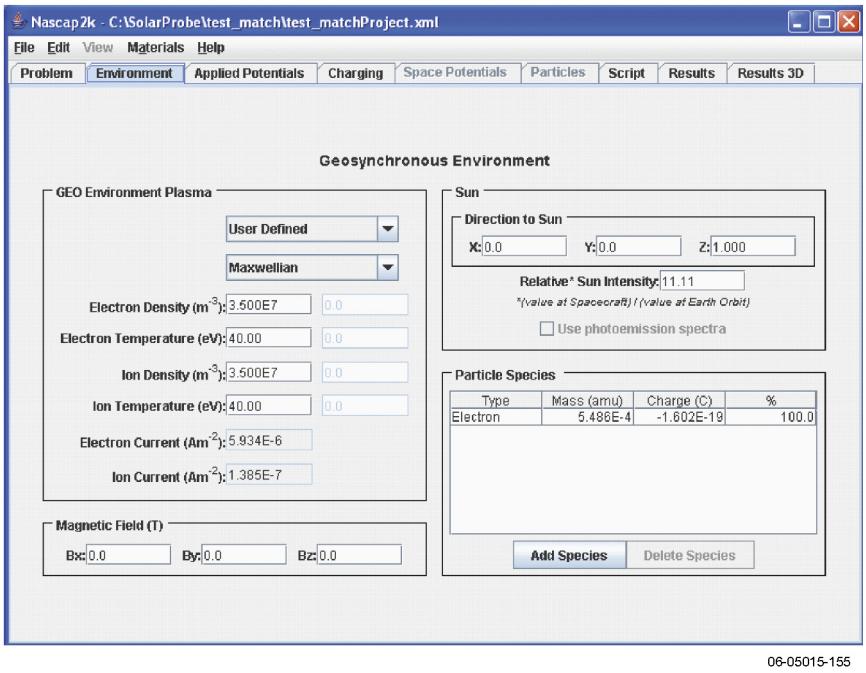

06-05015-155

Figure 6-4. The NASCAP radiation environment definition window.

It should be noted that the charging code treats the model in a manner that considers all components to be electrically connected, regardless of whether they are attached physically. Even though the spacecraft bus appears to be floating when viewing the model, it is evaluated by NASCAP-2K as being electrically connected to all the other components. By allowing quicker solution times, this simplistic model is useful both for evaluating several different materials at numerous trajectory points and for evaluating the sensitivity to spacecraft charging of the environmental variables at these trajectory points.

3.3 Spacecraft Geometry

A simplified model of the solar probe spacecraft was created using the NASCAP-2K Object Toolkit (Figure 6-5) to access the distribution of charging at different environments along the spacecraft's trajectory. Model geometry is one of the three main inputs that the charging code requires. The software's algorithm accounts for the model surface area and for the relative position of the various components when the charging solution is computed. The simplified model was crafted primarily to accurately model the surface areas of the three major spacecraft components: the primary shield, the secondary shield, and the spacecraft bus. Additionally, the heat shield system support truss was added to enhance the visual realism of the model. The truss is accurately modeled for both physical dimensions and surface area but does not contribute appreciably to overall charging results.

6.4 Materials Overview

The baseline for coating the Solar Probe primary shield is a thin (nominal thickness of 0.005 in.) coating of alumina (Al_2O_3) on a carbon–carbon (C-C) composite. Two other coating materials also

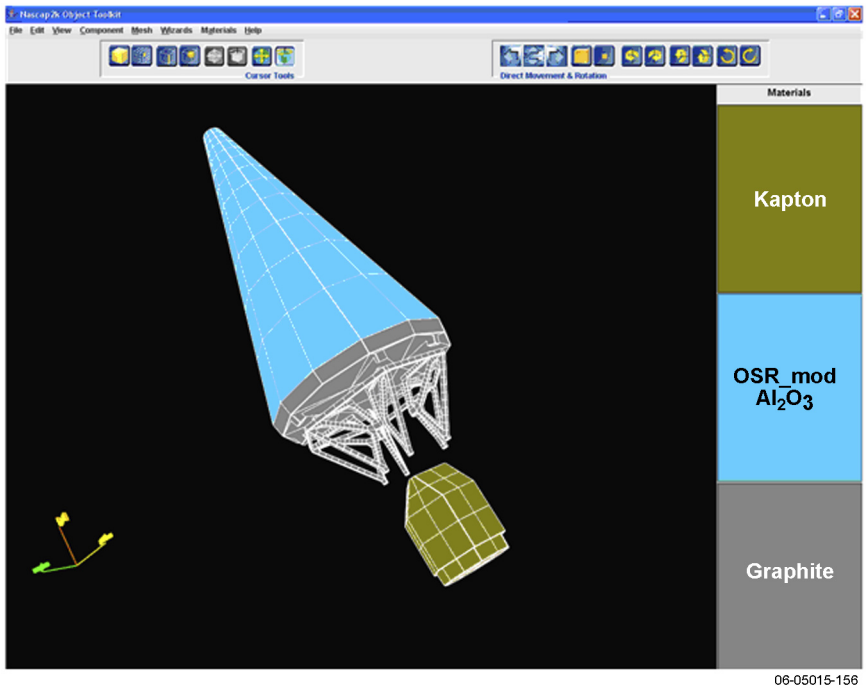

06-05015-156

Figure 6-5. The NASCAP Object Toolkit for specifying spacecraft geometry.

are under consideration: pyrolytic boron nitride (PBN) and barium zirconium phosphate (BaZP). All three materials have very high electrical resistivity at room temperature (~10^{15} Ω cm). They become more electrically conductive with increasing temperature, becoming conductive at the very high temperatures expected near perihelion.

These materials are ceramics and were chosen because of their outstanding optical properties (very low absorptivity-to-emissivity ratio α/ε, as documented in Chapter 4). Their ability to reflect incident solar irradiance and emit thermal energy will enable the mission by decreasing the equilibrium temperature of the primary shield, thus decreasing launch mass and costs. Please refer to Chapter 4 for a full discussion of the coating optical properties and thermal performance.

6.5 Testing at Utah State University

The electron emission properties of materials (yields and energy spectra of electrons emitted due to electron, ion, and photon bombardment) are key to modeling the extent of spacecraft charging.[2] The emitted electrons can be divided into two categories: (1) secondary electrons (SE) (<50 eV by convention) that originate within the material, and (2) backscattered electrons (BSE) (>50 eV by convention) that originate from the incident electron source.[3,4] SE and BSE yields are defined as the ratios of the emitted electrons to the total incident electrons. Of particular importance for solar probe spacecraft charging are emission characteristics of insulators.[5,6] However, accurate absolute electron yield measurements are much more difficult to make on dielectrics than on conductors, since any charge that is deposited in the material is not highly mobile and cannot easily be neutralized. The surface and bulk potentials and internal charge distributions that develop as a result of electron bombardment can subsequently affect electron emissions by influencing incident electron energies, or by creating electric fields that affect the escaping SEs and BSEs. Without the implementation of neutralization techniques, an irradiated insulator will eventually charge to a (quasi-) steady-state current equilibrium such that the net current to the sample approaches 0 or the total electron yield is ~1.[3,4]

NASCAP-2K requires detailed information about the material properties that in part govern charging, such as resistivity, dielectric constant, SE emission parameters, photoemission spectra, etc. (Figure 6-6.) These parameters must be as accurate as possible to ensure model validity and can be measured by a series of experiments designed to accurately probe the emission of a given material under various conditions. Dr. J. R. Dennison of Utah State University (USU) is an expert at making such measurements and in electron emission phenomena. Under contract to NASA, Dr. Dennison has determined all previous NASCAP-2K material property inputs.

Dr. Dennison studied secondary and backscattered electron yield curves of thin-film dielectrics by using pulsed, low-current electron beam methods to minimize insulator charging. These capabilities allowed investigation of the evolution of surface and internal charge profiles as a function of low-energy electron (<1 to 20 keV) pulsed-electron fluence to determine how quickly the insulators charge and how this can affect subsequent electron emission properties.

Pulsed-yield methods with alternating charge neutralization were used to make reliable and

[2]Hastings, D., and H. Garrett, *Spacecraft–Environment Interactions,* New York, NY, Cambridge Press (1996).

[3]Reimer, L., Scanning electron microscopy, in *Physics of Image Formation and Microanalysis*, New York, Springer-Verlag, pp. 119-121 (1985).

[4]Seiler, H., Secondary electron emission in the scanning electron microscope, *J. Appl. Phys.,* **54** (11), R1-R18 (1983).

[5]Thompson, C. D., et al., Electron emission properties of insulator materials pertinent to the International Space Station, *Proc., 8th Spacecr. Charging Tech. Conf.*, Huntsville, AL (2004).

[6]Thompson, C. D., *Measurements of Secondary Electron Emission Properties of Insulators,* Ph.D. dissertation, Utah State University, Logan, UT (2004).

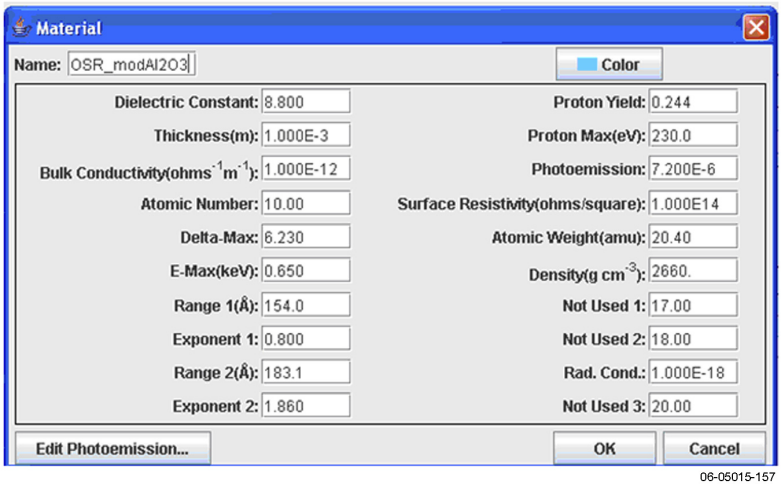

Figure 6-6. The NASCAP material properties window.

reproducible measurements of the absolute total yield curves of insulators.[6,7] These measurements showed very little evidence of the results of surface charge accumulation for PBN, whereas BaZP was found to charge significantly. When all pulsed yields had been measured, the electron gun was turned to continuous emission to deposit large amounts of charge in the material, and the evolution of the steady-state total yields were monitored as a function of total incident electron fluence and energy.

The direct-current and pulsed-electron yield methods used here are described fully elsewhere.[6-8] Briefly, for pulsed measurements on insulators, the electron guns delivered 5-μs, 20–60 nA incident pulses with ~106 electrons/pulse. A low-energy (<1 eV) electron flood gun was used to neutralize positive surface charging between pulses.[7-9] Numerous conductor and insulator electron spectra, yield curves, and yield parameters have been measured at USU.[5,7,10] The electron gun setup is shown schematically in Figure 6-7, and a photograph of the measurement chamber is shown in Figure 6-8.

Figures 6-9 through 6-11 show the results of these experiments to determine charging-related material properties. Many materials, when irradiated with photons or electrons, will emit electrons. The number of these emitted electrons and their energies quantify the SE emission, BSE emission, and photoemission data used by NASCAP-2K to model spacecraft charging. Thus it was important both to acquire these data and to understand how NASCAP-2K uses them to determine voltage potentials on the spacecraft.

The SE emission curve for alumina, our baseline material, is taken from Dawson (1966)[11] and is shown in Figure 6-9. (USU measurements for Al_2O_3 are anticipated but have not yet been completed.) The red points are the measured data for the total yield (electrons out per electron in), and the blue and red curves represent

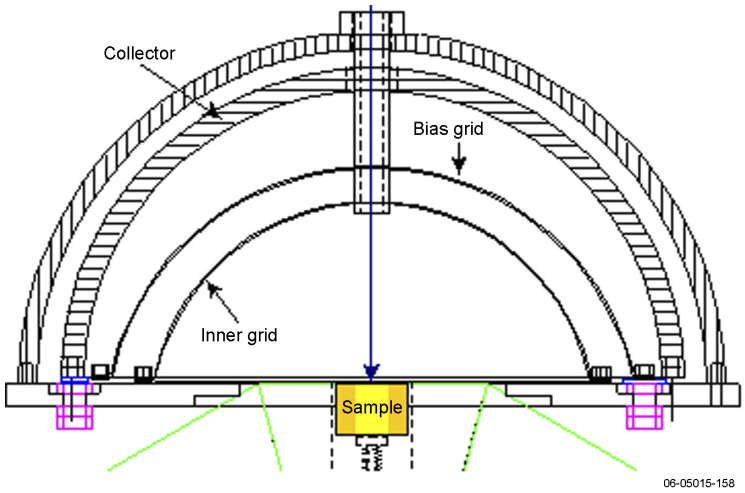

Figure 6-7. Schematic depiction of electron emission measurement setup used by J. R. Dennison to determine electron emission behavior of candidate Solar Probe materials. A flood gun sits adjacent to the sample in the block and neutralizes the sample between incident beam pulses by showering the charged sample with low-energy electrons.

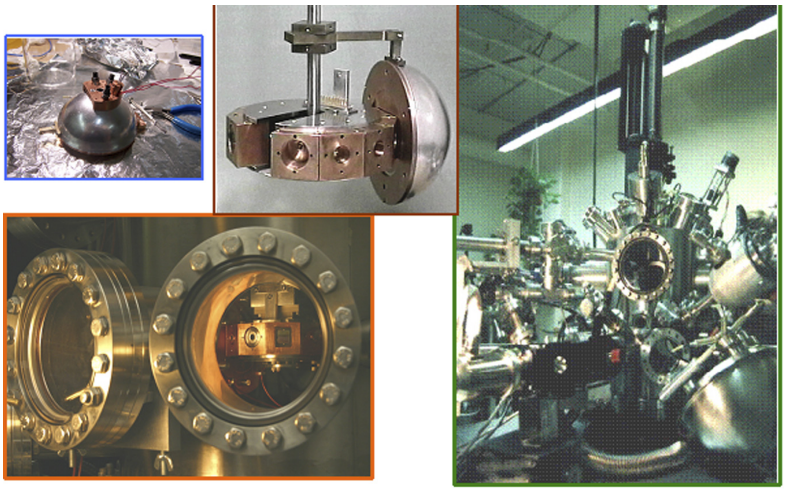

Figure 6-8. Ultra-high vacuum chamber for electron emission studies at Utah State University.

[7]Dennison, J. R., et al., Materials characterization at USU: Facilities and knowledgebase of electronic properties applicable to spacecraft materials, *Proc., 8th Spacecr. Charging Tech. Conf.,* Huntsville, AL (2004).

[8]Thomson, C. D., et al., Instrumentation for studies of electron emission and charging from insulators, *Proc., 8th Spacecr. Charging Tech. Conf.,* Huntsville, AL (2004).

[9]Krainsky, I., et al., *Secondary Electron Emission Yield Annual Report for Period July 1, 1980, to June 30, 1981,* Case Western Reserve University, Cleveland, OH, (1981), unpublished.

[10]Dennison, J. R., et al., Final report part III: Materials reports, in *Electronic Properties of Materials with Application to Spacecraft Charging*, NASA Space Environ. and Effects Program (September 2002), published at http://see.msfc.nasa.gov/scck/.

[11]Dawson, P. H., Secondary electron emission yields of some ceramics, *J. Appl. Phys.*, **37**, 3644 (1966).

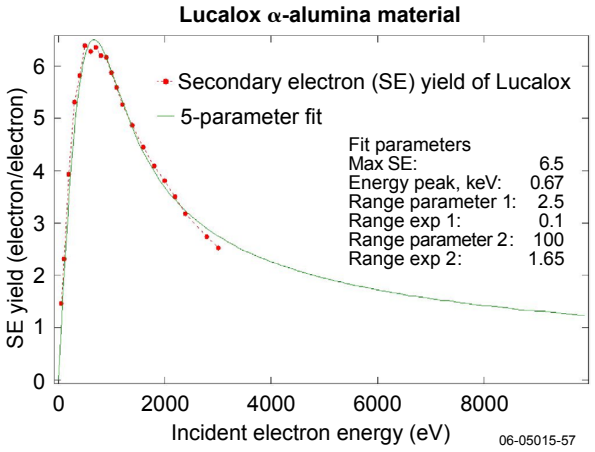

Figure 6-9. SE yield with full 5-parameter NASCAP fit for Lucalox α-alumina material.

the SE yield and BSEs, respectively. Note that at the incident electron energy of ~200 eV, Al_2O_3 emits more electrons than are bombarding it, a behavior that is typical of metal oxides and certain ceramics. Consequently, a material may acquire a positive rather than a negative charge even in an electron environment, depending on the radiation distribution of fluences and energies. The fitting parameters of the electron emission curves, which define the shape of the curves and thus the energy dependence of the secondary electron emission, also define the material and must be entered into NASCAP-2K. The maximum electron yield is termed the δ_{max}, and the energy at which it takes place is E_{max}.

Figures 6-10 and 6-11 show electron emission curves and fits for the other two candidate coatings, PBN and BaZP. They include the SE yield data, BSE yield data, and corresponding curve fits. The fits to the BSE curves for these materials were typically good, accurately reflecting the actual material's emission. In the case of the secondary emission curves however, the standard 3-parameter fit did not accurately reflect the steep shape and large δ_{max} of the ceramics. In addition to performing a 5-parameter fit, this NASCAP fit was tailored to more accurately reflect the SE emission of metal oxides and ceramics at the energies of interest (<400 eV).

The electron emission studies of BaZP largely showed erratic behavior indicative of severe charging. Evidence of this charging is given in Figure 6-12, which shows electron emission curves of charged BaZP at 1 hour, 1 day, and 5 days after initial irradiation. Most materials, including insulators and specifically the PBN sample, will discharge within seconds following the termination of electron irradiation. BaZP's emission curve did not return to that of an uncharged sample until 5 days after irradiation.

These results indicate that BaZP has a very high resistivity and possibly a high dielectric constant as well, both of which would lead to these very long charge decay times. Experiments focused on determining the resistivity BaZP (as well as PBN and Al_2O_3) will be necessary to accurately quantify this property. Temperature-dependent resistivity measurements are required to quantify how conductive these insulators become at elevated temperatures. A good understanding of this behavior is of critical importance to charging studies of the ceramic-coated Solar Probe spacecraft.

6.6 Charging Analyses

The 2005 report of the Solar Probe Science and Technology Definition Team[12] presented results of NASCAP-2K charging simulations for the Solar Probe spacecraft with an alumina-coated C-C primary shield. These simulations were performed for the estimated Jovian environment corresponding to 12 Jovian radii (R_J); for two points in deep space (2.5 and 5 AU); and for 0.3 AU. More recently, SAIC was retained as a consultant to aid in improving the fidelity of the NASCAP-2K predictions. SAIC's role includes assisting in modeling the unusually shaped Solar Probe spacecraft, identifying proper time steps for model calculations, and recommending other model refinements (such as improved material models.) The NASCAP-2K model was revised to reflect the updated design of the struts (the truss design), and the simulations were run at the following points along the trajectory: 12 R_J; deep space (2.5 and 5 AU); and various near-solar locations (0.5, 0.4, 0.3, 0.2, 0.1 AU and 4 R_S).

The primary concern for the two deep-space trajectory points is to avoid elevated charging levels that may result in an arcing event. The resulting differential charge for an alumina-coated TPS is about 65 V for both 2.5 AU and 5.0 AU. The charging levels are independent of spacecraft orientation, since photoemission does not play a large role in these deep-space environments.

The current trajectory around Jupiter brings the spacecraft within 12 R_J at closest approach. For the case where closest approach occurs outside the Jovian radiation belts and for an alumina-coated TPS, the spacecraft charges to a differential voltage of 2.8 V. All charging results in these deep-space

[12] *Solar Probe: Report of the Science and Technology Definition Team,* NASA report NASA/TM—2005–212786, E9-E10 (September 2005).

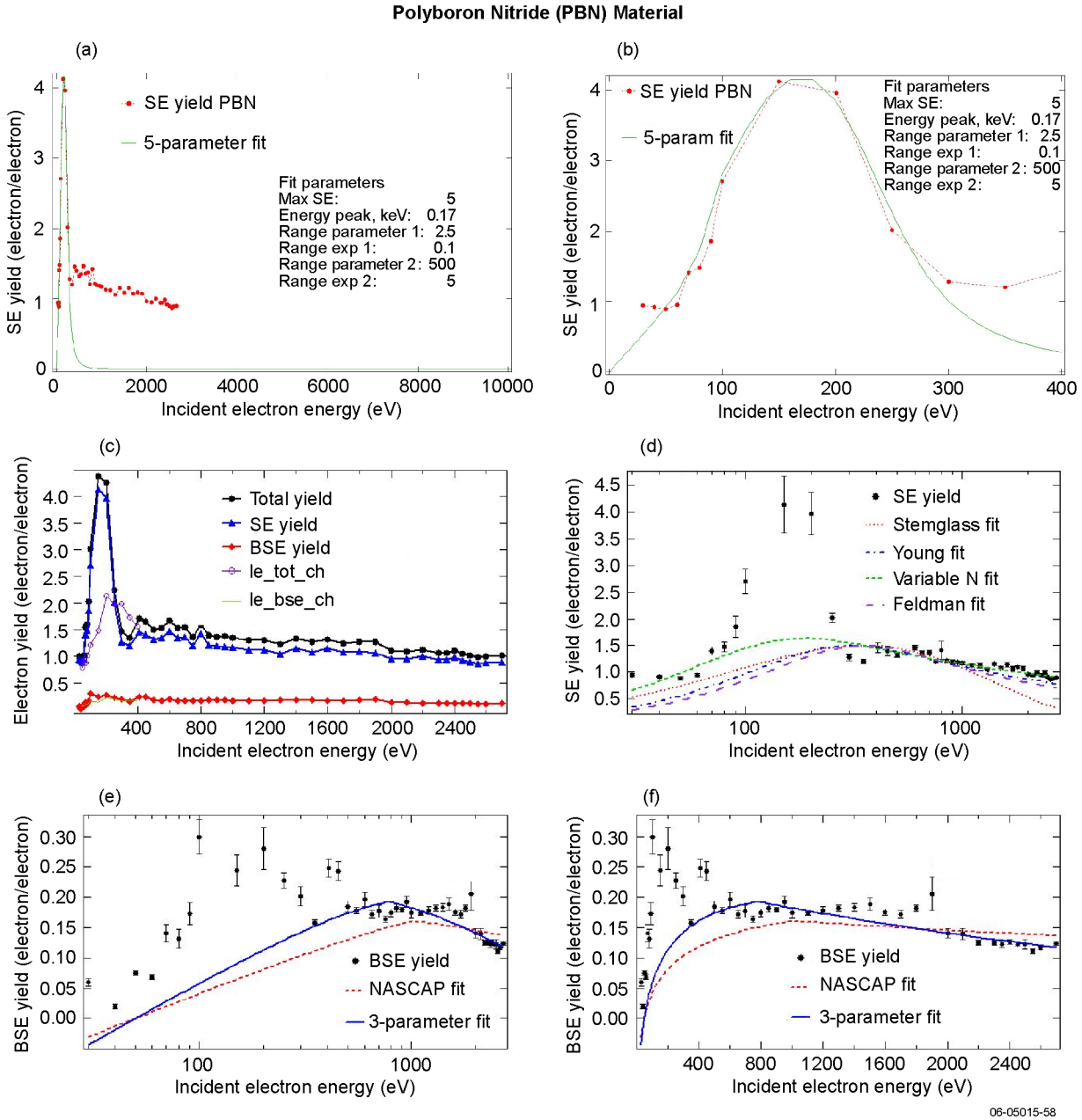

Figure 6-10. Electron emission curves and fits for PBN. (a) SE yield with full 5-parameter NASCAP fit. (b) Detail of leading edge for 5-parameter NASCAP fit of SE yield curve. (c) Total (black), secondary (blue), and backscattered (red) yield curves. (d) SE yield curve with several fits. (e) BSE yield curve with fits—semilog scale. (f) BSE yield curve with fits—linear scale.

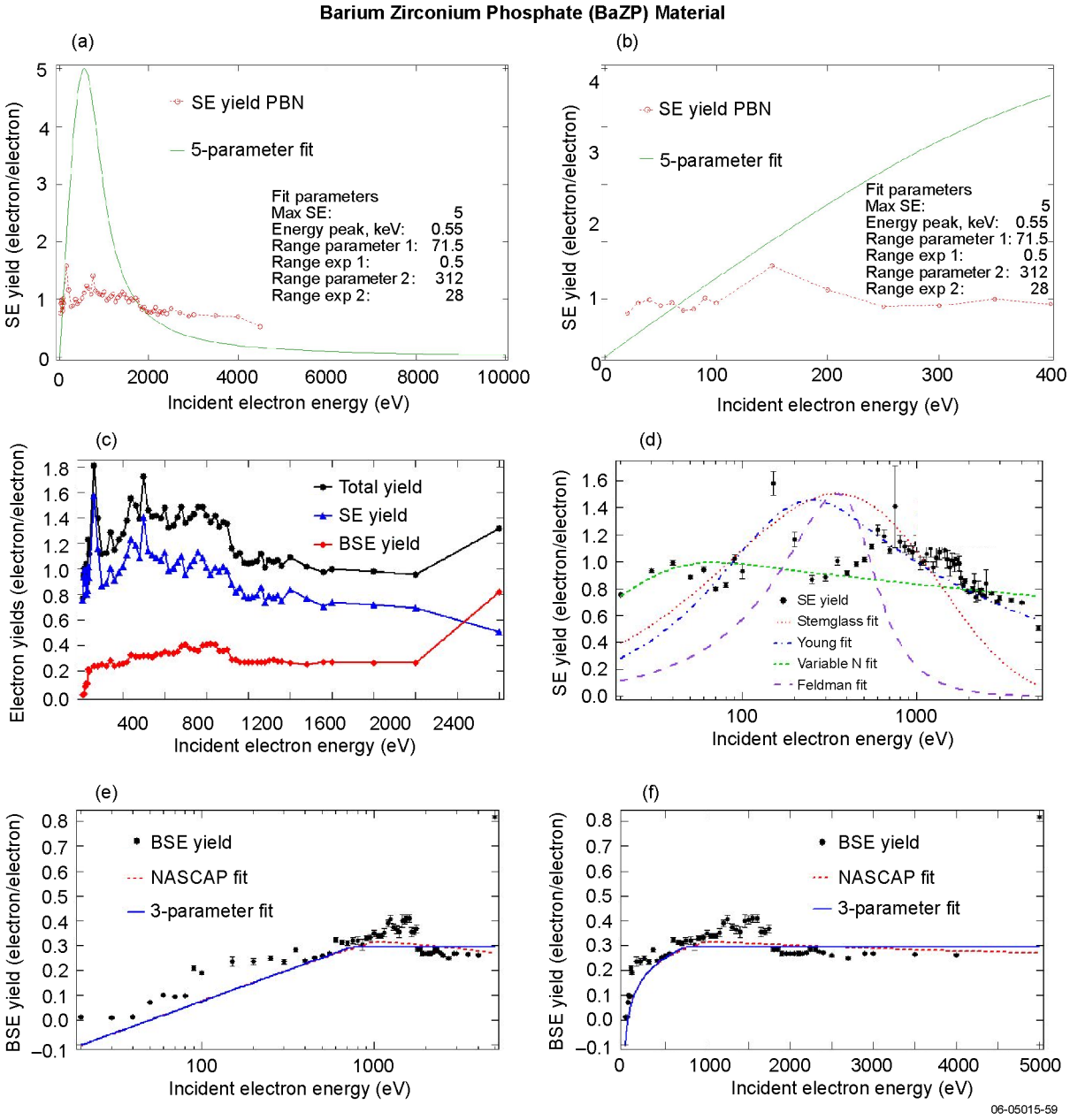

Figure 6-11. Electron emission curves and fits for BaZP. (a) SE yield with full 5-parameter NASCAP fit. (b) Detail of leading edge for 5-parameter NASCAP-2K fit of SE yield curve. (c) Total (black), secondary (blue), and backscattered (red) yield curves. (d) SE yield curve with several fits. (e) BSE yield curve with fits—semilog scale. (f) BSE yield curve with fits—linear scale.

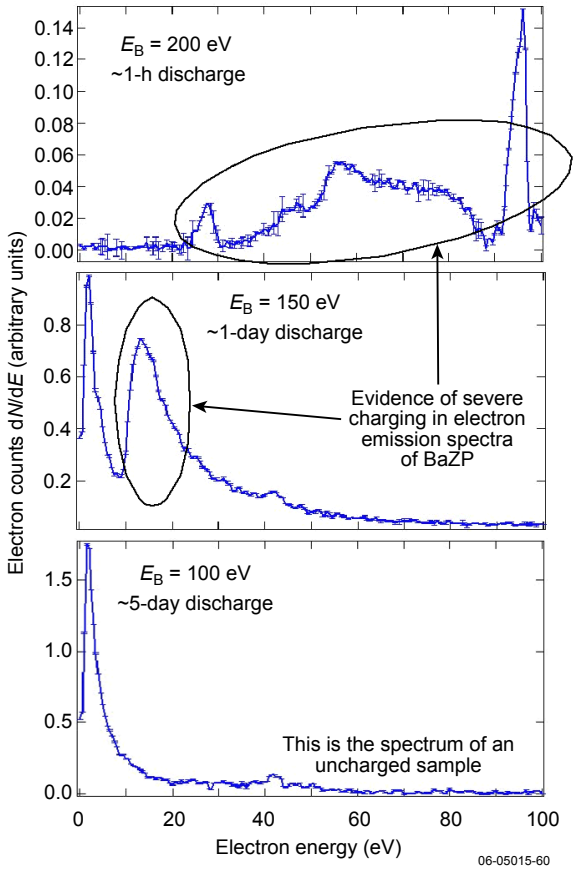

Figure 6-12. Charge decay curve for BaZP. Emission curves show evidence of charging up to 5 days after initial tests for BaZP, whereas PBN (and most insulators) discharged in seconds.

and Jovian environments showed charging to be significantly below the 100-V threshold for damage of electronics.

The NASCAP-2K charging simulation at the 4 R_S radiation environment is shown in Figure 6-13. A uniform potential of ~2 V is seen to develop. At this point in the trajectory, the ceramic is electrically conductive due to its elevated temperature.

The results for the 0.3 AU case are shown in Figure 6-14. Note the smooth potential contours along the length of the spacecraft. These results show differential charging of ~36 V from cone tip to the bus, likely due to the electrically insulating ceramic cone photoemitting while the instrument bus is shaded. Lack of electrical conduction between the two (due to the relatively high resistivity of Al_2O_3 at this point in the trajectory) results in the potential differential.

To better understand the charging behavior near 0.3 AU, the team performed additional NASCAP runs for the trajectory points at 0.1, 0.2, 0.4, and 0.5 AU. The spacecraft is expected to become more conductive fairly rapidly as it moves closer to the Sun, so that at 0.2 AU the differential charge decreases to 6 V. Table 6-2 contains a complete summary of the results for the alumina-coated TPS.

For comparison, the NASCAP-2K results are presented for PBN at 12 R_J, 2.5 AU, 5.0 AU, 0.3 AU, and 4 R_S. Differential charging for the 0.3 AU case is ~8 V, which is less severe than for alumina. The spacecraft charges to a uniform potential of ~2 V in the 4 R_S environment, which is very similar to the result for alumina. However, very little data are available for the temperature-dependent material properties of PBN, and more data are needed to increase the fidelity of the NASCAP results and to thoroughly evaluate the material's charging performance. The charging results for the TPS coated with PBN are summarized in Table 6-3.

Additional trades were performed focused on further reducing the predicted voltage potential near 0.3 AU. Exposure of portions of the C-C substrate on the TPS to the radiation environment results in photoemission from the C-C when the TPS is sunlit. By electrically connecting the TPS to the shaded bus, the exposed C-C portion of the TPS may become an effective photoemission mechanism for the bus. The two scenarios investigated are illustrated in Figure 6-15: one for which the tip of the TPS is exposed, and one for which a ring at the base is exposed; the remaining surface area is ceramic-coated. As shown in Table 6-4, this approach significantly reduces the differential charging potential range to near the level predicted for an all-C-C TPS. These small regions of exposed C-C would have the effect of raising the effective cone temperature by about 10 K and increasing the total mass loss rate by about 0.05 mg/s, or 2% of the value for the fully coated cone.

6.7 Remaining Work

Spacecraft charging can be investigated and characterized using a combination of modeling and experimental activities. The quantitative estimates of spacecraft response will be improved by better characterization of the material properties of the ceramic coating, including the electronic properties as a function of temperature. While the 5-parameter NASCAP fit to the secondary electron emission, tailored to the low-energy range, is an improvement upon previous efforts, the results are still not generally well tailored to insulators. Accommodations within NASCAP to better represent insulating materials will greatly improve the fidelity of charging results for ceramic coatings. Confidence in NASCAP results would also

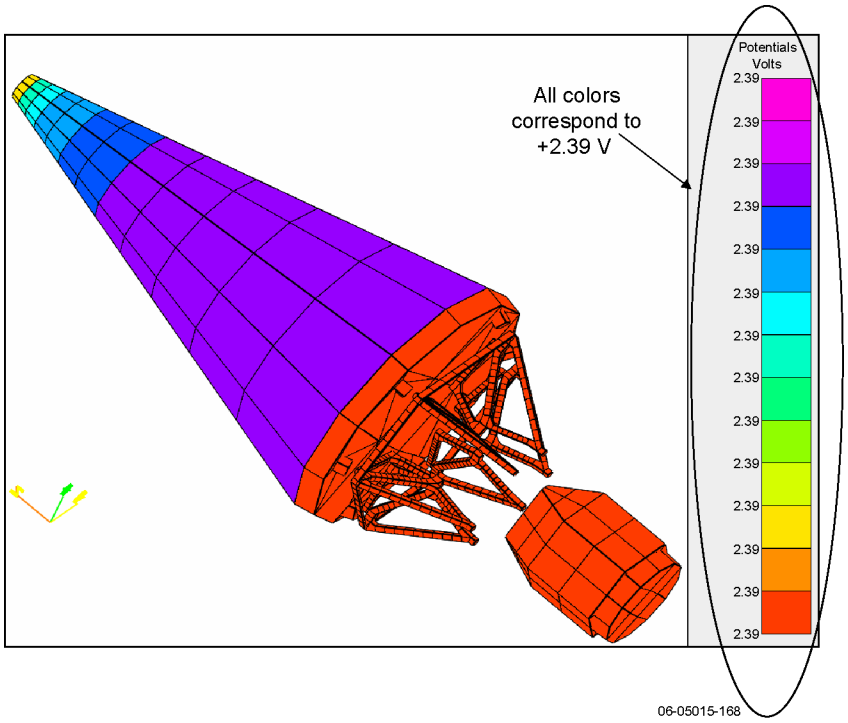

Figure 6-13. NASCAP-2K analysis of alumina on the C-C primary shield at 4 R_S.

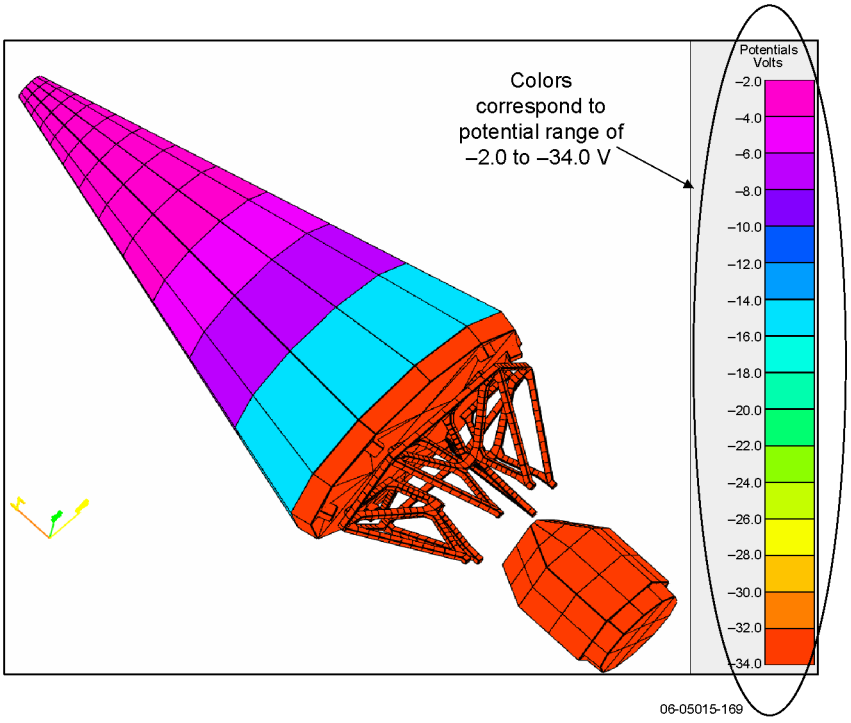

Figure 6-14. NASCAP-2K analysis of alumina on the C-C primary shield at 0.3 AU.

Table 6-2. NASCAP-2K results for alumina-coated TPS at various trajectory points.

Environment		Charging Potential Range (V)
Near Sun	4 R_S	+2.39
	0.1 AU	+1.0 to +6.0
	0.2 AU	0.0 to +6.0
	0.3 AU	–34.0 to –2.0
	0.4 AU	–38.0 to –2.0
	0.5 AU	–36.0 to –2.0
Deep space	2.5 AU	–62.0 to –5.0
	5.0 AU	–68.0 to +2.0
Jovian	12 R_J	–0.2 to +2.8

Table 6-3. NASCAP-2K results for PBN-coated TPS at various trajectory points.

Environment		Charging Potential Range (V)
Near Sun	4 R_S	+2.27
	0.3 AU	–4.0 to +4.0
Deep space	2.5 AU	–5.0 to –38.0
	5.0 AU	–2.0 to –47.0
Jovian	12 R_J	–0.3 to +1.7

be enhanced by experimental verification of NASCAP predictions.

Additionally, a qualitative assessment of the impact of charging on the fidelity of the science measurements can be conducted via first-order NASCAP modeling to establish trends in the interactions of charged particles with the spacecraft and to define the strategic placement of the instruments to minimize the effects of charging on science measurements. For example, more detailed evaluations of the spacecraft wake and environmental interaction can be performed with high-fidelity coupled electromagnetic and Direct Simulation Monte Carlo (DSMC) charged-particle tracking. These analyses will help to clarify the effect of the spacecraft on both the local environment and the ability of the instruments to collect accurate data.

Both material solutions (i.e., increasing surface conductivity) and system solutions (such as exposing regions of the TPS) can be employed to negate voltage potential issues if they arise. Modeling will be performed to evaluate and optimize charge mitigation strategies, such as optimization of material properties, to improve the low-temperature electronic properties. Additional studies will be conducted to optimize the "passive emitter" approach (using the exposed C-C surfaces) and to investigate the impact on TPS thermal performance.

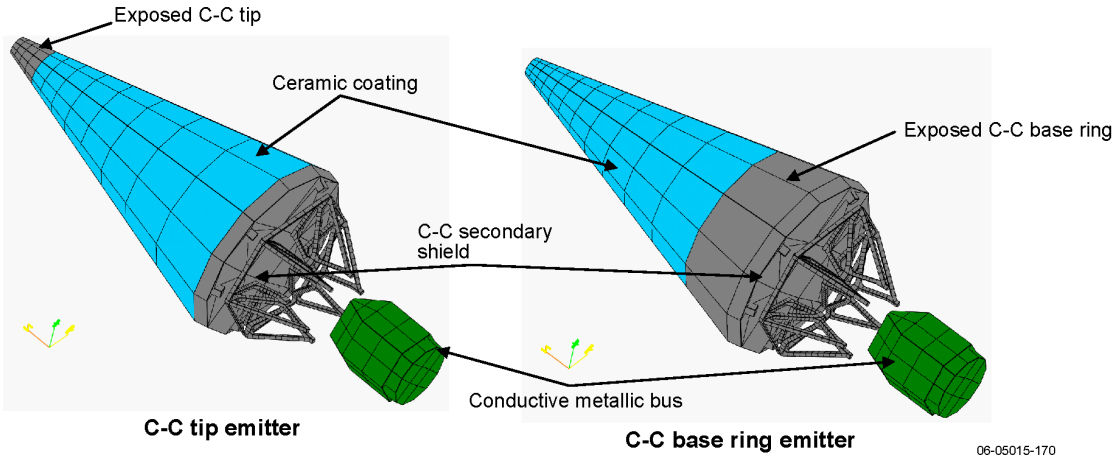

Figure 6-15. Exposed C-C regions of primary shield.

Table 6-4. NASCAP-2K results for exposed regions of primary shield.

Environment		Coating Material	Charging Potential Range (V)
Near Sun	0.3 AU	Uncoated graphite	+2.12
		Al_2O_3, graphite band at base	+0.6 to +5.6
		Al_2O_3, graphite at tip	–0.2 to +3.4
		PBN, graphite at tip	–0.5 to +4.5

7 Material and Process Development

Data related to the use of carbon–carbon (C-C) and carbon foams in space applications fall under the purview of the U.S. Munitions List, as defined in the International Traffic in Arms Regulations (ITAR). Therefore, the related information developed during the Solar Probe Thermal Protection System (TPS) Risk Mitigation study is published in a separate, restricted-access volume. Although all information presented in that ITAR-restricted-access volume is not restricted, for continuity in the report, all the materials and process development work done as part of the 2006 Risk Mitigation Study was placed in this restricted-access volume. A summary of some of the key findings from the ITAR-restricted volume is presented here.

7.1 Carbon–Carbon Composites

- C-C materials have an extensive heritage associated with thermal protection applications in highly stressing and oxidizing environments.
- Over the past decade, the use of C-C materials has evolved into more structural designs that must withstand very high temperatures.

7.1.1 Materials

- Both two-dimensional and three-dimensional C-C fabrication techniques are well developed.
- The carbon fibers used in conventional composites are available for C-C applications.
- The structural capabilities of C-C have evolved as the demand has increased for complex structures in high-temperature applications.

7.1.2 Processing

- Two C-C densification processes are presently being used.
- Both have a long heritage, and process and control techniques are well understood.

7.1.3 Material Properties

- While available, distribution of design data on C-C materials at high temperatures is limited.
- One focus of the TPS Risk Mitigation Study was on developing reliable material property information based on the existing databases, supplemented with our own coupon and element testing.

Available Databases

- C-C material test data have been taken on several recent and ongoing programs involving reentry or high-speed atmospheric structures. The programs include Mars Sample Return, HyFly, X-37, and Falcon.
- Mechanical test data and some joint design information have been published and presented at ITAR-restricted conferences.

Physical Properties

- For the materials tested, ply thickness was not a function of the fiber or the C-C densification process.
- Material density was a function of the C-C densification process.

Mechanical Testing

- Mechanical testing was a significant focus of the TPS Risk Mitigation Study. The effort was to ensure that specific materials planned for the TPS design were “in-family” with existing database information.
- Coupon mechanical testing was done on C-C samples from different vendors by using different densification processes. Medium- and high-modulus materials were tested, for different thicknesses, ply orientations, and heat treatment temperatures.
- Mechanical test data included
  - Tensile strength and modulus
  - Poisson’s ratio
  - Compressive strength and modulus
  - Interlaminar tensile strength
  - Interlaminar shear strength
  - In-plane shear strength and modulus
  - Flexural strength
- Thus far, mechanical test coupons have displayed properties in family with those conveyed in the database.
- While mechanically testing thin laminates posed new challenges, methods have been

developed to accurately obtain the properties of these materials.

7.1.4 Element Testing

- Elements tested are full-sized test specimens developed to represent critical parts of the TPS structure.
- Element testing was used to set design allowables for complex joint designs and to compare the analytically predicted performance against the actual performance of complex, three-dimensional structures.

T-Section

- T-section tests have been completed on elements from one vendor. Results were in the expected range for bolt shearing. Design of co-processed joints requires B-studding.
- The critical failure mode demonstrated by the T-section coupon testing is bolt shear. Allowable T-section forces are well within the maximum predicted joint loads.

Struts

- Residual stresses developed during processing limit the thickness of material that can be processed at one time. Thicker sections have to be built up in incremental stages.
- Maintaining co-linearity of a long tube requires special processing and tooling design.

Ball and Socket

- The ball-and-socket element has not yet been delivered. Element testing will focus on comparing analytical performance predictions to test data.

Jack Stand

- The jack stand is a new element identified during this TPS study. It will be used to test the joint between the primary shield cone and the support structure.

7.1.5 Nondestructive Evaluation

- A focus of NASA and the Department of Defense in the last 5 years has been on improving and characterizing the effectiveness of nondestructive evaluation (NDE) techniques to support fabrication and acceptance of C-C structures for flight programs.
- The Carbon-Carbon Advanced Technologies, Inc. (C-CAT) study used C-scan and computed tomography to locate bond line anomalies.

7.1.6 Vendors

- Three U.S. manufacturers have extensive experience with two-dimensional structural C-C design and fabrication.
- Two of those vendors participated in the 2006 Risk Mitigation Study. The third opted not to participate.

7.2 Carbon/Polymer Laminates

- The truss TPS design allows the use of lower-temperature materials for the support truss. One such material option is carbon polyimide composite.

7.2.1 Materials

- Qualified resin systems exist that are designed for continuous temperatures up to 300°C.
- New polyimide formulations have been developed that have service temperatures between 300°C and 400°C.
- Existing efforts have focused on fibers with characteristics compatible with jet engine and reentry applications. A high-modulus fiber would be more mass efficient for the TPS support structure as specific stiffness is increased. Initial contacts with vendors indicate that there should be no issues with different combinations of fiber/resin systems.

7.2.2 Processing

- High-temperature carbon-polyimide composite processing is complicated by the need to find bagging materials that are compatible with the temperatures required and with the required control of volatiles present during the curing process.

7.2.3 Material Properties

- Some mechanical property data exist for specific combinations of high-temperature resin/fiber systems.
- Extensive property data exist for lower-temperature systems.

7.2.4 Vendors

- Several component fabricators have established themselves as qualified suppliers of high-quality polyimide composite structures.

7.3 Carbon Foam Insulation

- Solar Probe's secondary shield requires a high-temperature insulation that protects the spacecraft from the primary shield around its closest approach to the Sun.
- Key parameters for the insulating materials are the density and thermal conductivity.
- Subcontracts were established with two companies having extensive experience in the formulation of high-temperature insulation materials to assess their present capabilities and to look into the potential for improved materials.

7.3.1 Materials

- A variety of insulation materials are used in high-temperature applications.
- The most promising, in terms of low density and low thermal conductivity, are carbon foams and carbon aerogels.
- Reticulated vitreous carbon (RVC) foam is the baseline material for the secondary shield insulation.
- Hybrid foam/aerogel composites have the potential to lower the thermal conductivity at high temperature with only a limited density penalty.

7.3.2 Processing

- Carbon foam and aerogel processing has been aimed at formulating insulating materials for atmospheric reentry.
- Work done at an external vendor indicates some density improvement can be obtained through relaxing the mechanical loading requirements on the material.

7.3.3 Material Properties

- High-temperature thermal conductivity testing can be performed at only a few places.
- Test data demonstrate that RVC foam is stable over the range of required temperatures.
- Existing property data are being used in the design; additional coupon testing is underway. The test setup has been hampered by the CTE change at high temperature.
- Thermal conductivity is a function of the pore size in the material at high temperatures due to radiative heat transfer through the materials.

7.3.4 Vendors

- Thermal insulation vendors are specific to the different types of materials. During this study, we have been working with both commercial and non-profit institutions.

Appendix: Risk Mitigation Results for the Ka-Band Portion of the Solar Probe RF Telecommunications Subsystem

This appendix describes preliminary risk mitigation work on the Ka-band portion of the RF subsystem for Solar Probe. It examines the performance requirements in light of state-of-the-art technology, and derives a reasonable design for the Ka-band circuit. Various components in the topology were procured as engineering models and then tested to make sure their performance is adequate for the application. These test results are described in some detail. Finally, the design of a critical transition from microstrip to waveguide is described. Recommendations are made for improving the design of this transition so that the Ka-band circuit will satisfy system requirements.

A.1 Introduction

A communication link analysis at 32 GHz performed by Dr. Brian Sequeira of APL for Solar Probe determined that an equivalent isotropic radiated power (EIRP) of 83 dBmi is needed for the communications link to function. The analysis assumed a bit rate of 25 kbits/s when the spacecraft is 1 AU from Earth and took into account Earth weather and the solar radio environment. Using 83 dBmi as a goal, the necessary output power and the power added efficiency (PAE) of the solid-state power amplifier (SSPA) was calculated for three different values of loss between the SSPA and the antenna, using antenna efficiency as a parameter. PAE calculations assume 20 W of available prime power, 80% efficiency of the power conditioning unit (PCU), and 1 W of miscellaneous losses so that 15 W of net power is delivered to the SSPA. Table A-1 summarizes these calculations. Figure A-1 graphs the results for 1 dB of loss between the SSPA and antenna and compares them to published state-of-the-art Ka-band SSPA performance. The two graphs intersect at an antenna efficiency of about 70%, a PAE of about 24%, and an output power of 4.6 W. If the RF power loss between the SSPA and the antenna can be reduced to less than 1 dB, then the antenna efficiency requirement and/or the SSPA performance requirements can be relaxed to some degree. Since the intersection point on the graph involves state-of-the-art SSPA performance and a highly optimistic antenna efficiency, the hardware design task is challenging. Any opportunity to make the the design challenge more manageable, especially by reducing RF power loss, should be considered.

The requirement to minimize RF power loss between the SSPA and the antenna favors the choice

Table A-1. PAE, output power, and corresponding antenna efficiency for EIRP = 83 dBmi and three values of antenna feed loss.

Antenna Efficiency	50%	55%	60%	65%
PAE, 1-dB loss	42.4%	38.5%	35.3%	32.6%
PAE, 1.4-dB loss	46.4%	42.2%	38.7%	35.7%
PAE, 2-dB loss	53.3%	48.5%	44.4%	41.0%
Pout, 1-dB loss	6.35 W	5.78 W	5.30 W	4.89 W
Pout, 1.4-dB loss	6.97 W	6.33 W	5.81 W	5.36 W
Pout, 2-dB Loss	8.00W	7.27 W	6.67 W	6.15 W
Antenna Efficiency	**70%**	**75%**	**80%**	**85%**
PAE, 1-dB loss	30.3%	28.2%	26.5%	24.9%
PAE, 1.4-dB loss	33.2%	31.0%	29.0%	27.3%
PAE, 2-dB loss	38.1%	35.6%	33.3%	31.4%
Pout, 1-dB loss	4.54 W	4.24 W	3.97 W	3.74 W
Pout, 1.4-dB loss	4.98 W	4.64 W	4.35 W	4.10 W
Pout, 2-dB loss	5.71 W	5.33 W	5.00 W	4.70 W

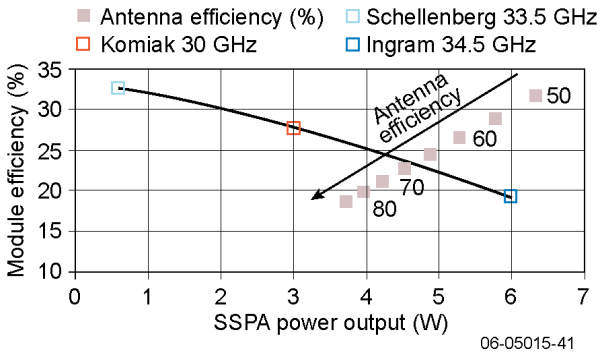

Figure A-1. Plot of PAE vs. output power for Ka-band SSPA.[1]

of waveguide transmission lines for this part of the RF communications system. Figure A-2 shows a block diagram of the proposed design. Orange indicates waveguide transmission line and waveguide components, and blue indicates microstrip transmission line and monolithic microwave integrated circuit (MMIC) components. The SSPA consists of eight Ka-band MMIC amplifiers in parallel and a power conditioning unit. Outputs from pairs of MMICs are combined in waveguide hybrid T-junctions and directed to a hybrid septum polarizer that converts the linear polarization of the waveguide to circular polarization. A cluster of four hybrid septum polarizers comprises the antenna feed that illuminates the antenna sub-reflector. The sub-reflector directs the energy into the main reflector of the antenna. Phase shifters are used to ensure proper phasing, so that the power from all four channels is combined to produce maximum power onto the sub-reflector. The use of waveguide between the SSPA and antenna serves to minimize RF power loss, provided that suitable low-loss transitions are implemented between the SSPA and the waveguide transmission lines.

[1]Komiak, J. J., W. Kong, P. C. Chao, and K. Nichols, Fully monolithic 4 watt high efficiency Ka-band power amplifier, M. Matloubian and E. Ponti, editors, *1999 IEEE MTT-S International Microwave Symposium Digest* (Cat. No. 99CH36282), 3, 947–950, IEEE, New York, NY (1999). Schellenberg, J. M., K. L. Tan, R. W. Chan, C. H. Chen, T. S. Lin, D. C. Streit, and P. H Liu, A 0.8-watt Ka-band power amplifier, *1992 IEEE MTT-S International Microwave Symposium Digest* (Cat. No. 92CH3141-9), 2, 529-532, IEEE, New York, NY (1992). Ingram, D. L., D. I Stones, T. W. Huang, M. Nishimoto, H. Wang, M. Siddiqui, D. Tamura, J. Elliott, R. Lai, M. Biedenbender, H. C. Yen, and B. Allen, A 6 watt Ka-band MMIC power module using MMIC power amplifiers, G. A. Koepf., editor, *1997 IEEE MTT-S International Microwave Symposium Digest* (Cat. No. 97CH36037), 3, 1183-1186, IEEE, New York, NY (1997).

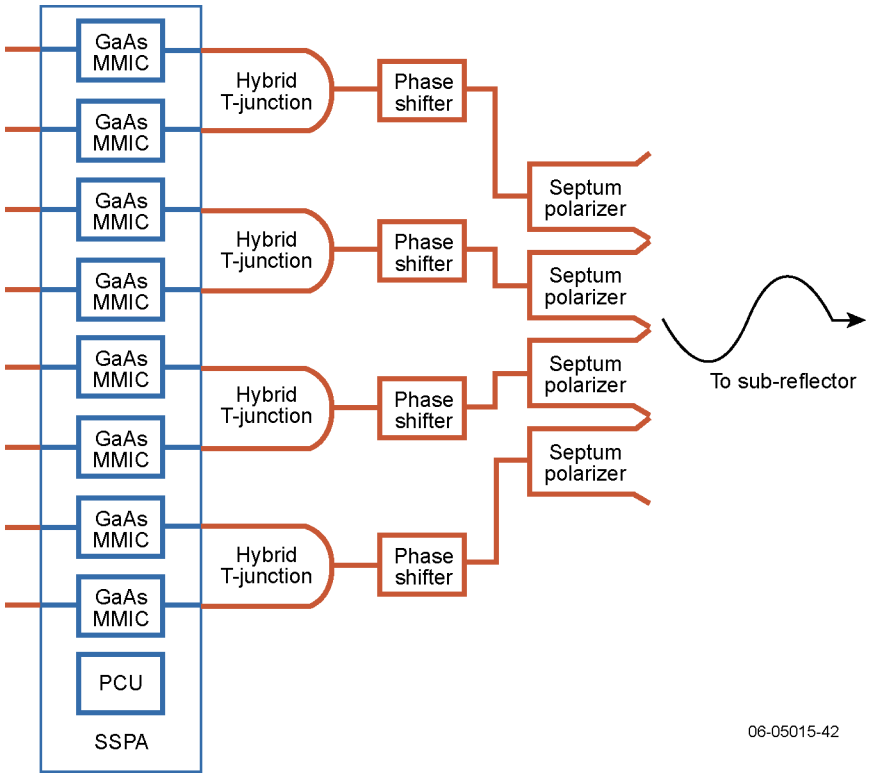

Figure A-2. Block diagram of Ka-band SSPA and antenna feed.

The transitions between waveguide and microstrip are discussed at length in Section A.3. Section A.2 discusses the three waveguide components: phase shifter, folded hybrid T-junction (also known as a folded magic T-junction), and hybrid septum polarizer. Engineering models of all three components were designed and manufactured by Renaissance Electronics (Harvard, MA). They were made in WR28 waveguide, and the performance was optimized at 32 GHz. The engineering models were shipped to APL, where they were tested.

A.2 Performance of Waveguide Components (Engineering Models)

A.2.1 Waveguide Phase Shifter (Renaissance Electronics Part #22WR28NA)

The waveguide phase shifter is a short section of WR28 waveguide with 10 tuning screws in one broad wall, and it is shown in Figure A-3. These tuning screws have sapphire rods on their tips. By adjusting the amount of insertion into the waveguide of the sapphire rods, an additional phase delay through the waveguide is realized. The adjustment also affects the insertion loss and return loss of the phase shifter. Measurements were made of relative phase delay and relative insertion loss (relative to the case of zero insertion of the screws) and return loss (absolute). All 10 screws were adjusted in unison to approximately the same insertion, one-quarter turn at a time, up to 2.5 turns. Table A-2 summarizes the performance of the phase shifter at 32 GHz, where the following notation convention is used: the magnitude and phase of an S-parameter are denoted as $|S_{xx}|$ and $\angle S_{xx}$, respectively. The phase shifter is capable of a maximum relative phase delay of approximately 60°. At this setting, the relative insertion loss is approximately 0.13 dB and the return loss is approximately 24 dB.

The performance of the phase shifter is well suited to its purpose in the RF system. Although it can provide only a maximum of about 60° in phase shift, this is adequate for our purposes. Any coarse phase adjustments that might be required will be built into the various MMIC amplifiers as needed, so the phase shifters are used only for fine tuning. There remains the issue of developing a phase shifter that is durable enough for space flight. One concern in particular is how to ruggedize the attachment between the tuning screws and the sapphire rods so that the device can withstand temperature fluctuation and vibration without having the sapphire rods break loose from the screws. Also, the flight version must have a scheme for locking the tuning screw positions once the tuning is complete.

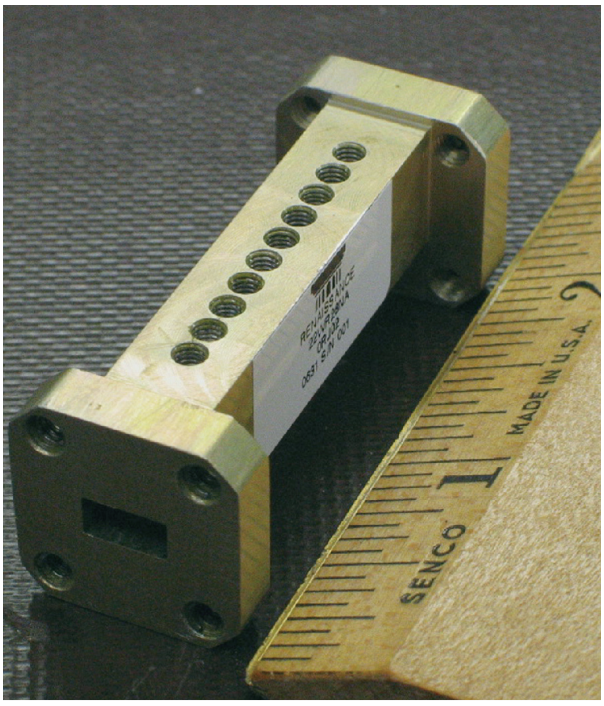

06-05015-43

Figure A-3. Waveguide phase shifter.

Table A-2. Measured performance of waveguide phase shifter at 32 GHz.

Turns of Screws	$\angle S_{21}$ Relative to 0 Turns	$\lvert S_{21}\rvert$ Relative to 0 Turns (dB)	$\lvert S_{11}\rvert$ Absolute (dB)
0.00	0.0°	0.0	–38.3
0.25	–2.8°	0.0	–37.0
0.50	–5.3°	0.0	–37.9
0.75	–9.8°	0.0	–35.5
1.00	–15.7°	–0.01	–36.4
1.25	–20.8°	–0.0	–39.1
1.50	–27.2°	–0.01	–32.0
1.75	–34.7°	–0.02	–41.5
2.00	–42.5°	–0.04	–37.9
2.25	–52.5°	–0.08	–28.0
2.50	–63.0°	–0.13	–24.3

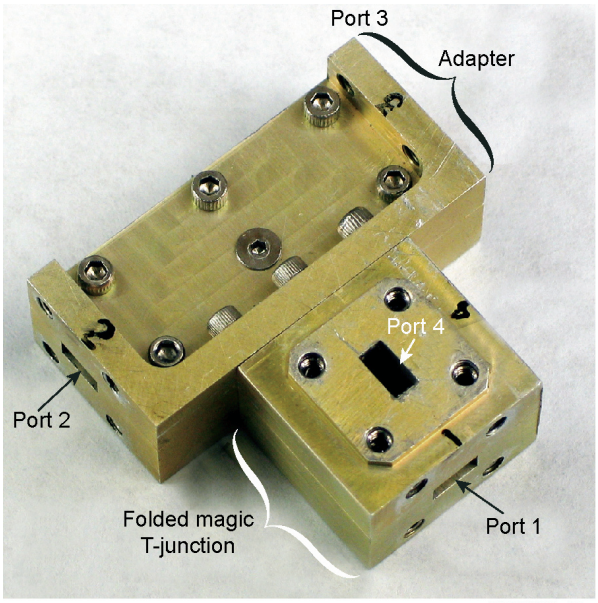

Figure A-4. Folded hybrid T-junction with adapter.

A.2.2 Folded Hybrid T-Junction (Renaissance Electronics Part #10WR28NA)

The folded hybrid T-junction is shown in Figure A-4. The T-junction itself is quite compact and almost cubic in form, and it is shown with an adapter bolted to it. The adapter allows attachment of standard waveguides to ports 2 and 3 for test purposes. For the flight model, it is anticipated that custom-fabricated waveguide will be integrated directly to the T-junction so no adapter will be needed. This junction operates as follows. For input signals to ports 2 and 3 that are equal in magnitude and phase (symmetric excitation), the sum of these signals emerges at port 1 (port 4 is isolated). For input signals to ports 2 and 3 that are equal in magnitude and 180° out of phase (antisymmetric excitation), the sum of these signals emerges at port 4 (port 1 is isolated). In general, any set of input signals to ports 2 and 3 may be described as a superposition of symmetric and antisymmetric excitations. For this application, the goal is a purely symmetric excitation so that power from pairs of MMIC amplifiers is combined at port 1 with little loss. A purely symmetric excitation is difficult to achieve in practice, so a matched load is always placed at port 4 to absorb what little RF power goes there.

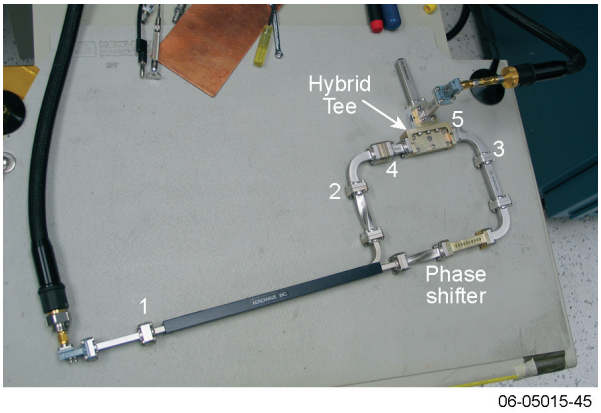

Figure A-5. Photograph of test setup used to evaluate hybrid T-junction.

The test setup shown in Figure A-5 was used to apply a mostly symmetric excitation to ports 2 and 3 of the hybrid T-junction. Labeled locations in the figure are where measurements were made during calibration of the setup. Location 1 is the input of a 1:1 power splitter. One branch of the power splitter goes through a clockwise twist to location 2. From location 2, signal is directed to location 4 (one input of the hybrid T-junction) through an H-plane bend, a stack of waveguide spacers, and a short straight section of waveguide. The other branch of the power splitter goes through a counterclockwise twist, the phase shifter, an H-plane bend, and a straight waveguide section to location 3. From location 3, signal is directed to location 5 (the other input of the hybrid T-junction) through an H-plane bend.

A Thru-Reflect-Line (TRL) calibration was performed by using an HP8510 network analyzer and waveguide test ports over a frequency range of 31 to 33 GHz. Measurements were made of S_{21}, S_{31}, S_{42}, and S_{53}, and the results at 32 GHz are shown in Table A-3.

It is evident that the path from location 4 to location 1 has a total phase of –27.1°, whereas the path from location 5 to location 1 has a total phase of –18.3°. The phase delay between location 4 and location 1 is 8.8° shorter than that of the other path. The phase shifter was adjusted to produce an additional phase delay of 8.8° in the path from location 5 to location 1. After this was done, direct

Table A-3. S-parameter measurements of test setup for hybrid T-junction at 32 GHz.

S_{21}	S_{42}	S_{31}	S_{53}
0.6803 ∠ +79.2°	0.9843 ∠ –106.3°	0.6673 ∠ +86.9°	0.9909 ∠ –105.2°

measurements of S_{41} and S_{51} were made, and the results at 32 GHz are shown in Table A-4.

The numbers in Table A-4 describe the excitation at ports 2 and 3 of the T-junction, and the excitation may be expressed as a superposition of symmetric and antisymmetric inputs. The purpose is to calculate how much power is expected to emerge at port 1 and then compare this result to the measured power. This comparison will give the insertion loss of the T-junction and adapter. The calculation suffers little error if the phases of S_{41} and S_{51} are assumed equal, since they are within 0.2° of each other. The amplitude of the symmetric inputs is (0.6679 + 0.6642)/2 = 0.66605, and the amplitude of the antisymmetric inputs is (0.6679 – 0.6642)/2 = 0.00185. The symmetric input voltages are reduced by a factor of $\sqrt{2}$ to account for the 3-dB coupler loss and then added together:

$$0.66605/\sqrt{2} + 0.66605/\sqrt{2} = 0.94194 \ .$$

The square of this quantity is proportional to the power coming out of port 1, so we have an expected power of 0.94194^2 = 0.88725 W. A measurement of voltage at port 1 at 32 GHz resulted in a value of 0.9106 ∠ +47.0°. The square of the magnitude is proportional to the measured power: 0.9106^2 = 0.82919 W. The insertion loss of the folded hybrid T-junction with adapter is thus

$$-10 \log_{10}(0.82919/0.88725) = 0.29 \text{ dB} \ .$$

It is reasonable to assume that this loss is shared about equally between the adapter and the hybrid T-junction, since the length of waveguide in each is about the same. Under this assumption, the insertion loss of the hybrid T-junction alone may be approximated as follows. The power lost in the T-junction with adapter is 0.88725 W – 0.82919 W = 0.05806 W. Half of this loss, or 0.02903 W, is due to the T-junction alone. The insertion loss for the T-junction alone is approximately

$$-10 \log_{10}[(0.88725 - 0.02903)/0.88725] = 0.14 \text{ dB}.$$

The loss through the hybrid T-junction is acceptable for the intended application. A flight version of this component would benefit from a dip-brazed or electroformed design rather than the split block construction of the engineering model, as substantial weight savings should be obtainable.

Table A-4. Salient S-parameters at 32 GHz of test setup for T-junction, after phase adjustment.

S_{41}	S_{51}
0.6679 ∠ –29.1°	0.6642 ∠ –29.3°

A.2.3 Hybrid Septum Polarizer (Renaissance Electronics Part #21WR28NA)

The hybrid septum polarizer is shown in Figure A-6. It has two WR28 input ports (P1 and P2), and one output port (P3) that is nearly square in aspect ratio. Applying power only to P1 results in a right-hand circularly polarized (RHCP) wave emerging from P3. Applying power only to P2 results in a left-hand circularly polarized (LHCP) wave emerging from P3. The loss through this device was measured by measuring signals at the input ports of the polarizer (P1 and P2) with the output port short-circuited. In this configuration, input to P1 will produce a right-hand circularly polarized wave at P3 that is then reflected as a left-hand circularly polarized wave. This reflected wave exits P2. The converse is true with input to P2. Measuring the insertion loss of this system gives twice the one-way RF power loss from an input port to P3. The waveguide test ports were calibrated by using a standard TRL method, and then the measurement was made relative to a "Thru" connection where the test ports were connected to each other. The S-parameters at 32 GHz for the Thru connection and for the hybrid septum polarizer measurement are shown in Table A-5.

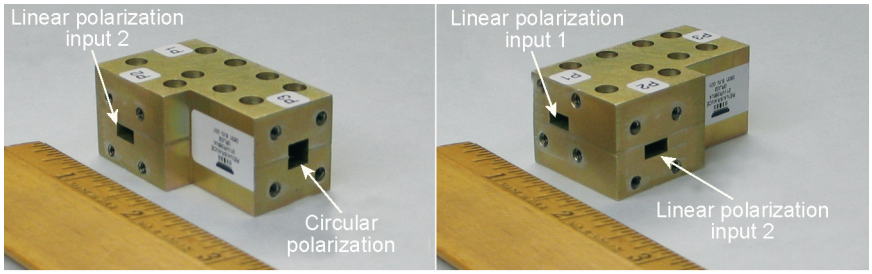

06-05015-46

Figure A-6. Two views of the hybrid septum polarizer.

Table A-5. S-parameter measurements of Thru connection and hybrid septum polarizer 32 GHz.

	S_{11}	S_{12}	S_{21}	S_{22}
Thru connection	0.0044 ∠ –47.14°	0.9981 ∠ –0.02°	0.9981 ∠ –0.02°	0.0035 ∠ –49.09°
Septum polarizer	0.1094 ∠ –147.7°	0.9551 ∠ –126.2°	0.9548 ∠ –126.3°	0.1082 ∠ +71.7°

Assuming that the Thru connection should have been ideal, the error in the measurement of Thru insertion loss is given by $1 - |S_{12}| = 1 - |S_{21}| = 0.0019$. This number is used to adjust $|S_{12}|$ and $|S_{21}|$ of the septum polarizer measurement so that the measurement is taken relative to an ideal Thru. Thus, the adjusted magnitudes of S_{12} and S_{21} for the septum polarizer are, respectively, 0.9551 + 0.0019 = 0.9570 and 0.9548 + 0.0019 = 0.9567. The amount of signal lost during a trip from P1 to P2 (with P3 short-circuited) is 1 – 0.9570 = 0.043. Similarly, the loss during a trip from P2 to P1 is 1 – 0.9567 = 0.0433. Using the larger loss number, we divide by 2 to get the amount of signal lost in an excursion from P1 to P3: 0.0433/2 = 0.02165. The insertion loss is obtained from the following formula:

$$-20 \log_{10}(1 - 0.02165) = 0.19 \text{ dB}$$

(the log function is multiplied by 20 in this case because the argument is expressed as a voltage rather than a power).

Antenna patterns measured for the hybrid septum polarizer are shown in Figure A-7. The device was configured to radiate RHCP radiation, and both this and the LHCP pattern were measured for the two principal plane cuts (elevation angles from –90° to +90°, azimuthal angles of 0° and 90°). On boresight, the RHCP pattern is at least 25 dB higher than the LHCP pattern for both principal plane measurements, which implies a good axial ratio.

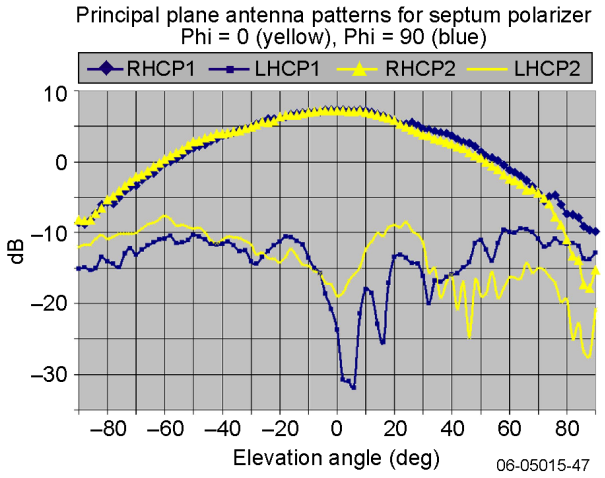

Figure A-7. Antenna patterns of hybrid septum polarizer.

Both the low insertion loss and the good axial ratio of the hybrid septum polarizer qualify it to be included in the Solar Probe Ka-band RF system. The flight version of the hybrid septum polarizer would benefit from a construction method other than the split block construction of the engineering model. A dip-brazed or electroformed device would have a substantial weight savings and smaller volume.

Unfortunately, Renaissance Electronics made the decision to discontinue support of its waveguide engineering capability just before publication of this memorandum report.[2] All three components can be produced by other vendors of waveguide hardware. One recommended vendor is Chelton Microwave, Atlantic Division, 58 Main St., Bolton, MA 01740, Tel: (878) 779-6963, Fax: (878) 779-2906, www.atlanticmicrowave.com.

A.3 Low-Loss Transitions Between Waveguide and Microstrip

An RF system design that uses waveguides for low-loss characteristics but also uses gallium arsenide (GaAs) MMIC technology for RF amplification must necessarily deal with the waveguide-to-microstrip transition. The goal of the waveguide-to-microstrip transition is to present the optimal source impedance at the input of the MMIC amplifier and the optimal load impedance at the output of the MMIC amplifier, while minimizing RF power loss.

A first draft of the MMIC amplifier topology was designed by Dr. Michel Reece and Mr. John Penn of APL, based on pHEMT technology by TriQuint (0.004-in.-thick GaAs substrate). This amplifier used a 30-Ω microstrip line on the input side and had an input impedance Z_{input} = 188 Ω. A 50-Ω microstrip line was used on the output side, and the output impedance was Z_{output} = 23 Ω.

[2]The engineer who was responsible for designing and fabricating the phase shifter, hybrid T-junction, and hybrid septum polarizer is Philip N. Walker, who has started his own consulting firm: Absolut Microwave, Sudbury, MA, Tel: (928) 443-8947.

Computer simulations in High-Frequency Structure Simulator (HFSS) software (Ansoft Corp.) were carried out to design two waveguide-to-microstrip transitions, one for the input side of the amplifier and the other for the output side. The transition on the input side was designed to present 188 Ω to the amplifier input port, while the transition on the output side was designed to present an impedance of 23 Ω at the output port. The concept is shown in Figure A-8.

The upper drawing in Figure A-8 shows a cutaway of the side view of the assembly. The input waveguide and output waveguide are joined by a tunnel that contains a GaAs board with the MMIC amplifier and the two transitions. The width of the tunnel is less than that of the waveguides, which means that the operating frequency of 32 GHz is below the cutoff frequency of the tunnel, so the tunnel effectively prevents RF from bypassing the MMIC and coupling directly from one waveguide to the other. The tunnel width is easily seen in the lower drawing of Figure A-8, which is a cutaway looking down on the GaAs board. Also visible in this view are the smaller waveguide probe with a 30-Ω microstrip line on the input side, the larger waveguide probe with a 50-Ω microstrip line on the output side, and the MMIC separating the two microstrip lines. The ground plane of the GaAs board ends at the point where the board enters the waveguides so that the microstrip probes can couple to the waveguide fields. The impedance presented to the MMIC amplifier depends on the dimensions of the microstrip probes; thus, the dimensions of the input probe are different from those of the output probe. The drawing at the right of Figure A-8 shows the width of the waveguide probe as W, the length of the probe as L, and the distance from the waveguide inner wall to the end of the microstrip line as D. There is a 20-mil length of line between the probe and the line of length D. The length D was chosen so that the impedance seen from the microstrip port is purely real. Table A-6 gives the values of W, L, and D for the input transition and the output transition.

These values were obtained from HFSS simulations, and the models are shown in Figure A-9. For the input transition at 32 GHz, the reflection coefficient seen by looking into the microstrip port is $\Gamma = 0.717 \angle +0.21°$. The characteristic impedance of the microstrip line is 30 Ω. Ignoring the

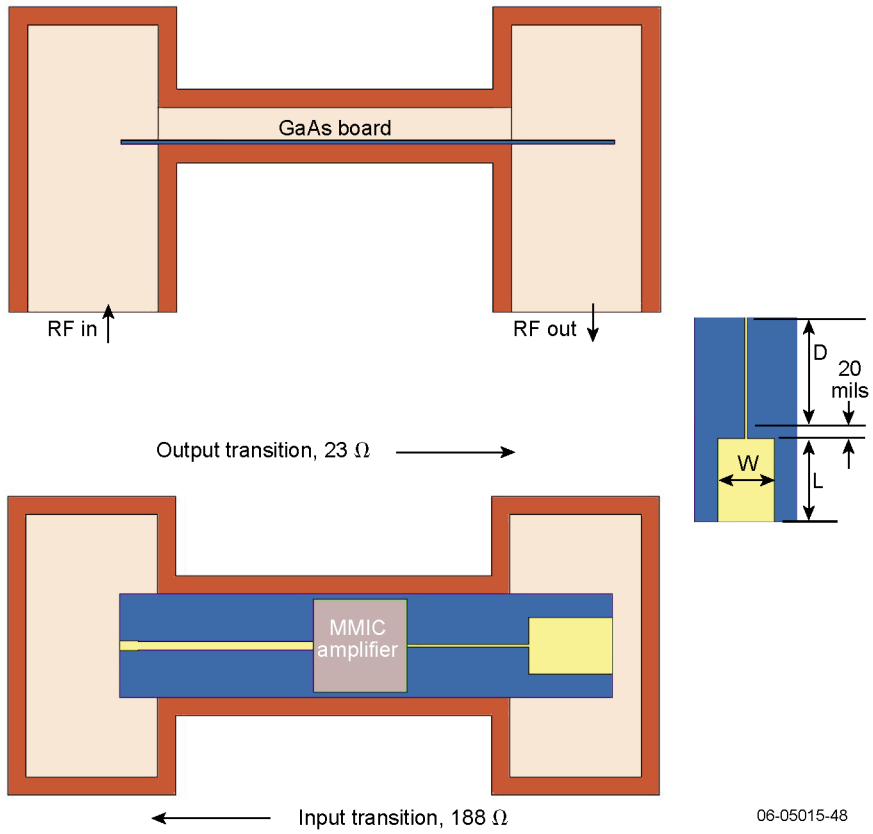

Figure A-8. Cutaway of transition assembly, side view (upper) and top view (lower).

Table A-6. Characteristic dimensions of microstrip probes and lines

	Probe W (mils)	Probe Length L (mils)	Microstrip Line Length D (mils)
Transition, input side of MMIC	11.1	20	167
Transition, output side of MMIC	60.2	90	110.6

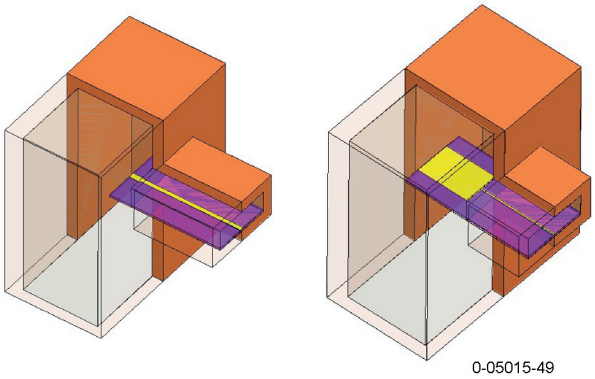

Figure A-9. HFSS models of input (left) and output (right) transitions.

negligible phase of Γ, we calculate the impedance seen by looking into the microstrip port:

$$Z_{\text{input}} = (30\ \Omega)\frac{1+0.717}{1-0.717} = 182\ \Omega\,.$$

For the output transition at 32 GHz, the reflection coefficient seen by looking into the microstrip port is Γ = 0.363∠ +179.3°. The characteristic impedance of the microstrip line is 50 Ω. Taking the value of the reflection coefficient as −0.363, we calculate the impedance seen by looking into the microstrip port:

$$Z_{\text{output}} = (50\ \Omega)\frac{1-0.363}{1+0.363} = 23.4\ \Omega\,.$$

These impedance values come reasonably close to the desired values.

As emphasized earlier, it is important to minimize power loss between the SSPA and the antenna. For this reason, low loss in the output transition is a critical parameter for system performance. At 32 GHz, the HFSS model of the output transition gives $|S_{21}|$ = −0.86 dB. Comparing this value with the measured loss figures for the hybrid T-junction and the hybrid septum polarizer, this output transition loss is too high. While the HFSS models have shown that it is possible to obtain the desired impedances for the input and output transitions, further work is needed to reduce the loss of the output transition.

To verify the accuracy of the HFSS models, engineering models of these transitions were fabricated so that measurements could be performed. One difficulty became clear: while it is easy to obtain the reflection coefficient of the microstrip port directly from the HFSS models shown in Figure 8-9, it would be difficult to conduct an actual measurement since the microstrip ports do not conform to standard measurement hardware. For this reason, a different approach was implemented for both simulation and measurement. The design of each transition is mirrored about the microstrip port to form a bilaterally symmetric circuit. The mirrored circuit has waveguide ports that conform to standard measurement hardware, so measurements are easily done. Figure A-10 illustrates the idea.

With this arrangment, S-parameters are obtained of the mirrored circuit for three different GaAs boards: a Thru, a Reflect, and a Line. Using the formalism for a standard TRL calibration procedure (described in detail in Section A.4), the reflection coefficient at the microstrip port (seen by looking into the microstrip reference plane toward the waveguide) may be expressed in terms of measured S-parameters of the mirrored circuit for the Thru, Reflect, and Line. This method was employed for the

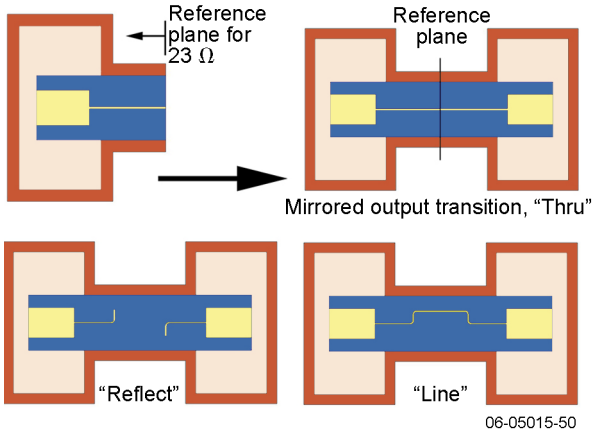

Figure A-10. Mirrored circuit concept with three measurement boards.

HFSS simulations, and the results were compared with those from an HFSS model of a single (non-mirrored) transition. The reflection coefficients at 32 GHz for the input and output transitions are shown in Table A-7. One set of values is taken directly from the HFSS model of the non-mirrored transitions (Γ_1), and the other set of values is derived from S-parameters of the mirrored circuits (Γ_2). (Plots of this comparison over a frequency sweep are shown in Figures A-11 and A-12.) The values compare well enough to validate the method of using measurements on mirrored circuits to obtain the reflection coefficient at the microstrip port. Note also that the HFSS results are most accurate at 32 GHz, since this is the adaptive frequency that was used in the models. HFSS extrapolates the field solution at 32 GHz across the requested frequency range by using an adaptive Lanczos-Padé sweep based solver, so accuracy decreases as the sweep frequency differs from the adaptive frequency.

Test hardware was designed to replicate as closely as possible the HFSS models that were used. The hardware consists of a test fixture body that connects to the network analyzer test ports, three GaAs boards that are each attached to a carrier plate, and an end cap. Figure A-13 shows photographs of these components, as well as the assembled hardware compared with the HFSS model. The carrier with a GaAs board is screwed into the end cap, and this assembly is then screwed down onto the test fixture body. The following principles were used in the design of the GaAs boards.

- The Thru is simply a direct mirroring of the microstrip-to-waveguide transition as shown in Figure A-10.
- The Reflect is a length of open circuited microstrip line attached to the waveguide probes.
  - Open circuits were selected instead of short circuits because they are easier to fabricate—they do not require vias to ground.
  - The TRL calibration procedure does not require a reflection coefficient of unity from the Reflect measurement, only that it be different from zero.
- The Line is a length of microstrip whose phase delay is approximately 90° greater than the phase delay of the Thru at 32 GHz.

The HP8510 network analyzer with waveguide test ports was calibrated by using a standard TRL calibration procedure. Test fixtures for both the

Table A-7. Comparison of Γ from non-mirrored (Γ_1) and mirrored (Γ_2) HFSS models at 32 GHz.

	Γ_1	Γ_2
Transition, input side of MMIC	0.717 ∠ +0.2°	0.727 ∠ +4.5°
Transition, output side of MMIC	0.363 ∠ +179.3°	0.341 ∠ –179.0°

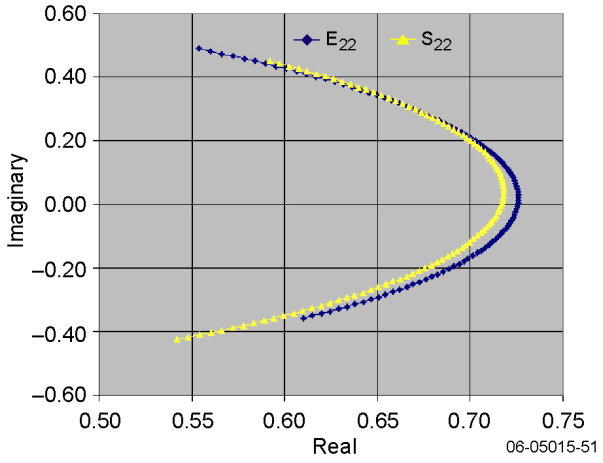

Figure A-11. Comparison of reflection coefficients from a HFSS single-sided model Γ (S_{22}) vs. mirrored model Γ (E_{22}), 31 to 33 GHz, input of SSPA.

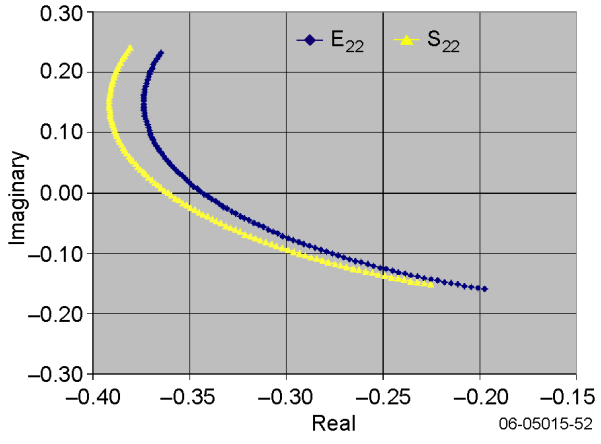

Figure A-12. Comparison of reflection coefficients from a HFSS single-sided model Γ (S_{22}) vs. mirrored model Γ (E_{22}), 31 to 33 GHz, output of SSPA.

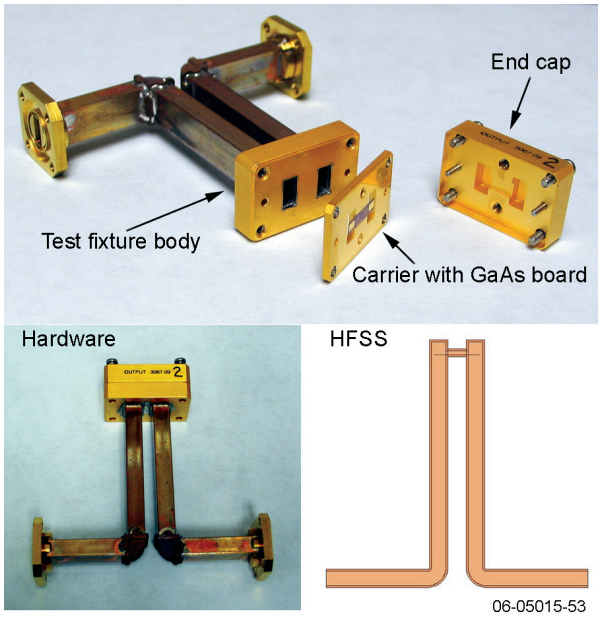

Figure A-13. Test hardware with transition on output side of MMIC, and HFSS model for comparison.

input transition and the output transition were measured with this calibrated setup; one measurement for each of the Thru, Reflect, and Line microstrip boards was taken for the two test fixtures. From these S-parameter data, the reflection coefficient of the microstrip port at the Thru reference plane was derived for the two cases.

This first measurement attempt did not compare well with HFSS predictions, and the hardware was scrutinized for defects. Two problems were quickly identified: excess silver solder under the GaAs boards extending into the waveguide space, and poor solder joints between the waveguide sections and the test fixture body. These problems were corrected and new measurements were taken. Table A-8 shows the results at 32 GHz and compares them to predictions of the HFSS mirrored models and to the original goal.

These results warrant some discussion. First, predictions from HFSS mirrored models come reasonably close to the intended goal. The difference between the two is larger for the output transition, but this is merely a matter of refining probe dimensions in the model to obtain results that are closer to the goal. Therefore, the difference between the HFSS mirrored models and the goals is not of concern. Of more concern is the difference between the measurement results and the model predictions. If the correlation between the two is not strong, then computer simulations are of limited value in designing a low-loss transition between microstrip line and waveguide.

An examination of the measurement data was undertaken. Three observations were noted and can be illustrated with the subset of measurement data presented in Table A-9. First, all measurements exhibited excellent reciprocity in that $|S_{21}|$ and $|S_{12}|$ are within 0.1% of each other and $\angle S_{21}$ and $\angle S_{12}$ are within 0.01% of each other across the frequency sweep. This behavior is expected of a mirrored circuit. Second, input transition measurements exhibited mediocre symmetry in that $|S_{11}|$ and $|S_{22}|$ are within 2.2% of each other with $|S_{11}|$ being consistently larger than $|S_{22}|$ across the frequency sweep. The phase difference between S_{11} and S_{22} is approximately 10° around 32 GHz with S_{22} having a consistently longer phase delay than S_{11}. The measured symmetry was not as bad for the output transition but still not nearly as good as the measured reciprocity. A 10° phase difference between S_{11} and S_{22} corresponds to a path length difference of 0.007 in. at 32 GHz. Such a path length difference is conceivable since there are several waveguide solder joints along the path and each one has a tolerance of ±0.002 in.

One way to improve the test hardware, that is, make it closer to the ideal HFSS models, would be to use electroforming to build the hardware and to implement tighter manufacturing tolerances.

Recommendations for further development of low-loss waveguide-to-microstrip transitions for flight include (1) strive for hardware and computer models that resemble each other more closely, and (2) incorporate into the hardware a mechanical fine-tuning capability. The first recommendation would involve more stringent mechanical tolerances in the manufacture of parts. A different method of manufacture such as electroforming may be helpful, since it would allow the test fixture

Table A-8. Comparison at 32 GHz of reflection coefficients from simulation and measurement.

	HFSS, Mirrored Model	Measurement	Goal
Transition, input side	0.7247 ∠ +1.0°	0.5996 ∠ –10.4°	0.7248 ∠ 0°
Transition, output side	0.339 ∠ –178.2°	0.4067 ∠ –171.6°	0.3699 ∠ 180°

Table A-9. Sample TRL measurements of test fixture for the input transition.

(a) Thru

f (GHz)	$\|S_{11}\|$	$\angle S_{11}$ (deg)	$\|S_{12}\|$	$\angle S_{12}$ (deg)	$\|S_{21}\|$	$\angle S_{21}$ (deg)	$\|S_{22}\|$	$\angle S_{22}$ (deg)
31.80	0.120	52.7	0.852	–138.1	0.851	–138.1	0.117	41.4
31.82	0.125	57.1	0.852	–145.6	0.851	–145.6	0.121	45.0
31.84	0.134	60.1	0.851	–153.1	0.851	–153.1	0.129	47.7
31.86	0.147	61.7	0.850	–160.6	0.850	–160.7	0.141	49.2
31.88	0.163	61.7	0.848	–168.2	0.848	–168.2	0.156	49.3
31.90	0.181	60.4	0.845	–175.7	0.845	–175.7	0.172	48.2
31.92	0.201	58.0	0.842	176.8	0.842	176.8	0.191	45.9
31.94	0.222	54.4	0.839	169.4	0.839	169.4	0.211	42.5
31.96	0.244	50.0	0.835	161.9	0.835	161.9	0.232	38.5
31.98	0.265	45.2	0.830	154.4	0.830	154.5	0.253	34.1
32.00	0.286	40.1	0.824	147.0	0.825	147.1	0.275	29.1
32.02	0.309	34.6	0.819	139.6	0.819	139.6	0.298	23.7
32.04	0.330	28.8	0.813	132.2	0.813	132.3	0.320	18.1
32.06	0.351	22.8	0.806	124.9	0.806	124.9	0.342	12.4
32.08	0.373	16.8	0.799	117.6	0.799	117.6	0.364	6.4
32.10	0.394	10.6	0.791	110.3	0.792	110.3	0.384	0.3
32.12	0.414	4.1	0.783	103.1	0.784	103.1	0.404	–5.9
32.14	0.433	–2.2	0.776	96.0	0.775	95.9	0.424	–12.1
32.16	0.452	–8.5	0.767	88.8	0.767	88.7	0.444	–18.5
32.18	0.471	–14.9	0.758	81.7	0.757	81.7	0.462	–24.9
32.20	0.489	–21.4	0.750	74.7	0.749	74.7	0.481	–31.3

(b) Reflect

f (GHz)	$\|S_{11}\|$	$\angle S_{11}$ (deg)	$\|S_{22}\|$	$\angle S_{22}$ (deg)
31.80	0.996	65.6	0.974	58.2
31.82	0.995	59.5	0.974	52.1
31.84	0.995	53.5	0.973	46.0
31.86	0.995	47.5	0.974	40.0
31.88	0.994	41.5	0.974	34.0
31.90	0.992	35.7	0.974	27.9
31.92	0.992	29.9	0.973	21.9
31.94	0.993	24.0	0.973	16.0
31.96	0.993	18.1	0.973	10.2
31.98	0.990	12.1	0.973	4.3

f (GHz)	$\|S_{11}\|$	$\angle S_{11}$ (deg)	$\|S_{22}\|$	$\angle S_{22}$ (deg)
32.00	0.989	6.3	0.975	–1.7
32.02	0.988	0.5	0.977	–7.7
32.04	0.986	–5.3	0.978	–13.6
32.06	0.985	–11.1	0.979	–19.4
32.08	0.986	–16.9	0.979	–25.2
32.10	0.985	–22.7	0.978	–31.0
32.12	0.985	–28.6	0.978	–36.7
32.14	0.984	–34.3	0.978	–42.6
32.16	0.984	–40.1	0.978	–48.3
32.18	0.984	–45.8	0.976	–54.1
32.20	0.984	–51.5	0.978	–59.8

(c) Line

f (GHz)	$\|S_{11}\|$	$\angle S_{11}$ (deg)	$\|S_{12}\|$	$\angle S_{12}$ (deg)	$\|S_{21}\|$	$\angle S_{21}$ (deg)	$\|S_{22}\|$	$\angle S_{22}$ (deg)
31.80	0.883	47.6	0.406	132.5	0.406	132.4	0.862	38.6
31.82	0.882	41.3	0.405	126.2	0.405	126.1	0.862	32.3
31.84	0.882	35.1	0.405	119.9	0.405	119.8	0.862	26.0
31.86	0.882	29.0	0.404	113.6	0.404	113.5	0.863	19.8
31.88	0.881	22.8	0.404	107.3	0.404	107.3	0.863	13.6
31.90	0.879	16.8	0.403	101.2	0.403	101.1	0.863	7.4
31.92	0.879	10.8	0.403	95.0	0.403	95.0	0.863	1.1
31.94	0.880	4.7	0.403	88.9	0.403	88.9	0.862	–5.0
31.96	0.879	–1.5	0.404	82.7	0.403	82.7	0.862	–11.0
31.98	0.876	–7.6	0.403	76.5	0.404	76.5	0.863	–17.1
32.00	0.874	–13.7	0.403	70.3	0.404	70.4	0.865	–23.4
32.02	0.873	–19.7	0.404	64.3	0.404	64.2	0.866	–29.5
32.04	0.872	–25.7	0.404	58.2	0.404	58.2	0.866	–35.6
32.06	0.871	–31.8	0.405	52.1	0.405	52.1	0.867	–41.7
32.08	0.871	–37.8	0.406	45.9	0.406	46.0	0.866	–47.7
32.10	0.869	–43.9	0.407	39.9	0.407	39.8	0.865	–53.8
32.12	0.868	–50.0	0.408	33.8	0.409	33.7	0.864	–59.8
32.14	0.867	–56.1	0.409	27.8	0.409	27.7	0.863	–65.9
32.16	0.867	–62.1	0.411	21.7	0.411	21.6	0.862	–71.9
32.18	0.866	–68.1	0.412	15.6	0.412	15.6	0.860	–77.9
32.20	0.865	–74.1	0.414	9.6	0.414	9.6	0.860	–83.9

to be made in once piece, thus eliminating imprecision in some of the assembly process. Also, the HFSS models can be modified to include known nonidealities in the hardware. The second recommendation is needed because, no matter how closely the the HFSS models represent the hardware, there is always some imprecision in the simulations. The simulation results may yield a hardware design that is close to the goal, but some fine tuning will be needed at the last step of hardware testing.

A.4. Thru-Reflect-Line (TRL) Formalism Applied to Design of Transition

This section describes how the standard TRL calibration procedure is applied to measurements of mirrored circuits and how desired quantities are derived from it. More specifically, three S-parameter measurements are performed on a bilaterally symmetric circuit. The circuit is formed by mirroring a waveguide-to-microstrip transition about the plane of the microstrip port. The three measurements are for the cases of a Thru, Reflect, and Line circuit board installed in the symmetric circuit. The formalism presented here follows the excellent discussion of TRL calibration in class notes written by Dr. Marion Lee Edwards and uses the same notation.[3]

The purpose of any RF calibration procedure is to reduce the errors in measurements by as much as possible. Each port of the two-port test setup is modeled as an error network followed by

[3]TRL calibration in class notes of Dr. Marion Lee Edwards are available at the website of EdCom Technologies, http://www.gee-cad.com/.

the test port that connects to the device under test (DUT). The error networks are characterized by their transmission parameters, or R-parameters (sometimes denoted as ABCD parameters). R-parameters are analogous to S-parameters in that they describe the behavior of two-port networks. The difference is that R-parameter matrices can be multiplied in a cascade to describe the response of several concatenated two-port networks. R-parameters are readily obtainable from S-parameters, and the transformation may be found in any basic microwave textbook.[4]

By measuring known standards (Thru, Reflect, Line) in place of the DUT, the error terms in the error networks may be derived and then used to correct the raw measurements made at the test ports. Among the error terms that are calculated are the reflection coefficients seen looking into ports 1 and 2. These error terms are denoted as e_{22} and f_{22}. The situation is illustrated in Figure A-14.

Recall that we are interested in the impedance seen by looking into a microstrip port toward a waveguide junction. This impedance can be obtained if we know the reflection coefficient of the microstrip port and the characteristic impedance of the microstrip. The reflection coefficient of the microstrip port is difficult to measure directly, since the port is incompatible with standard test port hardware. Instead, the waveguide-to-microstrip transition is mirrored about the microstrip port to form a bilaterally symmetric circuit with two waveguide ports. The waveguide ports are compatible with standard test port hardware, so S-parameter measurements of the mirrored circuit are easy to perform. The mirrored transition effectively becomes a Thru standard for a TRL calibration procedure (see Figure A-10). Two other S-parameter measurements are made with this mirrored circuit, with a Reflect and a Line microstrip circuit installed. In this method, the waveguide-to-microstrip transition essentially becomes part of the error network. The error term e_{22} give us the reflection coefficient seen by looking into the microstrip port at the reference plane of the Thru, looking toward port 1. Likewise, the error term f_{22} gives us the same information seen by looking toward port 2. In this case, ideally, the two error terms should be identical. Only the term e_{22} will be discussed from here onward.

The formula for e_{22} is

$$e_{22} = \pm\sqrt{\left(\frac{b - G_{MX}}{a - G_{MX}}\right)\left(\frac{c + G_{MY}}{d + G_{MY}}\right)\left(\frac{b - G_{M1}}{a - G_{M1}}\right)}.$$

The quantities G_{MX} and G_{MY} are, respectively, S_{11} and S_{22} of the Reflect measurement. The quantity G_{M1} is S_{11} from the Thru measurement.

The quantities a and b are roots of the quadratic equation $M_{21}X^2 + (M_{22} - M_{11})X - M_{12} = 0$ such that $|b| < |a|$. The quantities M_{xy} are elements of the 2×2 matrix M, which is given by

$$M = R_{\text{Line}} R_{\text{Thru}}^{-1},$$

where R_{Line} is the R-matrix obtained from the S-parameter measurements of the Line circuit and R_{Thru} is the R-matrix obtained from the S-parameter measurements of the Thru circuit.

Similarly, the quantities c and d are roots of the quadratic equation $N_{12}Y^2 + (N_{22} - N_{11})Y - N_{21} = 0$ such that $|d| < |c|$. The quantities N_{xy} are elements of the 2×2 matrix N, which is given by

$$N = R_{\text{Line}}^{-1} R_{\text{Thru}},$$

where R_{Line} and R_{Thru} are the same as defined previously.

The sign of e_{22} is chosen to yield the expected phase angle. For example, when designing the waveguide-to-microstrip transition at the input side of the MMIC, we want an impedance of 188 Ω. This impedance is on the high-impedance side of the Smith chart, so the expected phase angle is near 0°, and not 180°. Conversely, when designing the transition at the output side of the MMIC, we want an impedance of 23 Ω. This impedance is on the low-impedance side of the Smith chart, so the expected phase angle is near 180°, and not 0°.

[4]For example, Pozar, David M., *Microwave Engineering*, 2nd Edition, Wiley, 1997, 736 pp.

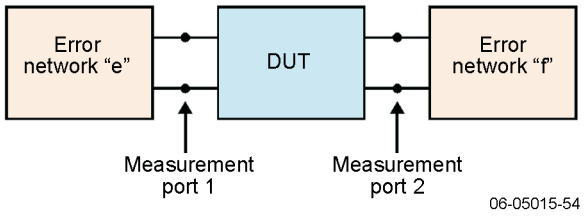

Figure A-14. Block diagram of general test setup with error networks.

A.5 Summary

A design for the Ka-band portion of the Solar Probe RF subsystem has been proposed. The design uses a solid-state power amplifier and waveguide

transmission lines to minimize RF loss between the amplifier and the antenna. Three waveguide components of the design were obtained as engineering models and tested. Test results show that these components perform well enough to satisfy system requirements. Some refinement is needed to realize these components in a flight-qualified version. The design of a transition from waveguide to microstrip line was presented, including results from computer simulation and hardware measurements. Computer simulations showed that it is possible to design transitions that present the desired impedances to the input and output ports of a GaAs MMIC amplifier. The insertion loss of the output transition needs to be reduced in order for the concept to be usable. Hardware measurement results were not as close to the computer simulations as desired, partly due to mechanical tolerance issues. To obtain a usable transition design, two recommendations were made. First, strive for better correlation between the computer models and the hardware design. This can be done by implementing a different construction method and tighter mechanical tolerances for the hardware and by including known nonidealities in the computer model. Second, implement some kind of fine-tuning apparatus in the hardware design so that desired performance can be obtained via tuning during integration and testing.


NASA
APL